First Solar Neutrinos from KamLAND:
A Measurement of the ^{8}B Solar Neutrino Flux

by

Lindley Anne Winslow

B.A. (University of California, Berkeley) 2001
M.A. (University of California, Berkeley) 2007

A dissertation submitted in partial satisfaction of the
requirements for the degree of
Doctor of Philosophy

in

Physics

in the

GRADUATE DIVISION
of the
UNIVERSITY OF CALIFORNIA, BERKELEY

Committee in charge:
Professor Stuart J. Freedman, Chair
Professor Marjorie Shapiro
Professor Leo Blitz

Fall 2008

The dissertation of Lindley Anne Winslow is approved:

_____

Chair   Date

_____

Date

_____

Date

University of California, Berkeley

Fall 2008

First Solar Neutrinos from KamLAND:
A Measurement of the ^{8}B Solar Neutrino Flux

Abstract

First Solar Neutrinos from KamLAND:
A Measurement of the ^{8}B Solar Neutrino Flux

by

Lindley Anne Winslow
Doctor of Philosophy in Physics

University of California, Berkeley

Professor Stuart J. Freedman, Chair

The result of this work is a measurement of the ^{8}B solar neutrino flux using neutrino-electron elastic scattering in KamLAND with a 5 MeV threshold. KamLAND is a 1 kilo-ton liquid scintillating detector located in Kamioka, Japan. The total 118 kt-day exposure results in a flux of 1.87 ± 0.24(stat.)±0.32(syst.)$\times10^6$ cm^{-2}s^{-1}. The uncertainty in the measurement is dominated by the statistics of the candidate sample and the uncertainty in ^{11}Be production from muon spallation. This result is consistent with previous measurements and predictions from the Standards Solar Model with matter enhanced neutrino oscillation.

Professor Stuart J. Freedman
Dissertation Committee Chair

To
Nancy
and
Jake

Contents

List of Figures

List of Tables

Acknowledgments

I was lucky enough to spend almost a year on site in Mozumi, spread over 17 trips, all of which were memorable. I need to thank Masayuki Koga for reminding me that I should eat something besides ramen, and I need to thank Kengo Nakamura for smiling the day the Berkeley car died. I also need to thank Greg Keefer and Chao Zhang for picking me up at the train station on many occasions and always being willing to eat CoCo's Curry. Finally, though she is not an official member of KamLAND, I need to thank Katsuko Shimizu for taking care of all the graduate students and making sure we did more than just work in the mine.

Berkeley has been my home now for eleven years and there are many who have inspired and guided me along the way. My advisor Stuart Freedman deserves much credit for encouraging me to work on many different KamLAND projects and for pushing me to make the present work as good as it could possibly be. I also appreciate the freedom and support he gave me to coordinate SWPS and serve as an officer of the APS. I need to thank my committee, Marjorie Shapiro and Leo Blitz, firstly for reading all of this and secondly for their valuable comments. The other person who has read almost every page is Patrick Decowski. He has been a great mentor and I cannot thank him enough for his help. Brian Fujikawa has taught me how to be a diligent physicist. His voice will always be the one I hear when I am tempted to be lazy with an analysis, and maybe if I am very good he will tell me my nickname one day. Jason Detwiler has taught me to love statistics or at the very least to respect them, and he helped immensely with the details of the neutrino oscillation section. Then there is the rest of the Berkeley post-docs, though you have moved on. I will always consider you "my post-docs" and I appreciate everything you taught me, Lauren Hsu, Reina Maruyama, Karsten Heeger, Fred Gray, Bruce Berger, Christian Lendvai, Tom Banks, Thomas Bloxham, and Koichi Ichimura. Finally, there is Dan Dwyer and Tommy O'Donnell, my fellow Berkeley graduate students. They are two of the nicest and smartest people I know and I am lucky to have had this experience with you both.

I need to thank my wonderfully supportive friends and family. Thank you to Annie Endozo for always being willing to go see movies that Jake will not watch, and thank you to Robert Barrueto and Erica Friesen for letting me invite myself and anyone else over to your house. Thank you to my Grandfather Ross Watson, otherwise known as GD, for

actually wanting to hear about eigenvalues. Thank you to Grandmother and Grandfather Winslow for purposely watching all PBS programs involving neutrinos, and thank you to all the Watson, Winslow, Wilson, Smiths for being there when I needed you. In the last year I gained several new family members who have made sure Jake and I still eat on occasion and have puppies to play with, Sharon, R.S., Jessica and Shawn, you have all been wonderful. Any mention of family is incomplete without my four wonderful siblings, Mary Beth, Sam, Tessa, and Julia, and my adorable niece Harmony. Whether you happen to be a "hamsterbrain" or not, I love you all. As to my husband Jake Siegel, there are not enough words to describe how wonderful you are. There will be a puppy for you soon, I promise. Lastly, I need to thank my parents Nancy and Dean Winslow. My mother did not live long enough to see me finish, but never do I doubt that she loved and supported me, and so much of who I am is thanks to her. For my dad who will understand, I will just finish by saying....

"Thank you Thank you Thank you".

Chapter 1

Introduction

The neutrino is a remarkable particle. From its birth as the solution to energy non-conservation in the beta decay of unstable nuclei to its signature in the cosmic microwave background, it has been the thread tying together nuclear physics, particle physics, astrophysics and cosmology. The last 10 years have seen great strides made in understanding the physics of the neutrino. It has been discovered through measurements of reactor, atmospheric and solar neutrinos that neutrinos oscillate and therefore have mass. The phenomenon of neutrino oscillation is the result of the flavor eigenstates of the neutrino being different than the mass eigenstates. Neutrinos are produced in definite flavor eigenstates, the electron flavor being the most familiar flavor eigenstate. However, the neutrino propagates through space as a definite mass eigenstate leading to a classic quantum oscillation scenario. The Standard Model of Particle Physics assumes a mass-less neutrino and therefore neutrino oscillation is evidence of new physics. The measurements of solar neutrinos provided the first clues that the physics of the neutrino was more complicated than predicted by the Standard Model.

Standard solar models predict that our sun is stable to gravitational collapse due to the power generated by a series of nuclear reactions that also produce neutrinos. It was verifying these reactions that led Ray Davis down into the Homestake mine in 1965 to measure solar neutrinos. However, the experiment consistently measured about half of the predicted flux. This result was verified by other experiments using different detector technologies, creating the famous "Solar Neutrino Problem". With the exception of the SNO neutral current results, all of these experiments were either more sensitive to or only sensitive to electron flavor neutrinos, the flavor of neutrinos from the sun. Neutrino oscillation solves the solar neutrino problem because an electron flavor neutrino that oscillates into another flavor will not be detected by these experiments, and the experiments will report a deficit of neutrinos.

The two key experiments that form the foundation of our understanding of oscillation in solar neutrinos are SNO and Super Kamiokande, both water Čerenkov experiments. SNO used heavy water, water formed with deuterium, to measure the total neutrino flux in all flavors. This measurement, the SNO neutral current result, is consistent with standard solar model predictions. Super Kamiokande used an immense volume of regular water to make a very precise measurement of the oscillated neutrino flux using neutrino elastic scat-

tering, a reaction that is mostly sensitive to electron flavor neutrinos. Čerenkov detectors are limited by a minimum energy threshold of $\sim 5\,\mathrm{MeV}$ and therefore only the highest energy solar neutrinos can be detected. At these energies the ^{8}B neutrinos dominate the flux even though they represent a very small fraction of the total solar neutrino flux.

This work presents the measurement of the ^{8}B solar neutrino flux using neutrino-electron elastic scattering in KamLAND. Due to its size and background levels, KamLAND is not the ideal detector for this measurement, but with almost 1500 days of data a reasonable measurement is possible. The KamLAND detector uses scintillation light to detect particles, so this measurement has different systematic uncertainties compared to the water Čerenkov measurements. The results of this work provide an important addition to the SNO and Super Kamiokande results. As a scintillating detector, KamLAND has the possibility of a lower energy threshold for both the measurement of ^{8}B neutrinos and the more numerous lower energy solar neutrino branches. The present analysis also explores this possibility.

The following chapters provide a more in depth explanation of the physics of the sun and solar neutrino production, Chapter 2, the experiments that molded our current understanding of neutrinos physics, Chapter 3, and the theory of neutrino oscillation, Chapter 4. The details of the measurement of ^{8}B solar neutrinos with KamLAND commences in Chapter 5 with the detector overview followed by descriptions of the algorithms that turn the output of the KamLAND electronics into possible neutrino events, Chapter 6.

Because of their nature as weakly interacting particles, the neutrino signal is easily overwhelmed by backgrounds. One of the most difficult backgrounds to quantify are those induced by muon spallation. This sort of background is ubiquitous to low background experiments whether they are looking to detect neutrinos, dark matter, or rare processes like neutrino-less double-beta decay. The light isotopes produced by muon spallation, especially ^{11}Be, are the most problematic background in the present analysis. For this reason, muon spallation is studied using both simulation, Chapter 7, and analysis of KamLAND data, Chapter 8. The other major backgrounds come from the decay of ^{208}Tl, a daughter of the ^{232}Th decay chain, and gamma rays produced in the detector and surrounding rock. These and other backgrounds are assessed in Chapter 9. This chapter also presents the details of the extraction and analysis of ^{8}B candidates that leads to the ^{8}B neutrino flux measurement.

This work concludes in Chapter 10 with a comparison of the KamLAND result with previous measurements, possible improvements of this measurement, and the prospects for future measurements of solar neutrinos with KamLAND and other experiments. One of the issues that will be introduced in Chapter 2 is a new solar model problem. It is the result of improved solar heavy element abundances leading to a discrepancy between Standard Solar Model predictions and helioseismology. The analysis of neutrino-electron elastic scattering, which is the subject of this analysis, does not have the sensitivity to differentiate between the heavy element abundances. However, Chapter 10 discusses new experiments that may resolve this issue.

Chapter 2

The Standard Solar Model

The Sun is our closest star. It is a rather boring, middle aged star, Fig. 2.1, especially compared to the more exotic objects the cosmos has to offer. Due to its proximity, its mass, radius, luminosity, and photon spectrum are all precisely measured unlike other objects where at most one property is measured to the same level of precision. The Earth's geological record is a rich source of data on the formation of the solar system, as is data from the other planets, meteorites, comets, and the solar wind. This is all information unique to our star. Since astrophysics extrapolates near objects to distant ones, a thorough understanding of our Sun is essential.

Solar neutrinos are produced by the nuclear reactions that power the Sun and provide a probe straight to the core of the Sun. The purpose of this chapter is to describe how stellar structure and evolution are used to calculate the present day neutrino fluxes. A brief explanation of helioseismology presents the important results that verify standard solar model predictions. Recently, new measurements of the heavy element abundance in the Sun have resulted in discrepancies between helioseismology and stand solar model results. The consequences of these discrepancies are discussed.

2.1 Standard Solar Models

Standard solar models are stellar evolution simulations that are constrained to converge to our present day Sun. The models typically start with a zero age main sequence star, ZAMS, with a mass of 1 $M_\odot$. This is a new star burning only hydrogen in its core. The mechanism describing how the gas coalesced is not necessary for the modeling the star's time on the main sequence, but these details are currently a major area of research. However, it is critical that the phase just prior to the ZAMS involves convection throughout the whole volume, implying complete mixing, and a homogenous composition.

As the model evolves in time, its structure is determined by the four equations of stellar structure. The notation is from Ref. [1]. Each equation includes approximations and assumptions. The first equation insures conservation of mass,

$$\frac{dm}{dr} = 4\pi r^2 \rho, \tag{2.1}$$
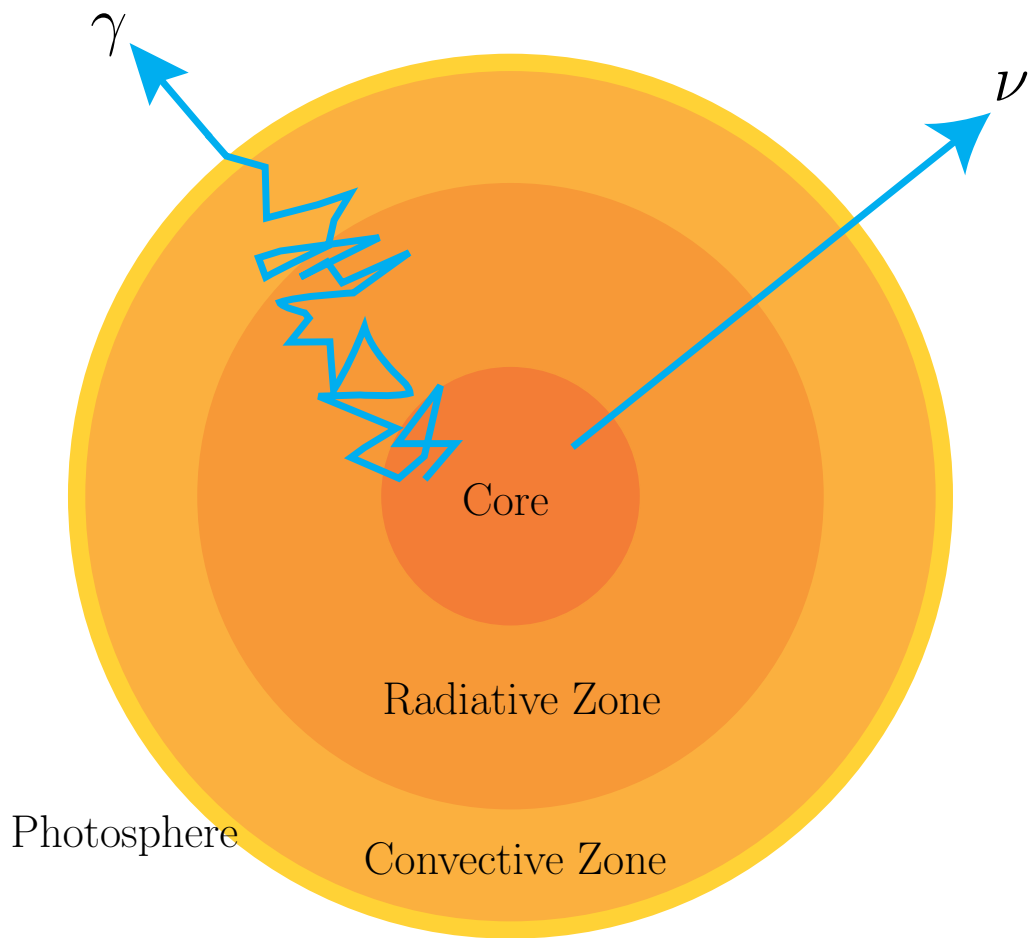
Figure 2.1: The basic structure of the Sun. Photons scatter many times due to the Sun's high opacity, in fact it takes a photon ∼10,000 yrs to escape the Sun. In contrast, the weakly interacting neutrinos stream out. The very thin photosphere is not shown to scale.

where m is the mass enclosed within r and ρ is the density as a function of r. The Sun will only lose 0.01% of its mass over its time on the main sequence, conservation of mass is a good approximation. The second equation is hydrostatic equilibrium, radiative and particle pressures balancing gravity,

$$\frac{dP}{dm} = -\frac{Gm}{4\pi r^4}. \tag{2.2}$$

If this equation were violated significantly, the Sun would collapse within about an hour. The most important equation for solar neutrinos accounts for energy production per unit mass,

$$\frac{dl}{dm} = \epsilon - \epsilon_\nu - C_P \frac{dT}{dt} + \frac{\delta}{\rho} \frac{dP}{dt}. \tag{2.3}$$

The variable l is the energy per unit time through a sphere of radius r. The term $\epsilon - \epsilon_\nu$ is the energy produced per unit mass by nuclear reactions minus that lost due to neutrinos free streaming from the Sun. The last two terms in Eq. 2.3 account for energy release due to gravity where C_P is the specific heat at constant pressure and δ is given by

$$\delta = -\left(\frac{\partial \ln \rho}{\partial \ln T}\right)_{P,X_i},$$

P, X_i indicates constant pressure and elemental composition. The fourth equation is energy transport with temperature at a give point as the proxy for energy,

$$\frac{dT}{dm} = -\frac{GmT}{4\pi r^4 P} \nabla. \tag{2.4}$$

The dimensionless quantity $\nabla = \frac{d \ln T}{d \ln P}$ is a function of the "microphysics" in the region it is describing. In the radiative zone, Fig. 2.1, it is given by

$$\nabla_{\text{rad}} = \frac{3}{64\pi\sigma G} \frac{\kappa l P}{mT^4} \tag{2.5}$$

where σ is the Stefan-Boltzmann constant and κ is the opacity. An adiabatic temperature gradient from the equation of state, $\nabla_{\text{ad}} = (\partial \ln T / \partial \ln P)_s$ where s is the specific entropy, can be used deep in the convective zone but not in the outermost layers. Convection and turbulence in these layers makes the calculation of ∇ difficult. Full solutions of the Navier-Stokes equations are computationally intensive especially since the time scales are much shorter than the 10 Myrs time scale used for stellar evolution. For this reason convection is modeled using mixing length theory, introducing a new free parameter α, the mixing length, to the model.

These equations determine the structure. An additional equation models the changing composition of the Sun due to nuclear reactions. The evolution of the mass fraction of the ith isotope, X_i is given by,

$$\frac{\partial X_i}{\partial t} = \frac{m_i}{\rho} \left[\sum_j r_{ji} - \sum_k r_{ik} \right], \tag{2.6}$$

where m_i is the mass of the particular isotope, r_{ji} is the rate that the isotope is being created from the jth isotope, and r_{ik} accounts for the destruction of the kth isotope. The effects of convection and diffusion needs to be included. Diffusion includes traditional diffusion and the gravitational settling of heavy elements. The inclusion of diffusion was a major improvement in the early 1990's [2].

Four boundary conditions are required for a particular solution. Normally, the first two are the solar radius and the luminosity evaluated at the center of the Sun, both zero. The second two are the temperature and pressure at the surface of the Sun. These are non-trivial; the solar atmosphere is not well defined. Thankfully for neutrino predictions, the precise treatment of these boundary conditions does not significantly affect the interior. The equation of state is also needed to relate the six unknowns, r, P, l, T, X_i, and ρ. The simplest equation of state is the ideal gas law, which effectively models stars since thermal pressure dominates. However, it neglects many non-negligible effects due to "microscopic" physics. These "microscopic" effects include ionization, radiation pressure, degeneracy, etc. The equation of state is usually tabulated by more elaborate algorithms, the details of which are determined by the goals of the solar model being constructed.

Solar models are often constructed for specific problems. Solar models focussing on neutrino flux predictions need to focus on the details of the nuclear reactions and the opacity. The opacity determines the temperature gradient which determines the reaction rates. The solar model that will be examined here is that of Bahcall, Serenelli, and Basu (BSB)[3]. This model is the last in a series spanning more than 40 years[2]. Monte Carlo techniques are exploited to study the error propagation, making this one of the best established models predicting neutrino fluxes.

The foundation of BSB is the Garching stellar evolution code. The radiative opacity is based on the individual elemental abundances, X_i, instead of the total heavy element abundance, Z[3]. For reference, abundances are usually defined, $X + Y + Z = 1$, where X is the hydrogen abundance, Y is the helium abundance, and Z is all heavier elements. Using the individual heavy element abundances is in the Garching code is an important improvement because the elements that remain only partially ionized until very deep in the Sun, like Fe, contribute much more to the opacity. The opacity is calculated using Opacity Project group codes, OP opacities[4]. The uncertainty in the opacity is estimated from solar models constructed with the OPAL opacities[5]. Both of these opacities do not incorporate molecular physics so the tables of Ferguson et al.[6] are used at lower temperatures. The equation of state that is from OPAL 2001[7] and the uncertainty from the OPAL 1996[8] equation of state.

The largest sources of uncertainty in the neutrino flux calculations are the heavy elemental abundances and to a lesser extent the nuclear reaction network. The abundances are determined from measurements of atomic and molecular line widths compared to simulations of the solar photosphere. The standard abundances are from Grevesse and Sauval, (GS98)[9]. These abundances use a 1D MHD simulation of the photosphere. Asplund et al. (AGS2005) use improved observations and a more complete 3D MHD simulation of the photosphere to determine the abundances[10]. These improved abundances find significantly lower abundances for C, N, O, Ne, and Ar as well as a slightly lower abundance of Si compared to GS98. The small reduction in Si is worth noting as this element ties

Table 2.1: Ten key inputs of the standard solar model of Bahcall, Serenelli, and Basu, BSBs[3]. A cross section factor is not presented for ^{7}Be electron capture since Eq. 26 in Adelberger et al.[12] is used.

Quantity	Value	1σ Uncertainty [%]
Age	4.57×10^6 yr	0.44
Diffusion Routine	-	15.0
Luminosity	3.8414×10^{33} ergs s^{-1}	0.4
Cross Section Factors		
p + p	3.94×10^{-25} MeV b	0.4
^{3}He+^{3}He	5.4 MeV b	6.0
^{3}He+^{4}He	0.53 keV b	9.4
^{7}Be+e$^-$	-	2
^{7}Be+p	20.5 eV b	3.8
^{3}He+p	8.6×10^{-20} keV b	15.1
^{14}N+p	1.69 keV b	8.4

the abundance of Mg, S, Ca, Fe and Ni in meteorites to that in the photosphere. The 3D MHD simulations have improved the agreement between abundances calculated from atomic line width versus those calculated from molecular line widths, but as will be argued here these lower abundances have caused discrepancies between standard solar models and helioseismology.

The diffusion of He and the heavy elements is modeled using the routine of Thoul et al. with an estimated uncertainty of 15%[11]. The remaining important inputs to the BSB model are the age, luminosity of the Sun, and the cross sections governing the nuclear reaction rates, Table 2.1. The uncertainty on these parameters is assumed to be gaussian distributed for the purpose of the standard solar model Monte Carlo.

An individual BSB standard solar model starts with a homogenous 1M$_\odot$ star. There are 19 inputs, 10 from Table 2.1 and 9 heavy element abundances (C, N, O, Ne, Mg, Si, S, Ar, and Fe). In addition, there are 3 free parameters, the initial helium abundance Y$_{init}$, the initial metallicity, Z$_{init}$, and the mixing length, α. The model evolves in time in steps of $\sim$10 Myrs. At each step the structure equations are solved and the composition recomputed. The free parameters are varied until the model converges to the current solar radius, luminosity and surface composition, Z/X. The convergence requirement is that the difference between the computed value and adopted values of these parameters agree to better than a part in 10^{-6}.

To study how the errors propagate, Monte Carlo BSB solar models are constructed with inputs that are selected randomly from within their uncertainties. In [3] the model was run 5,000 times using the AGS05 composition and the "optimistic" uncertainties presented in that work (BSB(AGS05)). The model was also run 5,000 times using the GS98 composition and "historical" uncertainties obtained from the difference between these two compo-

sitions(BSB(GS98)). Finally, the model was run 1,000 times using the AGS05 composition and the "historical" uncertainties. The solar model neutrino fluxes and helioseismology predictions come from these simulations.

2.2 Solar Neutrino Production

In our Sun the proton-proton chain provides the bulk of the energy to balance gravity, Table 2.2 . The outcome of one cycle is four protons converted to ^{4}He and 26.731 MeV of energy of which $\sim$0.6 MeV is carried by neutrinos. In stars great than $\sim$1.5 M$_\odot$, the CNO cycle dominates, Table 2.3. The CNO cycle was the original set of reactions proposed by Bethe[13] for the Sun, but the central temperature of the Sun appears too low, and the CNO cycle accounts for only $\sim$1.5% of the total energy[14].

Table 2.2: The nuclear reactions of the proton-proton chain. The common name for the neutrinos from a particular nuclear reaction are listed for reference.

Reaction	Name
$p + p \longrightarrow d + e^+ + \nu_e$	pp
or	
$p + e^+ + p \longrightarrow d + \nu_e$	pep
$p + d \longrightarrow {}^3\mathrm{He} + \gamma$	
$^3\mathrm{He} + {}^3\mathrm{He} \longrightarrow \mathbf{{}^4He} + p + p$	
or	
$^3\mathrm{He} + p \longrightarrow \mathbf{{}^4He} + e^+ + \nu_e$	Hep
or	
$^3\mathrm{He} + {}^4\mathrm{He} \longrightarrow {}^7\mathrm{Be} + \gamma$	
$^7\mathrm{Be} + e^- \longrightarrow {}^7\mathrm{Li} + \nu_e$	^{7}Be
$^7\mathrm{Li} + p \longrightarrow \mathbf{{}^4He} + \mathbf{{}^4He}$	
or	
$^7\mathrm{Be} + p \longrightarrow {}^8\mathrm{B} + \gamma$	
$^8\mathrm{B} \longrightarrow {}^8\mathrm{Be}^* + e^+ + \nu_e$	^{8}B
$^8\mathrm{Be}^* \longrightarrow \mathbf{{}^4He} + \mathbf{{}^4He}$	

The solar neutrino fluxes from the BSB model and the uncertainties from 10,000+ Monte Carlo models are presented in Table 2.4. The flux of neutrinos from the pp and pep reactions are tightly constrained by the solar luminosity, and are relatively insensitive to the composition choice. The Hep and ^{7}Be reactions are dominated by cross section uncertainties and are also insensitive to compositions changes. In contrast, the CNO neutrinos are very sensitive to the exact compositions, and as a result have large uncertainties. The CNO

Table 2.3: The nuclear reactions of the CNO cycles. The common name for the neutrinos from a particular nuclear reaction are listed for reference.

Reaction	Name
$p + {}^{12}C \longrightarrow {}^{13}N + \gamma$	
${}^{13}N \longrightarrow {}^{13}C + e^+ + \nu_e$	${}^{13}N$
$p + {}^{13}C \longrightarrow {}^{14}N + \gamma$	
$p + {}^{14}N \longrightarrow {}^{15}O + \gamma$	
${}^{15}O \longrightarrow {}^{15}N + e^+ + \nu$	${}^{15}O$
$p + {}^{15}N \longrightarrow {}^{12}C + {}^{\mathbf{4}}\mathbf{He}$	
or	
$p + {}^{15}N \longrightarrow {}^{16}O + \gamma$	
$p + {}^{16}O \longrightarrow {}^{17}F + \gamma$	
${}^{17}F \longrightarrow {}^{17}O + e^+ + \nu_e$	${}^{17}F$
$p + {}^{17}O \longrightarrow {}^{14}N + {}^{\mathbf{4}}\mathbf{He}$	
or	
$p + {}^{17}O \longrightarrow {}^{18}F + \gamma$	
$e^- + {}^{18}F \longrightarrow {}^{18}O + \nu_e$	-
$p + {}^{18}O \longrightarrow {}^{19}F + \gamma$	
$p + {}^{19}Fe \longrightarrow {}^{16}O + {}^{\mathbf{4}}\mathbf{He}$	

Table 2.4: The neutrino flux results at the Earth from BSB for the two compositions considered[3]. The conservative (Cons.) and optimistic (Opt.) uncertainties are quoted for the AGS05 composition.

Neutrino Source	GS98 Comp.	Cons. 1σ	AGS05 Comp.	Opt. 1σ	Cons. 1σ	Normalization (ν cm^{-2}s^{-1})
pp	5.99	0.05	6.06	0.04	0.05	10^{10}
pep	1.42	0.02	1.45	0.02	0.02	10^8
Hep	7.93	1.23	8.25	1.28	1.26	10^3
^{7}Be	4.84	0.51	4.34	0.40	0.45	10^9
^{8}B	5.69	$+0.98$ -0.84	4.51	$+0.57$ -0.51	$+0.73$ -0.64	10^6
^{13}N	3.05	$+1.12$ -0.82	2.00	$+0.29$ -0.25	$+0.71$ -0.52	10^8
^{15}O	2.31	$+0.86$ -0.63	1.44	$+0.24$ -0.20	$+0.52$ -0.38	10^8
^{17}F	5.83	$+4.22$ -2.45	3.25	$+0.54$ -0.46	$+2.20$ -1.31	10^6

neutrino fluxes' sensitivities are from both the opacity and the initial abundances of C, N, and O. A precise measurement of the CNO fluxes would be useful for determining initial abundances and testing the assumption of a homogenous ZAMS[15]. ^{8}B decay produces the most high energy neutrinos. The uncertainty in the flux comes equally from the cross section and the composition. The "optimistic" uncertainties for the AGS05 compositions are too small to explain the difference between the GS98 compositions.

The region of the core in which each of the neutrinos is produced is important for the neutrino physics issues in Chapter 4. The predictions for BSB are shown in Fig. 2.2 for p-p and in Fig. 2.3 for CNO. These regions are insensitive to compositions[3]. They can help visualize why certain branches are more sensitive to changes in the abundances. Among the p-p neutrinos, ^{8}B is produced closest to the high temperature center. The temperature gradient is sensitive to the opacity and consequently the abundances. The double peaked distribution for ^{13}N in Fig. 2.3 comes from the CNO cycle operating in steady state near the center, but stalling as the radius grows and the p+^{13}C step has insufficient energy to overcome coulomb repulsion. At even larger radii, the burning of residual ^{12}C through ^{12}C(p, γ)^{13}N produce another source of neutrinos.

The neutrino energy spectra are shown in Fig. 2.4. The pp neutrinos are the most abundant but detecting them directly is difficult. The far less numerous ^{8}B neutrinos at higher energies are "easier" to detect since cross sections are higher and backgrounds are lower. Beta decays in the Sun are all positron emissions and there is always a competing electron capture branch, but for light nuclei these branchings are negligible[16]. Because of the importance of the ^{8}B neutrinos, it is critical to understand the neutrino spectrum. ^{8}B
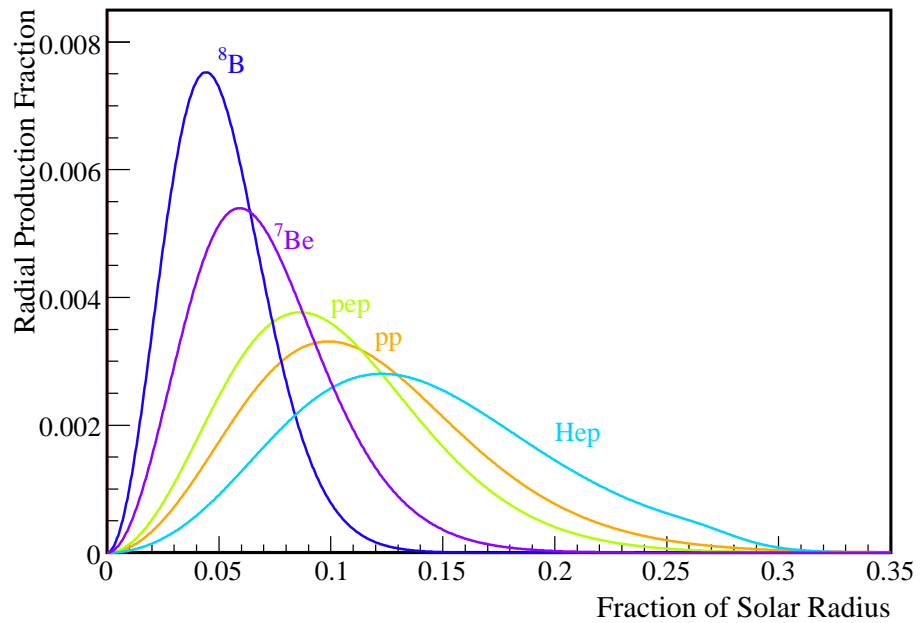
Figure 2.2: The p-p chain's neutrino producing reactions versus solar radius.
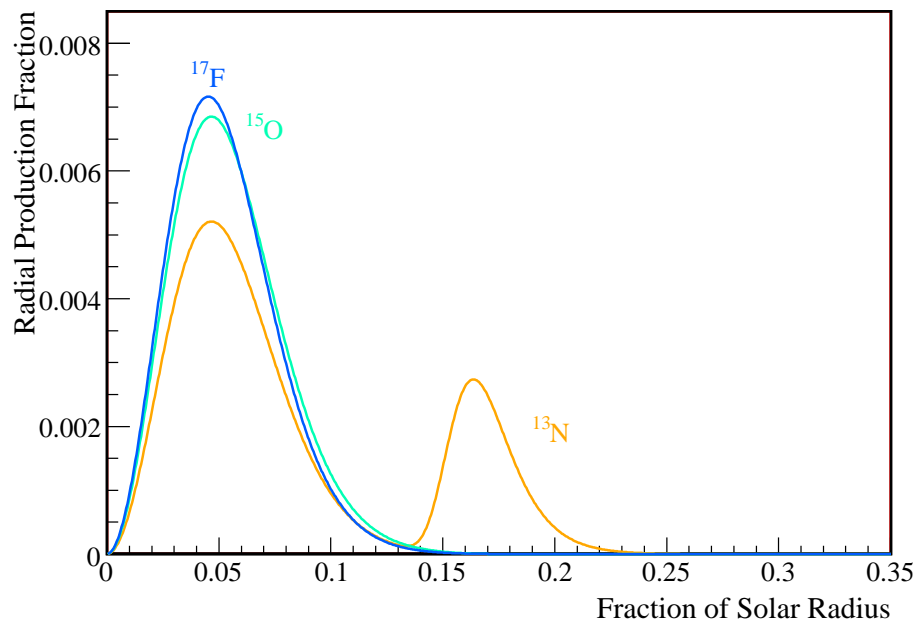
Figure 2.3: The CNO cycle's neutrino producing reactions versus solar radius.

decays to a broad state of ^{8}Be that decays to two ^{4}He. The principle decay is to an unusually broad 2^+ first excited state and the spectrum shows significant deviation from the allowed shape. There have been several recent measurement of the ^{4}He spectrum to determine the neutrino spectrum including Winter et al.[17] and Ortiz et al.[18]. These experiments have improved the precision of the measurement compared to the data review by Bahcall et al.[19], but they disagree especially above $\sim$12 MeV, a region critical for experiment. The measurement of Winter et al.[17] agrees with the beta spectrum measurement from Ref. [20] and the recent alpha spectrum from Ref. [21]. The Ortiz et al.[18] spectrum does not. The Winter spectrum is adopted by SNO[22] but the Ortiz spectrum is still used by Super Kamiokande[23]. This work will use the Winter spectrum. The experimental limit on the branching ratio to the ground state of ^{8}Be is $< 7.3 \times 10^{-5}$ at the 90% confidence level, and it is neglected[24].
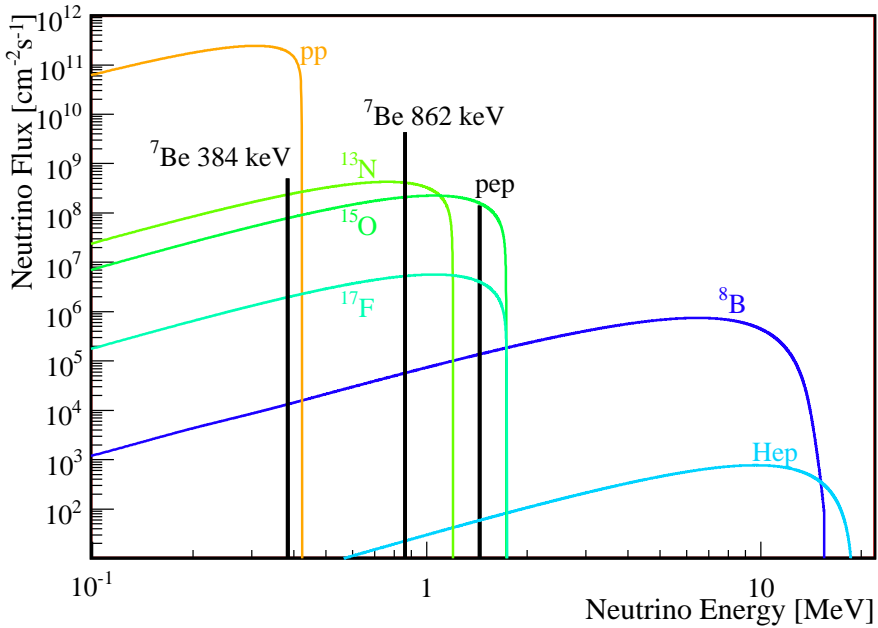
Figure 2.4: The solar neutrino energy spectra. The neutrino branches with beta spectra are in units of flux at the Earth per 0.001 MeV. The electron capture lines are shown with their total fluxes.

2.3   Helioseismology

Helioseismology is the study of solar oscillations, the vibrations of the Sun. The present summary of this subject relies heavily on the excellent review by Basu and Anitia[1]. The Sun acts as a resonance cavity for acoustic waves produced by turbulence in the convective zone, Fig. 2.1. If the oscillations are assumed to be linear and adiabatic then their

frequencies can be described by the solution to the the four basic equations of fluid dynamics, the continuity equation, the energy equation in the adiabatic approximation, the momentum equations and the poisson equation. The modes can be expressed in terms of the spherical harmonics with n, the number of nodes in the radial direction, l, the number of nodes along the surface, and m, the number of nodes along the equator. The modes with $n > 0$ correspond to the p-modes, so called since the dominant restoring force is pressure. The $n = 0$ correspond to the fundamental or f-modes. The modes with $n < 0$ correspond to the g-modes, g for gravity. Due to their smaller amplitude, the g-modes have not been reliably detected[1]. The frequencies, $\nu = \omega/2\pi$ are expressed in two terms,

$$\nu_{nlm} = \nu_{nl} + \sum_{j=1}^{J_{\max}} a_j^{nl} P_j^l(m) \tag{2.7}$$

where a_j^{nl} are the splitting coefficients and $P_j^l(m)$ are orthogonal polynomials in m of degree j. This second term comes from rotations and magnetic fields which lift the $(2l + 1)$-fold degeneracy. The ν_{nl} frequencies describe spherically symmetric effects and are the focus of most standard solar model comparisons.

The results of a solar model calculation for the frequencies are compared to observations as shown in Fig. 2.3. The first curve is the $n = 0$, f-mode, and each subsequent curve corresponds to series of p-mode oscillations with incremented n. For the p-modes, the radius at which the increasing sound speed causes total internal reflection, the "lower turning point", is approximately given by

$$\omega^2 = l(l + 1)\frac{c^2(r)}{r^2}. \tag{2.8}$$

where $c(r)$ is the sound speed as a function of radius. Therefore, the frequency and the degree of a mode in Fig. 2.3 corresponds to the depth in the Sun probed by the mode. The low degree modes probe through to the center of the Sun, while higher degree modes get trapped in the outer most layers of the Sun.

The measured frequencies are usually interpreted relative to a known solar model where the difference between the frequencies and the model are

$$\frac{\delta\nu_{nl}}{\nu_{nl}} = \int_0^R K_{c^2,\rho}^{nl}(r)\frac{\delta c^2(r)}{c^2(r)}dr + \int_0^R K_{\rho,c^2}^{nl}(r)\frac{\delta\rho(r)}{\rho(r)}dr. \tag{2.9}$$

The $K^{nl}(r)$'s are kernels that relate the frequency changes to sound speed and density changes respectively; they are unique to a particular solar model. The accuracy with which the density and sound speed profiles can be extracted is limited by the accuracy of the solar models to and the validity of the linear and adiabatic assumptions for the fluid equations. It is known that the outermost layers are not well modeled due to convection and that the linear and adiabatic assumptions break down. The presented treatment can be improved but helioseismology is limited to $r < 0.95R_\odot$ due to uncertainties. A lower limit comes from a deficit of low degree modes. The measurements are limited to $r > 0.05R_\odot$.

Even with these limitations, helioseismology probes 85.75% of the solar volume. The results for the BSB solar model and the 360 day data set from MDI aboard SOHO[25]

are shown in Fig. 2.3[26]. The good agreement between the sound speeds and density profiles from helioseismology and solar models is a major achievement. The discrepancies introduced by the AGS05 abundances is worrisome. Fig. 2.3 is shown because it presents several models where larger abundances of Ne, Ar and other elements are modeled. It is interesting to note that models with more Ne and Ar agree with the helioseismology measurements at the same level as for the GS98 abundances. Because Ne and Ar can not be measured spectroscopically, their abundances are measured in regions that are not well understood. Perhaps their uncertainties should be larger than quoted, allowing for such increases.

The depth of the convective zone is a quantity that is easily extracted from helioseismology data since the change in the temperature gradient at this boundary causes a discontinuity in the sound speeds. This is actually the most precise measurement made by helioseismology, and the physics at this boundary is an area of particular interest. The best value for the position of the convective zone is $R_{cZ} = 0.713 \pm 0.001 R_{\odot}$[3]. Because this is an effect due to the temperature gradient, it is particularly sensitive to the composition. The result for BSB(GS98) is $0.7132 R_{\odot}$ while BSB(AGS05) gives $0.7279 R_{\odot}$[3]. Once again the improved AGS05 abundance causes a discrepancy between helioseismology and the BSB standard solar model.

This discrepancy between helioseismology and the BSB standard solar model is the latest solar model problem. An accurate measurement of ^{8}B neutrino flux will help distinguish between different compositions. Even current measurements limit more exotic solutions to the problem. However, this problem is small compared to the original "Solar Neutrino Problem" that plagued the field for more than 40 years. The experimental evidence for this problem is presented in the next chapter, Chapter 5. It is the physics of neutrino oscillation which explains these results, and will be tested by a measurement of ^{8}B neutrinos with KamLAND.
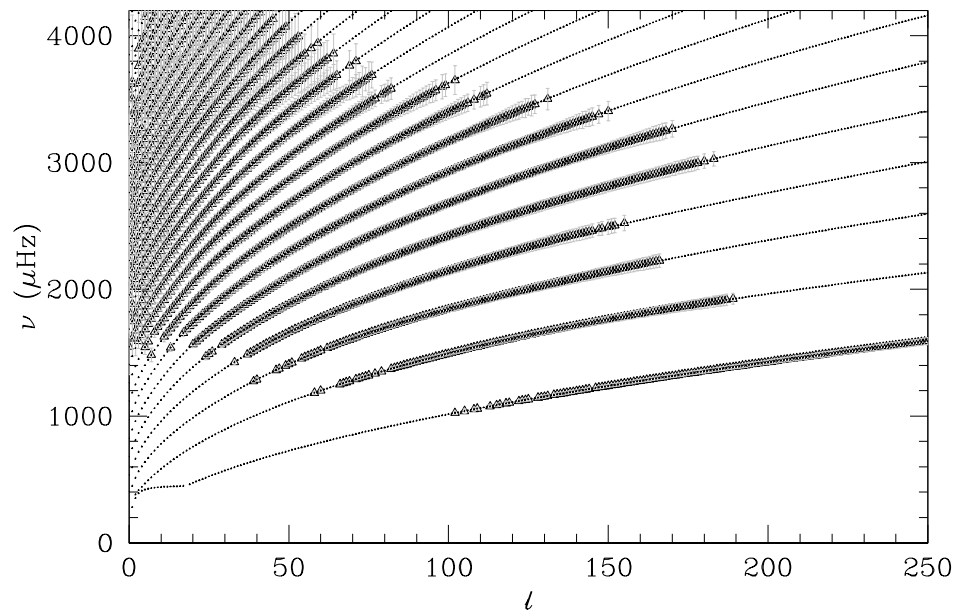
Figure 2.5: The frequencies of a solar model plotted as a function of degree l. The curves correspond to solar model calculations (dotted lines). The triangles are the data from the first 360 days of observations from the MDI instrument aboard SOHO. The data points have error bars that are difficult to see even though they correspond to 5000σ error bars. (Reproduced from Basu and Antia[1]).
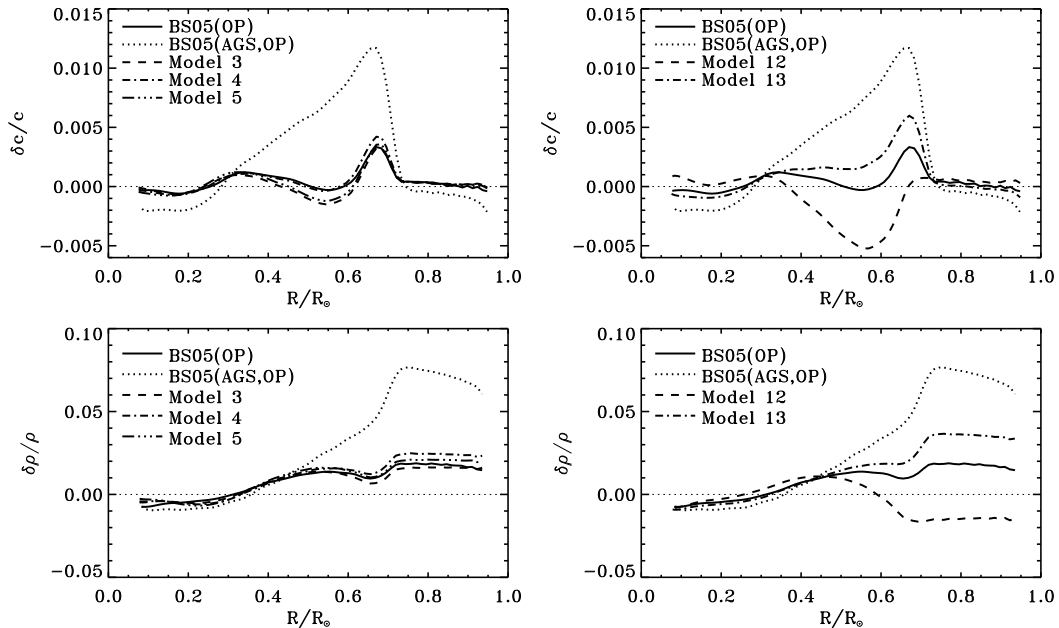
Figure 2.6: The relative sound speed, $\delta c/c = (c_\odot - c_{\mathrm{model}})/c_\odot$, and relative density differences $\delta\rho/\rho = (\rho_\odot - \rho_{\mathrm{model}})/\rho_\odot$ from the solar model. The BSB(GS98) is very similar to BS05(OP). BS05(OP) is in much better agreement with the helioseismology measurements than the BS05 model with AGS05 abundances. Models 3-5 have increased Ne and Ar abundances while Models 12 and 13 also have increased C, N, O and Si abundances. (Reproduced from Bahcall, Basu and Serenelli[26]).

Chapter 3

History of Experiments

The history of solar neutrino experiments begins in the early 1960's with the Homestake Solar neutrino detector and its prototypes. This experiment's purpose was to verify the fusion reactions that power the sun by measuring the resulting neutrino flux. Instead of confirming the predictions of the Standard Solar Model it measured a significant deficit which came to be known as the solar neutrino problem. The mystery of the missing neutrinos deepened as subsequent experiments were performed. Some of these experiments attempted to measure solar neutrinos using other techniques while other experiments looked for the answer in atmospheric neutrinos, neutrinos made in particle interactions in the upper atmosphere, or anti-neutrinos from nuclear reactors. Throughout this time the Standard Solar Model, as presented in Chapter 2, was refined and the theoretical uncertainties reduced but the deficit remained. The following chapter outlines the experiments that were critical in developing our current understanding of the complex interaction between the properties of the neutrino as a weakly interacting particle, Chapter 4, and the Standard Solar Model, Chapter 2.

3.1   Homestake

The Homestake experiment was one of the longest continuously running physics experiments. The experiment started taking data in 1967 and released its first results in 1968[27]. After several upgrades, data taking resumed in 1970 and the experiment proceeded to collect data almost continuously until 1994[28]. The experiment was located in the Homestake Gold Mine in Lead, South Dakota. The experimental hall was located at the 4850 ft level of the mine which provided the detector with an average overburden of 4200 ± 100 meters water equivalent (m.w.e) to shield the detector from cosmic radiation. Prototypes at the surface had indicated the need for such a depth to reduce these backgrounds.

The heart of the Homestake detector was 615 tons of perchloroethylene, C_2Cl_2, or dry cleaning fluid. The neutrinos were detected via the reaction,

$$^{37}\text{Cl} + \nu_e \longrightarrow {}^{37}\text{Ar} + e^-. \tag{3.1}$$

The natural abundance of ^{37}Cl is 24.23% which translates into 2.16×10^{30} target atoms for the reaction. The ^{37}Ar remains in solution until such time as it is removed or it decays.

The half-life of ^{37}Ar is 35 days. The energy threshold for this reaction is 0.814 MeV which means the Homestake experiment was predominately sensitive to the solar neutrinos from the capture of electrons on ^{7}Be and the beta decay of ^{8}B.

A solar neutrino data run started with the purge of He gas through the fluid to remove any Ar gas already collected in the detector. The next step was the addition of 0.1 cm^3 of pure ^{36}Ar or ^{38}Ar to the tank followed by 1-3 months of exposure time. When the exposure time for that run had completed 4×10^5L or 1 tank of He was bubbled through the liquid removing all gases present. Since the Ar needed to be isolated the extracted gas was run through a condenser at -32°C, a molecular sieve at room temperature, and finally a charcoal trap at liquid nitrogen temperature. The charcoal trap was then warmed and the volume of gas measured and the isotopic composition measured with a mass spectrometer. These measurements combined with the known volume of ^{36}Ar or ^{38}Ar added at the beginning of the run provided the efficiency for extracting Ar from the detector fluid. The gas from the charcoal trap was then loaded into miniature proportional counters with volumes of 0.25 or 0.5 cm^3 so that the decay of ^{37}Ar could be observed. During this step a small amount of tritium free methane was added to the gas to allow for the proper operation of the proportional counters.

The decay of ^{37}Ar is an electron capture decay, 81.5% of which are a K orbital electron capture with the emission of 3-5 Auger electrons with a total energy of 2.82 keV. This small signal and the low expected rates, ∼6 counts per run, make the rejection of backgrounds from external beta decays, cosmic rays and Compton electrons critical. The most important improvement between the 1968 result and subsequent runs was the addition of pulse rise time discrimination. Since the range of the Auger electrons is very small, <0.1mm, the rise time of the signal from the proportional counter is much shorter than that of the other backgrounds and this data can be used to eliminate 95% of background events.

The first results from the Homestake mine could only put an upper limit on the solar neutrino flux of 3 SNU, solar neutrino units or one interaction per 10^{36} target atoms per second[27]. This result was a factor of 2 smaller than the most probable theoretical prediction at the time[29]. After the inclusion of pulse rise time discrimination, an actual measurement of the solar neutrino flux could be made. The final data set consisted of 108 ^{37}Ar extractions over more than twenty years. The results are summarized in Fig. 3.1. The final result from the Homestake experiment was a measured rate of 2.56±0.16(stat.)±0.16(syst.)SNU[28]. In the mean time, the theoretical estimate converged to 8.5±1.8SNU[30]. Detailed studies of all aspects of the experiment, from the extraction of Ar to the sources of various backgrounds, were done, but no solution to this discrepancy could be found in the experimental technique or the modeling of the sun. Bahcall [14] and the final results presented in [28] provide an exhaustive summary of the Homestake experiment.

3.2 Kamiokande

The first verification of the Homestake experiment came from the Kamiokande II experiment in 1989[31]. The Kamiokande detector was an imaging water Čerenkov detector.
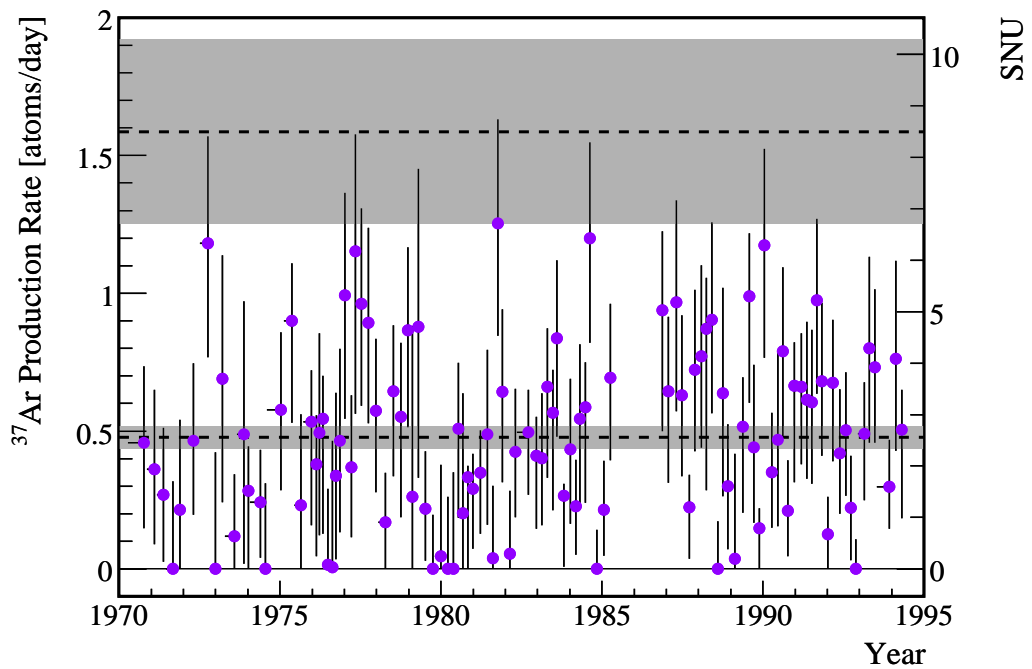
Figure 3.1: A summary of the results of the Homestake experiment from 1970 to 1994, in this time 108 neutrino data runs or extractions were performed culminating in an average measured rate of 2.56±0.16(statistical)±0.16(systematic)SNU[28]. The discrepancy with the theoretical prediction persists to this day. The current best estimate is shown at 8.5±1.8 SNU[30].

Particles moving faster than the speed of light in the water produce rings of Čerenkov light, and these rings are imaged by the detectors photo-multiplier tubs (PMTs). The reconstruction of the rings could be used to determine the energy and direction of particles moving through the detector and the position of any interactions. An algorithm was also developed to separate Čerenkov rings made by muons from those made by electrons. This algorithm quantified the "fuzziness" of the reconstructed ring. The electrons are more likely to multiple scatter compared to the more massive muons and therefore should have less sharp rings. This sort of detector was capable of obtaining information on individual solar neutrino candidate events in real time, compared to the time-integrating measurements of Homestake.

The Kamiokande experiment was constructed in the Kamioka mine in the Gifu prefecture of Japan. The cavern constructed for this experiment would later become the home of KamLAND of which much more will be discussed later. It was originally designed to search for proton decay and derives is name from the name of the mine, "Kamioka", and Nucleon Decay Experiment, "nde". A combination of upgrades to the electronics, increased PMT coverage, improved water purification and the addition of an outer veto, allowed the energy threshold to be lowered to $\sim 9\,$MeV. The lowering of the energy threshold officially started the second phase of the Kamiokande experiment. At this threshold the experiment was sensitive to about half of the neutrinos coming from the beta decay of ^{8}B in the sun.

The Kamiokande detector was a cylinder 14.4m in diameter and 13.1m in height containing 2142 metric tons of water. The solar neutrinos were detected by observing the Čerenkov ring of the recoil electron that is the result of solar neutrinos elastically scattering off the water's electrons,

$$e^- + \nu \longrightarrow e^- + \nu. \tag{3.2}$$

Since the scattering angle is relatively small, the incident neutrino direction is preserved. The quoted angular resolution was 28° at 10 MeV[32]. The recoil electrons energy could also be reconstructed with a quoted resolution of 20% at 10 MeV[32]. It is important to note that this reaction is sensitive to all flavors of neutrinos, ν_e, ν_μ, ν_τ, though it is predominantly sensitive to the electron flavored neutrino, ν_e. In comparison, the neutrino capture reaction used by Homestake is only sensitive to electron flavored neutrinos.

The main backgrounds to the measurement were gamma rays and neutrons propagating into the detector from the surrounding rock, short lived light isotopes made by muon spallation and radioactivity present in the water due to the daughters of the ^{232}Th and ^{238}U decay chains. To eliminate backgrounds from the rocks, a central cylinder of 680 tons was used for analysis. To eliminate muon spallation backgrounds, the detector or some subset of the detector was vetoed following a muon event. A water purification system was used to eliminate natural radioactivity from the water.

The experiment took solar neutrino data from January 1987 to April 1990. The data set was split into two periods. The first was 450 days with an energy threshold of 9.3 MeV. The gain of the PMTs was then increased, improving the energy resolution of the detector. In addition the detector was sealed better preventing Rn contamination. Isotopes of Rn are daughters of both the ^{232}Th and ^{238}U decay chains and because they are gases they are particular pernicious backgrounds. The combination of lower background levels and improved energy resolutions, allowed the energy threshold to drop to 7.5 MeV for the

second data taking period of 590 days.

The two data sets were combined and compared to the standard solar model (SSM) of Bahcall and Ulrich [33]. The resulting ratio was Data/SSM = 0.46±0.05(stat)±0.06(syst), assuming electron flavor neutrinos as predicted by SSM, confirming the deficit seen by the Homestake experiment[32]. Using the reconstructed direction, it was shown that the candidates "point" back to the sun as would be expected for solar neutrinos. It was also shown that the candidates had the predicted energy spectrum though the statistics were limited.

As noted previously, Kamiokande was primarily a proton decay experiment. The Irvine Michigan Brookhaven experiment (IMB) was a contemporary experiment. In the process of setting limits on the lifetime of the proton, these experiments produced another key result that made it seem likely that the solar neutrino problem was linked to the physics of the neutrino rather than that of the sun. These experiments studied neutrinos that are the result of decays of particles in showers in the upper atmosphere, the so-called atmospheric neutrinos. These particle showers are the result high energy particles, most likely protons, interacting in the upper atmosphere. The ratio of muon to electron flavored neutrinos should be 2 to good approximation because pions and kaons, the most numerous members of any particle shower, will decay to a muon giving one muon flavored neutrino. The muon will then decay providing the second muon flavored neutrino and one electron flavored neutrino. The IMB threshold was too high for solar neutrino detection.

The ability to differentiate between electron-like events and muon-like event was used to construct the flux ratio, $(\mu/e) = (\nu_\mu + \bar{\nu}_\mu)/(\nu_e + \bar{\nu}_e)$. In Kamiokande, electron-like candidates with momentum 0.1< p_e < 1.33 GeV/c and muon-like candidates with momentum 0.2 < p_μ <1.5 GeV/c were used to construct this ratio. The result for the combined Kamiokande I-II data set, 4.92 kilo-ton years exposure, was compared to a detailed Monte Carlo of the atmospheric particle showers (MC). The result was $(\mu/e)_{\text{data}}/(\mu/e)_{\text{MC}} = 0.60^{+0.07}_{-0.06}$(stat.)±0.05(syst.)[34]. In addition the energy spectrum of the electron-like events agreed very well with the Monte Carlo while the muon-like events showed a significant deficit[34]. Using candidates with similar energy,0.1< p_e < 1.5 GeV/c and 0.3 < p_μ <1.5 GeV/c, IMB found the same effect. A ratio of electron-like events to muon-like events was found to be e/μ =0.36±0.02(stat.)±0.02(syst.) when e/μ =0.51±0.01±0.05 was predicted[35]. This indicated either an excess of electron-like events or a deficit of muon-like events.

3.3   Gallex, GNO, and SAGE

The discrepancy between the results of the Homestake and Kamiokande II experiments and the Standard Solar Model were compelling. However, both of these experiments were primarily sensitive to the relatively rare neutrinos from the decay of ^{8}B in the sun. Two experiments proposed to use the capture reaction

$$^{71}\text{Ga} + \nu_e \longrightarrow \ ^{71}\text{Ge} + e^-, \tag{3.3}$$

which has an energy threshold of 0.2332 MeV, to try to measure the lowest energy and most abundant p-p neutrinos. The Standard Solar Model prediction for a gallium experiment is

131^{+12}_{-10}SNU[30]. These experiments would be very similar to the Homestake experiment in that the ^{71}Ge is chemically extracted from a larger target mass and then as it decays with a half-life of 11.43 days counted in specially designed low background miniature proportional counters. The two experiments were Gallex and SAGE. Gallex planned to use ^{71}Ga in an aqueous solution of gallium chloride while SAGE proposes to use Ga metal. In this way these experiments formed a complementary pair of experiments as the main systematic, the efficiency for extracting ^{71}Ge would be very different. These experiments also had the nice feature that background estimates could be extracted accurately from the production of ^{69}Ge. This isotope cannot be made from solar neutrinos but will be made by the same processes that would make ^{71}Ge from muons, fast neutrons or radioactivity intrinsic to the target material.

The Gallex target was 100 tons of an aqueous solution of gallium chloride with hydrochloric acid located at the Gran Sasso Underground Laboratory. Of the 100 tons 30.3 tons was gallium of which 39.6% is ^{71}Ga. This corresponded to 1.03×10^{29} target atoms. The acidity of the solution ensured that the Ge remains in the form of the volatile $GeCl_4$ while the Ga remained in the more stable $GaCl_3$. The extraction of ^{71}Ge began with the bubbling of the target with nitrogen gas and the absorption of the ^{71}Ge in water. After several volume reductions, the Ge was converted to GeH_4 gas. The GeH_4 gas was then purified and loaded into miniature proportional counters to detect the decays of ^{71}Ge. The experiment took data from May 1992 to January of 1997. In this period, 65 solar neutrino runs were completed leading to an effective exposure of 1594 days. The result was 77.5 ± 6.5(stat.)$^{+4.3}_{-4.7}$(syst.) SNU[36].

The experiment was shut down for most of 1997 to perform upgrades to the experiment, most importantly upgrades to the counting electronics[37]. The experiment started taking data again in May 1998 as the Gallium Neutrino Observatory, GNO. As GNO, an additional 58 solar neutrino runs were completed by April 2003. The result for GNO alone was $62.9^{+5.5}_{-5.3}$(stat.)±2.5(syst.) SNU which shows a marked improvement in the systematic error [38]. Combining the Gallex and GNO results, 123 solar neutrino runs were completed and a complete solar cycle observed. The final result was 69.3 ± 5.5 SNU[38].

The Russian American Gallium Experiment (SAGE), originally the Soviet American Gallium Experiment, used metallic Ga to measure the production of ^{71}Ge from solar neutrinos [39]. The experiment was located in the Baksan Neutrino Observatory in the northern Causaus mountains. The target at its largest was 60 tons of metallic Ga stored in chemical reactors. The Ge was extracted from the Ga by an oxidation reaction and then put into an aqueous solution. This solution was concentrated and the Ge was swept by a gas flow into de-ionized water as the volatile compound $GeCl_4$. A solvent extraction further concentrated the Ge and finally GeH_4 gas was synthesized, purified, and loaded into proportional counters for analysis. The experiment took data from January 1990 to December 1997. The final result was $67.2^{+7.2}_{-7.0}$ (stat.)$^{+3.5}_{-3.0}$(sys.)[39].

The results from the Ga experiments are consistent with each other and would be consistent with the Standard Solar Model prediction of 131^{+12}_{-10}SNU[30] if the detectors were only measuring the p-p neutrinos and none of the neutrinos from the other branches. Though Homestake and Kamiokande detected a deficit of solar neutrinos, they reported non-zero fluxes from the higher energy solar neutrino branches. Therefore, the combination

of the Ga results with the Homestake and Kamiokande results means a deficit is observed in all solar neutrino branches though not the same size deficit.

3.4 Super Kamiokande

Super Kamiokande is the successor of the Kamiokande II experiment and is located in the same mine in Kamioka, Japan. At 50 kilo-tons of purified water it is in fact a super-sized version of the original Kamiokande experiment described in Section 3.2. The PMT coverage was increased to 40.4% to ensure better energy resolution, 14.2% at 10 MeV, and a lower energy threshold, 6.5 MeV. Following more improvements, the energy threshold was placed as low as 4.5 MeV. There was also a modest increase in the angular resolution to $25°$ at 10 MeV. These improvements coupled with the 22.5 kilo tons of active volume lead to an impressive measurement of the solar neutrino flux from neutrino elastic scattering.

Super Kamiokande started taking data in April of 1996 and completed the first phase of data taking in July of 2001. In this 1496 days of data, $22404 \pm 226(\text{stat.})^{+784}_{-717}(\text{syst.})$ solar neutrino candidates are observed [40]. This translates to a solar neutrino flux from the decay of ^{8}B in the sun of $2.35 \pm 0.02(\text{stat.}) \pm 0.08(\text{syst.}) \times 10^6 \text{cm}^{-2}\text{s}^{-1}$. This confirms a deficit compared to the Standard Solar Mode, $5.79 \times 10^6 \text{cm}^{-2}\text{s}^{-1}$[30], with the highest statistics of any solar neutrino experiment to date.

The large data set allows for several other interesting analyses by dividing the data in time and energy. The first such study looks for a deficit of neutrinos due to their propagation through the earth. The asymmetry in the flux between day and night is used for this purpose. The result of the analysis shows that the day-night asymmetry must be small if it exists [40],

$$A = (\Phi_{day} - \Phi_{night})/(\frac{1}{2}(\Phi_{day} - \Phi_{night}))$$
$$= -0.021 \pm 0.020(\text{stat.})^{+0.013}_{-0.012}(\text{sys.}). \tag{3.4}$$

A second analysis can be performed by dividing the data into the time of year it was collected. It is predicted that the flux should change by 7% due to the eccentricity of the earth's orbit. The data is consistent with the prediction with a $\chi^2/$d.o.f of 4.7/7 or a 69% C.L. [40]. The data can also be examined as a function of energy. The energy spectrum is consistent with the shape predicted by the Standard Solar Model. By looking at the highest energy bin, 18.0~21.0 MeV, a limit on the flux of solar neutrinos from the ^{3}He + p $\longrightarrow$ ^{4}He + e$^+$ + ν_e reactions is determined to be $< 73 \times 10^3 \text{cm}^{-2}\text{s}^{-1}$ at the 90% C.L.. This is within an order of magnitude of the Standard Solar Model prediction of $7.88 \times 10^3 \text{cm}^{-2}\text{s}^{-1}$ [30].

As with the solar neutrino measurements, the detector upgrades and shear number of candidates greatly improved the analysis of atmospheric neutrinos. The atmospheric neutrino data set was 1489 days taken at the same time as the solar neutrino data set. The analysis was divided into sub-GeV events and multi-GeV plus those events where only part of the event was reconstructed in the detector. Once again a ratio is constructed between the data and a detailed Monte Carlo. For the sub-GeV group the reported ratio[41] is

$$(\mu/e)_{\text{data}}/(\mu/e)_{\text{MC}} = 0.658 \pm 0.016(\text{stat.}) \pm 0.035(\text{syst.}) \tag{3.5}$$

while the multi-GeV group also shows a deficit with larger uncertainty

$$(\mu/e)_{\text{data}}/(\mu/e)_{\text{MC}} = 0.7024^{+0.032}_{-0.030}(\text{stat.}) \pm 0.101(\text{syst.}). \qquad (3.6)$$

The electron-like neutrino candidates agree well with the Monte Carlo while the muon-like candidates show a deficit. With this larger data set, it was possible to analyze the zenith-angle distribution of the candidates. What was seen was that the muon-like candidates that had passed through the earth before arriving at Super Kamiokande, upward going events, were responsible for the deficit compared to Monte Carlo while the downward going muon-like events agreed well with the Monte Carlo [41]. The distance dependence of this effect will become a key observation for understanding the physics of the neutrino described in Chapter 4.

3.5 SNO

The Sudbury Neutrino Observatory, SNO, is an imaging water Čerenkov detector that operates very similarly to Kamiokande and Super Kamiokande. The SNO experiment is unique because instead of H_2O its active volume is 1 kilo-ton of heavy water, D_2O. The heavy water allows for additional interactions for neutrino detection. The same elastic scattering reaction used by Super Kamiokande and Kamiokande,

$$e^- + \nu_x \longrightarrow e^- + \nu_x,$$

is also used in SNO. Neutrinos can be detected by charged current reactions on deuterons, CC,

$$\nu_e + d \longrightarrow p + p + e^-,$$

and neutral current reactions, NC,

$$\nu_x + d \longrightarrow p + n + e^-.$$

The elastic scattering interaction has some sensitivity to muon or tau neutrinos but is predominantly sensitive to electron neutrinos. The charged current reactions are only sensitive to electron neutrinos. The neutral current reaction is equally sensitive to all neutrinos and can be distinguished from the other two interactions by the detection of the neutron. The charged current and elastic scattering reaction are separated statistically using detector response parameters.

The SNO experiment is located in the Inco's Creighton mine near Sudbury Ontario at a depth of 6100 meters water equivalent. This large depth drastically reduces backgrounds from cosmic muons. The D_2O is kept in a 12m diameter spherical acrylic vessel. The acrylic vessel is surrounded ultra pure H_2O which acts as a buffer for external neutron and γ backgrounds. The light water is kept in a cylindrical barrel with a diameter of 22m and a height of 34m. In the light water, a stainless steel structure of 17.8m diameter holds the 9456 PMTs which gives the experiment about 55% PMT coverage. This relatively large amount of PMT coverage leads to an energy resolution of ~14.5% at 10 MeV[42]. This is comparable to Super Kamiokande as is the 26.7° angular resolution.

The SNO experiment had three distinct stages of running. The first stage was pure D_2O from November 1999 to May 2001 [43, 44, 45, 46]. The second stage or salt phase from June 2001 to October 2003 where 2000 kg of NaCl was added to the D_2O to increase the neutron detection efficiency [47, 42]. The third and final phase saw the removal of the salt and the addition 36 strings of ^{3}He proportional counters, Neutral Current Detectors or NCDs, to provide an independent detection of neutrons[22]. The third phase ran from November 2004 to November 2006.

The three stages of the SNO running can be thought of three distinct experiments measuring the flux of ^{8}B solar neutrinos flux with the neutral current reaction as these three stages have very different systematic uncertainties for the detection of neutrons. The measurements of the elastic scattering and charged current fluxes are more correlated. The first phase of running, pure D_2O, reports the three fluxes as

$$\Phi_{CC} = 1.76^{-0.06}_{-0.05}(\text{stat.})^{-0.09}_{-0.09}(\text{syst.}) \times 10^6 \text{cm}^{-2}\text{s}^{-1}$$
$$\Phi_{ES} = 2.39^{-0.24}_{-0.23}(\text{stat.})^{-0.12}_{-0.12}(\text{syst.}) \times 10^6 \text{cm}^{-2}\text{s}^{-1}$$
$$\Phi_{NC} = 5.09^{-0.44}_{-0.43}(\text{stat.})^{-0.46}_{-0.43}(\text{syst.}) \times 10^6 \text{cm}^{-2}\text{s}^{-1}$$

for a data set of 306.4 days and a 5 MeV energy threshold [42]. The second phase of running, the salt phase, reports the three fluxes as

$$\Phi_{CC} = 1.68^{-0.06}_{-0.06}(\text{stat.})^{-0.08}_{-0.09}(\text{syst.}) \times 10^6 \text{cm}^{-2}\text{s}^{-1}$$
$$\Phi_{ES} = 2.35^{-0.22}_{-0.22}(\text{stat.})^{-0.15}_{-0.15}(\text{syst.}) \times 10^6 \text{cm}^{-2}\text{s}^{-1}$$
$$\Phi_{NC} = 4.94^{-0.21}_{-0.21}(\text{stat.})^{-0.38}_{-0.34}(\text{syst.}) \times 10^6 \text{cm}^{-2}\text{s}^{-1}$$

for a data set of 254.2 days and a 5.5 MeV energy threshold[46]. Finally, the third phase of running following the installation of the NCDs measures

$$\Phi_{CC} = 1.67^{-0.04}_{-0.04}(\text{stat.})^{-0.07}_{-0.08}(\text{syst.}) \times 10^6 \text{cm}^{-2}\text{s}^{-1}$$
$$\Phi_{ES} = 1.77^{-0.24}_{-0.21}(\text{stat.})^{-0.10}_{-0.09}(\text{syst.}) \times 10^6 \text{cm}^{-2}\text{s}^{-1}$$
$$\Phi_{NC} = 5.54^{-0.33}_{-0.31}(\text{stat.})^{-0.36}_{-0.34}(\text{syst.}) \times 10^6 \text{cm}^{-2}\text{s}^{-1}$$

with 385.2 days of data and a 5 MeV energy threshold[22]. The charged current fluxes show a greater deficit compared to the Standard Solar Model, $5.79 \times 10^6 \text{cm}^{-2}\text{s}^{-1}$ [30], than what was seen by Super Kamiokande using neutrino elastic scattering. The elastic scattering measurements from the first two phases are in agreement with the Super Kamiokande elastic scattering measurement. The third phase is low by 2.2σ but a simple statistical fluctuation is the most likely explanation[22].

By far the most interesting result is provided by the neutral current measurement, the reaction that is equally sensitive to all neutrino flavors. The flux measured by the neutral current reaction is consistent with the Standard Solar Model prediction. This result indicates that the Standard Solar Model is correctly modeling the sun but some of the ν_e are detected with a different flavor. This flavor change leads to a deficit of neutrinos detected by reactions that are only sensitive or predominantly sensitive to electron flavor neutrinos.

The effect of this flavor change can be visualized by plotting the results of each of the three different channels on a plot of $\Phi_{\mu/\tau}$ versus Φ_e as shown in Fig. 3.2. The charged
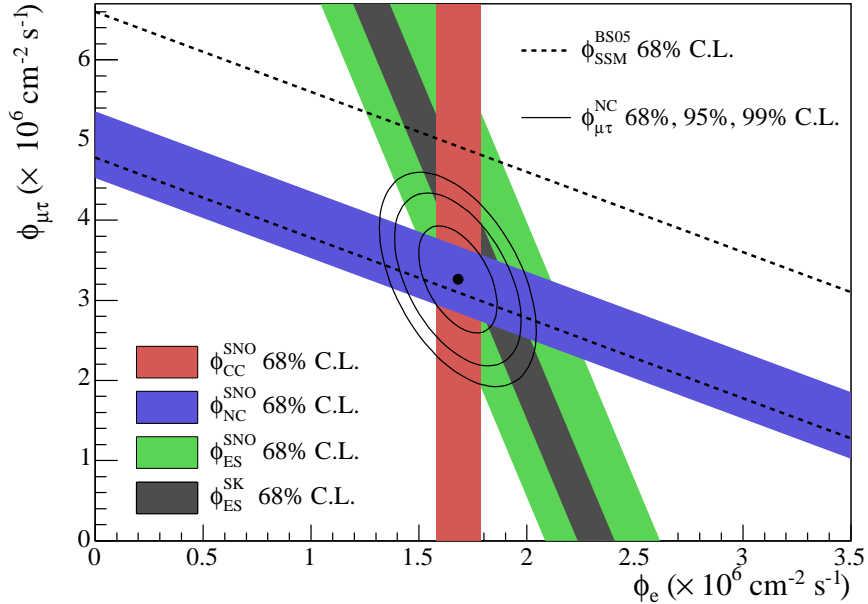
Figure 3.2: Flux of $\mu + \tau$ neutrinos versus flux of electron neutrinos. CC, NC and ES flux measurements are indicated by the filled bands. The total ^{8}B solar neutrino flux predicted by the Standard Solar Model [48] is shown as dashed lines. The narrow band parallel to the SNO ES result corresponds to the Super-Kamiokande elastic scattering result in [23]. The intercepts of these bands with the axes represent the $\pm 1\sigma$ uncertainties. The non-zero value of $\phi_{\mu\tau}$ provides strong evidence for neutrino flavor transformation. The point represents ϕ_e from the CC flux and $\phi_{\mu\tau}$ from the NC-CC difference with 68%, 95%, and 99% C.L. contours included. The figure is reproduced from [46].

current interaction will be a vertical on this plot because it is only sensitive to electron flavor. The neutral current will be a diagonal line as it is equally sensitive to all three flavors and the elastic scattering reaction will be a diagonal with a steeper negative slope as it is more sensitive to electron flavor. The three measurement overlap nicely indicating that only 1/3 of solar neutrinos are detected on Earth with their original electron flavor.

3.6   Reactor Experiments and KamLAND

Nuclear reactors are powerful sources of anti-neutrinos. The history of reactor experiments starts in 1953 with the first detection of the neutrino by Reines and Cowan at the Hanford reactor[49] and the confirmation in 1960 at Savannah River[50]. At the time it was not clear whether neutrinos and anti-neutrinos were distinct. A precursor to the Homestake experiment using anti-neutrinos from the Brookhaven reactor showed that neutrinos and anti-neutrinos were in fact different particles[51]. It was natural to try

to reproduce the observed deficit of neutrinos from the sun with an observation of anti-neutrinos from nuclear reactors. Experiments were done at Savannah River[50], ILL [52], Bugey [53], Gösgen [54], Rovno [55, 56], Krasnoyarsk [57], Chooz [58], and Palo Verde [59]. The experiments ranged from 10 m to 1 km but none saw a deficit like that seen in the solar neutrinos.

The KamLAND reactor experiment is the most recent experiment to measure the flux of anti-neutrinos from a reactor. It is located in the Kamioka mine in the same cavity that housed the Kamiokande experiment and near the location of the Super Kamiokande experiment. Japan has 55 nuclear reactor complexes that provide much of the electricity for the country. Due to the geography of Japan and the need for cooling water, most of the nuclear reactors are on the coast while the mine is located in the center of the island. This means that to a good approximation the 55 reactors can be thought of as one very large anti-neutrino source at distance of ∼200 km. At this distance from the reactors a large mass of target material is needed to provide reasonable statistics. The requirement for such a large detector mass lead some to believe that such an experiment would never be built [60].

KamLAND's target is 1 kilo-ton of liquid scintillator. Like its predecessors it uses the inverse beta decay reaction to detect the reactor anti-neutrinos:

$$\bar{\nu}_e + p \longrightarrow e^+ + n.$$

In this interaction the positron will annihilate immediately stopping depositing most of the kinetic energy of the incoming anti-neutrino in addition to the annihilation gammas. The energy of this event can be related to the initial anti-neutrino energy by $E = E_{\bar{\nu}_e} - 0.8$ MeV, neglecting the recoil energy of the neutron. The neutron from the interaction will bounce around, thermalize, before capturing on a proton within ∼200 μs emitting a 2.2MeV gamma ray. This pair of events provides a very nice signal that is easy to extract even in the presents of large backgrounds. The details of the KamLAND experiment will be presented in Chapter 5.

The companies that operate the nuclear reactors provide KamLAND with the number of fissions per reactor core per isotope per day. This information is input to a model that was developed for KamLAND to predict the anti-neutrino flux and energy spectrum at KamLAND[61]. Using this information and the number of anti-neutrinos detected by KamLAND, the results can be compared to the other reactor experiments. KamLAND released it first results in 2002, the ratio of measured anti-neutrinos to the number of anti-neutrinos predicted by the reactor data was

$$\frac{N_{obs} - N_{bg}}{N_{reactor}} = 0.611 \pm 0.085(stat.) \pm 0.041(syst.). \tag{3.7}$$

For the first time a reactor neutrino experiment saw a significant deficit, see Fig. 3.3. Since this result, KamLAND has also detected a distortion in the predicted reactor neutrino energy spectrum [62]. The most current result with almost 1500 days of data rules out a scaled undistorted energy spectrum at $> 5\sigma$ as shown in Fig. 3.4 [63]. The distance and energy dependence of the effect seen by KamLAND will be key to understanding the physics that is at work here and will be outlined further in Chapter 4.
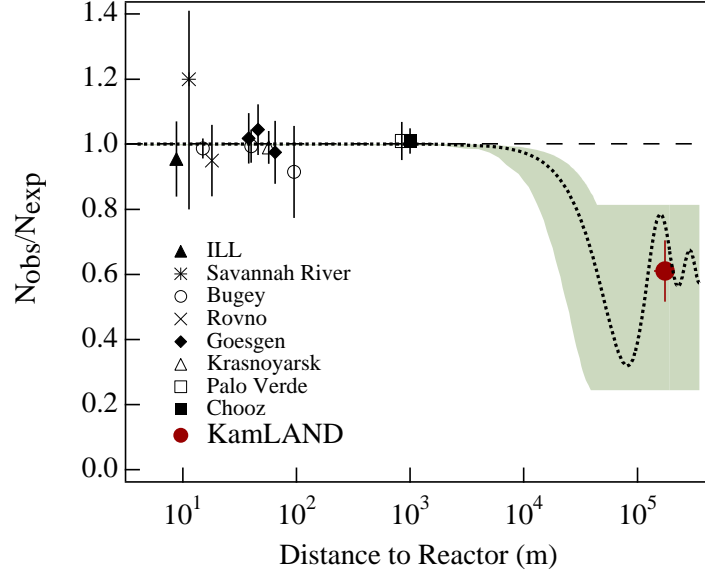
Figure 3.3: The measured versus predicted flux for experiments preceding Kamland [49, 50, 52, 53, 54, 55, 56, 57, 58, 59] and that for KamLAND from the first data set of 162 ton-years[64]. The experiments preceeding KamLAND were consistent with the expect flux while KamLAND at an average difference of ∼200 km sees a significant deficit.
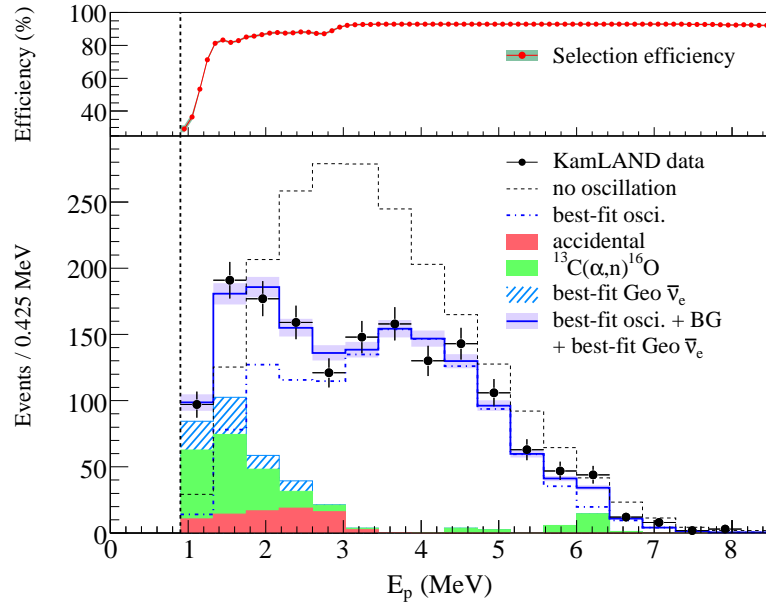
Figure 3.4: The energy spectrum of anti-neutrino candidates in KamLAND. The energy spectrum disagrees with a scaled undistorted reactor anti-neutrino spectrum at $> 5\sigma$[63].

3.7   Summary of Experiment

The solar neutrino experiments, Homestake, Gallex, SAGE, Kamiokande, Super Kamiokande, SNO have established that the flux of electron flavor neutrinos detected is smaller than predicted by the Standard Solar Model. This deficit is dependent on the energy threshold of the experiment. The lower threshold gallium experiments report a smaller deficit than the other experiments. The SNO experiment showed that the total flux of ^{8}B neutrinos measured with the flavor independent neutral current reaction is consistent with the Standard Solar Model. This implies that the electron flavor neutrinos change flavor on their journey to the earth.

In addition to solar neutrinos, Kamiokande and Super Kamiokande measured the flux of atmospheric neutrinos. These experiments found that unlike the solar neutrinos, the electron flavor neutrinos agree with model predictions. However, the muon flavor neutrinos do not and in particular the agreement worsens with the distance between production point and the detector. Finally, KamLAND became the first reactor anti-neutrino experiment to detect a deficit of anti-neutrinos from a reactor. The detector is much farther away than previous experiment and as in the solar neutrinos, the deficit is energy dependent. The combination of these results have nurtured and now form the foundation for our understanding of the physics of neutrinos and more particularly neutrino oscillations as outlined in the next Chapter 4.

Chapter 4

Neutrino Physics

The mystery of the missing neutrinos outlined in Chapter 3 had two possible solutions. The Standard Solar Model was not correctly predicting the solar neutrino fluxes or the Standard Model of particle physics was not correctly describing the neutrino properties or interactions. The Standard Solar Model as described in Chapter 2 was verified by other measurements of solar properties, most notably those from helioseismology. There was no room within the uncertainties in the Standard Solar Model to explain the experimental results. This seemed to eliminate an astrophysical solution to the problem, leaving a particle physics solution as the only viable explanation. Any particle physics solution had to also be consistent with the measurements of atmospheric and reactor neutrinos described in Chapter 3.

4.1 Standard Model of Particle Physics

The Standard Model of particle physics is the framework on which our current knowledge of particle physics is built. In this model all matter is composed of six quarks,

$$\begin{pmatrix} u \\ d \end{pmatrix} \quad \begin{pmatrix} c \\ s \end{pmatrix} \quad \begin{pmatrix} t \\ b \end{pmatrix} , \tag{4.1}$$

and six leptons,

$$\begin{pmatrix} e \\ \nu_e \end{pmatrix} \quad \begin{pmatrix} \mu \\ \nu_\mu \end{pmatrix} \quad \begin{pmatrix} \tau \\ \nu_\tau \end{pmatrix} . \tag{4.2}$$

The interaction of these particles are described by three forces, the strong, the weak, and the electromagnetic force which are mediated by vector bosons. The most familiar of these vector bosons being the photon, γ, for the electromagnetic force. The force of gravity is not incorporated in the Standard Model. The correct accommodation of the Standard Model with General Relativity is currently one of the most difficult problem plaguing theoretical physics.

In the framework of the previously established Standard Model of particle physics, the neutrino is a weakly interacting mass-less particle. As a weakly interacting particle its interactions are those of the weak force and can be divided into two categories, neutral

currents mediated by the Z^0 vector boson, and charged currents mediated by the $W^{\pm}$ vector bosons. The neutrino does not have mass in the Standard Model and no neutrino mass terms were included in the theory. While the neutrino is mass-less, the quarks and charged leptons gain masses through Yukawa couplings to the scalar field of the Higg's boson.

There is no theoretical reason for the neutrino to have zero mass. However, neutrino helicity experiments show that the neutrino interacts as a purely left handed helicity state while the anti-neutrino interacts as a purely right handed helicity state. If a particle has mass, it is always possible to boost to a reference frame of the opposite helicity, so this seems consistent with idea that the neutrino is a mass-less particle. There have been experiments that have search from neutrino mass. These "direct" searches have not had sufficient sensitivity and are are consistent with zero neutrino mass[65, 66]. The tritium beta decay endpoint experiment KATRIN should start data taking shortly and may have the required sensitivity to directly detect neutrino mass[67]. If the neutrino is allowed to have mass then this opens the door to many interesting phenomenon.

The first issue when adding the neutrino mass to the standard model is what sort of mass to add. The neutrino is usually included in the standard model as a Dirac particle and as such would add a mass term to the standard model Lagrangian

$$L_{mass} = -\nu_R^\alpha m_{\alpha\beta} \nu_L^\beta + h.c. \tag{4.3}$$

where $\nu^\alpha = (\nu^e, \nu^\mu, \nu^\tau)$ using the notation of Fukugita and Yanagida, $h.c.$ refers to the Hermitian conjugate[68]. As a Dirac particle the neutrino would have distinct particle and anti-particle states. The Dirac neutrino is described by a quadruplet of states with the same mass, $\nu_L, \bar{\nu}_R, \bar{\nu}_L, \nu_R$.

Since the neutrino is a neutral particle, electric charge is not available to distinguish it from its anti-particle. Theoretically there is no reason to believe that the neutrino is a Dirac particle, a particle distinguishable from its anti-particle. It may be that the neutrino and the anti-neutrino are the same particle, a Majorana particle. For the case of a Majorana particle an additional mass term

$$L_{mass} = -\frac{1}{2}\nu_L^{\alpha T} C^{-1} m_{\alpha\beta} \nu_L^\beta + h.c. \tag{4.4}$$

may be added to the Standard Model Lagrangian.

This Majorana mass term is not invariant under charge conjugation, C. The invariance of the Dirac mass term under charge conjugation leads to the conservation of a quantum number usually referred to as "lepton number". The fact that a Majorana neutrino can lead to processes that cause "lepton number" violation has major consequences for the formation of the universe and could lead to an understanding of the matter anti-matter asymmetry in the universe by leptogenesis. The search for one of these processes, neutrino-less double beta decay, is currently an area of intense research. One neutrino-less double beta decay experiment using ^{76}Ge has reported controversial evidence[69].

A massive Dirac neutrino also allows for interesting new physics. A massive Dirac neutrino naturally develops a magnetic moment. When the Standard Model is extended to

include mass for neutrinos, the magnetic moment can be written

$$\mu = \frac{3eG_F}{8\pi^2\sqrt{(2)}}m_\nu \sim 3 \times 10^{-19}\frac{m_\nu}{1eV}\mu_{Bohr}. \tag{4.5}$$

This is a very small magnetic moment but other extensions to the Standard Model predict larger magnetic moments. In a strong magnetic field, one of these larger magnetic moments could lead to a $\nu - \bar{\nu}$ transition, but this is an extremely small effect compared to the neutrino flavor oscillation described in the next section.

4.2   Neutrino Oscillation in Vacuum

A massive neutrino in the Standard Model will interact in definite flavor eigenstates but will propagate forward in time as definite mass eigenstates. If the mass eigenstates do not correspond to the flavor eigenstates, the classic quantum oscillation scenario develops. The consequence of this is that a neutrino that is created as one flavor will propagate forward in time as the mass eigenstates. A later measurement of the neutrino flavor may find that the neutrino has now changed flavor. If an experiment is not sensitive to the new flavor or is less efficient at detecting this second flavor then the experiment will report a deficit of neutrinos from the source. This is an attractive explanation for the experimental results presented in Chapter 3.

Neutrino oscillation was first proposed by Pontecorvo though his mechanism was the oscillation of $\nu - \bar{\nu}$, similar to the oscillation seen in the quarks with systems like $K^0 - \bar{K}^0$ [70] . The flavor oscillations that are the proposed solution to the solar neutrino problem were first outlined by Maki, Nakagawa and Sakata[71]. The flavor eigenstates of the weak interaction are described by the superposition of the mass eigenstates as

$$|\nu_\alpha\rangle = \sum_j U^*_{\alpha j}|\nu_j\rangle. \tag{4.6}$$

where the matrix U describes the mixing of the mass eigenstates. In honor of the original formulators it is often called the MNSP matrix. If it is assumed that there are three neutrinos it takes the form,

$$
\begin{aligned}
U_{\alpha j} &= \begin{pmatrix} \cos\theta_{12} & \sin\theta_{12} & 0 \\ -\sin\theta_{12} & \cos\theta_{12} & 0 \\ 0 & 0 & 1 \end{pmatrix} \begin{pmatrix} 1 & 0 & 0 \\ 0 & \cos\theta_{23} & \sin\theta_{23} \\ 0 & -\sin\theta_{23} & \cos\theta_{23} \end{pmatrix} \begin{pmatrix} \cos\theta_{13} & 0 & \sin\theta_{13}e^{-i\delta} \\ 0 & 1 & 0 \\ -\sin\theta_{13}e^{i\delta} & 0 & \cos\theta_{13} \end{pmatrix} \\
&\times \begin{pmatrix} e^{i\xi_1/2} & 0 & 0 \\ 0 & e^{i\xi_2/2} & 0 \\ 0 & 0 & 1 \end{pmatrix}
\end{aligned}
\tag{4.7}
$$

where θ_{ij} are the three mixing angles and δ is a complex phase. The complex phase gives rise to CP violation in the lepton sector. If neutrinos are Majorana particles then there are two addition non-zero phases, ξ_1 and ξ_2.

4.2.1   Derivation of Oscillation Probability

The interesting expression to derive for the analysis of experiments, is the probability that a neutrino produced in one flavor will oscillate and then be detected in another

flavor, $P(\nu_\alpha \to \nu_\beta)$. The derivation of this expression is fairly simple but there are subtleties in the derivation, especially in the treatment of the ultra-relativistic nature of the neutrino. The following derivation follows and expands upon the derivations of B. Kayser in Ref. [72, 73].

The neutrinos will be made in definite flavor states, ν_α, but will propagate as the different mass eigenstates, ν_i. The relative phase difference of the propagation of these mass eigenstates is the oscillation. From quantum mechanics the propagation of a particle is given by $e^{-im_i\tau_i}$ where m_i is the mass of ν_i and τ_i is the elapsed propagation time in the ν_i rest frame. As such the relative phase difference between the first and second mass eigenstate, ν_1 and ν_2, is given by

$$\delta\phi_{12} = (p_1 - p_2)L - (E_1 - E_2)t, \tag{4.8}$$

in an arbitrary frame. Measuring the propagation time of neutrinos is not experimentally feasible. However, to very good approximation the velocity of the neutrino can be taken to be the average velocity of the different eigenstates,

$$\bar{v} = \frac{p_1 + p_2}{E_1 + E_2}. \tag{4.9}$$

The phase then becomes

$$\delta\phi_{12} \simeq \frac{p_1^2 - p_2^2}{p_1 + p_2}L - \frac{E_1^2 - E_2^2}{p_1 + p_2}L$$
$$= (m_1^2 - m_2^2)\frac{L}{p_1 + p_2} \simeq (m_1^2 - m_2^2)\frac{L}{2E}. \tag{4.10}$$

The last step uses the fact that for ultra-relativistic neutrinos their momentum is approximately equivalent to their energy. This means that we can write the propagator for a single mass eigenstate as

$$Prop(\nu_i) = e^{-im_i^2 L/2E} \tag{4.11}$$

and the amplitude to oscillate from one phase to another will be given by

$$Amp(\nu_\alpha \to \nu_\beta) = \sum_i U_{\alpha i}^* e^{-im_i^2 L/2E} U_{\beta i}. \tag{4.12}$$

The probability that a neutrino of flavor ν_α will oscillate into a flavor of ν_β is then the square of this amplitude,

$$P(\nu_\alpha \to \nu_\beta) = |Amp(\nu_\alpha \to \nu_\beta)|^2$$
$$= \sum_{i,j} U_{\alpha i}^* U_{\beta i} U_{\alpha j} U_{\beta j}^* e^{-i\Delta m_{ij}^2 L/2E} \tag{4.13}$$

where Δm_{ij}^2 is $m_i^2 - m_j^2$, the difference in the squared masses of the states. This form of the expression is not particularly enlightening. By writing out some of the first terms,

$$\begin{aligned} P(\nu_\alpha \to \nu_\beta) &= U_{\alpha 1}^* U_{\beta 1} U_{\alpha 1} U_{\beta 1}^* + U_{\alpha 1}^* U_{\beta 1} U_{\alpha 2} U_{\beta 2}^* e^{-i\Delta m_{12}^2 L/2E} + \dots \\ &+ U_{\alpha 2}^* U_{\beta 2} U_{\alpha 2} U_{\beta 2}^* + U_{\alpha 2}^* U_{\beta 2} U_{\alpha 1} U_{\beta 1}^* e^{i\Delta m_{12}^2 L/2E} + \dots, \end{aligned} \tag{4.14}$$

we see that the sum can be broken up as follows,

$$P(\nu_\alpha \rightarrow \nu_\beta) = \sum_{i=j} U_{\alpha i}^* U_{\beta i} U_{\alpha j} U_{\beta j}^* +$$

$$\sum_{i>j} \left[U_{\alpha i}^* U_{\beta i} U_{\alpha j} U_{\beta j}^* e^{-i\Delta m_{ij}^2 L/2E} + (U_{\alpha i}^* U_{\beta i} U_{\alpha j} U_{\beta j}^* e^{-i\Delta m_{ij}^2 L/2E})^* \right] \quad (4.15)$$

$$= \sum_{i=j} U_{\alpha i}^* U_{\beta i} U_{\alpha j} U_{\beta j}^* + 2 \sum_{i>j} Re[U_{\alpha i}^* U_{\beta i} U_{\alpha j} U_{\beta j}^* e^{-i\Delta m_{ij}^2 L/2E}].$$

Now using the following facts $Re(a*b) = Re(a)*Re(b) - Im(a)*Im(b)$, $Re(e^{i\phi}) = \cos\phi$, $Im(e^{i\phi}) = \sin\phi$, and $\cos 2\theta = 1 - 2\sin^2\theta$, we can write,

$$P(\nu_\alpha \rightarrow \nu_\beta) = \sum_{i=j} U_{\alpha i}^* U_{\beta i} U_{\alpha j} U_{\beta j}^* + 2 \sum_{i>j} Re[U_{\alpha i}^* U_{\beta i} U_{\alpha j} U_{\beta j}^*]$$

$$- 4 \sum_{i>j} Re[U_{\alpha i}^* U_{\beta i} U_{\alpha j} U_{\beta j}^*] \sin^2 \frac{\Delta m_{ij}^2 L}{4E} \quad (4.16)$$

$$+ 2 \sum_{i>j} Im[U_{\alpha i}^* U_{\beta i} U_{\alpha j} U_{\beta j}^*] \sin \frac{\Delta m_{ij}^2 L}{2E}.$$

The first two terms are equivalent to evaluating the oscillation probability at $L = 0$ or $t = 0$, $P(\nu_\alpha \rightarrow \nu_\beta)_{L=0}$. The unitarity of U implies that $\sum_i U_{\alpha i}^* U_{\beta i} = \delta_{\alpha\beta}$. If U is not unitary then this is evidence for an additional neutrino flavor taking part in the oscillation and the matrix must be enlarged to account for the new flavor. Using the unitarity condition,

$$P(\nu_\alpha \rightarrow \nu_\beta)_{L=0} = |\sum_i U_{\alpha i}^* U_{\beta i}|^2 = |\delta_{\alpha\beta}|^2 = \delta_{\alpha\beta}, \quad (4.17)$$

$P(\nu_\alpha \rightarrow \nu_\beta)$ becomes,

$$P(\nu_\alpha \rightarrow \nu_\beta) = \delta_{\alpha\beta}$$

$$- 4 \sum_{i>j} Re[U_{\alpha i}^* U_{\beta i} U_{\alpha j} U_{\beta j}^*] \sin^2 \frac{\Delta m_{ij}^2 L}{4E} \quad (4.18)$$

$$+ 2 \sum_{i>j} Im[U_{\alpha i}^* U_{\beta i} U_{\alpha j} U_{\beta j}^*] \sin \frac{\Delta m_{ij}^2 L}{2E}.$$

So far the derivation has centered on neutrinos. To derive the equivalent expression for anti-neutrinos, $P(\bar{\nu}_\alpha \rightarrow \bar{\nu}_\beta)$, the symmetries of the oscillation should be examined. All local field theories require CPT invariance. For neutrino oscillations this means

$$P(\bar{\nu}_\alpha \rightarrow \bar{\nu}_\beta) = P(\nu_\beta \rightarrow \nu_\alpha). \quad (4.19)$$

Looking at both sides of this equation individually, we find

$$P(\nu_\beta \rightarrow \nu_\alpha; U) = P(\nu_\alpha \rightarrow \nu_\beta; U^*) \quad (4.20)$$

and by CPT invariance again

$$P(\bar{\nu}_\alpha \to \bar{\nu}_\beta; U) = P(\nu_\alpha \to \nu_\beta; U^*). \tag{4.21}$$

This means Eq. 4.18 can be generalized

$$
\begin{aligned}
P(\overset{(-)}{\nu_\alpha} \to \overset{(-)}{\nu_\beta}) = \ &\delta_{\alpha\beta} \\
&- 4\sum_{i>j} Re[U^*_{\alpha i} U_{\beta i} U_{\alpha j} U^*_{\beta j}] \sin^2 \Delta m^2_{ij} L/4E \\
&\overset{+}{(-)} 2\sum_{i>j} Im[U^*_{\alpha i} U_{\beta i} U_{\alpha j} U^*_{\beta j}] \sin \Delta m^2_{ij} L/2E
\end{aligned}
\tag{4.22}
$$

where $(-)$ indicates the probability for anti-neutrinos. This equation is completely general for N-neutrino mixing provided that the mixing matrix, U, is unitary. Eq. 4.22 also highlights several key consequences of an observation of neutrino oscillation as well as the limitations of these sorts of experiments. Obviously a detection of neutrino oscillation proves neutrinos have mass and non-trivial mixing. Observation of neutrino oscillation can measure mass differences but not the absolute masses nor the Majorana or Dirac nature of the neutrino. Finally, neutrino oscillation experiments comparing $P(\bar{\nu}_\alpha \to \bar{\nu}_\beta)$ to $P(\nu_\alpha \to \nu_\beta)$ with sufficient sensitivity would be able to measure CP violation in neutrino oscillation.

4.2.2 Quasi Two-Neutrino Mixing

Section 4.2.1 culminated in a completely general expression for neutrino oscillation. In practice, most experiments are sensitive to only an effective two neutrino mixing. This can come about for one of two reasons. The first reason would be if one of the mass splittings is much larger than the others, $\Delta M^2 \gg \Delta m^2$. If an experiment is performed such that $\Delta M^2 L/E = \mathcal{O}(1)$, then $\Delta m^2 L/E \ll 1$ and the experiment will only be sensitive to the larger splitting. In this limit Eq. 4.22 simplifies to

$$P(\overset{(-)}{\nu_\alpha} \to \overset{(-)}{\nu_\beta}) \simeq S_{\alpha\beta} \sin^2 \frac{\Delta M^2 L}{4E} \tag{4.23}$$

and

$$P(\overset{(-)}{\nu_\alpha} \to \overset{(-)}{\nu_\alpha}) \simeq 1 - T_\alpha(1 - T_\alpha) \sin^2 \frac{\Delta M^2 L}{4E}. \tag{4.24}$$

The unitarity of the mixing matrix has once again been exploited and $S_{\alpha\beta}$ and T_α are defined by

$$S_{\alpha\beta} \equiv 4 \left| \sum_{i>\underset{small}{j}} U^*_{\alpha i} U_{\beta i} \right|^2, \tag{4.25}$$

$$T_\alpha \equiv \sum_{i>\underset{small}{j}} |U_{\alpha i}|^2, \tag{4.26}$$

where $i > \underset{small}{j}$ is the sum over those mass eigenstates that lie above ΔM^2.

In the case of three neutrino oscillation, the convention is to declare ν_3 as the neutrino mass eigenstate at the one end of the large splitting. Then $P(\overset{(-)}{\nu_\alpha} \to \overset{(-)}{\nu_\beta}) = 4|U_{\alpha 3}|^2|U_{\beta 3}|^2 \sin^2 \Delta m_{32}^2 L/4E$ and $P(\overset{(-)}{\nu_\alpha} \to \overset{(-)}{\nu_\alpha}) = 1 - 4|U_{\alpha 3}|^2(1 - |U_{\alpha 3}|^2) \sin^2 \Delta m_{32}^2 L/4E$. At this point we can evaluate the matrix elements of U,

$$
U = \begin{array}{c} \\ \nu_e \\ \nu_\mu \\ \nu_\tau \end{array}
\begin{array}{c} \nu_1 \qquad\qquad \nu_2 \qquad\qquad \nu_3 \end{array}
\begin{pmatrix}
c_{12}c_{13} & s_{12}c_{13} & s_{13}e^{-i\delta} \\
-s_{12}c_{23} - c_{12}s_{23}s_{13}e^{i\delta} & c_{12}c_{23} - s_{12}s_{23}s_{13}e^{i\delta} & s_{23}c_{13} \\
s_{12}s_{23} - c_{12}c_{23}s_{13}e^{i\delta} & -c_{12}c_{23} - s_{12}c_{23}s_{13}e^{i\delta} & c_{23}c_{13}
\end{pmatrix} . \tag{4.27}
$$

In the assembly of the matrix the possible Majorana phases have been neglected as they are undetectable in oscillation experiments and the shorthand $s_{ij} = \sin\theta_{ij}$ has been used. The oscillation probability is then

$$
P(\overset{(-)}{\nu_\alpha} \to \overset{(-)}{\nu_\beta}) = 4s_{23}^2 c_{23}^2 c_{13}^4 \sin^2 \frac{\Delta m_{32}^2 L}{4E} = \sin^2 2\theta_{23} \cos^4 \theta_{13} \sin^2 \frac{\Delta m_{32}^2 L}{4E}. \tag{4.28}
$$

The second reason for an experiment to be sensitive to only an effective two neutrino mixing is if only two mass eigenstates couple significantly to one of the charged leptons. This is equivalent to one of the mixing angles being vanishingly small. If this is the case then U is greatly simplified,

$$
U = \begin{array}{c} \\ \nu_\alpha \\ \nu_\beta \end{array}
\begin{array}{c} \nu_1 \quad\ \nu_2 \end{array}
\begin{pmatrix}
\cos\theta & \sin\theta \\
-\sin\theta & \cos\theta
\end{pmatrix} . \tag{4.29}
$$

The oscillation probability is then,

$$
P(\overset{(-)}{\nu_\alpha} \to \overset{(-)}{\nu_\beta}) = \sin^2 2\theta \sin^2 \frac{\Delta m^2 L}{E}. \tag{4.30}
$$

In the limit that one of the mixing angles is very small Eq. 4.28 and Eq. 4.30 become equivalent.

4.2.3 Analysis of Atmospheric Neutrinos

The atmospheric neutrino results from Kamiokande, IMB and Super Kamiokande, outlined in Chapter 3, all found that the Monte Carlo predictions for electron flavor neutrinos were in good agreement with the data while the predictions for muon flavor neutrinos were not. The Monte Carlo predictions for several event types as a function of zenith angle and the discrepancies with the data are shown in Fig. 4.1. Since the electron neutrinos do not show a deficit, this result can be interpreted in terms a two neutrino oscillation of ν_μ into ν_τ with an oscillation probability given by Eq. 4.30. The Super Kamiokande data set has the best statistics of the three experiments. The analysis of the Super Kamiokande data for the oscillation parameters uses a χ^2 fit between the Monte Carlo and data with the zenith angle as a proxy for the distance, L. The result of this analysis is $\sin^2 2\theta_{23} > 0.92$ and $1.5 \times 10^{-3} < \Delta m_{32}^2 < 3.4 \times 10^{-3}$ at the 90% confidence level[41]. This analysis shows that one of the neutrino mixing angles is very large, essentially maximal. This is in great contrast to the small mixing angles seen in the quarks.
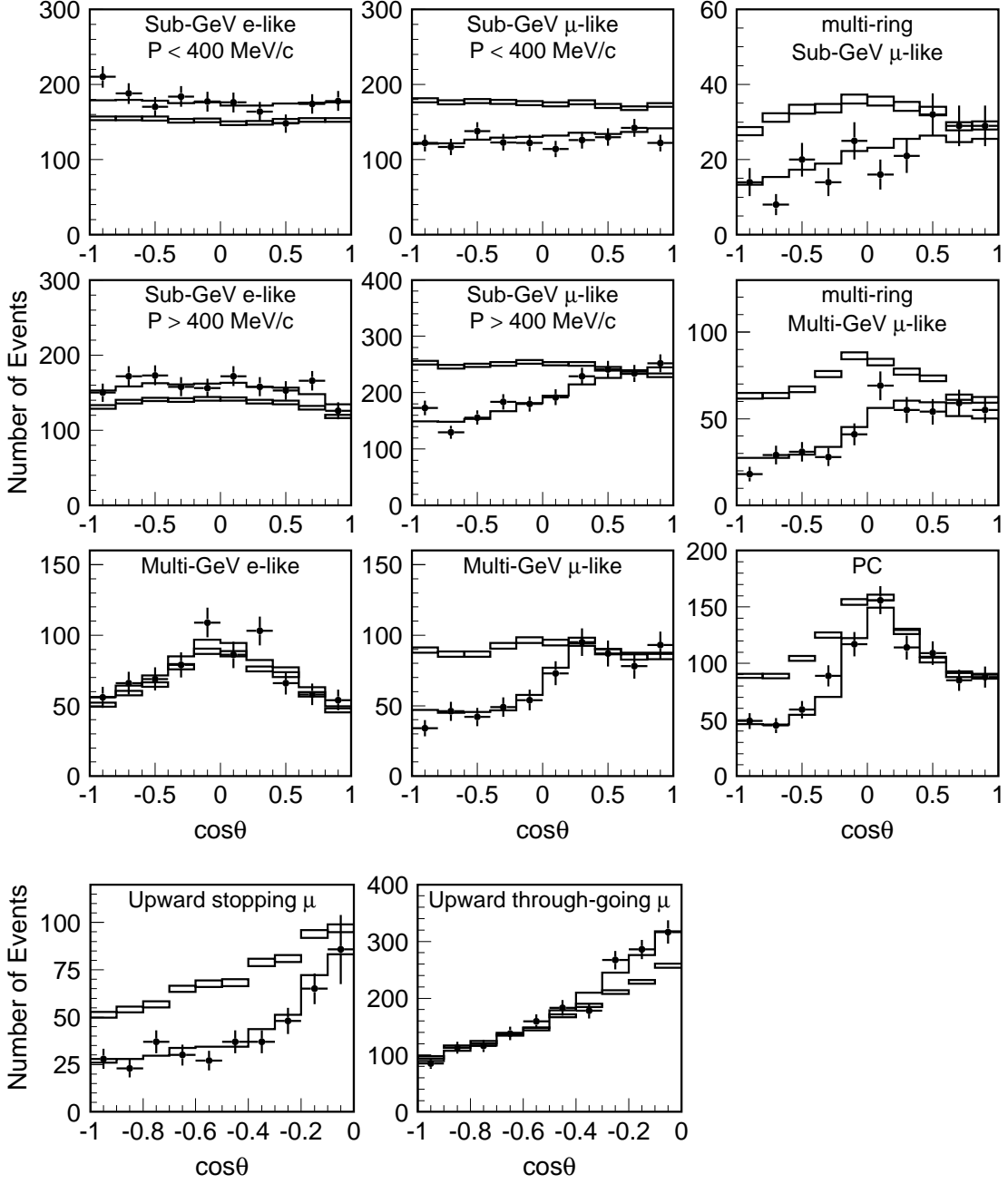
Figure 4.1: The zenith angle distribution for several different Super Kamiokande event types: fully-contained 1-ring events, multi-ring events, partially-contained events and upward going muons. The points show the data, box histograms show the non-oscillated Monte Carlo events and the lines show the best-fit expectations for $\nu_\mu \leftrightarrow \nu_\tau$ oscillations with $\sin^2 2\theta = 1.00$ and $\Delta m^2 = 2.1 \times 10^{-3}$ eV^2. The height of the boxes shows the statistical error of the Monte Carlo. This is reproduced from Ref. [41].

4.2.4 Analysis of Reactor Experiments

Experiments that measure anti-neutrinos made in nuclear power reactors are a good probe for vacuum neutrino oscillations. Reactors are a source of electron flavor anti-neutrinos with energies less than 8.5 MeV. Of all the reactor experiments, the one furthest from the source is KamLAND. KamLAND observes anti-neutrinos from multiple reactors, with an average baseline of 180 km. Over this distance the neutrinos will propagate as if they were in vacuum. From the general Eq. 4.22, the oscillation probability is given by

$$P(\bar{\nu}_e \to \bar{\nu}_x) = 4 \sum_{i>j} |U_{ei}|^2 |U_{ej}|^2 \sin^2 \Delta m_{ij}^2 L/4E. \tag{4.31}$$

This can be expanded using matrix elements of U found in Eq. 4.29 and the fact that $\Delta m_{32}^2 + \Delta m_{21}^2 = \Delta m_{31}^2$. The oscillation probability then becomes

$$\begin{aligned} P(\bar{\nu}_e \to \bar{\nu}_x) =\ & \sin^2 2\theta_{13} \sin^2 \frac{\Delta m_{31}^2 L}{4E} \\ & - \frac{1}{2} \sin^2 \theta_{12} \sin^2 2\theta_{13} \sin^2 \frac{\Delta m_{31}^2 L}{2E} \sin^2 \frac{\Delta m_{21}^2 L}{2E} \\ & + \left(\cos^4 \theta_{13} \sin^2 2\theta_{12} + \sin^2 \theta_{12} \sin^2 2\theta_{13} \cos^2 \frac{\Delta m_{31}^2 L}{2E} \right) \sin^2 \frac{\Delta m_{21}^2 L}{4E}. \end{aligned} \tag{4.32}$$

This is in agreement to the erratum for Ref. [74]. Beware that a mistake in this derivation was propagated in some of the literature.

Examining Eq. 4.32 shows that the oscillation probability a reactor neutrino experiment will measure depends on a long oscillation period defined by Δm_{21}^2 and a short oscillation period defined by Δm_{31}^2. In the limit that θ_{13} is small the oscillation will revert to an effective two neutrino mixing. This is a good assumption as analysis of atmospheric neutrinos shows that the θ_{23} angle is essentially maximal. In this limit the probability and using practical units, Eq. 4.32 becomes

$$P(\bar{\nu}_e \to \bar{\nu}_x) = \sin^2 2\theta_{12} \sin^2 \left(1.27 \Delta m_{21}^2 \frac{L(m)}{E(MeV)} \right). \tag{4.33}$$

This is in agreement with the equation derived for two neutrino mixing, Eq. 4.30. The quantity measured by reactor neutrino experiments is actually the survival probability,

$$P(\bar{\nu}_e \to \bar{\nu}_e) = 1 - \sin^2 2\theta_{12} \sin^2 \left(1.27 \Delta m_{21}^2 \frac{L(m)}{E(MeV)} \right). \tag{4.34}$$

The deficit of measured anti-neutrinos and the distortions in the energy spectrum observed by KamLAND and desribed in Section 3.6 can now be analyzed with respect to $P(\bar{\nu}_e \to \bar{\nu}_e)$. An un-binned log-likelihood fit to the neutrino candidates finds $\Delta m_{21}^2 = 7.58^{+0.14}_{-0.13}(\text{stat.})^{+0.15}_{-0.15}(\text{syst.}) \times 10^{-5} \text{eV}^2$ and $\tan^2 \theta_{12} = 0.56^{+0.10}_{-0.07}(\text{stat})^{+0.10}_{-0.06}(\text{syst.})$[63]. It is illustrative to re-plot the KamLAND energy spectrum with respect to the average baseline and $P(\bar{\nu}_e \to \bar{\nu}_e)$. As is shown in Fig. 4.2, this procedure pulls out the sinusoidal
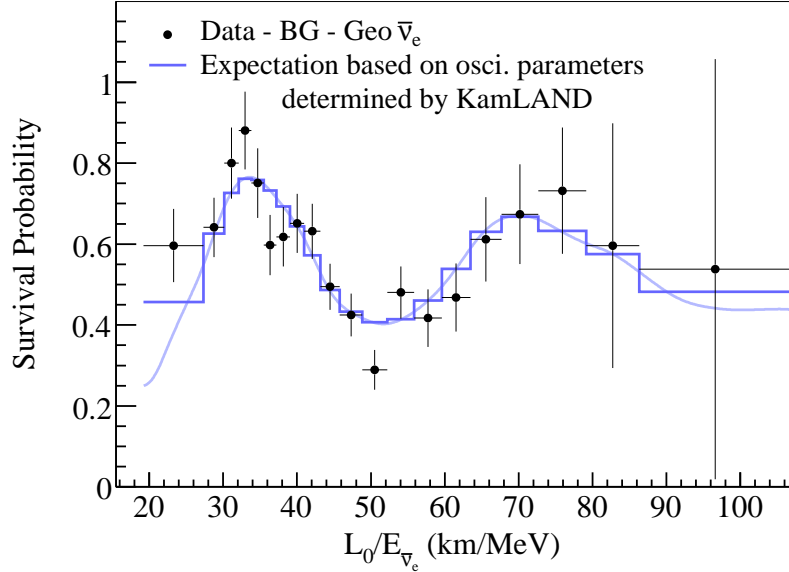
Figure 4.2: Ratio of the $\bar{\nu}_e$ energy spectrum with backgrounds and geologically produced $\bar{\nu}_e$ subtracted to the no-oscillation predicted $\bar{\nu}_e$ flux. This is plotted in equal probability bins of L_o/E where L_o is the flux weighted average baseline. The data points are in black with the prediction from neutrino oscillations overlaid in blue. For this dataset L_o is 180km[63].

behavior predicted by neutrino oscillation and expressed in Eq. 4.34. The sinusoid is washed out due to the fact that multiple reactors contribute and the experiment has a finite energy resolution. This result is compelling evidence for vacuum neutrino oscillations with baselines of $\sim$100km.

4.3 Neutrino Oscillation in Matter

As a weakly interacting particle, the neutrino's interaction cross sections are very small, on the order of the Fermi coupling constant squared, G_F^2. Such small cross sections result in long mean free paths so it would seem that matter effects are negligible. As was shown in the previous section, neutrino oscillation is a phenomenon that depends on the phase of the neutrino wave function. It was pointed out by Wolfenstein that the neutrino's phase change as it passes through matter is proportional to G_F. Therefore, matter effects can be significant especially in very dense media like in the Sun or to a lesser extent in the Earth [75]. Mikheyev and Smirnov expanded on this work by realizing that the oscillation takes on a resonance form which could lead to very efficient mixing even with small mixing parameters [76]. The combined work of Mikheyev, Smirnov, and Wolfenstein on the effect of matter on neutrino oscillation is referred to as the MSW effect.

In Section 4.2.2 it was shown that in the limit of one large mass splitting or one small mixing angle, three neutrino oscillation revert to an effective two neutrino mixing. For simplicity the two neutrino case will be used to examine the MSW effect. The fol-

lowing derivation follows the work of Bruggen, Haxton, and Qian and that of Kuo and Pantaleone[77, 78]. The effect is best understood as the solution to a Schrödinger like equation. The propagation equation for a neutrino in matter expressed in the flavor basis is

$$-i\frac{d}{dt}\left|\nu_\alpha\right\rangle = \frac{M^2}{2p}\left|\nu_\alpha\right\rangle$$

$$M^2 = U\begin{bmatrix} m_1^2 & 0 \\ 0 & m_2^2 \end{bmatrix}U^\dagger + \begin{bmatrix} V_W & 0 \\ 0 & 0 \end{bmatrix} + \begin{bmatrix} V_Z & 0 \\ 0 & V_Z \end{bmatrix}. \tag{4.35}$$

The first term of M^2 is the neutrino propagation in vacuum as seen in Eq. 4.11 where U is given by Eq. 4.29. The second and third terms are the potentials that are the result of the neutrino's interactions with matter.

As most matter contains no muons or taus, only the electron flavor gains a potential due to charged current interactions, V_W, while all flavors gain a potential due to neutral current interactions, V_Z. As neutrino oscillation is caused by phase differences, the last neutral current term , V_Z, can be dropped. The electron flavor neutrino becomes effectively heavier by V_W. The charged current potential is given by $V_W = 2\sqrt{2}G_F\rho_e E$ where ρ_e is the electron density and E is the neutrino energy. The neutrino propagation equation can now be rewritten with $t \to x$ and the expansion of the flavor eigenstate $\left|\nu_\alpha\right\rangle$ as

$$i\frac{d}{dx}\begin{bmatrix} \nu_e \\ \nu_\mu \end{bmatrix} = \frac{1}{4E}\left[(\Sigma + V_W) + \begin{bmatrix} V_W - \Delta m_{21}^2\cos 2\theta & \Delta m_{21}^2\sin 2\theta \\ \Delta m_{21}^2\sin 2\theta & -V_W + \Delta m_{21}^2\cos 2\theta \end{bmatrix}\right]\begin{bmatrix} \nu_e \\ \nu_\mu \end{bmatrix} \tag{4.36}$$

where $\Sigma = m_1^2 + m_2^2$ and Δm_{21}^2 is the normal definition $\Delta m^2 = \Delta m_{21}^2 = m_2^2 - m_1^2$. Now it will be useful to define U_m such that $U_m^\dagger M^2 U_m$. The analogous parameterization to U is

$$\begin{bmatrix} \nu_1^m \\ \nu_2^m \end{bmatrix} = \begin{bmatrix} \cos\theta_m & -\sin\theta_m \\ \sin\theta_m & \cos\theta_m \end{bmatrix}\begin{bmatrix} \nu_e \\ \nu_\mu \end{bmatrix}. \tag{4.37}$$

The mixing of neutrinos in matter is now given by the modified mixing angle,

$$\sin 2\theta_m = \frac{\Delta m^2\sin 2\theta}{\sqrt{(V_W - \Delta m^2\cos 2\theta)^2 + (\Delta m^2\sin 2\theta)^2}} \tag{4.38}$$

and the effective mass

$$M_{1,2}^2 = \frac{(\Sigma + V_W) \mp \sqrt{(V_W - \Delta m^2\cos 2\theta)^2 + (\Delta m^2\sin 2\theta)^2}}{2}. \tag{4.39}$$

There are two things to notice about the mixing given in Eq. 4.38. The mixing now depends upon the electron density of the material through which the neutrino is propagating. There is also a resonance effect where mixing becomes maximal when $V_W = \Delta m^2\cos 2\theta$.

In practice neutrinos will be traveling through a medium with changing density which makes calculating the neutrino propagation slightly more complicated as the mass eigenstates now become density dependent. We may rewrite Eq. 4.36 as

$$i\frac{d}{dx}\begin{bmatrix} \nu_e \\ \nu_\mu \end{bmatrix} = \frac{1}{2E}U_m\begin{bmatrix} M_1^2 & 0 \\ 0 & M_2^2 \end{bmatrix}\begin{bmatrix} \nu_1 \\ \nu_2 \end{bmatrix} \tag{4.40}$$

Now extracting the position dependence of U_m which comes from the changing electron density, $\rho_e(x)$, Eq. 4.40 becomes

$$i\frac{d}{dx}\begin{bmatrix}\nu_1\\\nu_2\end{bmatrix} = \left[\frac{1}{2E}\begin{bmatrix}M_1^2 & 0\\0 & M_2^2\end{bmatrix} - U_m^\dagger i\frac{d}{dx}U_m\right]\begin{bmatrix}\nu_1\\\nu_2\end{bmatrix}$$
$$= \begin{bmatrix}-(M_2^2-M_1^2)/4E & -id\theta_m/dx\\id\theta_m/dx & (M_2^2-M_1^2)/4E\end{bmatrix}\begin{bmatrix}\nu_1\\\nu_2\end{bmatrix}. \tag{4.41}$$

A common diagonal phase factor of $e^{i(M_2^2+M_1^2)x/4E}$ has been neglected and

$$(M_2^2 - M_1^2) = \sqrt{(V_W - \Delta m^2\cos 2\theta)^2 + (\Delta m^2\sin 2\theta)^2} \tag{4.42}$$

$$\frac{d\theta_m}{dx} = \frac{1}{2}\frac{\Delta m^2\sin 2\theta}{(V_W - \Delta m^2\cos 2\theta)^2 + (\Delta m^2\sin 2\theta)^2}\frac{dV_W}{dx}. \tag{4.43}$$

The following sections will explore several approximations for the solution to these equations in the Sun.

4.3.1 Adiabatic Neutrino Propagation

The solution to Eq. 4.41 is trivial if the off-diagonal terms are much smaller than the diagonal terms. This condition can be evaluated by looking at the ratio

$$\gamma(x) = \left|\frac{(M_2^2 - M_1^2)/4E}{d\theta_m/dx}\right|$$
$$= \frac{\sin^2 2\theta}{\cos 2\theta}\frac{\Delta m^2}{2E}\frac{1}{\left|\frac{1}{\rho_c}\frac{d\rho(x)}{dx}\right|}\frac{1}{\sin^3 2\theta_m(x)} \gg 1 \tag{4.44}$$

where $2\sqrt{2}EG_F\rho_c = \Delta m^2\cos 2\theta$ is the resonance condition and ρ_c is the resonance density. At the resonance density this condition becomes more stringent

$$\gamma_c = \gamma(x_c) = \frac{\sin^2 2\theta}{\cos 2\theta}\frac{\Delta m^2}{2E}\frac{1}{\left|\frac{1}{\rho_c}\frac{d\rho(x)}{dx}\right|_{x=x_c}} \gg 1. \tag{4.45}$$

If $\gamma \gg 1$ then the off diagonal terms are negligible and ν_1 and ν_2 are eigenstates of the Hamiltonian.

The condition $\gamma \gg 1$ is predominantly a condition on the electron density. An electron neutrino, ν_e, that is produced in a dense region becomes associated with the heavier mass eigenstate ν_2. If the electron density is varying slowly, $\frac{d\rho(x)}{dx}$ is small, then the ν_e will emerge associated with ν_2. However, the flavor composition of ν_2 is now determined by the mixing angle in vacuum and the ν_2 is now mostly ν_μ. This scenario is the adiabatic propagation, top diagram of Fig. 4.3. With the understanding that in the adiabatic limit ν_1 and ν_2 are eigenstates of the Hamiltonian, the calculation of the electron neutrino survival
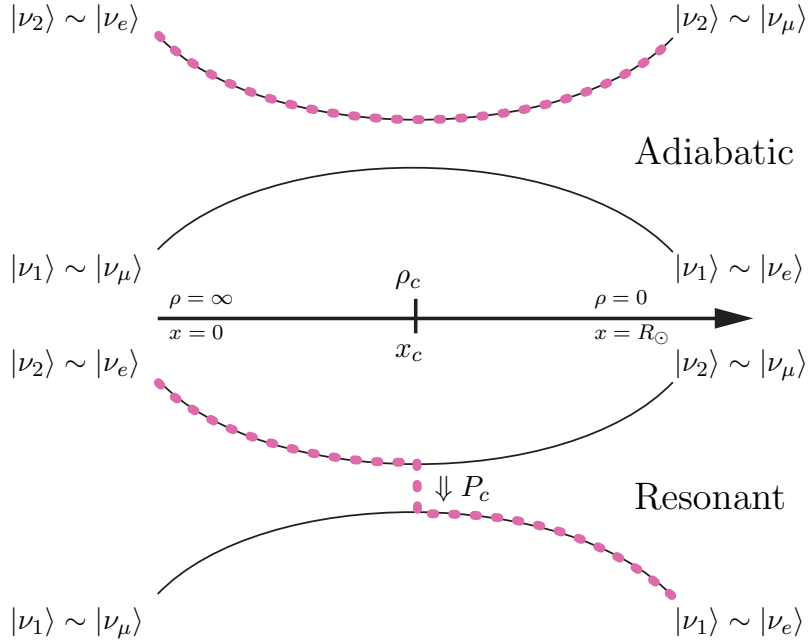
Figure 4.3: Adiabatic and resonant neutrino propagation. The electron flavor neutrino gains an effective mass and becomes associated with the heavier mass eigenstate, ν_2. If the neutrino propagates adiabatically out of the sun it will emerge still associated with ν_2 (top). However, if the electron density changes fast enough that a resonance occurs then there is some probability the neutrino will cross to the lighter mass eigenstate, ν_1 (bottom).

probability is simply given by

$$
\begin{aligned}
P(\nu_e \to \nu_e) &= \sum_i P(\nu_e \to \nu_i) P_m(\nu_i \to \nu_e) \\
&= \begin{bmatrix} 1 & 0 \end{bmatrix} \begin{bmatrix} \cos^2\theta & \sin^2\theta \\ -\sin^2\theta & \cos^2\theta \end{bmatrix} \begin{bmatrix} 1 & 0 \\ 0 & 1 \end{bmatrix} \begin{bmatrix} \cos^2\theta_m & \sin^2\theta_m \\ -\sin^2\theta_m & \cos^2\theta_m \end{bmatrix} \begin{bmatrix} 1 \\ 0 \end{bmatrix} \\
&= \frac{1}{2} + \frac{1}{2}\cos 2\theta \cos 2\theta_m .
\end{aligned}
\tag{4.46}
$$

4.3.2 Corrections to the Adiabatic Approximation

In the limit that $\gamma \gg 1$, Eq. 4.46 offers a nice simple analytic expression for the survival probabilty of electron neutrinos traversing a dense region. When $\gamma \simeq 1$, corrections to this probability will need to be included because the off diagonal terms of 4.41 will become of the same order as the diagonal terms. These correction terms take the form of level crossings. The adiabatic condition was shown to be even stricter at the resonance, Eq. 4.45, so as the neutrino propagates through the resonance if the adiabatic condition

breaks down the neutrino will have some probability, P_c, to cross to the other level, the lighter mass eigenstate ν_1. The crossing of the neutrino means that its flavor is that of the vacuum mixing of the ν_1 eigenstate, see bottom diagram of Fig. 4.3. This means that there could be a regeneration of the ν_e flavor in comparison to a purely adiabatic propagation of the neutrino. If unitarity is assumed, Eq. 4.46 can be modified to account for P_c,

$$
\begin{aligned}
P(\nu_e \to \nu_e) &= \sum_i P(\nu_e \to \nu_i) P_m(\nu_i \to \nu_e) \\
&= \begin{bmatrix} 1 & 0 \end{bmatrix} \begin{bmatrix} \cos^2\theta & \sin^2\theta \\ -\sin^2\theta & \cos^2\theta \end{bmatrix} \begin{bmatrix} 1-P_c & P_c \\ P_c & 1-P_c \end{bmatrix} \begin{bmatrix} \cos^2\theta_m & \sin^2\theta_m \\ -\sin^2\theta_m & \cos^2\theta_m \end{bmatrix} \begin{bmatrix} 1 \\ 0 \end{bmatrix}. \\
&= \frac{1}{2} + (\frac{1}{2} - P_c) \cos 2\theta \cos 2\theta_m
\end{aligned} \tag{4.47}
$$

where all of the details of solving the wave equation, Eq. 4.41, for a particular density profile of interest are contained in P_c. An analytic expression for the level crossing probability was derived by Landau and Zener for an infinite linear density profile as the solution to the same problem in atomic collisions 4.41[79, 80]. In the Landau-Zener approximation, P_c is given by

$$
P_c = \exp\left[-\frac{\pi}{2}\gamma_c\right] \tag{4.48}
$$

where γ_c is the adiabatic parameter defined in Eq. 4.45. An analytical expression also exists for the infinite exponential profile where

$$
P_c = \frac{\exp\left[-\pi\delta(1 - \cos 2\theta)\right] - \exp\left[-2\pi\delta\right]}{1 - \exp\left[-2\pi\delta\right]} \tag{4.49}
$$

and $\delta = (\cos 2\theta / \sin^2 2\theta)\gamma_c$. These approximations to the actual electron density profiles in the sun are generally good because the non-adiabatic region is a small region centered around x_c. The exact solution for the neutrino propagation is recoverable by choosing boundary conditions matching the adiabatic solution.

There is a good chance that some of the neutrinos will pass through two resonances on their way to the earth. In this case Eq. 4.47 is modified to account for this second resonance. Eq. 4.47 becomes

$$
\begin{aligned}
P(\nu_e \to \nu_e) &= \sum_i P_m(\nu_e \to \nu_i) P_m(\nu_i \to \nu_e) \\
&= \begin{bmatrix} 1 & 0 \end{bmatrix} \begin{bmatrix} \cos^2\theta & \sin^2\theta \\ -\sin^2\theta & \cos^2\theta \end{bmatrix} \begin{bmatrix} 1-P_c & P_c \\ P_c & 1-P_c \end{bmatrix} \times \\
&\qquad \begin{bmatrix} 1-P_c & P_c \\ P_c & 1-P_c \end{bmatrix} \begin{bmatrix} \cos^2\theta_m & \sin^2\theta_m \\ -\sin^2\theta_m & \cos^2\theta_m \end{bmatrix} \begin{bmatrix} 1 \\ 0 \end{bmatrix} \\
&= \frac{1}{2} + \left(\frac{1}{2} - P_{2c}\right) \cos 2\theta \cos 2\theta_m
\end{aligned} \tag{4.50}
$$

where $P_{2c} = 2P_c(1 - P_c)$.

4.4 Neutrino Oscillation for Solar Neutrinos

The general expressions derived in Section 4.3 can now be applied to the special case of solar neutrinos. The survival probability of a solar neutrino depends on the energy of the neutrino, the electron density where it is produced and the electron density profile as it propagates. As is shown in Fig. 4.4, depending on the production position and energy of the neutrino, it may or may not pass through a resonance. To derive an expression for E_c, the minimum neutrino energy that will see a resonance, we will start with the resonance condition and define E_c such that

$$V_W - \Delta m^2 \cos 2\theta = 2\sqrt{2} G_F \rho_e(x) E - \Delta m^2 \cos 2\theta$$
$$0 \equiv 2\sqrt{2} G_F \rho_{max} E_c - \Delta m^2 \cos 2\theta \tag{4.51}$$

With a little bit of algebra we arrive at a function for the minimum energy that will see a resonance,

$$E_c = \frac{\Delta m^2 \cos 2\theta}{2\sqrt{2} G_F \rho_{max}}. \tag{4.52}$$

Neutrinos produced below this energy will not experience the MSW effect.

If the neutrino's energy is above E_c, then depending on its production position it will either see no resonance, see a resonance, or see two resonances if produced on the far side of the sun and propagating back through the center. A function $E_a(r)$ can be defined that determines the energy of a neutrino produced at the radial position r that would be produced in the middle of the resonance. Once again starting with the resonance condition,

$$V_W - \Delta m^2 \cos 2\theta = 2\sqrt{2} G_F \rho_e(r) E - \Delta m^2 \cos 2\theta$$
$$V_W - \Delta m^2 \cos 2\theta \equiv 2\sqrt{2} G_F \rho_e(r)(E - E_a). \tag{4.53}$$

With a little bit of algebra we arrive at a function for the energy of a neutrino that would be produce in the resonance,

$$E_a(r) = \frac{\Delta m^2 \cos 2\theta}{2\sqrt{2} G_F \rho_e(r)} \tag{4.54}$$

where r continues to be the radial production position of the neutrino.

A function $\Theta(E, r)$ can be constructed to summarize the the four possible scenarios for a neutrino produced in the sun,

$$\Theta(E, x) = \left\{ \begin{array}{ll} 0 & E < E_c), \\ P_c & E > E_a(x) \\ 0 & E < E_a(x), \ near \\ P_2 c & E < E_a(x), \ far \end{array} \right\}. \tag{4.55}$$

where *near* indicates the solar hemisphere closer to the earth and *far* indicates the farther solar hemisphere. The survival probability can now be written

$$P_{\nu_e \to \nu_e}(E, r, x) = \frac{1}{2} + \left(\frac{1}{2} - \Theta(E, r, x) \right) \cos 2\theta \cos 2\theta_m. \tag{4.56}$$
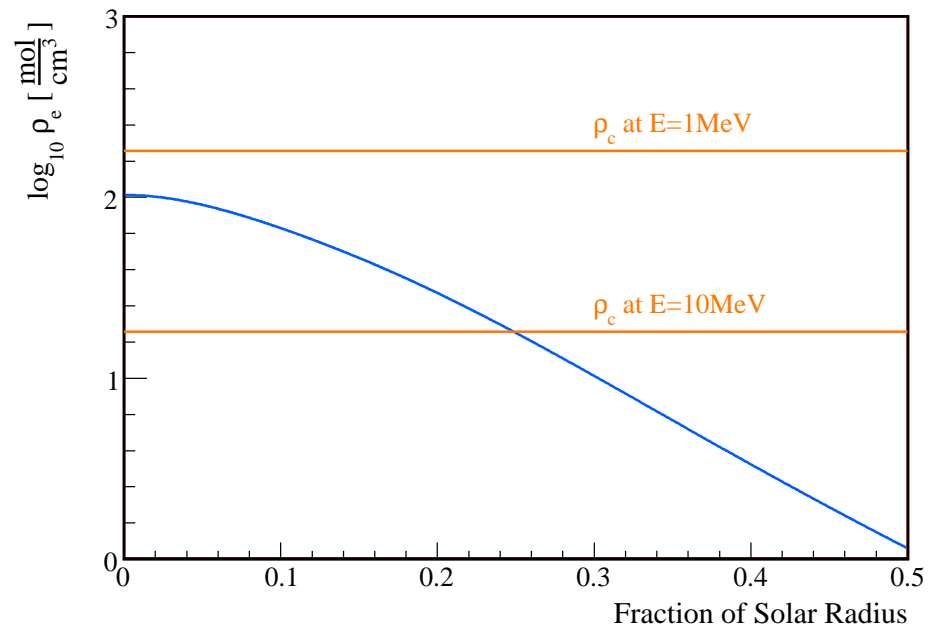
Figure 4.4: Solar electron density, ρ_e, as a function of radius. The solar electron density (blue line) is an exponential to good approximation. Overlaid are two lines representing the resonance density, ρ_c, for neutrinos at 1MeV and 10MeV. Neutrinos produced at 1MeV are produced below the resonance density at all locations within the sun compared to those at 10 MeV which will cross a resonance at $\sim 0.25 R_\odot$
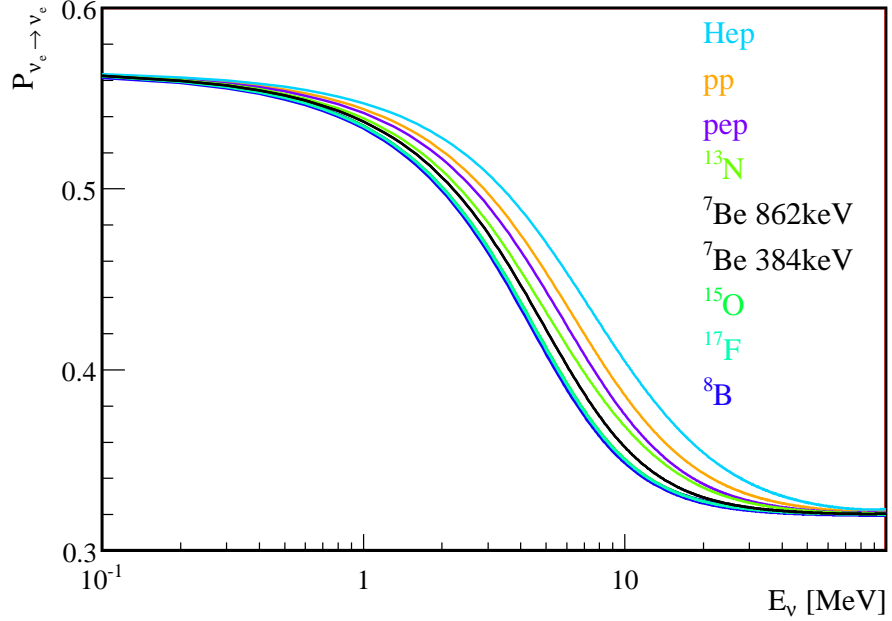
Figure 4.5: The survival probability of electron flavor neutrinos shown as a function of energy for each of the neutrino producing nuclear reactions in the Standard Solar Model.

Ultimately what is measured by solar neutrino experiments is the average of the survival probability over the neutrino production region,

$$\langle P_{\nu_e \to \nu_e}(E)\rangle = \int dx^3 P_{\nu_e \to \nu_e}(E, x, P_c)\Phi(x). \tag{4.57}$$

where $\Phi(x)$ is the neutrino production at a given position. The results of this calculation for the neutrino producing nuclear reactions of the standard solar model are summarized in Fig. 4.4. The solar model used for the production as a function of radius is BS05(OP)[81] and the oscillation parameters used are $\Delta m^2 = 7.59 \times 10^{-5} \text{eV}^2$ and $\tan^2 \theta_{12} = 0.47$ [63]. The differences in the production regions for the neutrinos from the different reactions means that the neutrinos have slightly different survival probabilities as a function of energy. Since the mixing angle is large the neutrinos propagate adiabatically out of the sun. If the mixing angle were small, the survival probability shown in Fig. 4.4 would show a drop followed by a sharp rise at low energies instead of the gradual rise that is shown.

So far all expressions for neutrino propagation in matter have been derived in the two neutrino approximation. Balantekin and Yüksel[82] derive nice extensions to these expressions if

$$\frac{\sqrt{2}G_F \rho_e(x)E}{\Delta m_{31}^2} < 1. \tag{4.58}$$

This condition is true for all of the neutrinos produced in the sun. Defining $\xi = \frac{\sqrt{2}G_F \rho_e(x)E}{\Delta m_{31}^2}$,

the three neutrino survival probability is

$$P_{3\times3}(\nu_e \to \nu_e) = \cos^4\theta_{13}P_{2\times2}(\nu_e \to \nu_e, \text{with } \rho_e = \rho_e\cos^2\theta_{13})$$

$$+ \sin^4\theta_{13}[1 + 2\xi cos^2\theta_{13}(1 + \frac{\Delta m_{21}^2}{\Delta m_{31}^2}\cos 2\theta_{12}) + \xi^2\cos^4\theta_{13}(2\frac{\Delta m_{21}^2}{\Delta m_{31}^2}\cos 2\theta_{12} - 1)]. \quad (4.59)$$

$$+ \mathcal{O}(\xi^3)$$

$P_{2\times2}(\nu_e \to \nu_e, \text{with } \rho_e = \rho_e\cos^2\theta_{13})$ is the standard two neutrino probability with ρ_e replaced with $\rho_e\cos^2\theta_{13}$ [82]. This expression can then be used in more complicated analyses of solar neutrinos with three neutrino flavors, though it is not used in the present analysis.

4.5 Neutrino Elastic Scattering Cross Section

With the neutrino fluxes predicted by the Standard Solar Model and the predicted survival probability, the number of neutrinos reaching the Earth may be calculated. All that is missing is a method to detect them and a calculation of the relevant cross section. Neutrino elastic scattering has been successfully used by Kamiokande, Super Kamiokande and SNO to directly detect neutrinos. In this process, some of an incoming neutrino's kinetic energy is transferred to an electron in the detector,

$$\nu + e^- \longrightarrow \nu' + e^-. \quad (4.60)$$

The e^- will deposit its energy and be detected if this energy is above the experiment's threshold. This is the process that this analysis will use to detect solar neutrinos.

The differential neutrino-electron elastic scattering cross section for producing a recoil electron with kinetic energy T, given an incoming neutrino with energy q is given to first order by

$$\frac{d\sigma}{dT} = \frac{2G_F^2 m_e}{\pi}\left[g_L^2 + g_R^2(1 - T/q)^2 - g_L g_R \frac{m_e T}{q^2}\right] \quad (4.61)$$

where

$$g_L = (\pm\frac{1}{2} + sin^2\theta_W), \quad g_R = sin^2\theta_W. \quad (4.62)$$

In the g_L factor the upper sign corresponds to ν_e scattering while the lower sign corresponds to ν_μ or ν_τ scattering. The current best value for the Weinberg angle is $\sin^2\theta_W = 0.23122 \pm 0.00015$ [66]. The possible sources of uncertainty in calculating the cross-section come from radiative corrections and effects due to the atomic binding of the electrons.

The effect on the cross section due to the atomic binding of the electrons is calculated by using a Fourier analysis of the wave function of the bound electron. A correction factor ϵ_b, which is the total relativistic energy of the bound electron divided by $m_e c^2$ is extracted. For a hydrogen like atom, this correction is given approximately by $\epsilon_b \simeq 1 - \frac{1}{2}(\alpha Z_{screened}/n)^2$ [83, 14]. KamLAND is mostly composed of hydrogen and carbon which would yield corrections on the order of α^2. These corrections would be much smaller than 0.1% and therefore can be neglected.

The radiative corrections to the cross section are effectively divided into two groups of $\mathcal{O}(\alpha)$ corrections. Corrections at order $\mathcal{O}((\alpha/2\pi)(q^2/m_W^2))$ are neglected [84]. The first

group contains all QED effects. The second group contains all other effects which are attributed to electroweak interactions. Bahcall, Kamionkowski, and Sirlin[85], present a simple expression for the differential cross section revised for the radiative corrections that is

$$
\begin{aligned}
\frac{d\sigma}{dT} = \frac{2G_F^2 m_e}{\pi} \bigg(& g_L^2(T)[1 + \frac{\alpha}{\pi} f_-(z)] \\
& + g_R^2(T)(1 - z)^2[1 + \frac{\alpha}{\pi} f_+(z)] \\
& - g_L(T)g_R(T)\frac{m_e}{q} z[1 + \frac{\alpha}{\pi} f_{+-}(z)] \bigg).
\end{aligned}
\tag{4.63}
$$

The QED functions, $f_+(z)$, $f_-(z)$, and $f_{+-}(z)$, describe the corrections due to virtual and real photons. The factors g_L and g_R are now functions of T. For ν_e scattering they are given by

$$
\begin{aligned}
g_L^{(\nu_e,e)}(T) &= \rho_{NC}^{(\nu,l)}[\frac{1}{2} - \hat{\kappa}^{(\nu_e,e)}(T) \sin^2 \theta_W] \\
g_R^{(\nu_e,e)}(T) &= -\rho_{NC}^{(\nu,l)} \hat{\kappa}^{(\nu_e,e)}(T) \sin^2 \theta_W
\end{aligned}
\tag{4.64}
$$

with

$$
\rho_{NC}^{(\nu,l)} = 1.0126 \pm 0.0016.
\tag{4.65}
$$

The function $\kappa^{(\nu_e,e)}(T)$ is given by

$$
\kappa^{(\nu_e,e)}(T) = 0.9791 + 0.0097I(T) \pm 0.0025
\tag{4.66}
$$

where the function $I(T)$ is given by

$$
I(T) \equiv \frac{1}{6}\left(\frac{1}{3} + (3 - x^2)[\frac{1}{2}x \ln\left(\frac{x+1}{x-1}\right) - 1]\right)
\tag{4.67}
$$

and $x = \sqrt{1 + 2m_e/T}$. The factors g_L and g_R in Eq. 4.64 are the same for ν_μ scattering but $\kappa^{(\nu_e,e)}(T) \to \kappa^{(\nu_\mu,\mu)}(T)$ where

$$
\kappa^{(\nu_\mu,\mu)}(T) = 0.9970 = 0.00037I(T) \pm 0.0025.
\tag{4.68}
$$

All of the QED effects enter through $f_+(z)$, $f_-(z)$, and $f_{+-}(z)$. The expansion of the g_L and g_R account for the electroweak effects. The uncertainty in $\rho_{NC}^{(\nu,l)}$ is due to the uncertainties in the top quark's and the Higg's masses. The uncertainties in κ are from QCD corrections.

The QED functions, $f_+(z)$, $f_-(z)$, and $f_{+-}(z)$, are calculated in the extreme relativistic limit in Ref. [84]. In this limit the mass of the electron is neglected so $q \gg m_e$. This is not a good approximation for solar neutrino experiments. Presented in Ref. [85] are approximate expressions for $f_+(z)$, $f_-(z)$, and $f_{+-}(z)$ that are determined using a modification of the extreme relativistic expressions. Exact expressions for the nonrelativistic domain are worked out in Ref. [86], but they must be numerically tabulated so are not as useful as those of Ref. [85].

In the expressions for $f_+(z)$, $f_-(z)$, and $f_{+-}(z)$, it is assumed that the QED photons are not detectable and an average is taken across their energy. An experiment like KamLAND will be sensitive to real photons due to QED corrections for a process like

$$\nu + e^- \longrightarrow \nu' + e^- + \gamma. \tag{4.69}$$

The treatment of the real photons is a correction to the already small , $\sim 1-4\%$, radiative corrections. Therefore, the uncertainty due to the real QED photons is neglected. The total uncertainty on the elastic scattering cross section as calculated by Bahcall, Kamionkowski, and Sirlin is 0.5% [42, 23]. This uncertainty is adopted in the present analysis.

In addition to these Standard Model processes, there could be corrections due to new physics. As was briefly described in Section 4.1, a massive Dirac neutrino naturally gains a magnetic moment which will change the cross section, especially at low energy. Vogel and Engle [87] use two phenomenological parameters to characterize the interactions of an ultra-relativistic Dirac neurino. These parameters are the magnetic moment, μ_ν, and the neutrino charge radius $\langle r^2 \rangle$. The neutrino-electron differential cross-section is then given by

$$\begin{aligned}
\frac{d\sigma}{dT} = \frac{G_F^2 m_e}{2\pi} &\left[(g_V + x + g_A)^2 + (g_V + x - g_A)^2 (1 - T/q)^2 \right. \\
&\left. + [g_A^2 - (g_V + x^2)] \frac{m_e T}{q^2} \right] \\
&+ \frac{\pi \alpha^2 \mu_\nu^2}{m_e^2} \frac{1 - T/q}{T}
\end{aligned} \tag{4.70}$$

where

$$g_V = (2\sin^2 \theta_W \pm \frac{1}{2}), \quad g_A = \pm \frac{1}{2}. \tag{4.71}$$

and

$$x = \frac{\sqrt{2}\pi\alpha \langle r^2 \rangle}{3 G_F} = \frac{2M_W^2}{3} \langle r^2 \rangle \sin^2 \theta_W. \tag{4.72}$$

In the g_V and g_A factors, the upper sign corresponds to ν_e scattering while the lower sign corresponds to ν_μ or ν_τ scattering. The effect of the magnetic moment is small for the ^{8}B neutrinos, but a measurement of ^{7}Be neutrinos could be used to extract interesting limits on the neutrino magnetic moment[88].

4.6 Predictions for Experimental Detection

In order to make predictions for experimental detection, the differential cross section, calculated in Section 4.5, has to be averaged over the neutrino energy spectrum of interest. Given the differential cross section, $\frac{d\sigma}{dT}$, the spectrum averaged cross-section is given by

$$\left\langle \frac{d\sigma}{dT} \right\rangle = \int_{qmin}^{qmax} dq S(q) \frac{d\sigma}{dT}. \tag{4.73}$$

Table 4.1: The total spectrum averaged cross sections for the neutrinos of the Standard Solar Model. The results are shown for both electron flavor neutrinos ν_e and muon or tau flavor neutrinos $\nu_{\mu/\tau}$ with and without radiative corrections.

Branch	First Order		with Radiative Corrections	
	σ_{ν_e}	$\sigma_{\nu_{\mu/\tau}}$	σ_{ν_e}	$\sigma_{\nu_{\mu/\tau}}$
	$\times 10^{-46}$ cm^2			
pp	11.8	3.2	11.5	3.3
pep	111.9	21.6	108.9	22.1
^{8}B	615.4	104.5	597.7	106.7
Hep	887.2	149.0	861.6	152.0
^{13}N	46.7	10.1	45.5	10.3
^{15}O	72.2	14.6	70.2	15.0
^{17}F	72.4	14.7	70.5	15.0
^{7}Be 862keV	58.1	12.2	56.5	12.5
^{7}Be 384keV	16.2	4.1	15.8	4.2

$S(q)$ is the neutrino energy spectrum normalized to unity and q is the neutrino energy. The lower limit of the integral is the minimum neutrino energy needed to produce an electron with a kinetic recoil energy of T. It is given by $q_{min}(T) = \{T + \sqrt{T(T + 2m_e c^2)}\}/2$. The upper limit of the integral is the maximum energy of the neutrino spectrum. The total cross section can be calculated by simply integrating over the electron recoil energy, T. The results for each of the nine neutrino producing nuclear reactions in the Standard Solar Model are summarized in Table 4.1. The total cross section is smaller for $\nu_{\mu/\tau}$, as expected as they can only scatter through neutral current interactions. The inclusion of the radiative corrections reduces all of the σ_{ν_e} cross sections by $\sim 3\%$ and only slightly increases the $\nu_{\mu/\tau}$ cross sections.

To include neutrino oscillation in the spectrum averaged cross section calculation, Eq. 4.73 becomes

$$\left\langle \frac{d\sigma}{dT} \right\rangle = \int_{qmin}^{qmax} dq S(q) \langle P_{\nu_e \to \nu_e}(q) \rangle \frac{d\sigma_{\nu_e}}{dT} + \int_{qmin}^{qmax} dq S(q)(1 - \langle P_{\nu_e \to \nu_e}(q) \rangle) \frac{d\sigma_{\nu_{\mu/\tau}}}{dT}. \quad (4.74)$$

where $\langle P_{\nu_e \to \nu_e}(q)) \rangle$ is the average electron neutrino survival probability given by Eq. 4.57. The predicted spectrum of neutrino elastic scatter events for an experiment is then given by

$$\frac{dN}{dT} = \left\langle \frac{d\sigma}{dT} \right\rangle N_e \Phi_\nu \quad (4.75)$$

where N_e is the number of electrons in the target volume, Φ_ν is the relevant neutrino flux, and $\left\langle \frac{d\sigma}{dT} \right\rangle$ is given by Eq. 4.73 for a prediction without oscillation or Eq. 4.74 for a prediction

with oscillation. The predicted spectra for a target of 10^{32} electrons are shown in Fig. 4.6. The top panel shows the prediction without neutrino oscillation. The bottom panel shows the prediction using the oscillation parameters from Ref. [63], $\Delta m^2 = 7.59 \times 10^{-5} \text{eV}^2$ and $\tan^2 \theta_{12} = 0.47$. The neutrino flux predictions are form the BSB(GS98)Standard Solar Model[3].

Neutrino oscillation reduces the event rate, as can be seen by comparing the two panels of Fig. 4.6. The distortion of the energy spectrum is not visible in Fig. 4.6. In Fig. 4.6, the spectra of ^{8}B neutrino elastic scatter events normalized to unity is plotted with and without oscillation. The shape of these two spectra is very similar. A detection of the predicted spectral distortion alone, like that seen in KamLAND's reactor data in Fig. 3.4, is very difficult with ^{8}B neutrinos. To verify, the predicted energy dependence of the survival probability measurement of ^{8}B and ^{7}Be are needed. The ^{8}B measurement is the subject of this work.
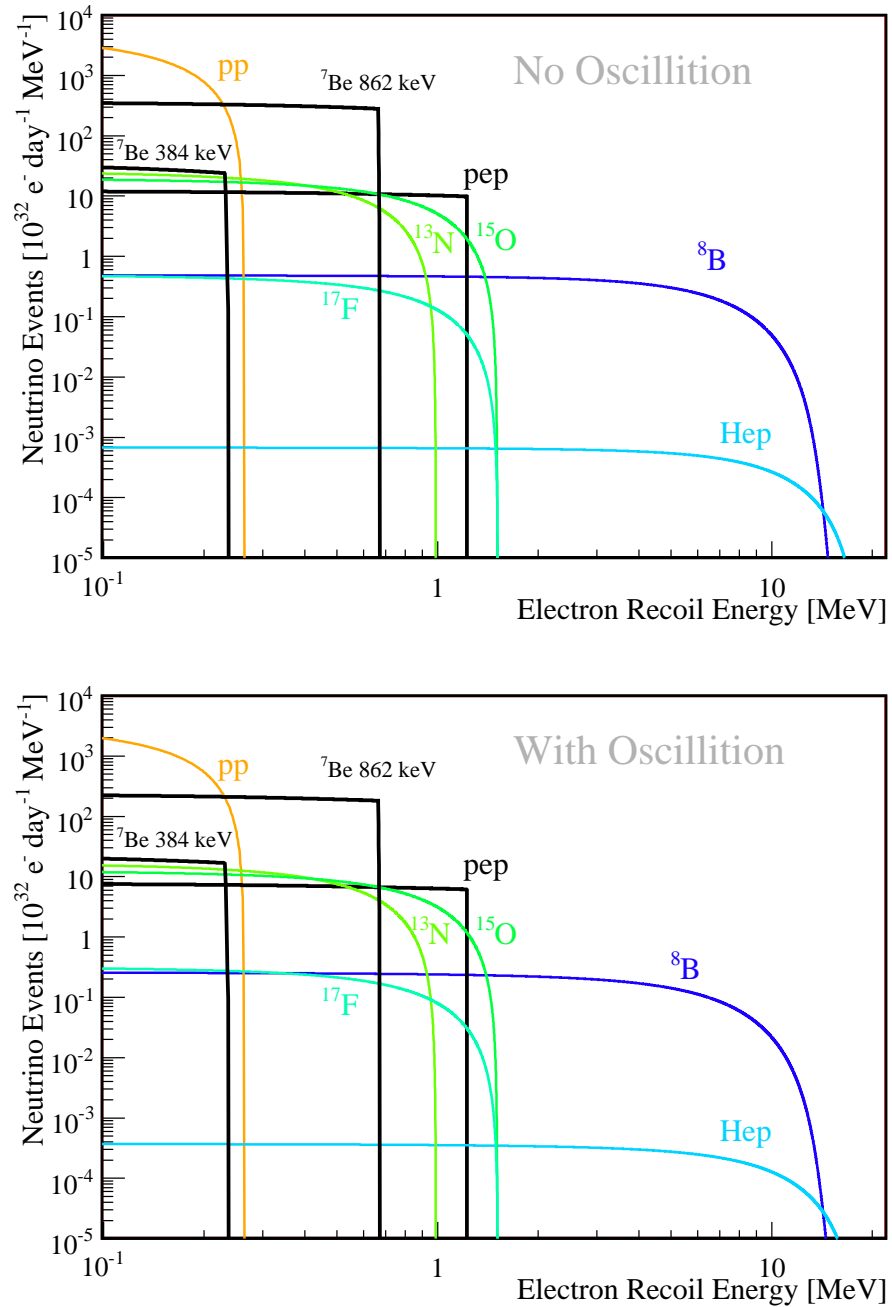
Figure 4.6: The neutrino elastic scatter spectra for the neutrino producing nuclear reactions of the Standard Solar Model normalized to an exposure of 10^{32} electron targets per day. The top shows the results without neutrino oscillation while the bottom shows the result with neutrino oscillation. The oscillation parameters are from Ref. [63].
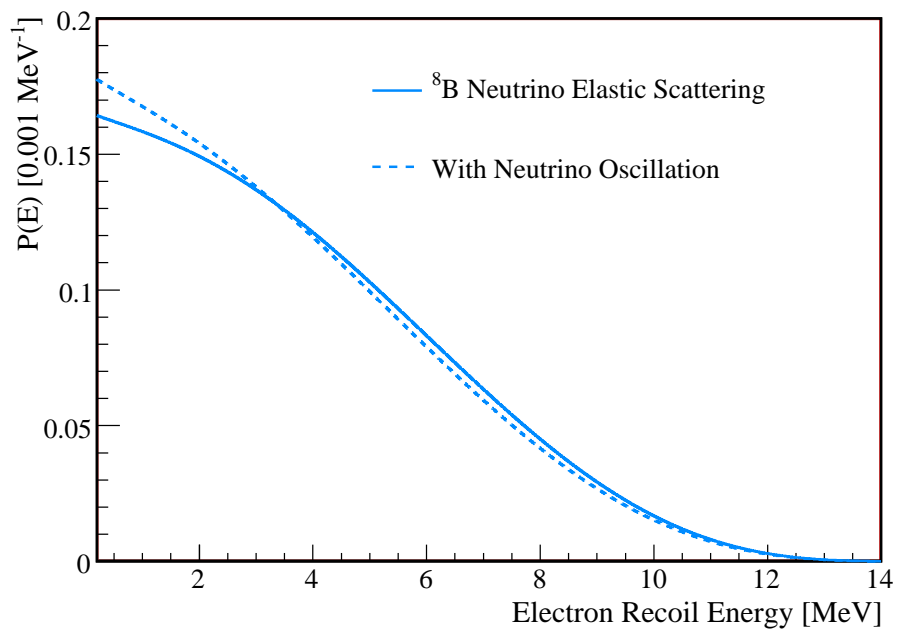
Figure 4.7: The elastic scatter spectrum of ^{8}B solar neutrinos with and without neutrino oscillation. The spectra have been normalized to unity. The oscillation parameters used are the best fit parameters of the global fit from Ref. [63].

Chapter 5

KamLAND Experiment

KamLAND is acronym for the Kamioka Liquid Scintillating Anti-Neutrino Detector. The detector is located in the Kamioka Mine near the city of Kamioka in the Gifu Prefecture of Japan. KamLAND occupies the old Kamiokande site within the mine. Mt. Ikeoyama rises approximately 1,000 m above this location providing an overburden of 2700 meters water equivalent (m.w.e.). The KamLAND detector uses 1000 metric tons of liquid scintillator, abbreviated 1 kilo-ton or 1kt, as both the target and detection medium for low energy nuclear/particle physics processes like neutrino elastic scattering and inverse beta decay. The molecules that compose the liquid scintillator give off light when charged particles move through the detector. KamLAND is designed and instrumented to detect this light and reconstruct the physics processes that produced the light.

5.1 Detector Layout

The detector has two distinct sections, referred to as the outer and inner detector, Fig. 5.1. The outer detector is a water Čerenkov detector which is filled with purified mine water. Particles moving faster than the speed of light through water produce Čerenkov light. The walls of the outer detector are lined with Tyvek sheeting to reflect this light and augment the light collecting capacity of the 220 Hamamatsu photo-multiplier tubes (PMTs). The purpose of the outer detector is to act as a muon veto for the inner detector.

The inner detector is the heart of the experiment and consists of a stainless steel sphere of 9m radius onto which 1,325 17-inch PMTs and 554 20-inch PMTs are mounted. The PMTs are mounted into diamond patterns, each consisting of 64 PMTs. Over each of the diamonds are mounted acrylic panels that form a sphere with an effective radius of 8.5 meters. The glass of a PMT can emanate radon and the acrylic panels prevent this and other radioactive backgrounds from leaking further into the inner detector.

Inside the PMT sphere is "buffer oil", a mixture of dodecane and isoparaffin, in which an approximately spherical balloon with a radius of 6.5m is suspended. The buffer oil attenuates fast neutrons and high energy gamma rays from outside of the detector. The buffer oil does not produce a significant amount of scintillation light so this guarantees that all but the highest energy events occur in the well defined volume of the balloon.

The balloon was constructed to hold the detecting medium, the liquid scintillator.
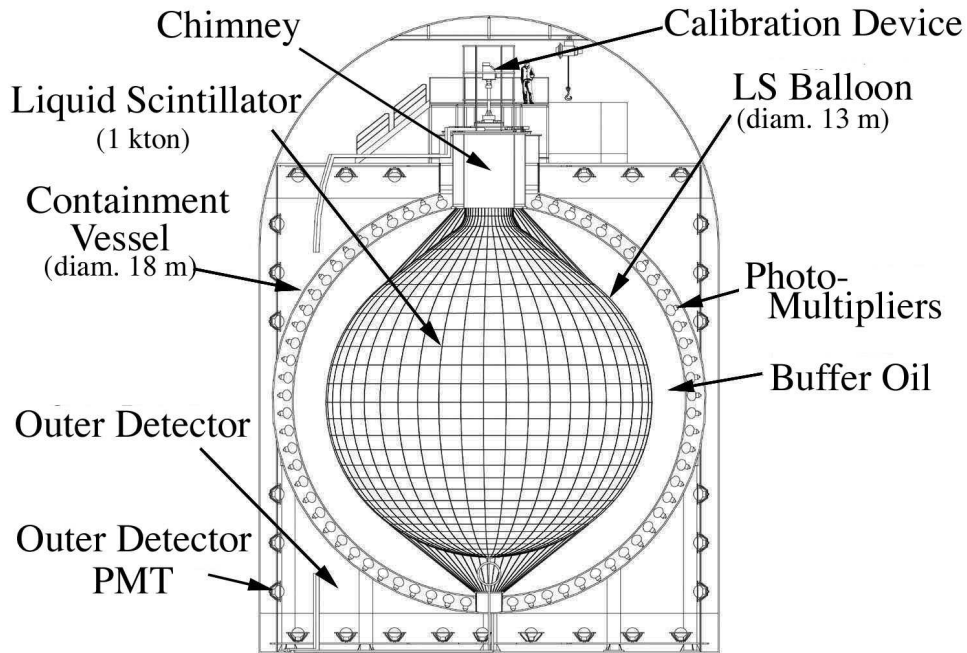
Figure 5.1: The KamLAND Detector. The active liquid scintillator volume is contained in a nylon balloon. The buffer oil acts as a shielding against radioactive backgrounds. The vessel holding the inner detector is surrounded by a water Čerenkov outer detector which acts as a muon veto.

The balloon is 135 μm thick and is made from 3 layers of nylon, 25 μm each, blanketed by a 15 μ m layer of EVAL, Ethylene Vinyl Alcohol or EVOH, from the Kurare Company on each side. The nylon was used for strength. The EVAL was chosen for its low gas permeability. The adhesive that joins these layers accounts for the remaining 30 μm. Both materials were found to be chemically compatible with the liquid scintillator. The layers are connected with an adhesive and the entire structure is suspended by kevlar ropes. The balloon was designed to support a density difference, $\Delta\rho$, of less than 0.3% between the buffer oil and the liquid scintillator. The buffer oil mixture was tuned to $\Delta\rho < 0.04\%$, so the balloon is stable as long as the temperature difference between the buffer oil and liquid scintillator remains less than a few ^{o}C[89].

Table 5.1: Number of targets in KamLAND liquid scintillator.

Element	Number per kilo-ton	with Dissolved Gas	e^- per kilo-ton	with Dissolved Gas
H	8.458×10^{31}	8.458×10^{31}	8.458×10^{31}	8.458×10^{31}
C	4.294×10^{31}	4.293×10^{31}	5.154×10^{32}	5.154×10^{32}
N	4.746×10^{27}	7.220×10^{27}	6.644×10^{28}	1.011×10^{29}
O	4.746×10^{27}	4.802×10^{27}	7.593×10^{28}	7.683×10^{28}
		Total	3.423×10^{32}	3.424×10^{32}

5.2 Liquid Scintillator

The KamLAND liquid scintillator (LS) is a mixture of pseudocumene (also known as 1,2,4-Trimethylbenzene, 19.8%) and dodecane (80.2%). Pseudocumene (PC) is a commonly used liquid scintillator due to its high light output. Unfortunately, it is also a powerful solvent and materials compatibility is an issue. A further complication is the low flash-point of pseudocumene, 48^oC. Due to mine safety concerns, it was diluted with the dodecane until the flash-point was above 60^oC. For the same reason, a nitrogen blanket is maintained in the top of the detector.

In addition to psuedocumene and dodecane, the LS contains 1.36 g/L of 2,5-Diphenyloxazole (PPO). This compound shifts the UV scintillation light to longer wavelengths, where the PMTs are more sensitive. The KamLAND design specifications stipulated 1.5 g/L, as bench measurements showed that higher concentrations increased the light yield [90]. During the original filling of KamLAND, the light output was carefully monitored but the chemical composition could not be controlled to high accuracy. The PPO concetration, 1.36 ± 0.02 g/L, was measured using a mass spectrometer [91]. The difference in these two values is too small to affect the isotopic composition of the liquid scintillator but is of some importance when simulating light transport in the detector.

5.2.1 Number of Targets

The KamLAND scintillator is both the detection medium and the target for neutrino interactions, so one of the key numbers is how many target particles of various elements are contained in the liquid scintillator. The chemical formulas are PC, C_9H_{12}, dodecane, $C_{12}H_{26}$, and PPO, $C_{15}H_{11}NO$. The density of the liquid scintillator is 0.780 g/cm^3 at 11.5^{o}C. The density and formula combine to give the number of proton, carbon, nitrogen, oxygen and electron targets, see Table 5.1. The uncertainty in the number of targets due to the PC and dodecane mixture is 0.1%. The amount of dissolved gases and density changes due to temperature and pressure will also affect the uncertainty in the number of targets.

Nitrogen and Oxygen are the two gases that will have the most opportunity to dissolve in the liquid scintillator due to the nitrogen blanket. A device was constructed to sample the liquid scintillator along the z-axis of KamLAND. The O_2 content of the samples was measured and found to be less than 3ppm [92]. The nitrogen content of the LS has never been measured. It is a good assumption that the LS has reached its saturation level for nitrogen. Battino et al. [93] have compiled and reviewed the solubility of nitrogen in

Table 5.2: Systematic uncertainties in the number of targets in the KamLAND liquid scintillator.

Source	Uncertainty
Scintillator Composition	0.10%
Temperature Variation	0.10%
Pressure Variation	0.01%
Total	0.14%

various liquids. Some of these references are old and inconsistent, so only rough estimations can be extracted from this data.

Dodecane is part of the more general group n-Alkanes. The solubility for this group is shown in Fig. 5.2 (Top). The KamLAND detector ranges in temperature from 9-22°C. In this range the solubility is 1.36 ± 0.02. For n-Decane the solubility is 0.962 ± 0.003. The evaluated data is plotted in Fig. 5.2 (Bottom). There is data for dodecane which at 298.15 K is 1.23. In general this work is not consistent with other measurements so is considered suspect by Battino et al.[93]. Instead, an upper limit of 1.38, 115 ppm, is adopted from the n-Hexane data.

There is no solubility data for Psuedocumene but there is data for Benzene, Toluene (methylbenzene), and Xylene (dimethylbenzene). This data is summarized in Fig. 5.3. It appears that the additional methyl groups allow the liquid to dissolve more nitrogen. A conservative upper limit for Psuedocumene is a molar ratio of 7 which is equivalent to 321 ppm. From these solubilities, the number of targets from dissolved gases is calculated. The inclusion of the dissolved gases almost doubles the number of nitrogen targets, but the other quantities of interest are not affected.

Uncertainties in the calculation of the number of targets also come from density changes due to temperature and pressure. The temperature gradient in KamLAND is shown in Fig. 5.2.1. The temperature coefficient of expansion for the liquid scintillator is 7.41×10^{-4}g cm^{-3}K^{-1}. The volume weighted average of the density change due to this temperature gradient is 0.1%. Density changes due to pressure changes are much smaller than those due to temperature. For materials similar to psuedocumene and dodecane, the maximum isothermal compressibility, $\Delta V/V$, is 0.01%[94] which corresponds to a density uncertainty of 0.01%. Combining these systematic uncertainties and neglecting those due to dissolved gases, a systematic uncertainty of 0.14% is assigned to the calculation of the number of targets. These values are summarized in Table 5.2.

5.3   Event Detection

The path from an interaction in the liquid scintillator to a recorded physics event is outlined in Fig. 5.5. The scintillation light from a physics event in the detector is detected by the PMTs which send pulses to the front-end electronics (FEE). The trigger monitors the data from the FEE, and if it determines that there is something interesting to record
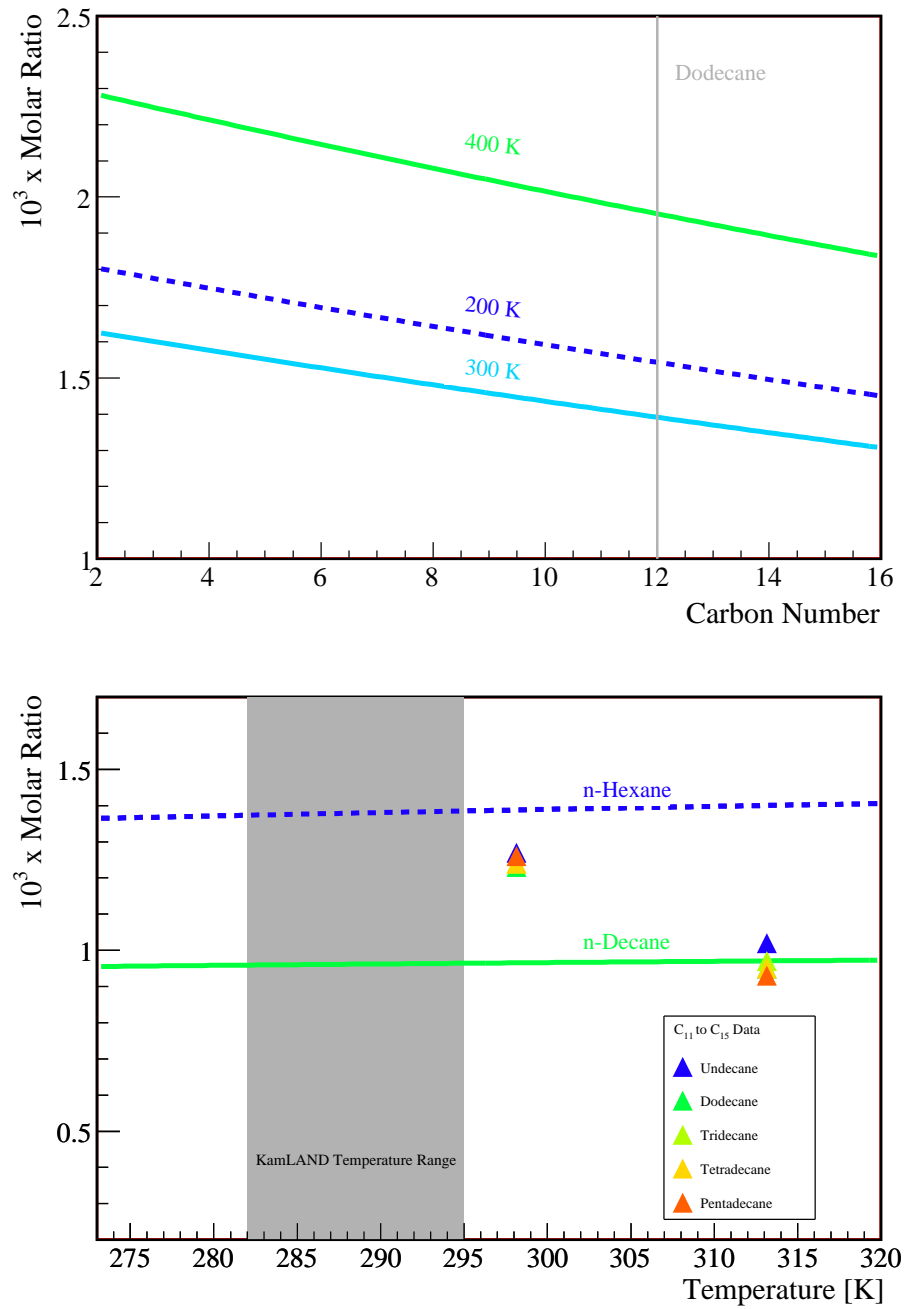
Figure 5.2: Nitrogen solubility in hydrocarbons:(Top) nitrogen solubility in the n-Alkanes group for several temperatures, (Bottom) evaluated nitrogen solubility data for the n-Decane group, data points are not used in the evaluation[93].
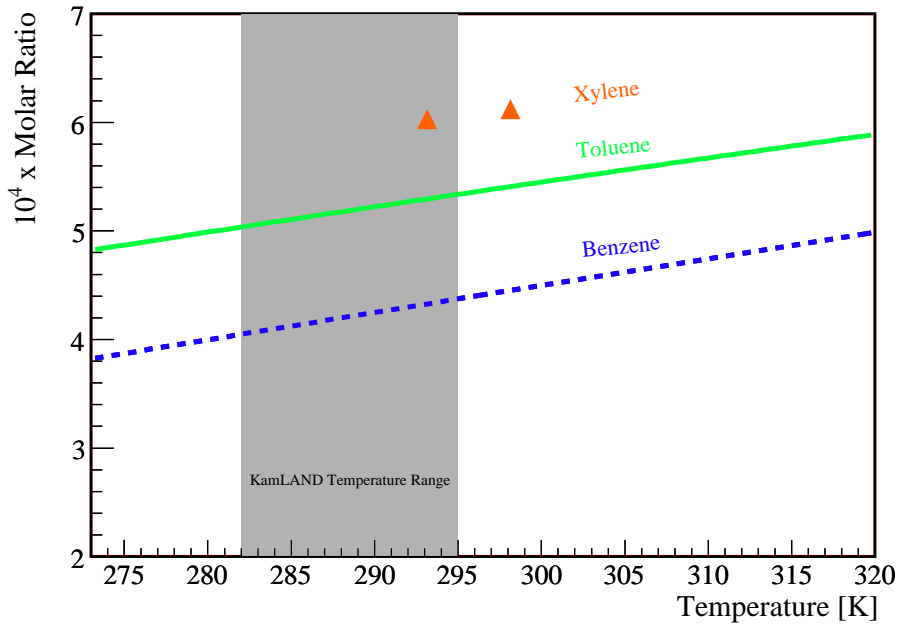
Figure 5.3: Nitrogen solubility in aromatic hydrocarbons.
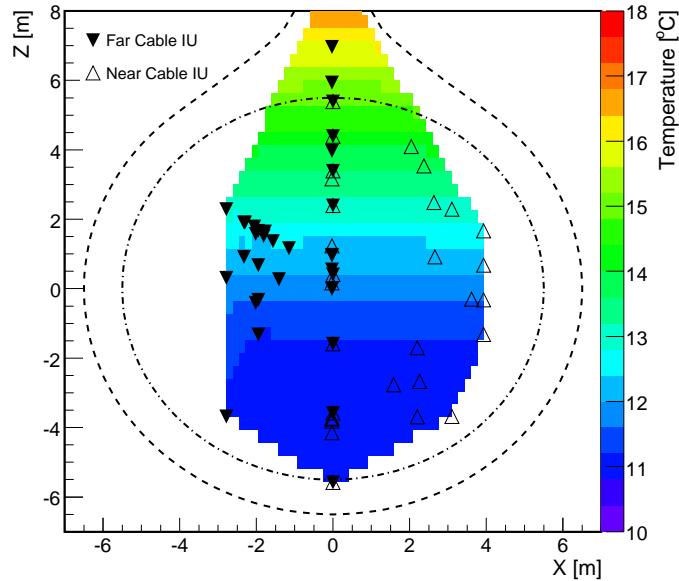
Figure 5.4: The temperature distribution in KamLAND. This data is from the deployment of the 4π calibration system.
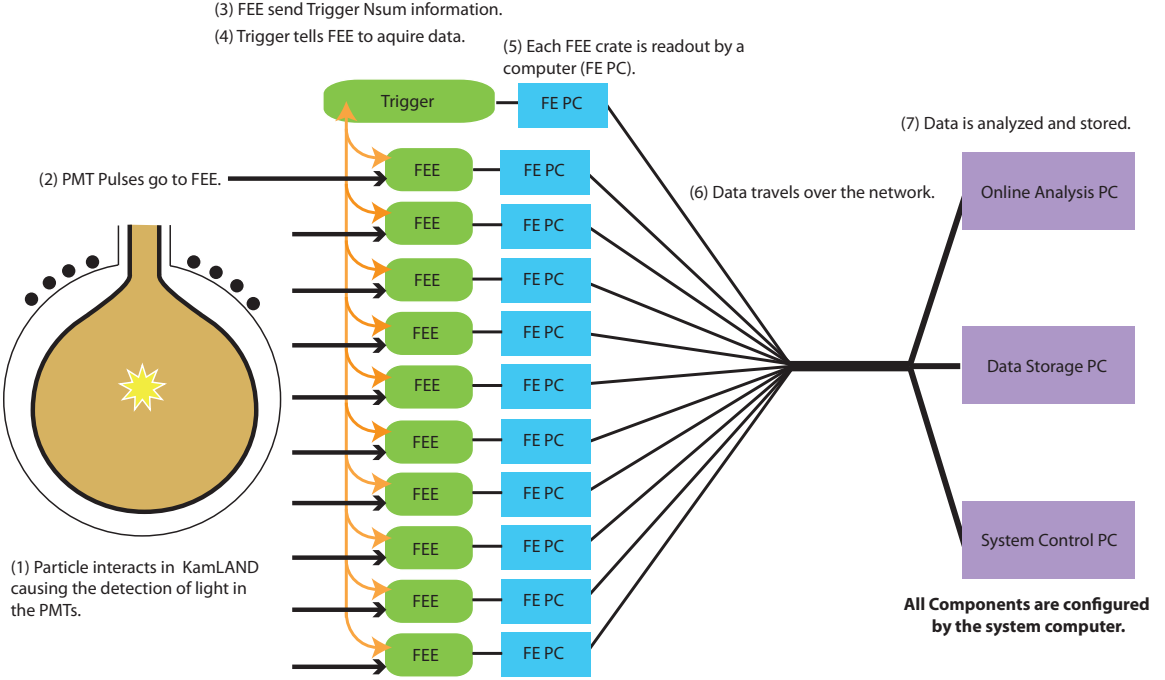
Figure 5.5: Data flow through KamLAND's data acquisition system. Scintillation light in the detector is observed by the photo-multiplier tubes (PMTs). The signals from the PMTs are digitized by the front-end electronics (FEEs) after receiving a trigger from the trigger electronics. The operation and configuration of both the FEE and trigger electronics are computer controlled.

then the event is read out by the data acquisition system, Kinoko. The readout from Kinoko is done asynchronously. The event builder takes the asynchronous Kinoko data (kdf) and organizes it into events, termed event built data (sf). Both the kdf data and the sf data are stored for offline analysis. The volume of data is such that both formats are compressed using a lossless algorithm. The compressed kdf and sf data, kdfz and sfz respectively.

5.3.1   Photo-Multiplier Tubes

KamLAND uses photo-multiplier tubes (PMTs) to detect the scintillation light produced by particles interacting in the detector. PMTs are very sensitive devices that can detect light levels down to individual photons. They work by the photo-electric effect. A photon hits the photo-cathode knocking off an electron. An electric field accelerates the electron across the PMT where it hits the first dynode knocking off additional electrons. These electrons are then accelerated to the second dynode thus creating a cascade effect as these electrons propagate down this chain of dynodes. By the end of the dynode chain, the tiny signal has been amplified to several milli-volts and is read out as an electric pulse.

Two varieties of PMTs are used in KamLAND, the Hamamatsu R3602 and the Hamamatsu R7250. These are usually referred to as the twenty-inch and seventeen-inch

PMTs. The twenty-inch PMTs were salvaged from the Kamiokande experiment, while the seventeen-inch PMTs were built for KamLAND. The later PMTs are identical to the twenty-inch PMTs, but the photo-cathode has been masked to create an area approximately seventeen inches in diameter. The dynode chain has been changed from a venetian-blind design to the fast linear focusing design. These two changes reduced the 10 ns transit time spread to 3 ns. This improvement was needed in order to achieve the desired position reconstruction accuracy. The twenty-inch PMTs are included in KamLAND to increase the area on the sphere that is instrumented.

5.3.2 Electronics

The signals from the PMTs travel through 40m of oil-proof solid-core coaxial cable with an 18m extension for the 17" PMTs and a 21m extension for the 20" PMTs in order to arrive at the KamLAND front-end electronics (FEE). These circuit boards were custom made by Lawrence Berkeley National Lab. They use Analog Transient Waveform Digitizers (ATWDs) to record the full waveform of the signal from the PMTs [95, 96, 97]. The ATWD acts as a mini-oscilloscope for every channel. Each board has 12 channels and each connected channel corresponds to one PMT. Signals from the PMTs first pass through the analog section of the board; here a discriminator compares the channel's pulse to a set threshold. The entire data acquisition system is synchronized by a 40MHz clock. Every clock tick the board tallies the number of channels above threshold and sends this information to the trigger. While the discriminator logic is working, a second copy of the PMT signal proceeds down the delay line to one of the ATWDs. The ATWD samples the signal in 128 consecutive bins of 1.5 ns each. These sampled values are stored on 128 capacitors while the trigger decision is awaited.

The Trigger makes the decision to acquire data by calculating the total number of hit channels from all the boards (Nsum). The Trigger calculates the Nsum separately for the inner and outer detectors. The outer detector Nsum is divided further into top, upper, lower, and bottom sections. If the Nsum for any of these regions is above threshold, the Trigger sends the command to the FEE to digitize all channels above the discriminator threshold. The Trigger writes out the Nsum data to its own data stream for every clock tick during which any section is above the history threshold. The history Nsum threshold is usually set slightly lower than the normal threshold, typically 120 versus 200 or 180.

Each ATWD has three gains to prevent saturation during high light level events and there are two ATWDs per channel to prevent dead time. In addition, each ATWD has a channel for recording its own copy of the 40MHz clock. When the trigger sends the command for the ATWD to commence waveform digitization, it also sends the number of clock ticks since the run beginning. This is called the time-stamp and it allows the Event Builder to associate the asynchronously collected waveforms with the right event. The number of clock ticks between when the channel went over threshold and the arrival of the acquire signal from the Trigger is called the launch offset. The digitized waveforms, the time-stamp and the launch offset are stored in the FEE's memory for future readout by the data acquisition system. Waveform digitization takes 30 μs per gain, but if no trigger signal is received the waveform is disposed of. In events separated by less than the digitization time some data may be lost due to both of a channel's ATWDs digitizing the previous

event's waveforms. This is a particular problem for high light level events. This is an effect for reconstruction algorithms need to take into account.

The Trigger can also initiate the acquisition of baseline data from the electronics like the forced digitization of a channel that has not gone above threshold (pedestal waveform) or the digitization of the 40MHz clock (clock waveform). The Trigger has specialized logic to properly handle the data from the deployments of various sources. It also has logic tailored to maximize data from a supernova. The last important duty of the Trigger is to interface with a Global Positioning System (GPS) receiver to allow the determination of an absolute time for a KamLAND event.

A second system of front-end electronics, MACRO, looks at the waveforms from 4 PMTs ganged together. MACRO is capable of digitizing much longer waveforms . Unfortunately, the readout is too slow for use as the primary system. Macro's purpose is to provide data following muon events where its ability to digitize longer events could be useful. Due to issues integrating this data into the main data stream, this data is not used in this work.

5.3.3 KiNOKO Data Acquisition System

The data acquisition system (DAQ) has three jobs, readout of data from the electronics, configuration of the running mode for the electronics, and data monitoring. The KiNOKO DAQ system that was specifically developed for KamLAND; it stands for "Kinoko Is Network distributed Object-oriented KamLAND Online-system". KamLAND has one computer reading each of the fifteen VME electronics crates used in the system. KiNOKO gives the framework to control processes running on these networked computers. It has a scripting language that allows you to configure the trigger and front-end electronics at start-up. KiNOKO also includes data analyzer classes and a viewer that allow for the monitoring of the KamLAND data as it is acquired.

At run beginning, all the hardware components are initialized by the system control computer. There are 10 computers reading out the 10 front-end VME crates. There are also 4 computers reading the four MACRO VME crates and 1 computer reading the Trigger VME crate. These 15 computers are constantly reading data from the boards through the crate's VME bus. Since the boards store data for some amount of time, the data will be organized by board, not by time. All of the data from the crates is sent to another computer for online analysis and then to a final computer for compression and storage. The data volume is compressed using Huffman encoding and some pruning of redundant data[98]. The data is then written out to KiNOKO files, kdfz, and sent on to the Event Builder for the next stage of processing. KiNOKO was written by Enomoto Sanshiro; for a more complete description of the system and its capabilities see [99].

5.3.4 Event Builder

The Event Builder's job is to organize the kdf data into events with the same time-stamp. Each FEE card has a maximum of 32MB of memory. This means that the data from a particular event could be up to 6400MB back in the data stream, 200 FEE cards × 32MB. As this is still too large of a buffer to maintain with current technology, KiNOKO limits itself to 8MB per read which means that the data will be separated by no

Table 5.3: Radioactive sources used to calibrate KamLAND.

Source	Deposited Energy	Radiation
^{60}Co	2.502 MeV	γ
^{65}Zn	1.352 MeV	γ
^{68}Ge	1.022 MeV	e^+ annihilation γ
^{137}Cs	0.662 MeV	γ
^{203}Hg	0.279 MeV	γ
AmBe	5.638 MeV	n with capture γ
PoC	6.130 MeV	n an de-excitation γ

more than 1600MB. Occasionally, there will be a bit error in the time-stamp of a particular waveform. If this happens, it will not be possible to match this waveform to its event. This is a negligible effect for data analysis, but it can affect the performance of the Event Builder because these orphaned waveforms will build up in the memory. The Event Builder, like Kinoko, uses Huffman encoding to compress the waveforms. It, too, prunes redundant data, but it goes one step further and drops some low level hardware data that is used for electronics diagnostics.

5.4 Calibration

In order to interpret the data being taken by KamLAND, sources of known energy need to be deployed to known positions inside the detector. Radioactive sources of gammas and neutrons were constructed for this purpose, see Table 5.3. Two systems were constructed to deploy these sources into KamLAND. The first system was capable of deploying sources at any position along the z-axis of the detector. The second system was designed to move of sources through out the balloon.

Two laser systems were also available for deployment into the detector. The Japanese Laser System is a 500 nm laser. This wavelength is too long for the absorption and reemission processes in the LS, so it is used to understand the timing offsets in the detector. The U.S. Laser System is a 337 nm nitrogen laser. This wavelength is in the middle of the range of wavelengths that are absorbed and reemitted, so it is used to understand light propagation through the LS.

5.4.1 The Z-Axis Calibration System

The Z-Axis System was installed in the Spring of 2002 in conjunction with the commissioning of the detector. The purpose the system was to position radioactive sources along the z-axis of KamLAND. The accuracy and reproducibility of the source position was required to be on the order of 2-3mm, so that the position uncertainty would be dominated by the timing uncertainty from the PMTs and electronics. The system used a motor to unspool a stainless steel cable and a pulley encoder to measure the amount of cable payed out. The number of encoder counts to distance calibration was done in the high bay of the

Cyclotron at Lawrence Berkeley National lab using a Starret precision tape measure and the golden marks positioned approximately every meter along the cable. The major worry with a pulley encoder is that the cable will slip over the pulley without turning it, introducing inaccuracy and irreproducibility in the positioning . To prevent this effect, a large cable was chosen and a stainless steel weight was incorporated into the source attachment design. The consistency of the encoder to distance calibration was checked routinely on site by monitoring the distance between the golden marks according to the control software. This test was referred to as the "Golden Mark Test". The calibration remained good to 2-3mm over the life of the system.

5.4.2   The 4π Calibration System

The 4π system was installed in December of 2005. The purpose of the system is to position radioactive sources throughout the active volume of the detector and test the performance of the reconstruction algorithms in r, θ and ϕ, not just z. The basic design of the system is a pole suspended by two cables. By moving one cable while fixing the other, a radial sweep can be performed through various θ positions. Additional points can be reached by moving both cables simultaneously translating the configuration in z. The radial reach of the system can be increased by changing the length of the pole or the weight distribution of the pole. Other phi positions can be obtained by rotating the Glovebox. The Glovebox covers the entry to the top of KamLAND and stores the calibration systems. The Z-Axis system is recreated by connecting the source to one of the cables therefore maintaining the ability to perform simpler less time consuming deployments. This is a very complex system that presented some unique design challenges. A full description is given in Ref. [100].

Chapter 6

Event Reconstruction

The interaction of a particle in KamLAND makes scintillation light that is detected by the PMTs which is then recorded by the electronics in the form of digitized PMT output pulses. The hardware that makes up the KamLAND experiment was described in Chapter 5. In order to start studying the physics taking place in KamLAND, these digitized PMT pulses, called waveforms, need to be used to reconstruct the energy and position of the original particle interaction. The lowest level analysis is done by algorithms that extract the arrival times and charges of the PMT pulses, the so-called waveform analysis. This low-level information can be used to identify different types of particle interactions or noise events in KamLAND, and provides low level event classification. The arrival times and charges of the PMT pulses are then used in the reconstruction to provide the position of the particle interaction (vertex reconstruction), and the energy of the particle interaction (energy reconstruction). In the case of events from muons passing through KamLAND, a track is reconstructed from the arrival times and charges of the PMT pulses rather than a vertex. The details of these algorithms are summarized. The final section presents the key efficiencies and software tools needed to convert the results of the reconstruction into the rates of different interactions in KamLAND, most notably the neutrino interaction rates.

6.1   Waveform Analysis

The reconstruction of a physics event in KamLAND starts with the extraction of the arrival time of light at the PMT and the number of photons. This information is recorded by the KamLAND electronics in the form of a digitized PMT pulse. The components of the KamLAND electronics that perform the digitization are the Analog Transient Waveform Digitizers, ATWD. The ATWD samples the input signal 128 times for about 1.5 ns and stores this information on internal capacitors. When the ATWD data is digitized it is the amount of charge on these 128 capacitors that is measured. The set of 128 values is called a waveform. A typical waveform from a single photon creating one electron at the PMT's cathode, a single photo-electron, is shown in Fig. 6.1 (a). Most particle interactions in KamLAND other than muons produce less than one photo-electron per PMT so this is a typical KamLAND waveform.

Each ATWD has a characteristic amount of charge on each of its capacitors which

adds structure and an offset to the waveforms, as can be seen in Fig. 6.1 (a). Before the pulse arrival time and charges can be extracted from the waveforms, this structure must be removed. At the beginning of each run each ATWD acquires 50 waveforms, most without pulses in them. These pulse-free waveforms are called pedestal waveforms and are a measurement of this residual charge on the ATWD's capacitors. An example pedestal waveform is shown in Fig. 6.1 (b). The 50 pedestal waveforms are averaged for each ATWD and stored in a file for use in processing the run. Due to the details of the board readout, the baseline of the waveform shifts between two values forming a bi-modal distribution. For this reason, the average pedestal is stored without the overall offset.

The time per sample for the 128 samples of a waveform is nominally 1.5ns. This value is set by the data acquisition system at the beginning of each run. Each ATWD will have a slightly different time per sample. This value could also be affected by changes in the environmental conditions in the room containing the electronics. The sample time will be used to determine the conversion from waveform sample to time so it is critical to eliminate the variations in this value. The time per sample is measured for each ATWD at the beginning of a run by collecting 50 waveforms per ATWD that use the signal from KamLAND's 40MHz clock as input. These are called clock waveforms. An example clock waveform is shown in Fig. 6.1 (c). A fast fourier transform is taken of each of these waveforms and the average sampling time is calculated.

After the pedestal and sampling time for each ATWD have been characterized, the pulse time and charge may be extracted from the waveform. This process has four steps as outlined in Fig. 6.2. The first step is the subtraction of the average pedestal that was calculated from the pedestal waveforms at the beginning of the run. The waveform is then smoothed with a Savitzky-Golay filter[101]. This eliminates higher frequency noise. Because of the baseline of the waveform changes slightly depending on other activity on the board, as was seen in the pedestals, the overall offset needs to be calculated for each waveform and subtracted. This offset is obtained by calculating the average ADC value for the waveform after removing samples with large ADC values that are outside of one standard deviation of a running average. The final step is to determine the time and charge of the pulses in the waveform. The algorithm used defines a pulse as any area above zero. The time of the pulse is the peak value as determined by a quadratic fit to the three points closes to the peak. The charge is the integral of the area between the position where the waveform crosses zero to where it returns to zero. This method finds many pulses that are simply fluctuations of the baseline. It was found that pulses that are less than 15% of the total area of the waveform are likely to be fluctuations, so a cut at this level successfully separates the pulses from the fluctuations, see Fig. 6.3.

This processing scheme has two main limitations. The first and most serious is its inability to resolve overlapping pulses. If the waveform does not return to zero between pulses, the two pulses will be considered one pulse with time associated with the larger pulse and the charge being the sum of the two pulses. The second limitation mostly affects the 20" PMTs. Due to their poorer time resolution sometimes the 125 ns delay lines on the electronics boards are not sufficient to sample the baseline before the pulse. This may cause the baseline of the waveform to be calculated incorrectly and lead to biases in the time and charge calculations. Examples of both of these issues are shown in Fig. 6.4. Algorithms
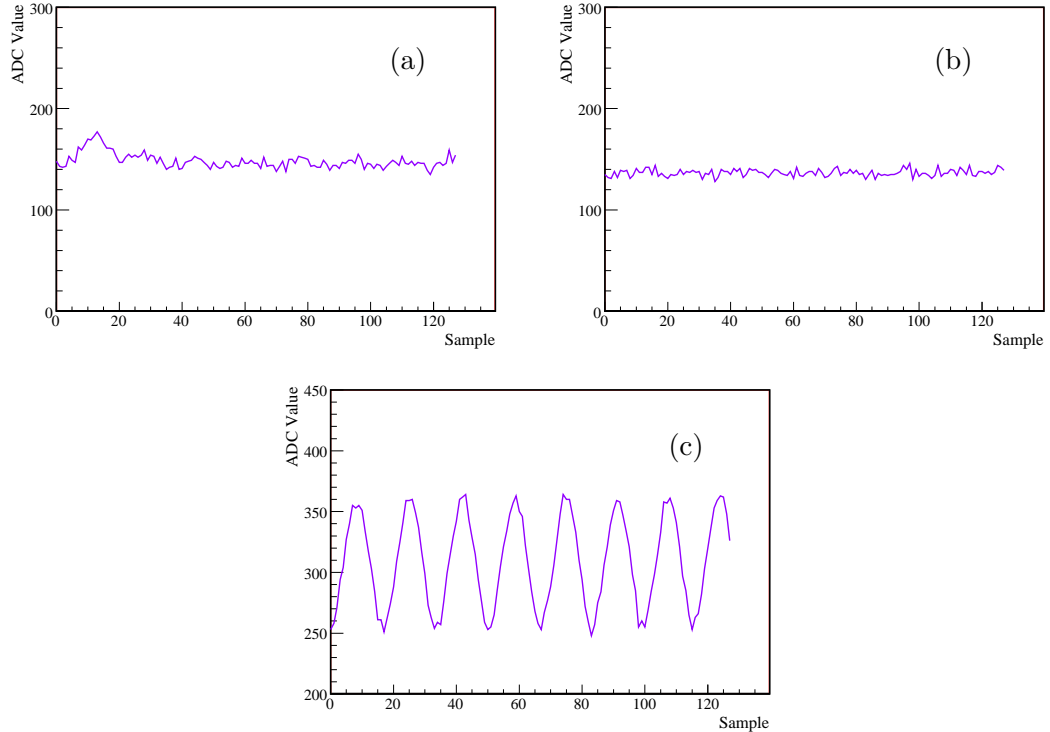
Figure 6.1: The lowest level of data from KamLAND are PMT pulses digitized by the Analog Transient Waveform Digitizers, ATWDs. The ATWD digitizes a pulse by sampling the signal input 128 times in ∼1.5ns bins. This collection of 128 samples is called a waveform. An example of a waveform containing a PMT pulse is shown in (a). Waveforms without pulses are collected at the beginning of a run to measure the characteristic charge on the ATWDs, shown in (b). To determine the exact integration time per waveform sample, waveforms containing the digitization of the KamLAND 40MHz clock are also acquired at the beginning of the run as shown in (c).
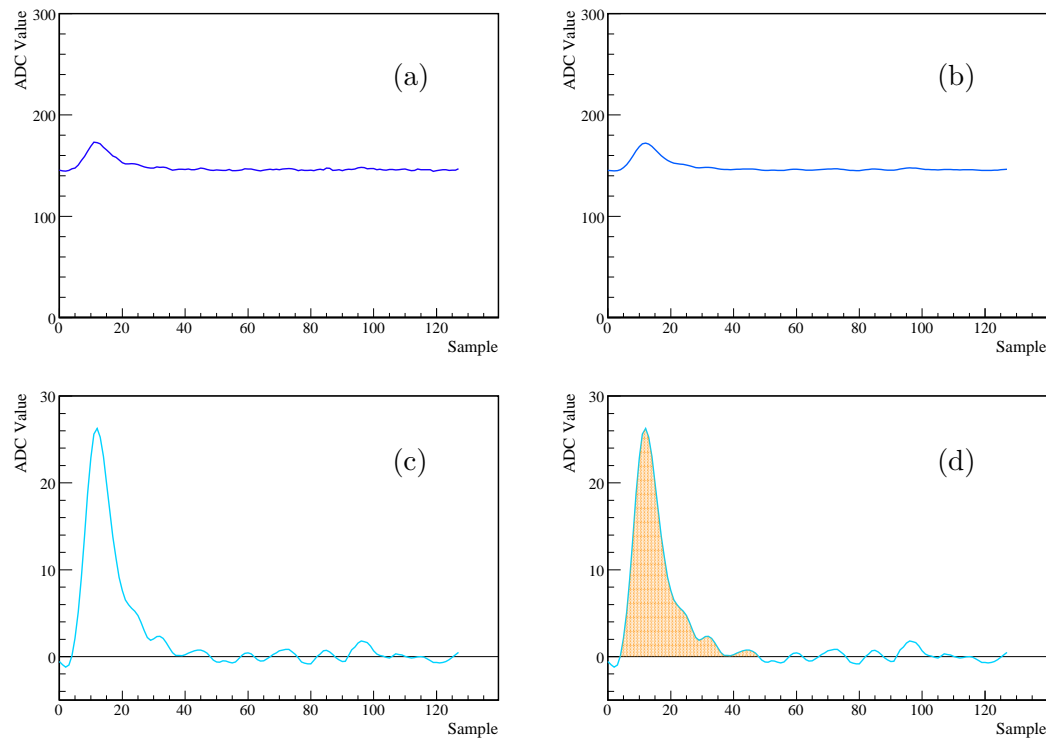
Figure 6.2: The four steps in the processing a raw waveform to extract times and charges: (a) after subtraction of the average pedestal to remove the intrinsic ATWD structure, (b) after smoothing of the waveform, (c) after re-normalization of the baseline to remove an overall offset, (d) location of pulses.
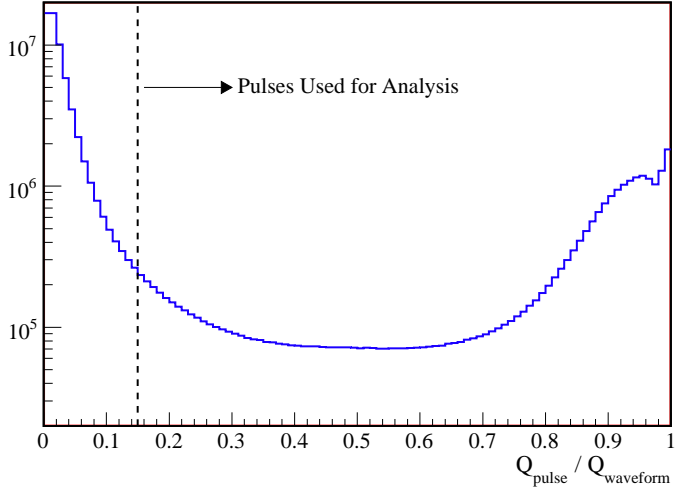
Figure 6.3: The ratio of the charge in a single pulse to the total charge of all pulses in the waveform. A cut is applied at 15% to eliminate pulses that are the results of baseline fluctuations.

that take pulses as input need to be aware of these issues in case they lead reconstruction uncertainties.

The waveforms from muon events are treated differently. The pulses from a muon are many photo-electrons and have peaks that correspond to volts instead of milli-volts. As is shown in Fig. 6.5, these waveforms often saturate the KamLAND electronics' highest gain, gain 0, and are captured by the medium, gain 1, or low gain, gain 2. The pedestal subtraction and smoothing are the same for these waveforms as for single photo-electron waveforms. Because the pulse takes up most if not all of the 128 samples, the method for calculating the baseline offset needs to be modified to use only the first 10 bins. With large pulses the peak of the pulse is no longer the best determination of the pulse time and a threshold gives a better determination of the arrival time. For this reason a threshold algorithm with a threshold of 50 ADC counts is used. A line is calculated from the leading edge of the pulse and the crossing time determined by the algorithm.

6.2   Low Level Event Classification

Before the times and charges from the previous section are reconstructed into positions, energies and tracks, more basic quantities like the total number of channels hit can be used to make some generalizations about the nature of the interaction responsible for the event. These initial guesses are used to make low level event classifications. There are three quantities that have been found to be the most useful for the classification of events, two quantities for the inner detector and one for the outer detector. For the outer detector the quantity of interest is "ODNsumMax" or the maximum number of hit PMTs in the
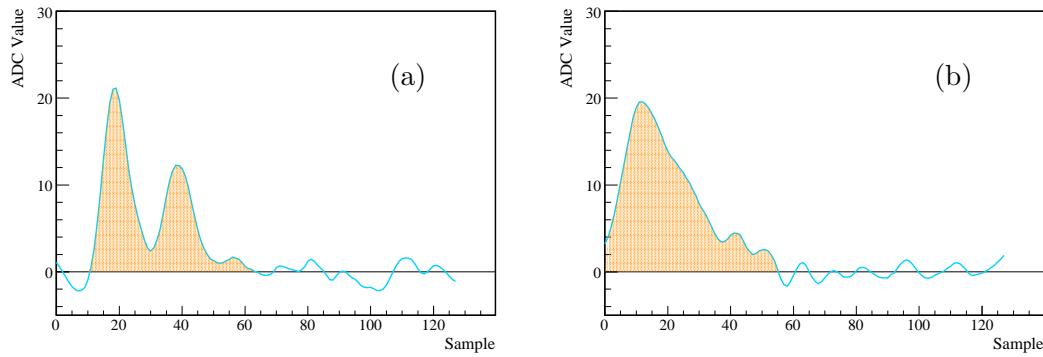
Figure 6.4: There are two main limitations to the waveform processing algorithms: (a) two overlapping pulses, (b) insufficient time delay for a 20" PMT.
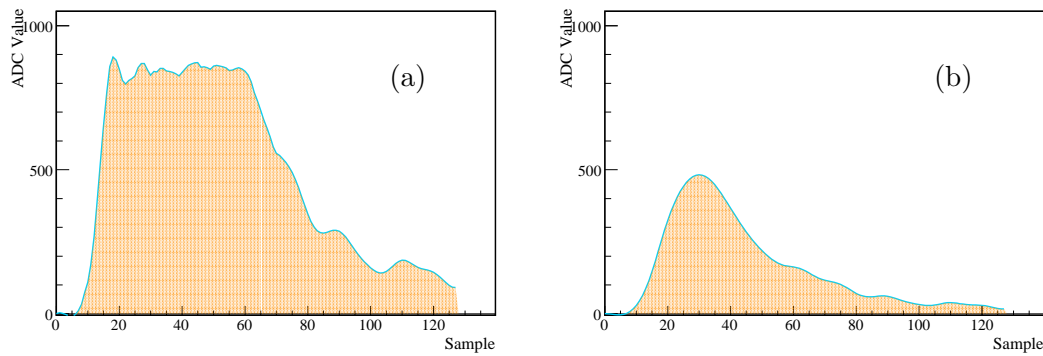
Figure 6.5: A typical muon signal. The signals from muon events are more than an order of magnitude larger than single photo-electron events. This signal has saturated gain 0 and been captured by gain 1, shown in (a) and (b) respectively.

outer detector during the event. For the inner detector the total number of photo-electrons and the average deviation in the number of photo-electrons between the PMTs is used. The total number of photo-electrons is given by,

$$N_{total} = \sum_{i}^{N_{17"PMTs}} g_i q_i = \sum_{i}^{N_{17"PMTs}} N_i \qquad (6.1)$$

where g_i is a rough conversion constant for the ith PMT between charge and number of photo-electrons and q_i is the total amount of charge collected by the ith PMT. The constant g_i is calculated from ^{60}C calibrations at the center of the detector. The average deviation in the number of photo-electrons between PMTs is calculated by,

$$\sigma_N = \sum_{i}^{N_{17"PMTs}} \sqrt{\frac{(N_i - \langle N \rangle)^2}{N_{total}}}. \qquad (6.2)$$

This quantity is a good measure of how the light is distributed in the event: a large value indicating all the light was in a small group of PMTs, and a small value indicating an isotropic distribution. A track-like event is expected to have a larger σ_N value than a point-like event.

These quantities, ODNsumMax, N_{total}, and σ_N, are used to divide events into classes. These classes will determine what type of reconstruction is used later. These classes correspond to the different detector response predicted for various regions and interaction types or classes of noise that occur in KamLAND. The classes are as follows:

Outer Detector Muon Event - Any event with ODNsumMax greater than 10. This value was chosen because it is the minimum value that avoids the noise found in the outer detector as can be seen in Fig. 6.6.

Liquid Scintillator Muon Event - These are events with the high light levels and larger σ_N values. They are found in Fig. 6.6 region (c) and Fig. 6.7 regions (f) and (g).

Shower Muon Event - These events are a subset of the liquid scintillator muons, 6.7 regions (g), that have highest light levels and have been found to produce more spallation products.

Buffer Oil Muon Event - These events have large σ_N values, like the liquid scintillator muons, but show lower light levels consistent with a muon passing only through the buffer oil. A muon passing through the buffer oil will not produce large amounts of scintillation light and relies on Čerenkov light for detection. These events are found in Fig. 6.6 region (b) and Fig. 6.7 region (d).

Post-Muon Noise - After high light level events like muons there is a lot of electronics noise mainly due to effects in the PMTs. This noise overlaps with the buffer oil muons, Fig. 6.7 region (d), but on average has lower σ_N values. These events are easily

removed with a full detector veto of 150 μs following a high light level events.

PMT Flasher - These are the most asymmetric events seen in KamLAND, large σ_N as seen in Fig. 6.7 region (e). A noise event causes one PMT or one small group of PMTs to collect a lot of charge. These events are very unphysical and are usually eliminated because of reconstruction failure though cuts can be applied to explicitly veto them.

Background Physics Events - The KamLAND Trigger acquires various events below the standard threshold for the purpose of monitoring backgrounds. These lower energy events are seen in region (b) of Fig. 6.7 .

Candidate Physics Events - The events that may become neutrino candidates are seen in regions (a) and (c) of Fig. 6.7. The lower light level events, region (a), are predominantly the result of radioactivity on the balloon. It is this region where reactor anti-neutrino candidates are expected to be. The higher light level region (c) is predominantly spallation products like ^{12}B that have high Q-value beta decays. It is this region where ^{8}B solar neutrino events are expected to be.

6.3   Position Reconstruction

The "Candidate Physics Events' identified in Section 6.2 produce isotropic scintillation light. The light hits the PMTs making the pulses extracted from the waveforms in Section 6.1. These pulses are used to reconstruct the position or vertex of the primary physics event. The vertex reconstruction algorithm used in this analysis is called the Peak Time Fitter. It uses the arrival time of the pulses of PMTs to find the vertex position, see Fig. 6.8.

The algorithm starts with a calculation of the PMT charge weighted mean position. This will be the starting point of the vertex reconstruction. The next step is to calculate the mean PMT hit time, $\langle t \rangle$. A typical hit time distribution is shown in Fig. 6.9 (a). Only the earliest pulses in waveforms from 17" PMTs are used and the times are corrected for slewing effects. The calculated mean PMT hit time is improved by eliminating pulses more than 10 ns from the mean until the remaining pulses are within 0.1 ns of each other or 100 iterations have taken place. The next step is to calculate the first iterative step for the vertex correction,

$$\langle \delta \vec{r} \rangle = \frac{1}{N} \sum_i^N \vec{r}_i (1 - \frac{t_i - \langle t \rangle}{\tau_i}). \tag{6.3}$$

The variable $\vec{r}_i$ is the vector from the current vertex to the ith hit PMT. The variable τ_i is the predicted travel time for the ith PMT given the current vertex. It is given by $\tau_i = c_{LS} * r_{LS_i} + c_{BO} * r_{BO_i}$ where c_{LS} and c_{BO} are the speed of light in the liquid scintillator and buffer oil respectively. The speeds of light are c_{LS}=196.1mm/ns and c_{BO}=220mm/ns. These values were tuned to optimize the performance of the fitter reconstructing sources along the z-axis of the detector. They do not correspond with the real speed of light in
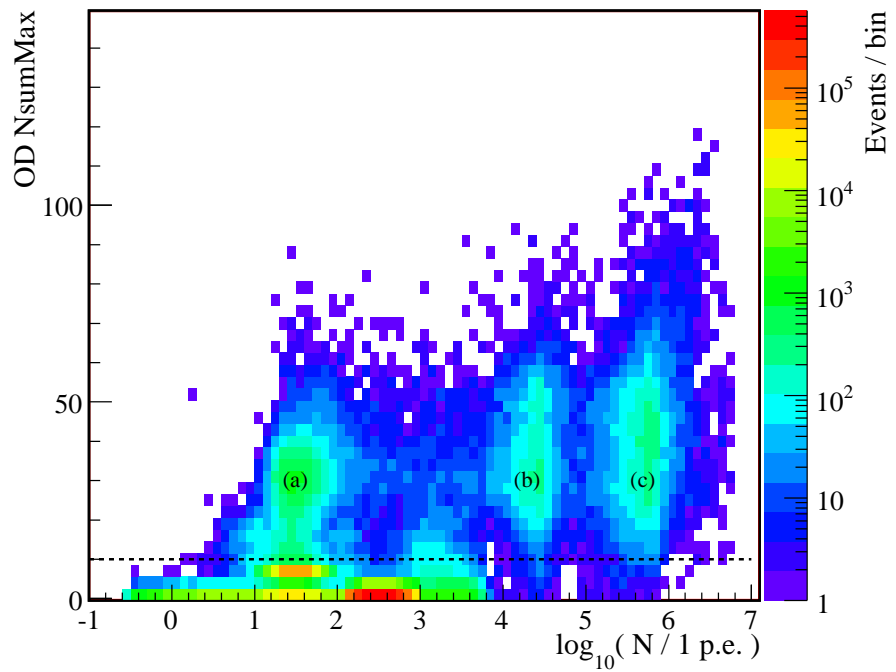
Figure 6.6: Total light level in the Inner Detector compared to the number of PMTs above threshold in the Outer Detector, OD NsumMax. Three distinct event categories are seen: muons only in the Outer Detector (a), muons that passed through the buffer oil but not the liquid scintillator (b), and the muons with the highest light levels because they passed through the liquid scintillator (c). The noise level in the Outer Detector rises rapidly below ODNsumMax=10 (dashed line).
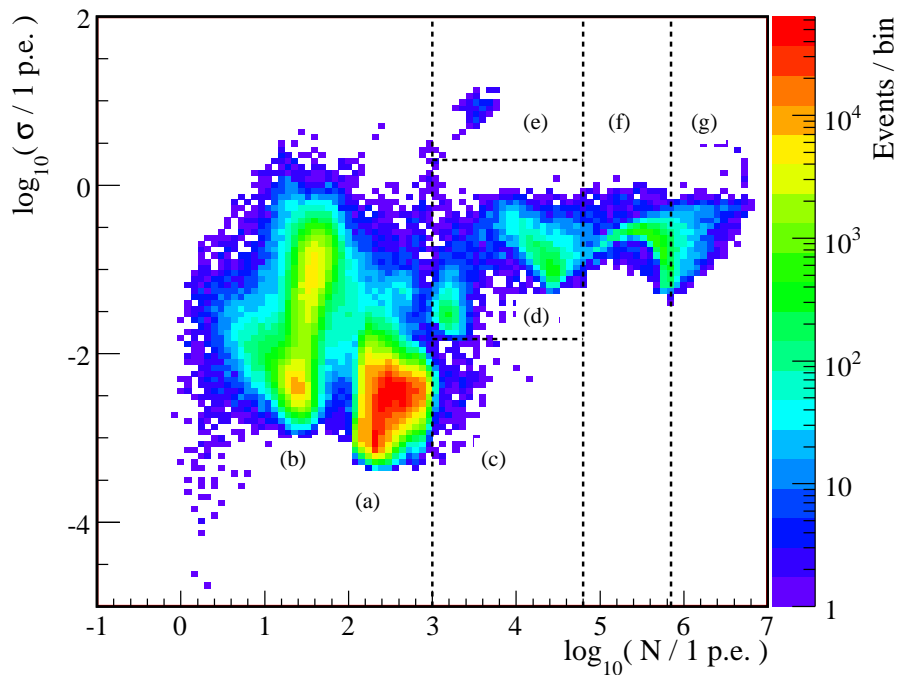
Figure 6.7: Total light level in the Inner Detector compared to the deviation in light level from PMT-to-PMT, $\log_{10}(\sigma/1$ p.e.). Several distinct event categories are identified. A physics event like a neutrino interaction or radioactive decay should produce isotropic light as seen in the event categories (a), (b), (c). In comparison single PMT noise events, (e) or muon events that leave tracks of light through the experiment, (d), (f), (g), are more asymmetric regardless of light level.
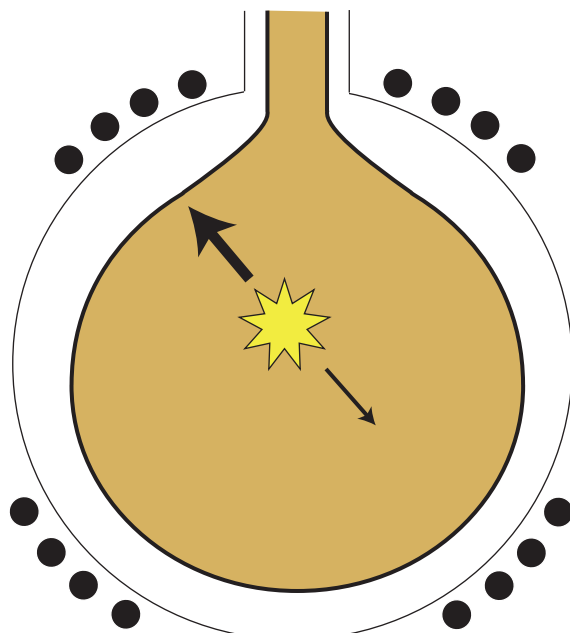
Figure 6.8: Vertex fitter diagram. The PMTs with pulses that arrive earlier are closer to the event vertex and should "pull" the reconstructed position closer to them. The PMTs with later pulse arrival times should not "pull" the vertex as hard, effectively "pushing" it away.
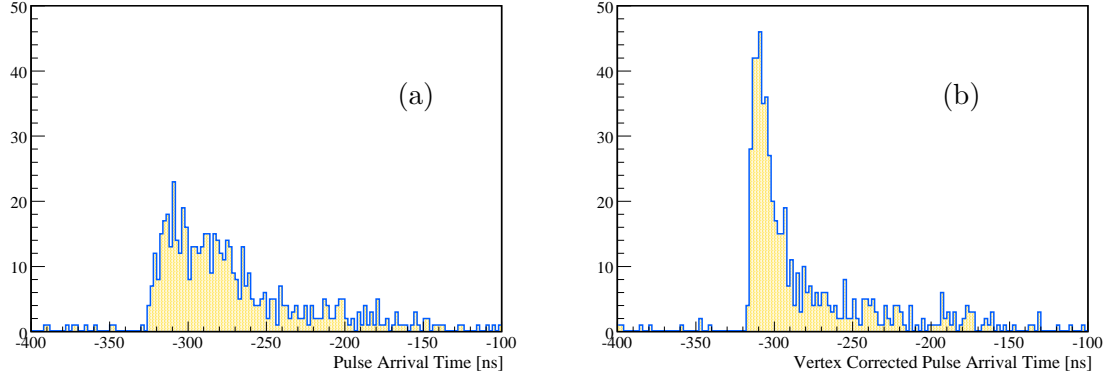
Figure 6.9: Distribution of the pulse times for light arriving at the PMTs for a single event: (a) arrival times before vertex reconstruction, and (b) arrival times corrected for the reconstructed vertex position.

Table 6.1: Reconstruction status as defined by the vertex reconstruction.

Status	Description
Valid	Fit was successful
Unknown	Less than 4 pulses in event
Not Valid	Fit reconstructed unphysically $(r > 10\,m)$
Bad Fit	Fit did not converge
Bad RMS	Residual timing distribution has an unphysical RMS
Bad Pulse Ratio	Unphysical fraction of pulses in the peak
Bad Peak RMS	Peak of residual timing distribution has an unphysical RMS

each medium because they include secondary effects such as scattering, absorption, and reemission by the scintillator. These secondary effects are also the reason the full time distribution is not used to calculate the position change. The N above is the number of pulses in the window -10ns to 5ns around the mean time, $\langle t \rangle$.

The vertex is moved until the $|\langle \delta \vec{r} \rangle| < 1$mm or 100 iterations have taken place. If after this first pass the vertex has converged to an unphysical location outside the detector, it is brought back in and another 100 iterations are performed. After the iterations are complete the vertex quality is assessed by looking at the residuals of the fit and the vertex is assigned a status. The possible vertex status' are summarized in Table 6.1. Only valid vertexes are used in this analysis and the reconstruction efficiency is included in the analysis to account for reconstruction issues.

The performance of the fitter can be evaluated by looking at the reconstruction of sources deployed to fixed locations along the z-axis of the detector, as shown in Fig. 6.10
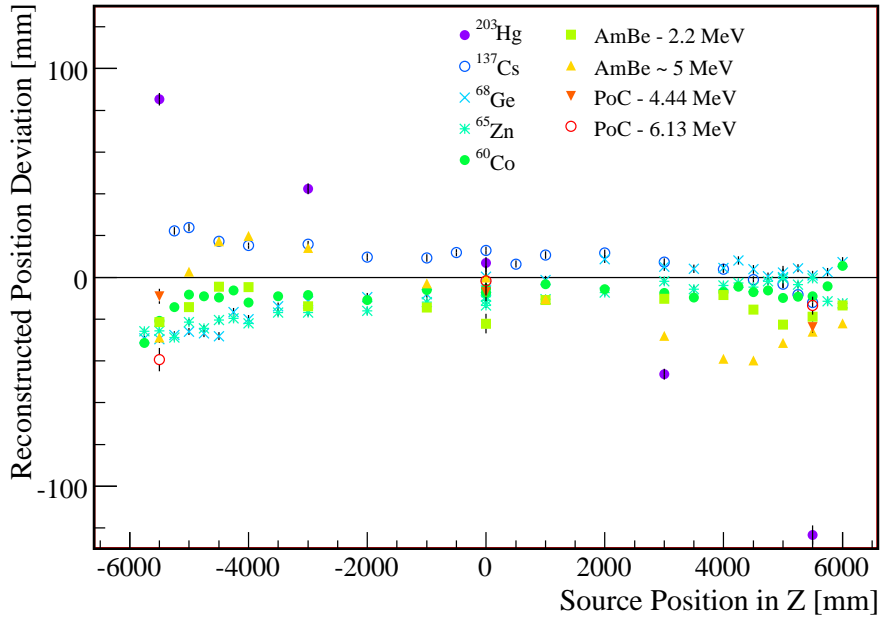
Figure 6.10: The performance of the vertex fitting algorithm is determined by comparing the reconstructed vertex positions to the known position of a radioactive source deployed a long the z-axis of the detector. The deviations from the nominal source position are less than 3 cm except for the low energy ^{203}Hg source.

and in Fig. 6.11. The sources in the range of 0.6 to 6 MeV show very similar behavior and reconstruct no more than 3 cm away from the nominal source position, and have resolutions of better than 30 cm. The lower energy ^{203}Hg source shows much larger deviations and poorer resolution. At these energies the number of dark hit pulses, pulses uncorrelated with the event, become equivalent to the number of pulses correlated with the event, decreasing the performance of the fitter. At these energies using the window around the mean time is severely limiting the number of pulses, further deteriorating the performance.

6.4 Energy Reconstruction

Once the position of the event is reconstructed it is used as input to the energy reconstruction algorithm. The energy algorithm uses the pattern of hit and not-hit PMTs and the amount of charge collected by the hit PMTs to determine the energy of the event. The fact that a PMT does not register a hit in an event gives almost as much information about the energy as a hit PMT. In this way the fitter is maximizing the information available to the energy reconstruction. A typical event is diagrammed in Fig. 6.12 (a). The PMTs closer to the event should be hit more and have more charge. For a more energetic event at the same position, PMTs farther from the event should be hit more and have more charge
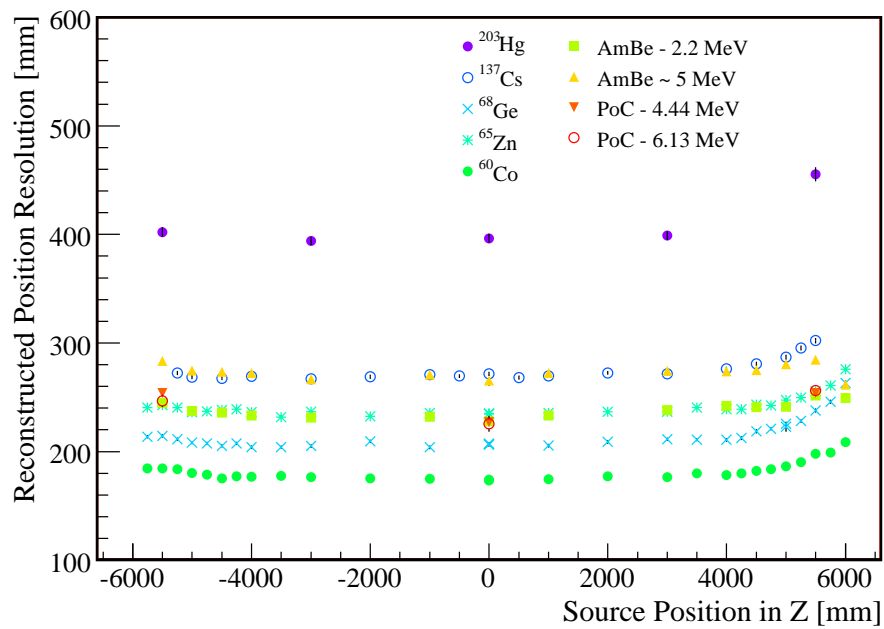
Figure 6.11: The resolution of the vertex fitting algorithm is determined by the width of the reconstructed vertex distribution of a radioactive source deployed along the z-axis of the detector. The resolution or the vertex fitting algorithm is better than 30 cm except for the low energy ^{203}Hg source.

as well.
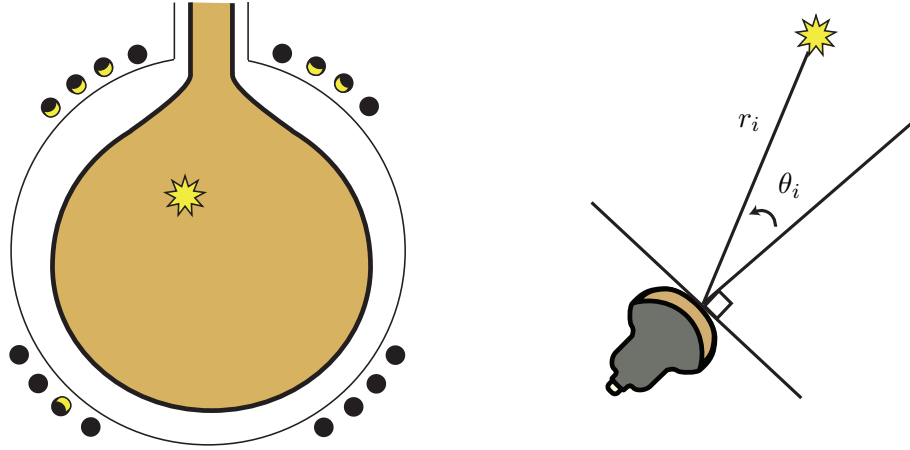
Figure 6.12: Energy fitter diagram (left) and the definition of the PMT geometry (right). PMTs closest to the event are more likely to be hit and collect more charge. The efficiency for the ith PMT to detect the light from an event is dependent on the angle, θ_i, of the event relative to the PMT normal vector in addition to its distance from the event, r_i.

The algorithm uses a maximum likelihood fit to obtain the energy given the distribution of charge in the detector. The likelihood function is assembled from the likelihood of the individual PMTs,

$$\ln(L(E)) = \sum_{N_{PMTs}} \ln(L_i(E, q_i)$$

$$L_i(E, q_i) = \left\{ \begin{array}{ll} e^{-\mu_i} & \text{If Not Hit} \\ \sum_{n=1}^{\infty} \frac{\mu_i^n e^{-\mu_i}}{n!} P(q_i|n) & \text{If Hit} \end{array} \right\}.$$

(6.4)

If the PMT is not hit then the likelihood is given by poisson statistics for zero photo-electrons given an expectation of μ_i photo-electrons. If the PMT is hit the likelihood is given by the probability $n > 0$ photo-electrons with an expectation of μ_i photo-electrons and the probability that the total charge in the event for that PMT, q_i, is n photo-electrons, $P_i(q_i|n)$.

The expected number of photo-electrons μ_i is a function of a geometrical factor, G, two constants, η_i and δ_i, for the i^{th}PMT and the energy to be fit,

$$\mu_i = \eta_i G(r_i, \theta_i, z_i)E + \delta_i.$$

(6.5)

The two constants for the PMTs are calculated from ^{60}Co data taken at the center of the detector. These constants are the number of photo-electrons uncorrelated with the event, dark photo-electrons, δ_i and the number of photo-electrons-per-MeV at the center of the detector, η_i.

The geometrical factor, $G(r_i, \theta_i, z_i)$, is normalized to the center. It accounts for exponential attenuation of the light with an average attenuation length, $\Lambda = 30$ m, for both the BO and LS. Ω is the solid angle subtended by the PMT given the geometry of the event. It is calculated using a numerical calculation that models the photo-cathode as a perfect hemisphere with uniform efficiency. $S(r_i, \theta_i, z_i)$ is a shadowing correction calculated from the full KamLAND Monte Carlo, KLG4sim, and the detailed balloon model implemented in that software. The shadowing correction becomes more important for events at the top and bottom of detector where there is more shadowing from the ropes supporting the balloon. The full expression for the geometrical factor is then given by

$$G(r_i, \theta_i, z_i) = \frac{\Omega(r_i, \theta_i) S(r_i, \theta_i, z_i) e^{-r_i/\Lambda}}{\Omega(r_c, \theta_c) S(r_c, \theta_c, z_c) e^{-r_c/\Lambda}} \tag{6.6}$$

where r_i and θ_i are defined for each PMT as in Fig. 6.12 and z_i is simply the z position of the PMT. The subscripts "c" indicate that these functions are evaluated at the center.

The conversion from q_i, the total charge collected in an event by the ith PMT, to number of photo-electrons requires two additional constants to model the function $P(q_i|n)$. These constants are the mean and width of the single photo-electron peak in units of charge, γ_i and σ_i. The probability of n photo-electrons for a given q_i is then assumed to be a gaussian with a width $\sqrt{n}\sigma_i$ and a mean given by $\gamma_i n$,

$$P_i(q_i|n) = e^{-\frac{(q_i - \gamma_i n)^2}{2n\sigma_i^2}} / \sqrt{2\pi n\sigma_i^2}. \tag{6.7}$$

These two constants, γ_i and σ_i, are calculated by fitting the charge distribution from ^{60}Co data at the center of the detector for each PMT.

If events are separated in time by less than 30μs then it is possible that one or both of the ATWDs in a particular electronics channel are not available to record new waveforms. This can cause a decrease in the reconstructed energy if this effect is not taken into account. This effect was seen in data from the AmBe source. The 2.22 MeV gamma from neutron capture reconstructed 6.5% low. This effect was corrected by including the hit information for each channel's two ATWDs. If one of the ATWDs had fired in the previous 30μs then the probability that the channel would fire was reduced to 94%, tuned to eliminate the bias in the 2.22 MeV capture gamma. If both ATWDs had fired then the probability was reduced to 0. This eliminated the bias though two spikes on the order of 2% remain right before the 30μs transition. These are attributed to noise generated by the VME interface as the board is being readout.

If there were no charge threshold in the electronics then the above would completely describe the detector model used for the energy reconstruction. However, threshold effects become significant in low energy events. Defining the charge threshold as q_o, $P(q_i|n)$ becomes

$$P_i(q_i|n) = \left\{ \begin{array}{ll} e^{-\frac{(q_i - \gamma_i n)^2}{2n\sigma_i^2}} / \sqrt{2\pi n\sigma_i^2} & q_i > q_o \\ 0 & q_i < q_o \end{array} \right\}. \tag{6.8}$$

The likelihood that the PMT is hit remains the same but the likelihood that a PMT is not
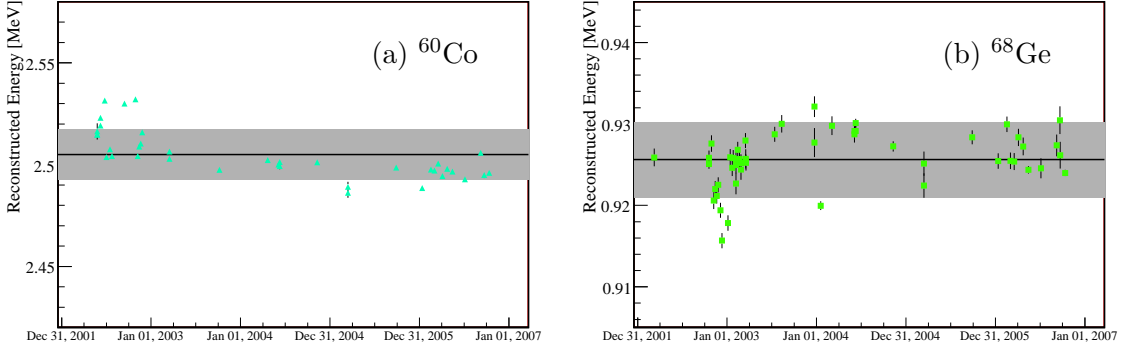
Figure 6.13: The reconstructed energy of radioactive calibration sources at the center of the detector as a function of time. The grey contour indicates $\pm 0.5\%$ for both (a) ^{60}Co and (b) ^{68}Ge.

hit gains a term to account for hits with charge below threshold,

$$
L_i(E, q_i) = \left\{
\begin{array}{ll}
e^{-\mu_i} + \sum_{n=1}^{\infty} \frac{\mu_i^n e^{-\mu_i}}{n!} \int_{-\infty}^{q_o} dq^{'} P(q_i^{'}|n) & \text{If Not Hit, } q < q_o \\
\sum_{n=1}^{\infty} \frac{\mu_i^n e^{-\mu_i}}{n!} P(q_i|n) & \text{If Hit, } q > q_o
\end{array}
\right\}.
\tag{6.9}
$$

The dark hit probability, δ_i, and the scintillator yield, η_i, now depend on the shape of the charge distribution, but the shape of the charge distribution depends on these constants. The constants are still extracted from ^{60}Co runs at the center of the detector. An iterative algorithm starts with the values for the constants which neglect the threshold effects and fits the charge distribution. The $L_i(q)$ is maximized for the data, fixing the energy at 2.506 MeV and allowing η_i and δ_i to float. This is repeated six times at which point the values obtained are no longer changed.

The detector is calibrated with a radioactive source twice a month. Half of these runs are used to calculate the constants used by the reconstruction algorithm. The other half can be used to monitor the stability of the energy reconstruction in time. Over the data set presented in this analysis the variation is less than 0.5%, corresponding the the shaded regions in Fig. 6.13. In early runs the variation of the energy reconstruction was larger. The tuning of the high voltage and the installation of a new high voltage system in December of 2003 improved the stability.

Deployments of radioactive sources along the z-axis of the detector had shown increasing deviation from the nominal source energy with source positions at positive z. Temperature gradients, shadowing effects, and other liquid scintillator properties were studied and found insufficient to explain the deviation. A correction of -8 cm to the center of the detector relative to the top of the detector, was found to reduce the deviation in positive z, but it also increased the deviation in negative z. Such a correction is possible since Kam-LAND was never surveyed as-built. This correction was tuned to minimize the deviation from the nominal source energy. The maximum deviation is now 3%, as shown in Fig. 6.4.
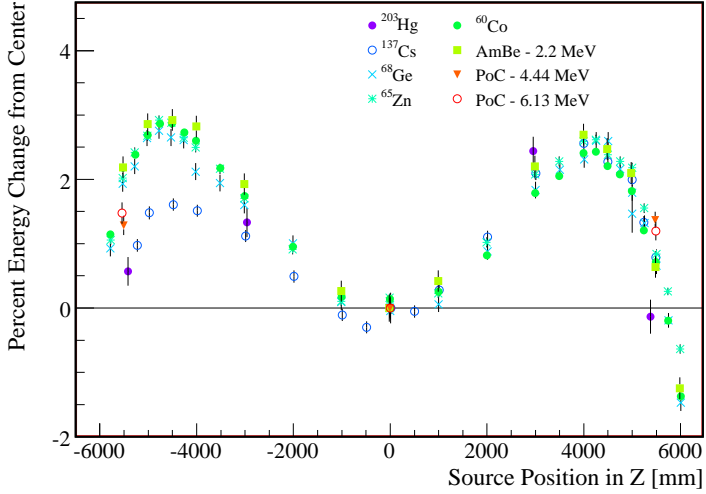
Figure 6.14: The reconstructed energy of radioactive calibration sources along the z-axis of the detector, all sources show the same deviation as a function of position.

All of the sources with energies above ^{137}Cs display the same deviation as a function of z position. Below this energy the performance of the vertex reconstruction decreases, degrading the energy reconstruction performance as well. The energy deviation as a function of position is constant in time.

6.5   Muon Reconstruction

Muons for the most part pass through KamLAND without stopping. The algorithms described in Section 6.3 and Section 6.4 are for point-like events and are not appropriate for muons. Muon tracks are reconstructed using the "Fastest-Light Model". Muons are minimum ionizing particles and deposit 2 MeV g^{-1}cm^2, the KamLAND scintillator produces ~500 photons per MeV, so these are very high light level events compared to other types of events, see Fig. 6.7. As such it is a good assumption that the first pulses extracted from the PMT waveforms correspond to the light that has taken the most direct path to the PMT. The scintillation light from the muon is emitted isotropically along the path. If it is assumed that the muon is moving at c, then the scintillation light's speed is c/n. The fastest light moves at a fixed angle relative to the muon track and this angle happens to correspond to the Čerenkov angle, as shown in Fig. 6.15.

This model is put into a maximum likelihood fit for the track position, $\vec{x}$. The likelihood is given by:

$$L(\vec{x}) = \sum_{i=0}^{N_{17"PMTs}} P(t_i - t_{fastest_i}(\vec{x})) \qquad (6.10)$$

The probability of a given PMT hit time, $P(t_i - t_{fastest_i}(\vec{x}))$, is modeled by a gaussian
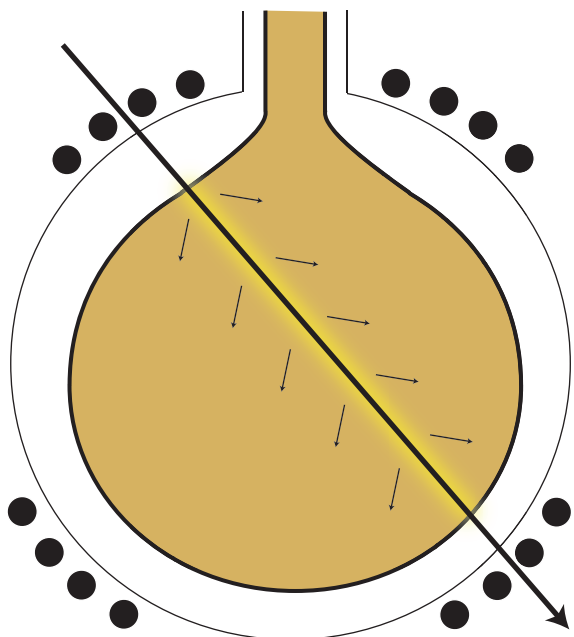
Figure 6.15: Muon Fitter Diagram, the muon passing through the detector deposits scintillation light all along the track. The first light to reach the PMTs will be the light that takes a path corresponding to the Čerenkov angle relative to the track. The muon reconstruction algorithm uses the times from this first light to reconstruct the muon track.
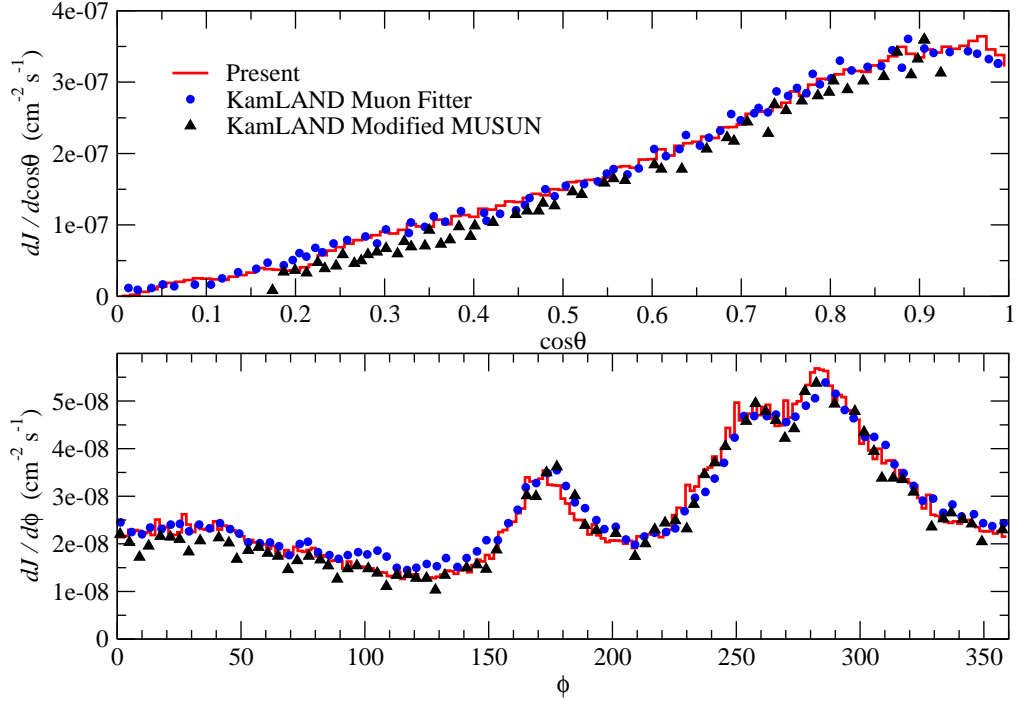
Figure 6.16: Comparisons of the $\cos\theta$ and ϕ distributions of muons reconstructed by the Fastest-Light Model and two muon flux simulations using the packages `MUSIC` and `MUSUN`. The codes use the detailed shape of the KamLAND overburden and are consistent with the distributions reconstructed in KamLAND. This figure is reproduced from Tang et al.[103].

plus an exponential tail. The parameters of this function are determined empirically from the KamLAND data. Minuit[102] is used to do the minimization of $\chi^2 = -2\ln(L(\vec{x}))$ to determine the $\vec{x}$. There are four possible outcomes of the minimization: Minuit fails to converge, Minuit converges but the χ^2 is too large, Minuit converges with an acceptable χ^2, and Minuit converges with a good χ^2. The last two categories may be used in analyses and are "usable" and "valid" tracks respectively.

Since it is not feasible to calibrate KamLAND with a muon source, the quality of tracks reconstructed has to be compared to simulations. Two muons codes have been used for comparison, `MUSIC` and `MUSUN`. They both start with the muon flux at sea level and propagate the muons through the mountain. The detailed shape of the mountain is included in both simulations though the assumptions on the rock composition vary slightly. The simulations show distinct features in ϕ and θ that are mirrored by the Fastest-Light model reconstruction. To the accuracy of these simulations, the reconstruction algorithm seems to be succeeding in reconstructing the direction of the muons entering KamLAND.

The flux of muons across KamLAND should be uniform. This leads to another important test of the muon reconstruction. The "impact parameter" of a muon track is the perpendicular distance from the center of the detector. If the flux is uniform, as expected, then the number of events should be proportional to the impact parameter squared. The
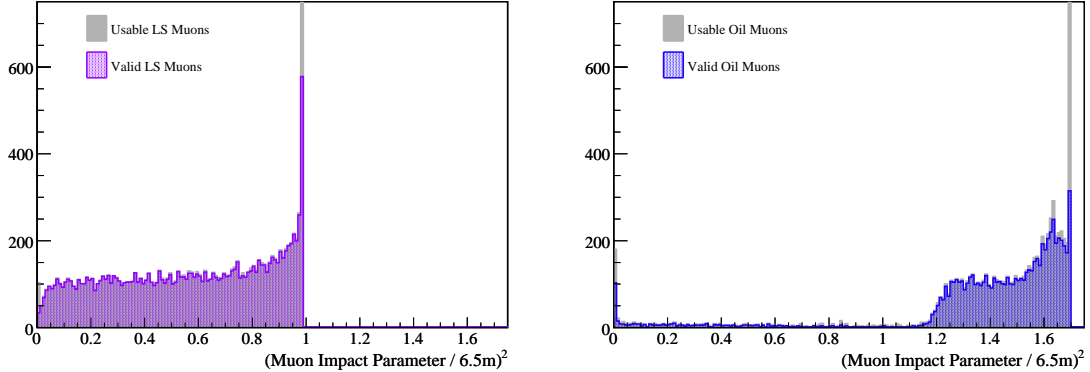
Figure 6.17: The impact parameter distributions of muons that pass through the liquid scintillator, LS muons (right), and muons that pass through the buffer oil, oil muons (left). The flux of muons across KamLAND is constant so the impact parameter distribution should be constant in impact parameter squared. Both muon types show large deviations from flat distributions. These deviations reduced by including only tracks with good χ^2's, "valid tracks".

reconstructed impact parameters of muons that pass through the liquid scintillator, LS muons, and those that only pass through the buffer oil, oil muons, are shown in Fig. 6.17, normalized to the balloons radius, 6.5 m.

There are several features in Fig. 6.17 to note. There are no LS muons within 5 cm of the balloon edge and there is a deficit of LS muons near the center of the detector. There is a pile up effect right before the balloon boundary which is made worse by including the "usable" tracks with only an adequate χ^2 from their reconstruction. There is also a deficit of oil muons on the balloon boundary and a pile up effect at the edge of the detector sphere. There is also a class of mis-reconstructed oil muons that have tracks that reconstruct within the balloon.

Understanding the reconstruction of the muons that pass through the liquid scintillator is especially important for understanding backgrounds from muon spallation processes. Some of the features seen in the impact parameter distribution are more easily seen in the distribution of reconstructed path lengths through the balloon, L_μ. The track length through the balloon is simply related to the impact parameter, b_μ, by $L_\mu = 2\sqrt{(6.5m)^2 - b_\mu^2}$. Fig. 6.18 shows this distribution for LS muons that have the more stringent valid reconstruction. The complete lack of tracks within 5 cm of the balloon is seen as is the pile up at the left of the distribution. There is also a deficit of tracks with long track-lengths corresponding to tracks going through the center of the detector. The average track length through the balloon should be 866.7cm. A linear fit to the distribution, excluding the pile up, yields 774 cm which indicates a net pull outwards.

In an attempt to understand the distortions in the reconstruction, a simple muon simulation was written. It randomly generates muons with tracks that are uniformly dis-
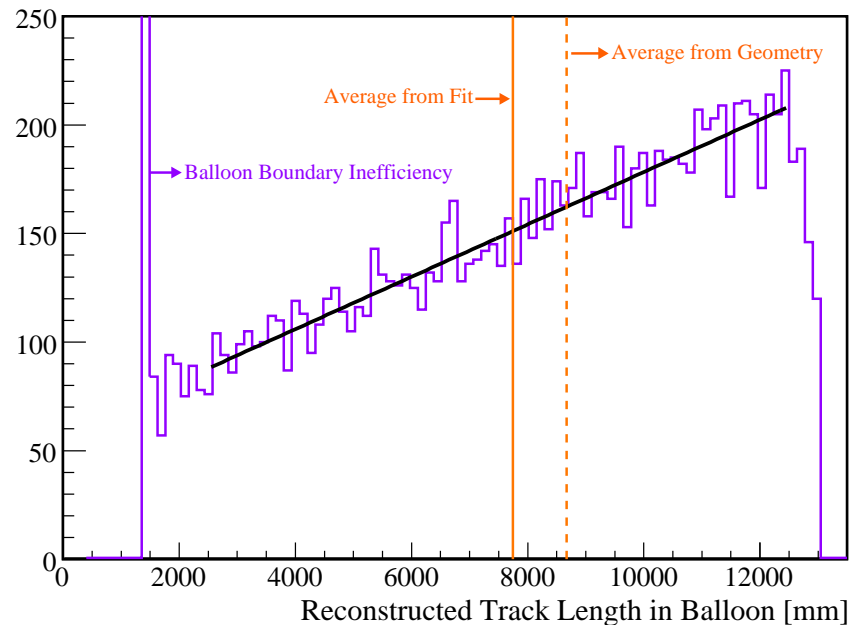
Figure 6.18: The reconstructed track length through the balloon for LS muons with valid reconstruction. A deficit of muons with short tracks corresponds to a reconstruction inefficiency at the balloon edge and a deficit of muons with long tracks corresponds to a reconstruction inefficiency for muons passing through the center. The average reconstructed track length is 774 cm almost a meter shorter than the expected value of 866.7 cm.
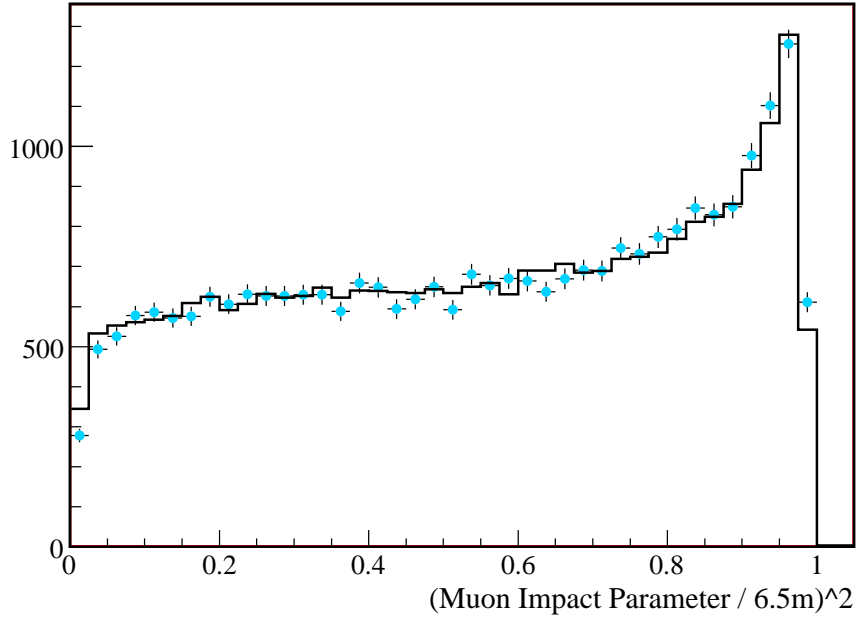
Figure 6.19: The impact parameter distribution of LS muons with valid reconstruction and an impact parameter of $b_\mu < 6.45$m is shown by the blue data points. The results of a simple muon simulation are overlaid in black. The simple simulation took muons from a typical muon distribution at KamLAND and shifted them by $\delta b_\mu = 0.3 - 0.6 e^{1.69 b_\mu}$ m.

tributed through a spherical balloon, have directions that correspond to a cosine squared zenith angle distribution, and an isotropic azimuthal distribution. It was found that to reproduce the reconstructed impact parameter distribution the simulated tracks needed to be moved by $\delta b_\mu = 0.3 - 0.6 e^{1.69 b_\mu}$. This corresponds to a net pull outwards of 0.3 m competing with an exponential pull inwards as the impact parameter increases. This distortion is most likely a result of not modeling the light propagation in the detector correctly, especially at the balloon boundary.

The last measure of the performance of the muon tracking algorithm is the reconstruction efficiency, the fraction of muons with "usable" or "valid" reconstruction. For oil muons 99.7% have usable tracks while 79.2% have valid tracks. Similarly for LS muons 99.7% have usable tracks while 87.4% have valid tracks. The fact that oil muons have a smaller fraction of valid tracks is probably a consequence of noise events being classified as oil muons, see Fig. 6.7. The subset of LS muons with higher light levels, the shower muons, may have a different reconstruction efficiency. Isolating these muons, their reconstruction efficiency is very similar with 99.9% having usable tracks and 86.3% having valid tracks. Now if a cut on the reconstructed track of $b_\mu < 6.45$m is applied in addition to a valid track requirement, the reconstruction efficiency is reduced to 84.0% for LS muons and 84.5% for shower muons. The uncertainty of these reconstruction efficiencies is 0.1%.

6.6 Detector Response and Efficiencies

There are two key numbers and one key function in understanding how to translate a group of reconstructed events into a rate of neutrino interactions in KamLAND. The first key number is the combined vertex and energy reconstruction efficiency to account for events lost in the data processing. The second key number is the size of the volume used for analysis, the fiducial volume. The fiducial volume is defined by a series of position cuts. The key function is the detector energy response function which defines the conversion from real particle energy to the energy reconstructed by KamLAND. The following describes how these quantities are determined for this analysis.

6.6.1 Combined Vertex and Energy Reconstruction Efficiency

Events that are used in the following analyses are required to have valid vertex and energy reconstruction as defined in Section 6.3 and Section 6.4. The exclusion of badly reconstructed events could lead to a bias in the number of observed events, so an efficiency needs to be included in the analysis to account this effect. This efficiency is studied in source data and physics data. In ^{60}Co, data $99.96 \pm 0.002\%$ of events are found to have valid reconstruction. In ^{68}Ge, $99.8 \pm 0.1\%$ of events are found to have a valid vertex. Physics data includes muon tracks which will not have valid vertex reconstruction. To eliminate the muons, a cut on NsumMax is applied, $350 <$ NsumMax < 800, and then the reconstruction efficiency is evaluated. From physics data, it is found that 99.98% of events have valid reconstruction. From these numbers the reconstruction efficiency is determined to be $99.9 \pm 0.1\%$.

6.6.2 Position Cuts and the Fiducial Volume

Two different fiducial volumes are used in this work, a spherical fiducial volume with a radius of 5.5m and cylindrical fiducial volume with a radius of 3m and a height of 6m, volumes 1 and 2 respectively in Fig. 6.20. The daughters of the U and Th chains are concentrated on the balloon and their concentration rapidly decreases towards the center of the detector. A spherical fiducial volume with a radius of 5.5m avoids much of this contamination. High energy gamma rays are produced by (n, γ) interactions in the KamLAND support structure and surrounding rocks. They are attenuated as they travel through the liquid scintillator so their flux decreases rapidly towards the center of the detector. Because the surrounding rock forms a cylinder, a cylindrical fiducial volume is a logical choice for limiting background from external gamma-rays.

Due to limitations in the position reconstruction algorithms, the volume selected with a particular position cut does not correspond to the exact geometric volume. To quantify this effect the reconstruction of short-lived spallation products are studied. The products are selected with a time window following muons of 2 ms$< \Delta t < 52$ ms. These products are mostly ^{12}B, but this is unimportant to this analysis. The key point is that they are uniformly produced and distributed throughout the liquid scintillator. The total volume of liquid scintillator within the KamLAND balloon is 1171 ± 25m^{-3} [104]. The ratio of those events reconstructed within the selected fiducial volume to the total number of
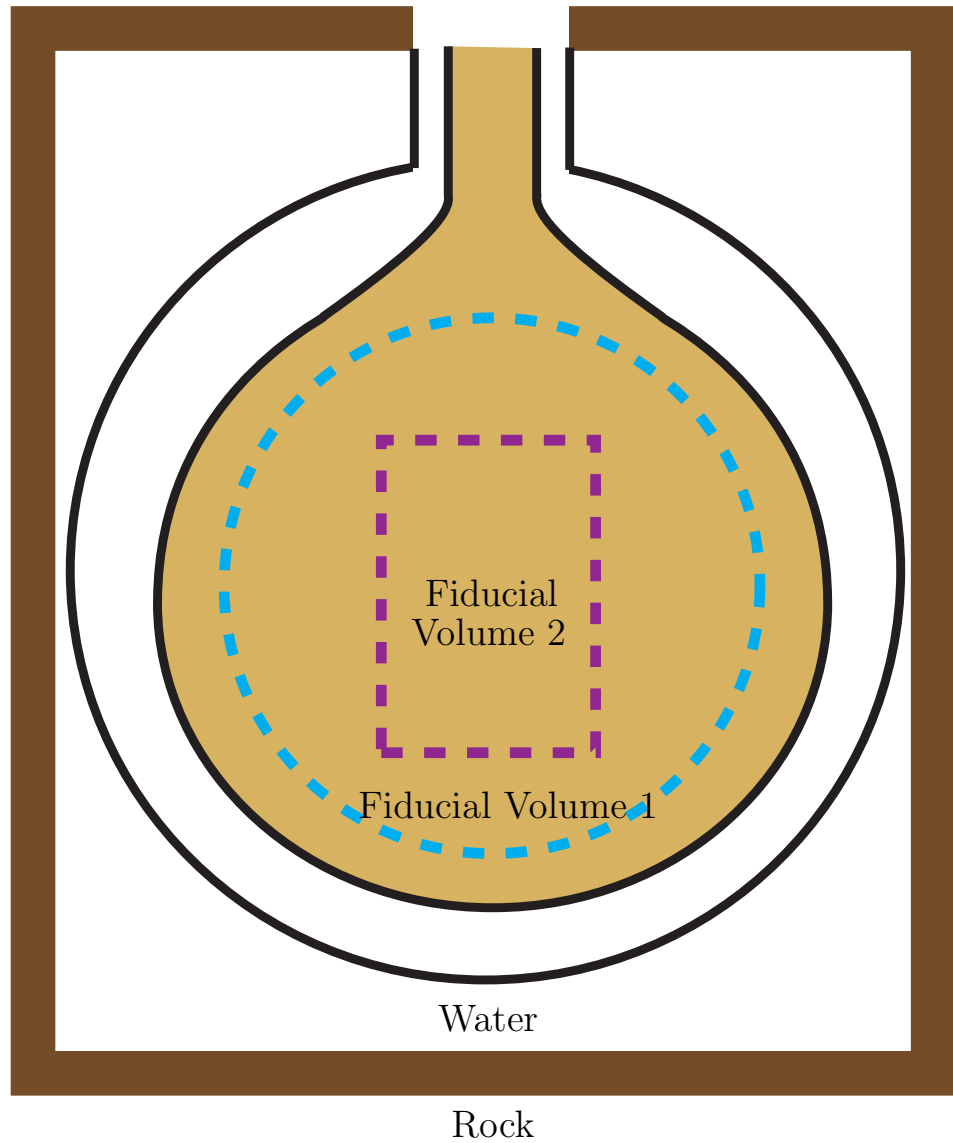
Figure 6.20: Diagram of two fiducial volumes within KamLAND. Fiducial volume 1 maximizes volume while avoiding contamination on the balloon. Fiducial volume 2 maximizes the distance from the cavern's rock walls.

events, multiplied by the total volume of liquid scintillator, provides the effective volume of the selected fiducial volume. To improve the event sample the muons used must be liquid scintillator or oil muons that have triggered the OD. The muons used must also be isolated by $\Delta t > 202$ms from the previous muon and the next muon. The events themselves cannot be muons and must be 0.2 ms away from any previous muons. Finally, events that are not correlated with muons should not be included in the ratio. An off-time window of 52ms$< \Delta t < 202$ms is used to assess this background. The ratio can then calculated,

$$f = \frac{s - \eta b}{s_{Total} - \eta b_{Total}}, \tag{6.11}$$

where s is the number of counts in the signal window, η is the ratio of the size of the time windows, and b is the number of counts in the background window.

The deviations in the reconstructed volume may differ for events of different energy. To evaluate this effect, the ratio is examined as a function of energy, Fig. 6.21 shows the result for the 5.5m spherical fiducial volume. The ratio is fit best by a line though a constant and quadratic both produce good fits. Using the fit results for $f(E)$ and the spectrum of events for a particular analysis, $S(E)$, a mean ratio, $\langle f \rangle$, and standard deviation, $\langle \sigma_f \rangle$, can be calculated,

$$< f >= \frac{\int_{E_0}^{E_1} f(E)S(E)dE}{\int_{E_0}^{E_1} S(E)dE} \tag{6.12}$$

$$< \sigma_f >= \frac{\int_{E_0}^{E_1} \sigma_f(E)S(E)dE}{\int_{E_0}^{E_1} S(E)dE}, \tag{6.13}$$

where σ_f is given by the uncertainty in the fit to $f(E)$,

$$\sigma_f = \sqrt{\sum_{i,j} Cov(i,j)\frac{\delta f(E)}{\delta a_i}\frac{\delta f(E)}{\delta a_j}}. \tag{6.14}$$

The energy window is defined by E_0 and E_1, E_0=5 MeV and E_1=18 MeV. Evaluating these quantities for the ^8B neutrino elastic scatter spectrum, a variety of beta decay spectra, and the three models for f(E), it is found that $\langle f \rangle$ and $\langle \sigma_f \rangle$, are insensitive to the choice of S(E) and f(E). The values obtained for the 5.5m spherical fiducial volume are $\langle f \rangle = 0.577$ with $\langle \sigma_f \rangle = 0.008$. The values obtained for the 3m cylindrical fiducial volume are $\langle f \rangle = 0.1506$ with $\langle \sigma_f \rangle = 0.0035$. Combining the total volume of liquid scintillator with these values, the effective fiducial volume and corresponding systematic uncertainties are summarized in Table 6.2. The systematic uncertainty is dominated by the uncertainty in the total volume of liquid scintillator. The uncertainty in the 3m cylindrical fiducial volume is slightly larger due to poorer ^{12}B statistics for determining this smaller fiducial volume. Additional results for the 3m cylindrical fiducial volume with a central 1m cylinder removed are also presented in Table 6.2.
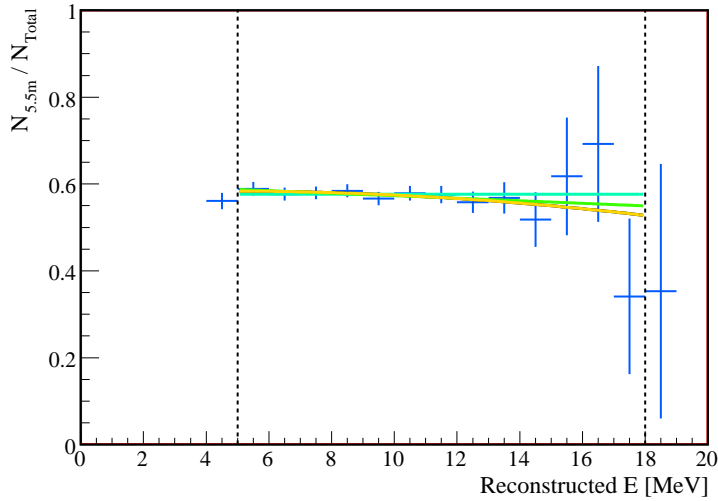
Figure 6.21: The ratio of spallation events within a spherical fiducial volume of radius 5.5m to all spallation events. The bias as a function of energy can be parameterized with a constant, line or quadratic.

Table 6.2: The effective fiducial volume calculated for a spherical fiducial volume with a radius of 5.5m and a cylindrical fiducial volume with a radius of 3m and a height of 6m. The resulting mass and systematic uncertainty are also presented.

Geometry	Volume in m^3	Mass in kt	Uncertainty
5.5m Sphere	675 ± 17	0.526 ± 0.013	2.5%
3m Cylinder	176.4 ± 5.5	0.1376 ± 0.0043	3.1%
3m - 1m Cylinder	158.3 ± 5.0	0.1235 ± 0.0039	3.2%

6.6.3 Detector Energy Response

For most studies the reconstructed energy of the events is the best indication of the underlying physics processes. Ideally the reconstructed data would be proportional to the real energy of the physics event. There are two processes that are known to cause deviations from this simple relation, scintillator quenching and Čerenkov photon production. Scintillator quenching is due to highly ionizing particles saturating the scintillators ability to produce light. Due to their high ionization, alpha particles are quenched heavily and reconstruct at a much lower energy than a gamma ray of the same energy. Čerenkov photon production occurs when a particle has a velocity greater than the speed of light in the KamLAND scintillator. This effect leads to more light production than predicted from scintillation alone and a higher reconstructed energy. Therefore, the conversion of real energy to to reconstructed energy is dependent the energy and the type of particle. As the reconstructed energy corresponds to the amount of light detected by the PMTs, it is also referred to as the "visible" energy", E_{vis}.

The particles that are of interest in KamLAND are γ's, α's, p's, n's, and $e^{\pm}$'s. The conversion function from reconstructed energy to the real energy of each of these particle types is constructed using Monte Carlo and fits to KamLAND data. The conversion function is modeled by

$$f(E) = \frac{E_{vis}}{E} = 1 - \delta_B(E) + k_c \delta_c(E) + k_0 \delta_0(E). \tag{6.15}$$

The term $\delta_B(E)$ accounts for the quenching. The $k_0 \delta_0(E)$ term accounts for particles falling below the tracking threshold in the Monte Carlo. The $k_c \delta_c(E)$ term accounts for the Čerenkov photon production. The Monte Carlo used for the p and α is the SRIM package[105]. The Monte Carlo used for the γ and $e^{\pm}$ is the EGSnrc package [106].

Starting with the quenching of p's and α's, scintillator quenching in general is described by Birk's Law,

$$\frac{dE_{vis}}{dx} = \frac{\frac{dE}{dx}}{1 + k_B \frac{dE}{dx}}, \tag{6.16}$$

where $\frac{dE}{dx}$ is the stopping power and k_B, Birk's constant, is a constant to be determined for the KamLAND scintillator. The composition of the KamLAND scintillator is entered into SRIM, which then calculates $\frac{dE}{dx}$ for a series of energies from 1keV to 30MeV. The term $\delta_B(E)$ is calculated with a series of k_B from $0.5 - 1.5 \times 10^{-2}$g/cm^2/MeV using

$$\delta_B(E) = \frac{1}{E} \int_0^{E_0} \frac{dE}{1 + k_B \frac{dE}{dx}}. \tag{6.17}$$

The quenching calculation for the γ's and $e^{\pm}$'s is slightly simpler. The EGSnrc package takes as input the Birk's constant of the scintillator and returns the energy deposited, dE, per Monte Carlo Step, L_{MC}. From these values $\delta_B(E)$ for γ and $e^{\pm}$ and various k_B over a series of energies can be calculated directly. Similarly, the term for the Čerenkov photon production, $k_c \delta_c(E)$ is calculated for γ and $e^{\pm}$ from EGSnrc using,

$$\delta_c(E) = \frac{L_{MC}}{E} \sin^2 \theta_c \frac{1\text{MeV}}{\text{cm}} \tag{6.18}$$

where θ_c is the Čerenkov opening angle. Like for the quenching parameter, this term is calculated when the simulation is run for each particle at several energies and values of the Birk's constant. The constant k_c is a constant defining the response of KamLAND to the Čerenkov photons. The final term, $k_0\delta_0(E)$, keeps track of the energy that is lost in either simulation due to particles dropping below the tracking threshold. The constant k_0 allows for the recovery of some of this energy.

The simulation results are tabulated and a spline is used to interpolate between the entries in this way the full parameter space for the KamLAND energy response can be explored. The three constants, k_B, k_c, k_0, need to be extracted from a fit to KamLAND data. The energy reconstruction algorithm is normalized such that $E_{^{60}\text{Co}} = E_{vis} = 2.506\text{MeV}$. The function the data is fit to becomes

$$f(E) = a_0 \frac{1 - \delta_B(E) + k_c\delta_c(E) + k_0\delta_0(E)}{1 - \delta_B(2.506\text{MeV}) + k_c\delta_c(2.506\text{MeV}) + k_0\delta_0(2.506\text{MeV})}. \tag{6.19}$$

The constant a_0 is added to account for any overall normalization. Fig. 6.22 shows the result of the simultaneous fit to the calibration gamma rays, spallation neutron capture gammas, ^{212}Po α and ^{214}Po α. The α from ^{210}Po is not used because of known reconstruction inefficiencies at those very low energies. The α's that are used in the fit demonstrate known non-linearites in the energy scale that are most likely due to distortions in the energy reconstruction. The results of the fit are summarized in Table 6.3.

Table 6.3: The constants that are used to define KamLAND's energy scale. They are determined by a simultaneous fit to gamma and alpha data.

Constant	Fitted Value	Description
a_0	1.128 ± 0.014	Overall normalization
k_B	0.0104 ± 0.002 g/cm^2/MeV	Birk's constant
k_c	0.204 ± 0.053	Čerenkov production normalization
k_0	0.649 ± 0.059	Monte Carlo tracking threshold normalization

Once the conversion from reconstructed energy to real energy is understood, $f(E)$, the total detector energy response can be constructed. The total detector energy response function can then be convolved with any real physical energy spectrum, $S(E)$, to predict the reconstructed energy spectrum in KamLAND, $S(E_{vis})$. This convolution is given by

$$S(E_{vis}) = \int_{-\infty}^{+\infty} dE \frac{1}{\sqrt{2\pi}\sigma} e^{-\frac{(E_{vis} - f(E)\cdot E)^2}{2\sigma^2}} S(E). \tag{6.20}$$

The remaining energy scale parameter to be determined is the energy resolution, σ.

The energy resolution of a scintillating detector is limited by the number of photo-electrons produced per energy deposit. In general, the more photo-electron the better the energy resolution. The detector energy resolution in KamLAND is modeled by,

$$\sigma^2 = \sigma_0^2 + \sigma_1^2 \frac{E}{1\text{MeV}}. \tag{6.21}$$
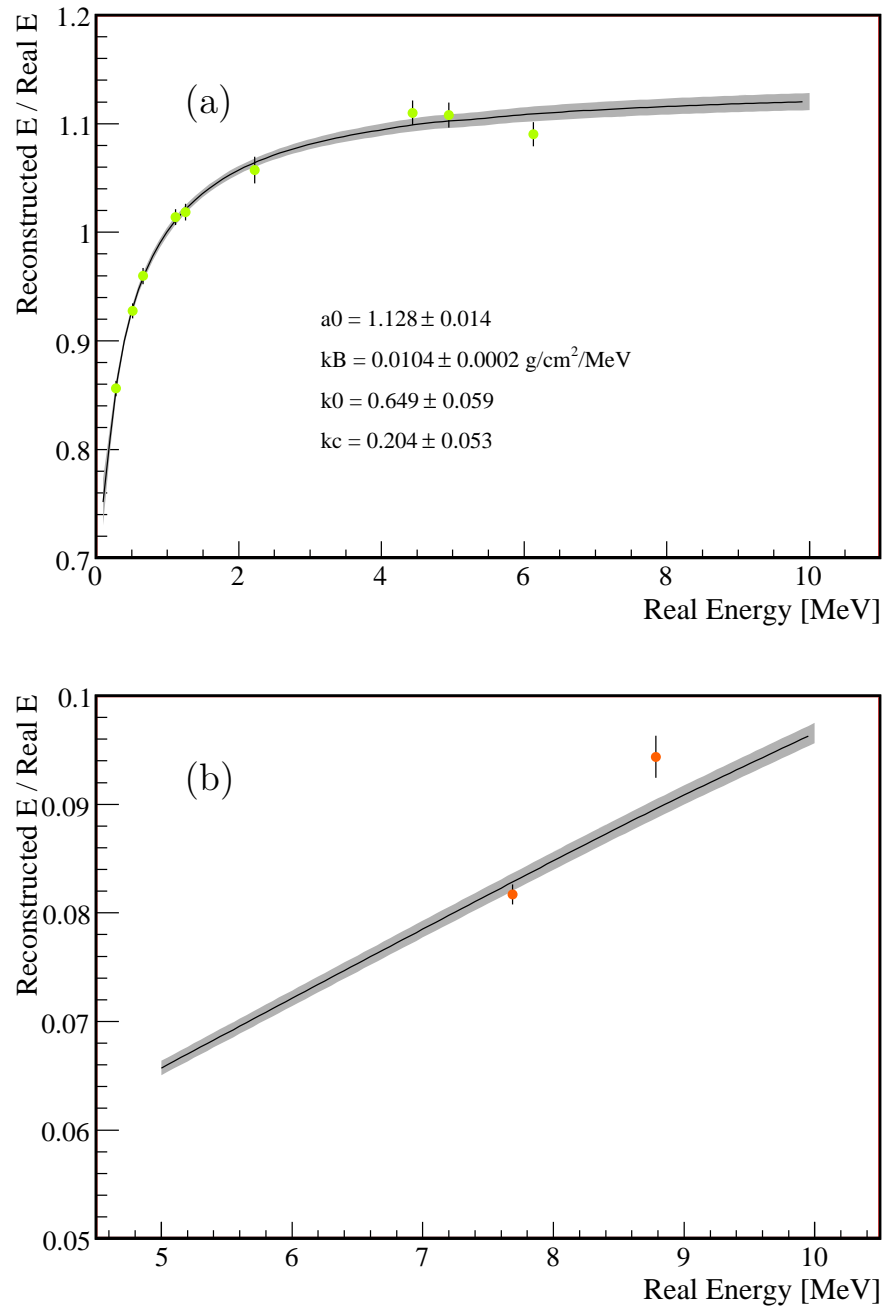
Figure 6.22: The determination of the KamLAND energy scale. The energy scale has four parameters, a_0, k_B, k_c, k_0. These parameters are determined by a simultaneous fit to gamma data (a) and alpha data (b).
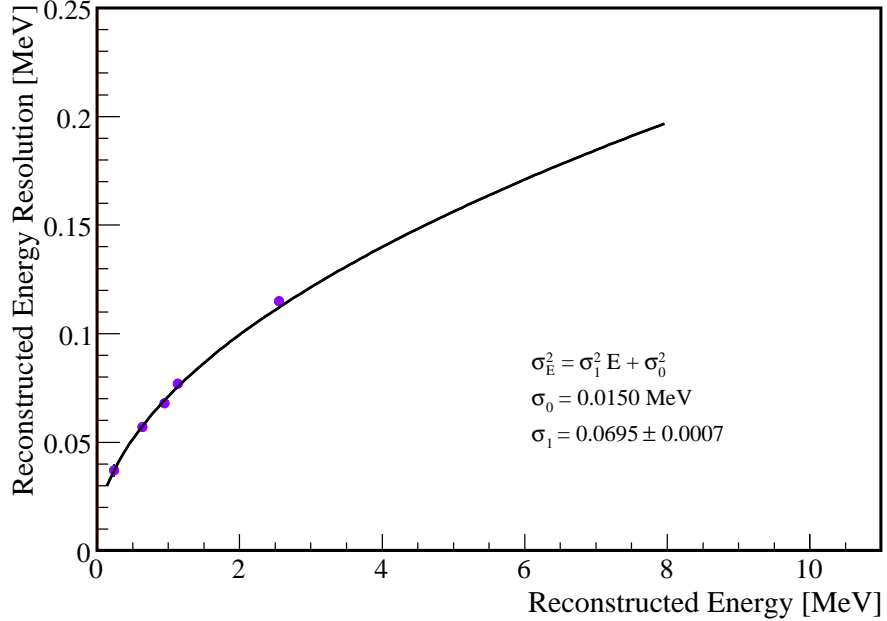
Figure 6.23: The energy reconstructed energy resolution. The detector is modeled with two parameters σ_0 and σ_1.

where σ_0 is the contribution from statistical fluctuations in the dark rate and σ_1 is the component due to the scintillator's ability to produce photo-electrons. Fitting the reconstructed energy of the snap shot trigger, a trigger that randomly acquires data to understand the dark hit rate, σ_0 is found to be 0.015MeV. The value for σ_1 is obtained from the fit to the calibration gammas' reconstructed width. The result of this fit is $\sigma_1 = 0.0695 \pm 0.0007$ with σ_0 fixed to the value from the snapshot trigger. The results of this fit are shown in Fig. 6.23. This energy resolution of $\sim 7\%$ is a factor of two better than either Super Kamiokande or SNO, and is one or the reasons that a measurement of the ^{8}B solar neutrino flux by KamLAND is of interest.

Chapter 7

Simulation of Muon Spallation

The top of the Earth's atmosphere is constantly bombarded by cosmic radiation. This radiation takes the form of electrons, p , He and other elements made in the big bang and stellar nuclear synthesis. It is theorized that these particles are accelerated in cosmic accelerators like supernovae, active galactic nuclei (AGN), and gamma ray bursts. Elements like Li, Be and B are added to this mixture through interactions with interstellar gas. This radiation has energies up to at least 10^{20} eV. As these particles enter the atmosphere they interact with the air and produce particle showers. The results of these particle showers can be divided into two groups: muons and neutrinos from the decay of charged mesons and protons and electrons from the decay of neutral mesons.

The muons, protons, electrons from the particle showers in the atmosphere together with the incident cosmic radiation are collectively called cosmic rays. For a review see Gaisser and Stanev in Ref. [66]. The first studies of cosmic rays were the first high energy particle physics experiments and the study of these particles continues to be an active area of research. The study of the highest energy cosmic rays by experiments such as Auger are starting to probe the acceleration mechanisms of the highest energy cosmic rays in AGN[107].

As interesting as the results of future cosmic ray experiments will be, cosmic rays are a source of backgrounds that are difficult for experiments doing rare event searches using low background detectors to quantify. The protons and electrons are effectively attenuated by $\sim$1m of material and therefore are only an issue at the surface. In comparison, the muons can propagate through several kilometers of rock depending on their energy. As muons pass through matter they can interact, producing secondary particles and excited nuclei. This process is called muon spallation. If these secondary particles and isotopes have long lifetimes they can become a significant background. For KamLAND, the production of neutrons and light elements, summarized in Table 7.1, lead to backgrounds in the analysis of reactor anti-neutrinos and solar neutrinos. For the analysis of ^{8}B solar neutrinos in this work, ^{8}Li, ^{8}B and ^{11}Be with their relatively long life times and high endpoint energies are of particular interest.

Predicting muon spallation backgrounds is difficult because it requires detailed information on the topology and compositions of the material through which the muons propagate to reach the detector in order to determine the muon rate. Then the cross sections

Table 7.1: Unstable isotopes lighter than ^{16}O.

Isotope	Half-Life	Endpoint	Decay Type
^{12}N	0.011 s	17.4 MeV	e^+
^{13}B	0.017 s	13.4 MeV	e^-
^{12}B	0.0202 s	13.4 MeV	e^-
^{11}Li	0.09 s	16.0 MeV	e^-
^{8}He	0.12 s	10.6 MeV	e^- with n
^{9}C	0.13 s	16.0 MeV	e^+ with p or α
^{9}Li	0.18 s	13.6 MeV	e^- with n
^{8}B	0.77 s	17.97 MeV	e^+ with α
^{6}He	0.81 s	3.5 MeV	e^-
^{8}Li	0.84 s	16.0 MeV	e^- with α
^{16}N	7.1 s	10.4 MeV	e^-
^{11}Be	13.8 s	11.5 MeV	e^- with α
^{10}C	19.3 s	1.9 MeV	e^+
^{14}O	71 s	5.15 MeV	e^+
^{15}O	122 s	2.76 MeV	e^+
^{11}C	20.38 min	0.96 MeV	e^+
^{13}N	9.97 min	2.22 MeV	e^+
^{7}Be	53 days	0.862 MeV	electron capture
^{10}Be	1.5×10^6 years	0.556 MeV	e^-

for producing the secondaries in the materials of interest must be known. This is further complicated by the fact that the primary muons at KamLAND depth and similar facilities is on the order of ~100 GeV, while the secondaries can be produced down to ~10 MeV so the cross sections must be extended correctly over several orders of magnitude.

In this chapter the properties of muons at KamLAND depth are presented as extracted from simulation and measurements by KamLAND and other experiments. These muon properties are used as input for studies of muon spallation at KamLAND using the simulation package FLUKA [108, 109]. The production of both particles and light isotopes through muon spallation is studied.

7.1   Muons at KamLAND Depth

KamLAND is located in the Kamioka mine underneath Mt. Ikeoyama. The mountain provides an average overburden of 2700 meters water equivalent (m.w.e). This is one of the deepest experimental sites in the world. As the muons propagate through the rock they lose energy through ionization, bremsstrahlung, e^+e^- pair production and photo-nuclear

Table 7.2: Measured and predicted muon rates for KamLAND. The uncertainties in the muon rates measured by KamLAND are the statistical uncertainties of the studies.

Muon Definition	Scaled Kamiokande	MUSIC Simulation[103]	KamLAND Measurement
	[Hz]	[Hz]	[Hz]
OD	0.73	0.676±0.001	0.62∼0.68
Oil	0.15	-	0.135±0.001
LS	0.21	0.246±0.001	0.205±0.001
Shower	-	-	0.037±0.001

interactions. The approximate energy loss is 2 MeV g^{-1} cm^2. The lowest energy muons will stop causing the total muon rate to decrease with depth while the average energy of the muons increases. At the surface the muon rate is approximately $1 \mu \, cm^{-2} \, min^{-1}$. At depths similar to KamLAND this rate drops to $\sim 1 \mu \, m^{-2} \, hour^{-1}$. The exact value will be determined from the KamLAND data.

Muon events produce very large amounts of light as they pass through KamLAND. For this reason the muon rate is a very sensitive indicator of detector performance and is monitored closely. There are three categories of muons identified by their light levels in the different detector volumes. The details of identifying the three types of muons were outlined in Chapter 6. These three types are muons that pass through the outer detector (OD muon), muons that pass through the liquid scintillator (LS muon), and muons that pass through the buffer oil but not the liquid scintillator (oil muon). The rates of each of these muons types are calculated for each run by constructing histograms of the time difference between events of the same type and fitting to an exponential. The average muon rate for each muon type over the run period used in this analysis is shown in Table 7.2. The OD muon rate is not well determined due to the inefficiencies in the outer detector that are the result of the high failure rate of PMTs in the outer detector.

The Kamiokande experiment was housed in the same cavern in which KamLAND was built. By scaling the Kamiokande rate of 0.37 Hz[32] by the different geometries of the two experiments, the consistency of the muon detection efficiency of the two experiments can be established. Kamiokande used Čerenkov light in water to detect muons while KamLAND uses scintillation light so the systematic effects in the two experiments are different. The agreement between the scaled Kamiokande rate and the KamLAND measurements shown in Table 7.2 is good for the LS muon rate while OD inefficiencies in KamLAND are probably to blame for the disagreement in the OD muon rate. The systematic uncertainty for the measure muons rates is determined by the discrepancy between the two measurements. The LS muon rate for KamLAND is 0.205 ± 0.010Hz or $5.56 \pm 0.27 \mu \, m^{-2} \, hour^{-1}$.

Simulations of muon propagation are critical in planning low background experiments and interpreting the data. MUSIC is a mature FORTRAN program that can simulate muon propagation in three dimensions. The input is a digital map of the mountain profile, the rock composition and the muon spectrum at the surface. Tang et al. constructed a digital map from that used by Super-Kamiokande, the composition of one typical type of rock from the Kamioka mine and a modified Gaisser parameterization of the surface muon
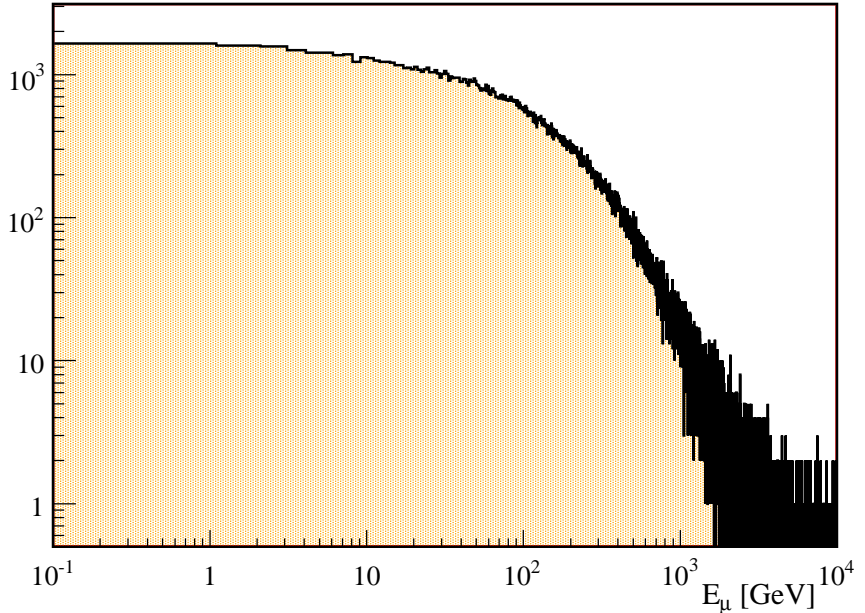
Figure 7.1: Muon energy spectrum at KamLAND predicted by Tang et al. using the MUSIC simulation package to propagate the muons through the mountain[103]. The average muon energy for this spectrum is $\langle E_\mu \rangle$=268 GeV.

spectrum as input to MUSIC[103]. The LS muon rate calculated by this simulation over-estimates the rate compared to the KamLAND LS muon rate and the scaled Kamiokande rate, and it underestimates the scaled Kamiokande rate for the KamLAND OD muons.

The muon energy spectrum is not easily measured by the experiment but it is one of the primary useful outputs of a simulation. The predicted muon spectrum at KamLAND is shown in Fig. 7.1. The muon spectrum at depth is characterized by the average muon energy. The average muon energy calculated by Tang et al. is $\langle E_\mu \rangle$=268 GeV. As muons propagate from the surface to KamLAND, the lowest energy muons stop and the average muon rate increases with depth. As expected, this energy is significantly higher than the ∼4 GeV average muon energy at the surface [66].

Another important characteristic of muons at depth is the ratio of μ^+/μ^-. The excess of μ^+'s reflects the excess of π^+ and K^+ in the particle showers generating the muons while the increase of the ratio with energy reflect the increasing importance of K^+ decay at higher energies[66]. Kamiokande measured the μ^+/μ^- by fitting the lifetime of the muons that stop in the detector. The lifetime of μ^- is shorter than μ^+ because of μ^- capture. They find a ratio of 1.37 ± 0.06(stat.)±0.01(syst.)[110] . The L3 collaboration precisely measured the ratio as a function of muon momentum and zenith angle at the surface. Averaging over zenith angle for muons between 200-300GeV, the charge ratio is 1.29 ± 0.04[111]. These values are consistent with the simulations of Honda et al. [112] and the muon spectrometer

measurement by the BESS collaboration[113, 114]. The average of the two measurements, 1.33 ± 0.07, is used for KamLAND.

7.2   FLUKA Simulation

With the muon rate, energy and charge ratio estimated they serve as inputs to simulations of particle and light element production due to muon spallation. Modeling muon spallation is difficult because the simulation must correctly model the primary muon interaction, the nuclear deexcitation and fragmentation, secondary particle production and the transport of neutrons to thermal energies. FLUKA [108, 109] is an established simulation that meets all of the above criteria. GEANT4[115, 116] is the standard toolkit for the modeling high energy particle interactions. GEANT4 uses a similar model to FLUKA to simulate muon interactions but at this point it is not as well tested as FLUKA and has known problems associated with neutron interactions[117]. MCNPX [118] is an extension of the well verified neutron transport code MCNP. It uses an early version of the FLUKA code to simulate the particle interactions above 150MeV. At this point FLUKA is the best verified package for muon spallation so will be used here to make predictions for KamLAND. In the future studies comparing the output of GEANT4 and MCNPX should be done as they would be valuable in the planning of future experiments.

FLUKA uses "microscopic models" of the particle interactions when possible. This is different than most codes which revert to empirical formulas to model the particle interactions. A large range of energies are modeled by FLUKA and different event generators are used. In general, hadron-nucleon interactions are modeled by resonance production and decay below $\sim$1 GeV and the Dual Parton model at higher energies. Hadron-nucleus interactions are modeled by Generalized Intra-Nuclear Cascade (GINC). At energies above 5 GeV the Gribov-Glauber multiple collision mechanism is included. At all energies hadron-nucleus interactions are followed by the equilibrium processes of nuclear evaporation, fission, Fermi break-up, and gamma deexcitation. The details of these models are described in Ref. [109]. The transport of charged hadrons and muons is done using Bethe-Bloch theory with the addition of a number of second order corrections [108]. For the transport of neutrons below 20 MeV FLUKA has its own compiled cross section libraries for neutrons in 72 energy groups. A standard multigroup treatment is used with photon and fission neutron generation[108].

The version of FLUKA used for this analysis is FLUKA 2006.3b. The information that was desired from the simulation was the total yield particles and isotopes as a function of muon energy and the processes that created the particles and isotopes. To extract this information FLUKA's mgdraw.f function was modified to output the particle data following an interaction. This data was then read into ROOT trees for analysis. As individual particle data was desired the CALORIME defaults were used when running FLUKA[108].

In these simulations, mono-energetic negatively charged muons, μ^-, are run down the length of a cylinder of KamLAND liquid scintillator with a length and radius of 40m. This simple geometry was chosen to eliminate geometry effects. As is shown in Fig. 7.2, the particle shower from the muon requires several meters to develop and some particles will escape from the far end. For these reasons the central 20m are used for analysis. Muons at very shallow sites will have very low energies and therefore lose a significant fraction of
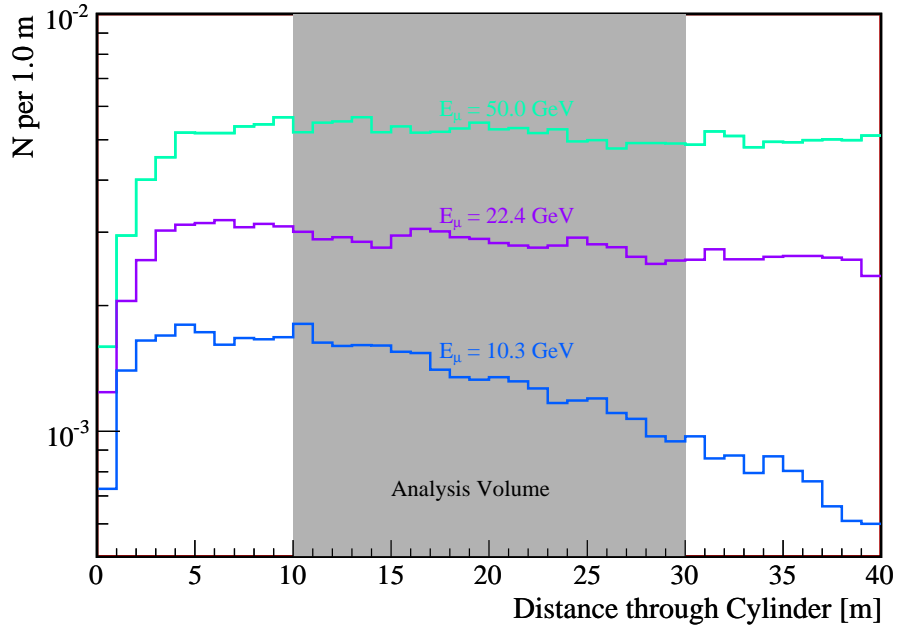
Figure 7.2: Neutron production along the path of the muon in a 40m long cylinder. The results for three different muon energies are shown. The central 20m volume is used for analysis to eliminate effects due to the initial shower development and loss of neutrons from the cylinder. At the lowest muon energies, shallowest experiment sites, the muon loses a significant amount of its energy propagating through the cylinder.

their energy as they propagate through the cylinder. This effect was not corrected for as it is a prediction of the Monte Carlo and it indicates that for the shallowest sites a detailed implementation of the geometry must be used to accurately predict the particle and isotope yields. The liquid scintillator composition is summarized in Section 5.2.1. Natural carbon is used so interactions on ^{13}C carbon will be simulated. For nitrogen and oxygen, only ^{14}N and ^{16}O are simulated as nitrogen and oxygen are already a very small fraction of the targets.

7.3   Simulation of Neutrons and Pions

Several detectors that use liquid scintillator at different depths have measured the spallation neutron flux [119, 120, 121, 122, 123, 124]. For this reason there have been a number of papers on simulations of spallation neutrons with FLUKA. Wang et al. [125] and Kudryavtsev et. al. [126] obtained results from FLUKA 1999. Mei and Hime [127] used FLUKA 2003.1. Finally Araujo et al. [128] compared the results of FLUKA 2003 and GEANT4. Since the spallation neutron yield is so well studied it is a good gauge of the performance of the FLUKA simulation used for this study of muon spallation.
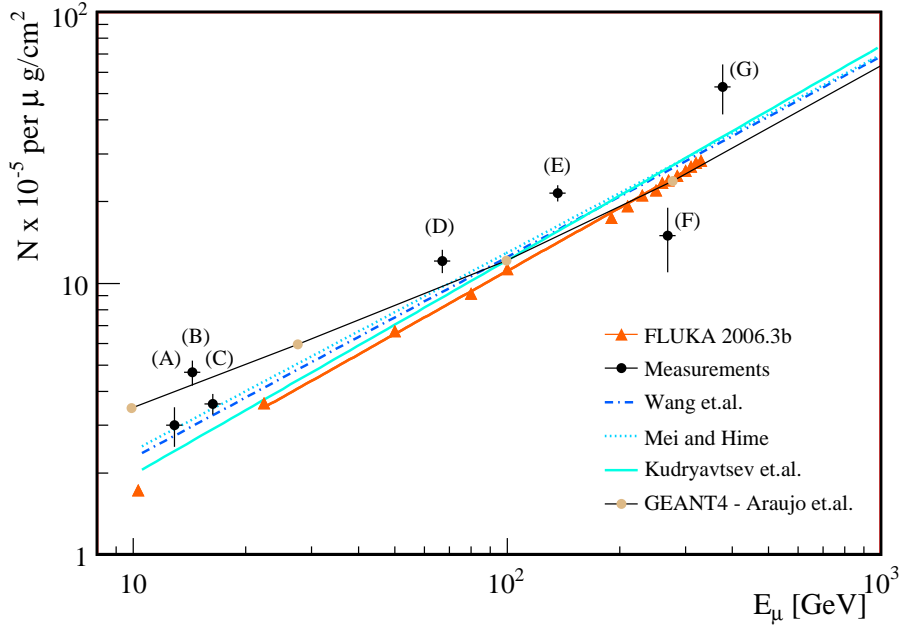
Figure 7.3: Neutron yield as a function of muon energy. The results of this work using FLUKA 2006.3b are shown in orange, the line is the fit to a power law. The results of previous spallation neutron studies are overlaid. Several measurements at different depths are plotted with black points. The measurements are: (A) Hertenberger et al.[119], (B) Bezrukov et al.[121], (C) Boehm et al.[120], (D) Bezrukov et al.[121], (E) Enikeev et al.[122], (F) LVD Experiment[123], (G) Aglietta et al.[124].

When extracting the neutron yield from the simulation care must be taken not to double count neutrons that are involved in reactions like X(n, nn′)X'. In this work if such an interaction occurs, the final state neutron with the highest energy is considered the original neutron and not added to the tally. The results of this study using FLUKA 2006.3b are shown in Fig. 7.3. The present results are 10% lower than previous work. Slightly different liquid scintillator compositions were run and they ruled out composition differences as the explanation for this difference. This leaves the neutron accounting and real differences between FLUKA versions as possible explanations. A fit to a power law,

$$N(E_\mu) = aE_\mu^x \times 10^{-6} \text{ per } \mu \text{ gcm}^{-2}, \tag{7.1}$$

results in $x = 0.773 \pm 0.001$ and $a = 3.15 \pm 0.02$. The slope of the power law, x, agrees well with the previous work leaving an overall normalization difference, a. It is interesting to note that these results agree very well the results obtained in Ref. [128] using GEANT4 for higher energy muons.

From Fig. 7.3 it is clear that this work along with the previous studies all under-estimate the measured neutron yield if the point from the LVD experiment[123] is ignored.
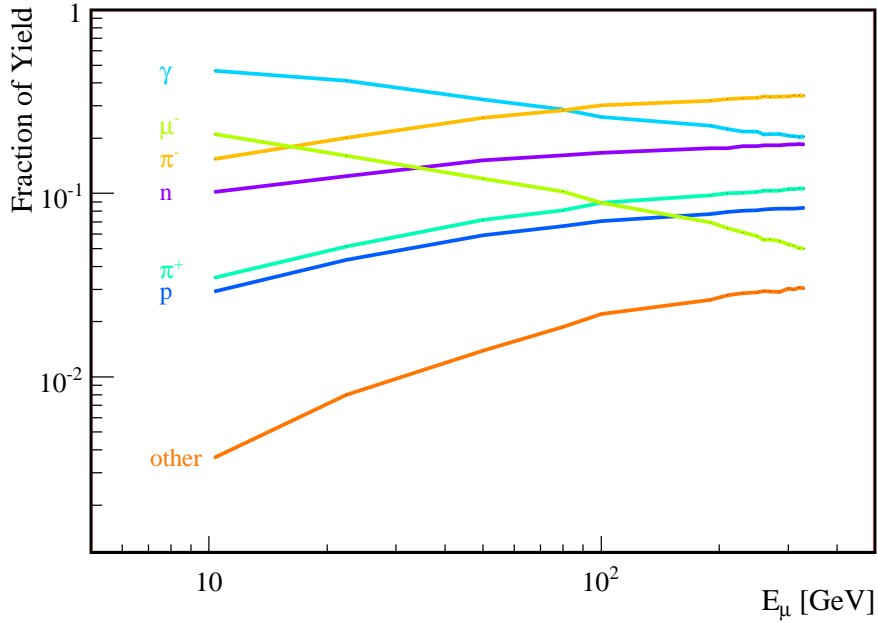
Figure 7.4: Neutron producing process initiator as a function of muon energy as calculated by FLUKA. At low energies most neutrons are produced by (γ, n) reactions. Above 100 GeV pion induced reactions dominate.

There is reason to believe that the point from the LVD experiment is low because the analysis neglected the quenching of scintillation light. The muon energy of the data are those corresponding to [125] assuming a flat overburden except those from Ref. [123, 124] which quote the muon energies.

It is useful to examine the processes that create the neutrons to understand what part of the model used by the simulation might be responsible for a discrepancy. As is shown in Fig. 7.4, up until a muon energy of 100 GeV neutron production is dominated by the (γ, n) reaction. It was pointed out by Mei and Hime[127] that the photonuclear cross section uncertainties were large enough to account for this difference and a simple scaling of the simulated results brings data and simulation into better agreement.

The yield of positive pions was measured by Hertenberger et al.[119], at the Stanford Underground Facility. This is a very shallow site with an overburden of only 25m. The simulations by Wang et al.[125], were corrected for the muon energy loss across the volume and show good agreement with the measurement. The simulations done here show the predicted reduction in yield at low muon energy but are in excellent agreement with the simulations of Wang et al. at higher muon energies. Fitting the yield of π^+ to a power law finds $x = 0.843 \pm 0.003$ which is slightly higher than $x = 0.8$ found in Wang et al.. Fitting the yield of π^- to a power law gives $x = 0.894 \pm 0.003$
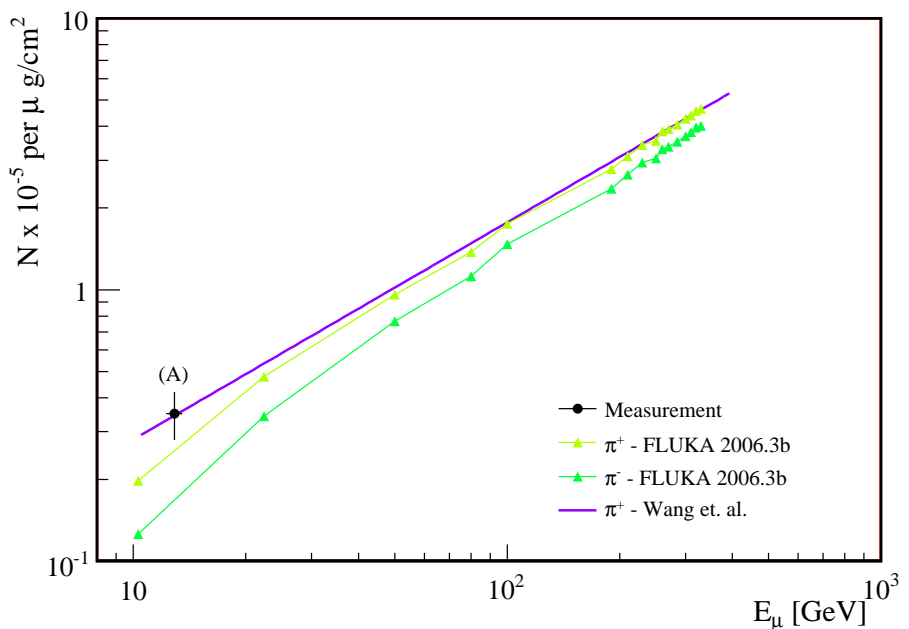
Figure 7.5: Pion yield as a function of muon energy. Hertenberger et al.[119], point (A), measured the π^+ yield at the Stanford Underground Facility. The simulations of Wang et al.[125] are corrected for muon energy loss and agree well with the measurement. The π^+simulations of this work agree well with Wang et al. at higher energies and disagree at low energy where energy loss is important.

7.4 Simulation of Light Isotopes

When particles are produced in muon spallation processes, it is very likely that the target nuclei fragment into lighter isotopes. Some of these light isotopes will be unstable, decay, and produce background in KamLAND. A list of the possible background producing isotopes with mass number less than 16 (^{16}O) is shown in Table 7.1.

The calculation of the production of light isotopes is critical to the correct modeling of muon spallation as it is intertwined with particle production. FLUKA can simulate the production of light isotopes. The results of the FLUKA simulations can be used to estimate the background rates from light isotopes. Furthermore, a comparison of the yield of each isotope to those measured by KamLAND will provide several opportunities to measure the performance of the simulations. As noted by Galbiati and Beacom[129], the yields of various isotopes could be especially useful for unfolding the energy spectra of neutrons and the primary interactions given the production cross section.

The same geometry, liquid scintillator composition and analysis method was used to study light isotope productions and the neutron and pion production described in the previous section. The accounting of light isotopes is straight forward and the analysis code can be checked with the results from the built in FLUKA function, RESNUC. As in the previous section the interesting quantities given by FLUKA simulation are the yields in units of number per muon g/cm^2, and the dominant production processes.

The results of this study using FLUKA 2006.3b are shown in Fig. 7.6 and summarized for $E_\mu = 260$GeV in Table 7.3. As would be expected from the composition of the KamLAND liquid scintillator, the products that are made in interactions with ^{12}C predominate. A fit of the data to a power law, neglecting the data below E_μ=50 GeV, is performed for each isotope. ^{11}C and ^{7}Be have a power law exponent similar to that for the neutrons. The rest of the isotopes have a larger exponent. Since (γ, n) interactions are the interactions that start the particle shower in muon spallation, the different scaling between the isotopes is the result of the physics of the particle shower. The weighted average of the power law exponent is 0.758 ± 0.008.

The listing of the dominant production mechanism in Table 7.3 in some cases is misleading. Fig. 7.7 shows the parent production process for three example isotopes as a function of energy. ^{11}C and ^{12}B are dominated by (γ, n) and (n, p) reactions respectively. However, ^{9}Li is produced about equally by neutrons and pions. As with the neutrons, measurements of the absolute yields and ratios of yields of the isotopes in combination with the production process information from simulation can improve the simulation and shed more light on the physics that produces these isotopes.

All these simulation are for mono-energetic negatively charged muons. The muons interacting in KamLAND have a spectrum of energies and a mixture of μ^- and μ^+. To assess the size of these effects, two additional calculations are performed. The first study employed mono-energetic μ^+ instead of mono-energeticμ^-. The second replaced the mono-energetic μ^- with μ^- with an energy sampled from the predicted muon energy spectrum at KamLAND shown in Fig. 7.1. The result of the calculation with μ^+ at 260 GeV is shown in Table 7.4. The result of the calculation using μ^- with a spectrum of energies is shown Table 7.5.

Both of the effects considered cause a reduction in the isotope yield. As shown in
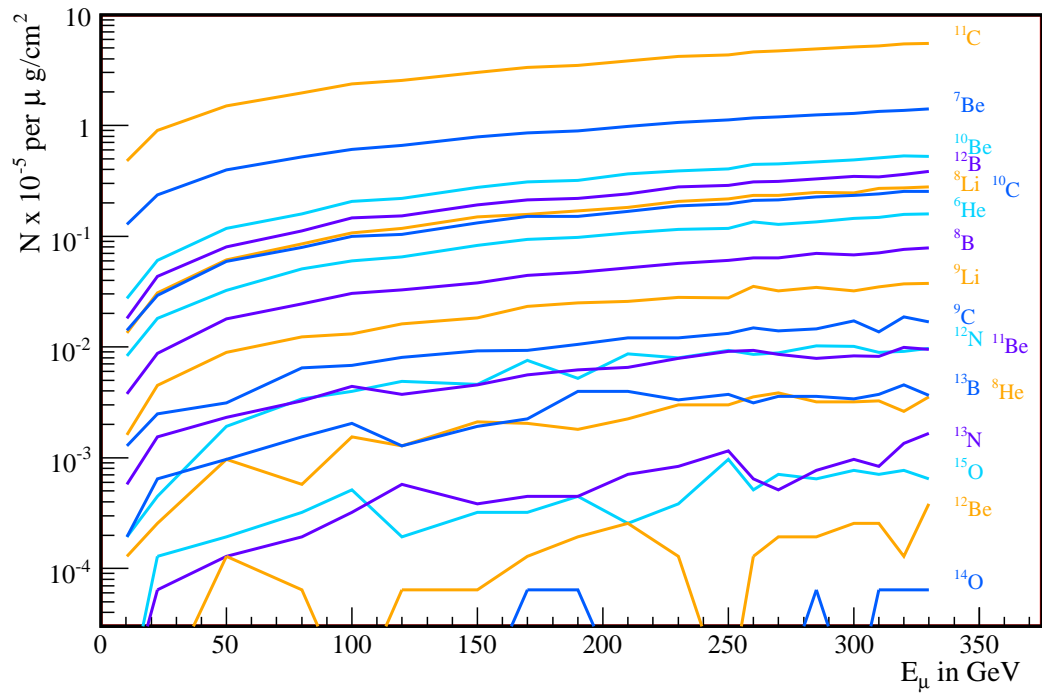
Figure 7.6: Isotope yields as a function of muon energy as calculated by FLUKA. ^{11}C is the most common product of muon spallation. Only trace amounts of products made from nitrogen or oxygen like ^{14}O are seen. In the muon energy range studied, all isotopes show a power law behavior similar to that seen in neutrons and pions.

Table 7.3: Light isotope production at $E_\mu = 260\text{GeV}$ and the exponent of a power law fit to the simulation data.

Isotope	N $\times 10^{-8}$ per μ g/cm^2	Dominant Process	Power Law Exponent
^{11}C	4608.33 ± 17.19	^{12}C$(\gamma,\, \text{n})$	0.703 ± 0.002
^{7}Be	1167.95 ± 8.65	^{12}C$(\gamma,\, \text{n}\alpha)$	0.684 ± 0.004
^{10}Be	446.35 ± 5.35	^{12}C$(\text{n},\, ^{3}\text{He})$	0.825 ± 0.007
^{12}B	308.53 ± 4.45	^{12}C$(\text{n},\, \text{p})$	0.828 ± 0.009
^{8}Li	234.17 ± 3.87	^{12}C$(\text{n},\, \text{p}\alpha)$	0.821 ± 0.010
^{10}C	211.28 ± 3.68	^{12}C$(\pi^{+},\, \text{np})$	0.810 ± 0.010
^{6}He	133.97 ± 2.93	^{12}C$(\text{n},\, 2\text{p}^{3}\text{He})$	0.818 ± 0.013
^{8}B	63.97 ± 2.03	^{12}C$(\pi^{+},\, ^{2}\text{H}^{2}\text{H})$	0.804 ± 0.019
^{9}Li	35.06 ± 1.50	^{12}C$(\pi^{-},\, ^{3}\text{He})$	0.801 ± 0.026
^{9}C	14.94 ± 0.98	^{12}C$(\pi^{+},\, ^{3}\text{H})$	0.772 ± 0.039
^{12}N	8.59 ± 0.74	^{12}C$(\text{p},\, \text{n})$	0.921 ± 0.045
^{11}Be	9.36 ± 0.77	^{12}C$(\text{n},\, 2\text{p})$	0.753 ± 0.051
^{8}He	3.53 ± 0.48	^{12}C$(\pi^{-},\, ^{3}\text{H})$	0.926 ± 0.078
^{13}B	3.14 ± 0.45	^{13}C$(\text{n},\, \text{p})$	0.742 ± 0.075
^{15}O	0.51 ± 0.18	^{13}C$(\text{p},\, \text{n})$	0.793 ± 0.244
^{13}N	0.64 ± 0.20	^{16}O$(\gamma,\, \text{n})$	1.120 ± 0.220
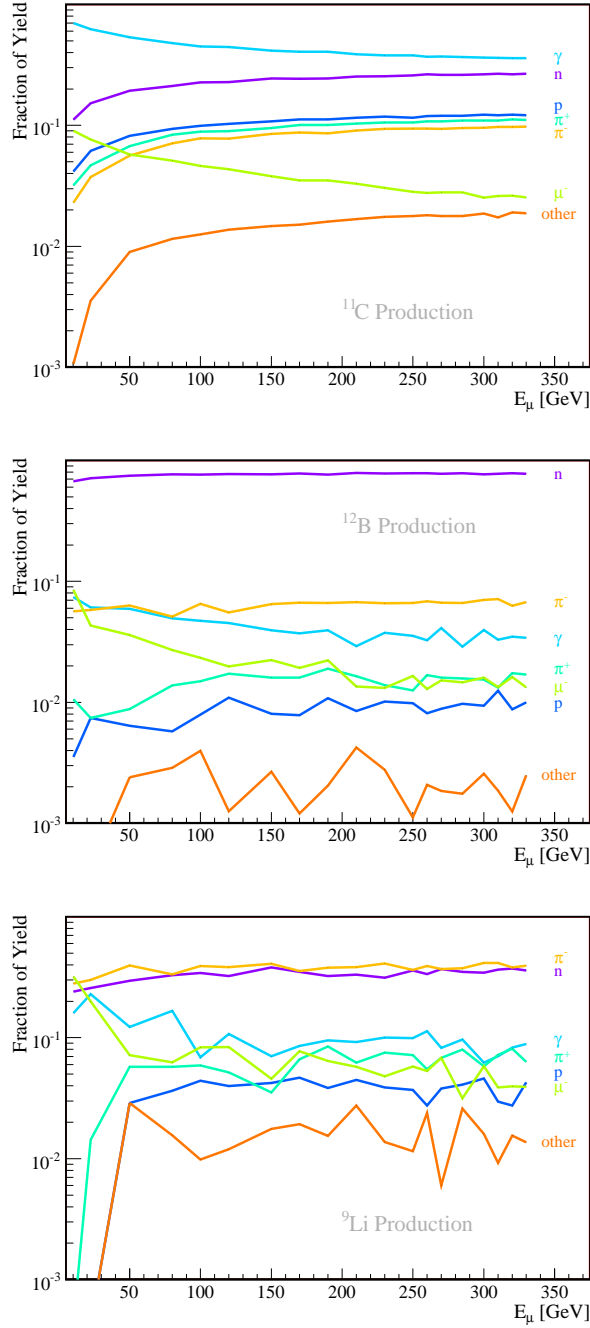
Figure 7.7: Isotope production processes as a function of muon energy for three example isotopes as calculated by FLUKA: ^{11}C (Top), ^{12}B (Middle), and ^{9}Li (Bottom). ^{11}C is predominantly made by (γ, n) interactions while ^{12}B is predominantly made by (n, p) interactions. ^{9}Li is made about equally by neutrons and pions.

Table 7.4: Light isotope production from mono-energetic μ^- and μ^+ at E_μ=260GeV.

Isotope	μ^-	μ^+	Ratio
	$N \times 10^{-8}$ per μ g/cm^2		
^{11}C	4608.33 ± 17.19	4476.86 ± 16.94	0.97 ± 0.01
^{7}Be	1167.95 ± 8.65	1151.79 ± 8.59	0.99 ± 0.01
^{10}Be	446.35 ± 5.35	428.53 ± 5.24	0.96 ± 0.02
^{12}B	308.53 ± 4.45	299.29 ± 4.38	0.97 ± 0.02
^{8}Li	234.17 ± 3.87	217.05 ± 3.73	0.93 ± 0.03
^{10}C	211.28 ± 3.68	207.56 ± 3.65	0.98 ± 0.03
^{6}He	133.97 ± 2.93	122.76 ± 2.81	0.92 ± 0.03
^{8}B	63.97 ± 2.03	63.72 ± 2.02	1.00 ± 0.04
^{9}Li	35.06 ± 1.50	30.00 ± 1.39	0.86 ± 0.07
^{9}C	14.94 ± 0.98	12.69 ± 0.90	0.85 ± 0.11
^{12}N	8.59 ± 0.74	8.27 ± 0.73	0.96 ± 0.13
^{11}Be	9.36 ± 0.77	7.88 ± 0.71	0.84 ± 0.15
^{8}He	3.53 ± 0.48	3.40 ± 0.47	0.96 ± 0.20
^{13}B	3.14 ± 0.45	3.21 ± 0.45	1.02 ± 0.20
^{15}O	0.51 ± 0.18	0.64 ± 0.20	1.25 ± 0.38
^{13}N	0.64 ± 0.20	0.96 ± 0.25	1.50 ± 0.27

Fig. 7.7, one of production processes for an isotope is muon capture,

$$\mu^- + p \longrightarrow n + \nu_\mu \tag{7.2}$$

A μ^+ cannot capture on a proton so this process will not contribute to the isotope yields from μ^+ causing a decrease in the isotope yields. The reduction in isotope yields due to the inclusion of the energy spectrum is straightforward. As was seen in the previous study the isotope yield scales with muon energy so when running with a muon energy spectrum the production from the lower energy muons is less and therefore the total yield is reduced relative to the mono-energetic muons. The average production decrease due to the muon energy spectrum is 0.918 ± 0.017, while the decrease due to μ^+ versus μ^- is 0.961 ± 0.009.

7.5 FLUKA Predictions for Muon Track Correlations

The distance between the production point of the spallation particle or isotope and the muon track is important because it gives clues to the physics of muon spallation and it is something that can be measured experimentally. In fact some experiments exploit the correlation of events in time and space to muons to identify spallation backgrounds. To compare the distributions of the different particles and isotopes, the fraction of events

Table 7.5: Light isotope production for mono-energetic muons, E_μ=268 GeV, compared to production from muons with an energy spectrum, $\langle E_\mu \rangle$=268 GeV, with the shape predicted for KamLAND by the simulations in [103].

Isotope	Monochromatic E_μ=268 GeV	Spectrum $\langle E_\mu \rangle$=268 GeV	Ratio $\langle E_\mu \rangle / E_\mu$
	$N \times 10^{-8}$ per μ g/cm^2		
^{11}C	4675.41 ± 17.27	4269.42 ± 16.54	0.91 ± 0.01
^{7}Be	1184.82 ± 8.69	1119.81 ± 8.47	0.95 ± 0.01
^{10}Be	449.78 ± 5.36	400.90 ± 5.07	0.89 ± 0.02
^{12}B	311.24 ± 4.46	291.22 ± 4.32	0.94 ± 0.02
^{8}Li	233.40 ± 3.87	218.46 ± 3.74	0.94 ± 0.03
^{10}C	212.36 ± 3.69	194.23 ± 3.53	0.91 ± 0.03
^{6}He	129.51 ± 2.90	118.85 ± 2.76	0.92 ± 0.04
^{8}B	63.92 ± 2.02	58.46 ± 1.94	0.91 ± 0.05
^{9}Li	32.60 ± 1.47	27.44 ± 1.33	0.84 ± 0.08
^{9}C	14.12 ± 0.96	13.40 ± 0.93	0.95 ± 0.10
^{12}N	8.79 ± 0.75	8.85 ± 0.75	1.01 ± 0.12
^{11}Be	8.69 ± 0.76	6.99 ± 0.67	0.80 ± 0.16
^{8}He	3.78 ± 0.49	2.18 ± 0.37	0.58 ± 0.37
^{13}B	3.50 ± 0.46	3.72 ± 0.49	1.06 ± 0.18
^{15}O	0.67 ± 0.20	1.09 ± 0.26	1.63 ± 0.23
^{13}N	0.54 ± 0.19	0.64 ± 0.20	1.19 ± 0.40
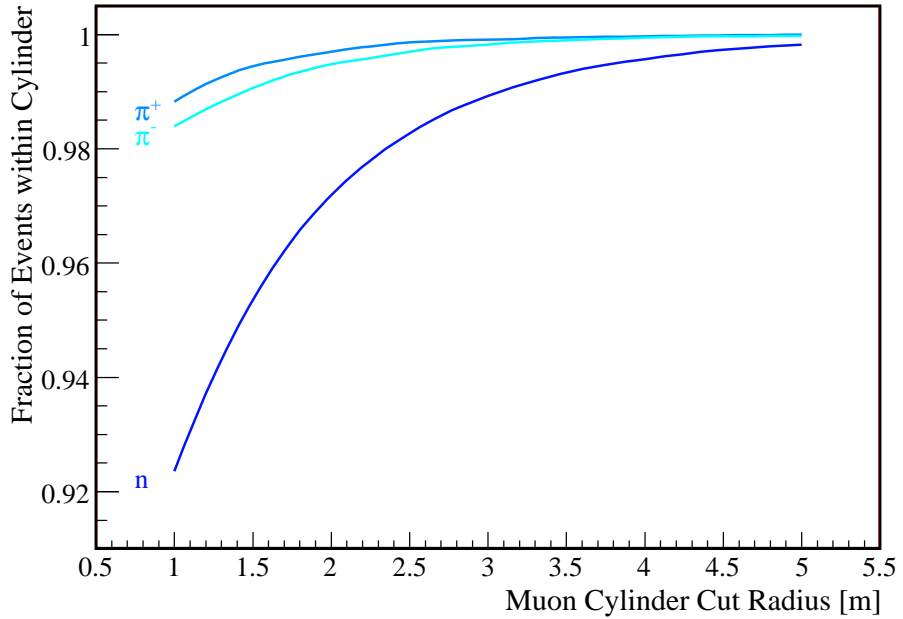
Figure 7.8: The correlation of particles made in muon spallation with the original muon track. Pions are more closely correlated with the muon track than neutrons.

within a cylinder of a give radius are examined. This quantity should approach one as all of the events are included within the larger cylinder. The result for neutrons and pions is shown in Fig. 7.9. The production of pions is much more closely correlated with the muon track than neutrons. As these two particles are the precursor to most of the light isotopes it is interesting to catalogue the light isotopes by their predominant production processes. As shown in Fig. 7.5, those isotopes made by neutrons reflect the broader neutron distribution while those isotopes made by pion or gamma interactions are on average found closer to the muon track.

7.6   FLUKA Comparison with NA54 Experiment

The experiment NA54 ran at the SPS muon beam at CERN to measure light isotope production from muons on liquid scintillator. The experiment is described in detail in [130]. The experiment ran with a μ^- beam at two energies, 100GeV and 190GeV. The muon beams went through 2.4m of concrete and 2m of water so that a realistic muon shower could develop before arriving at the samples. The ^{7}Be yield with its 53 day half life was measured by exposing polyethylene disks to the beam and sending them offsite for counting in a Germanium detector. The main focus of the experiment was to determine the ^{11}C production rate. As ^{11}C has a 20 minute half life, it was possible to expose a sample of liquid scintillator, remove it from the beam line and then count the induced activity at a
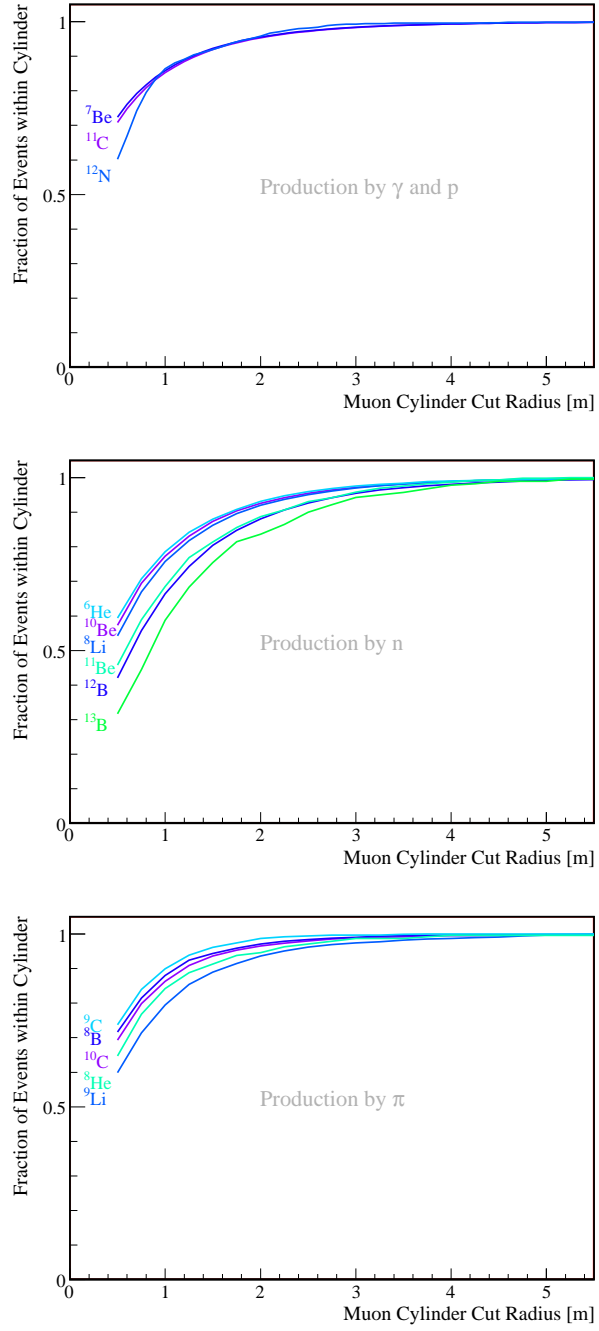
Figure 7.9: The spatial correlation of isotopes made in muon spallation with the original muon track: (Top) isotopes whose dominant production mechanisms are γ or proton interactions, (Middle) isotopes whose dominant production mechanisms are neutron interactions, and (Bottom) isotopes whose dominant production mechanisms are pion interactions.

nearby location.

The isotopes with shorter half lives than ^{11}C were measured *in situ* in the periods between muon bunches. This technique could also be used for ^{11}C. The detector used at the beam line consisted of an array of acrylic tubes filled with the liquid scintillator NE235C and instrumented with PMTs at both ends. These tubes were originally used in the Gösgen reactor neutrino experiment and more details can be found in [54]. The central tube was was used as the target with the surrounding tubes were used to tag a coincidence annihilation γ from β^+ decays.

This experiment is very similar to the geometry and monochromatic μ^- beam used in the simple FLUKA simulations. To do a more accurate comparison, the FLUKA simulation was run with a target matching the composition of NE235C, instead of the KamLAND liquid scintillator composition used previously. The simulation results and the experiment are summarized for 100GeV muons in Table 7.6 and for 190GeV muons in Table 7.7. The numbers reported in [130] were in units of cross section where

$$\sigma = \frac{N}{\mathrm{n}_{^{12}\mathrm{C}} \, \ell_\mu \, N_\mu}.$$

The quantity $\mathrm{n}_{^{12}\mathrm{C}}$ is the number density of ^{12}C in the scintillator and ℓ_μ is the muon track length. To convert to the units used in the present analysis, only the density of the scintillator is needed, $Y = \sigma \, \mathrm{n}_{^{12}\mathrm{C}}/\rho \times 10^{-8}$ per μ g/ cm^2.

The comparison between the FLUKA simulation and the NA54 are not as direct as those between the neutron yield measurements and simulation. FLUKA shows very good agreement for ^{7}Be and a slightly low for number for ^{11}C. There are major discrepancies for the shorter lived spallation products. Of particular interest to ^{8}B solar neutrinos is ^{8}Li and ^{8}B. The simulation indicates almost ten times more ^{8}Li than reported by NA54. NA54 reports almost equal amounts of ^{8}Li and ^{8}B. Examining the reactions that produce these nuclei, more ^{8}Li is expected. ^{8}B is a positron emitter so decays of ^{8}B are tagged by anihillation gammas. The ^{8}B rate is calculated from this coincidence data. From this data their rate is calculated. The rate of ^{8}B is then estimated for the larger data-set. A large efficiency error might explain this discrepancy. This may also be a problem with the model of nuclear breakup used by FLUKA. Analysis of muon spallation of data should be useful for untangling the discrepancy.

7.7 Predictions for KamLAND

The FLUKA simulation and the results of NA54 can each be used to make predictions for light isotope production in KamLAND. The experiment NA54 used mono-energetic μ^-, at lower muon energies, and a different liquid scintillator than KamLAND. Each of these factors requires a correction:

$$Y_{\mathrm{KamLAND}} = Y_{\mathrm{NA54}}(190\mathrm{GeV}) \times \left(\frac{268}{190}\right)^\alpha \times C_{^{12}\mathrm{C}} \times C_{\mathrm{spectrum}} \times C_{\mu^+/\mu^-}. \qquad (7.3)$$

The measurements at 190 GeV are used with Eq. 7.3 since they are more complete. The average power law scaling from the NA54 data is used, $\alpha = 0.73 \pm 0.07$. The correction

Table 7.6: Comparison of FLUKA with NA54 at E_μ=100 GeV.

Isotope	FLUKA	NA54 [130]
$N \times 10^{-8}$ per μ g/ cm^2		
^{11}C	2340.97 ± 11.68	2527.47 ± 197.48
^{7}Be	615.68 ± 5.99	557.27 ± 57.05
^{11}Be	4.37 ± 0.50	< 5.35
^{10}C	94.70 ± 2.35	339.63 ± 21.50
^{8}Li	104.60 ± 2.47	12.86 ± 3.51
^{6}He	59.56 ± 1.86	44.54 ± 4.39
^{8}B	29.72 ± 1.32	18.25 ± 3.55
^{9}C	6.06 ± 0.59	N/A
^{9}Li	14.34 ± 0.91	N/A
^{8}He	1.05 ± 0.25	

Table 7.7: Comparison of FLUKA with NA54 at E_μ=190 GeV

Isotope	FLUKA	NA54 [130]
$N \times 10^{-8}$ per μ g/ cm^2		
^{11}C	3687.18 ± 14.66	3971.12 ± 254.54
^{7}Be	957.63 ± 7.47	1009.23 ± 100.93
^{11}Be	6.59 ± 0.62	< 10.27
^{10}C	164.45 ± 3.10	506.37 ± 64.07
^{8}Li	184.97 ± 3.28	17.64 ± 6.41
^{6}He	103.09 ± 2.45	70.30 ± 7.02
^{8}B	50.17 ± 1.71	31.29 ± 6.41
^{9}C	10.31 ± 0.78	21.19 ± 6.63
^{9}Li	23.02 ± 1.16	9.30 ± 1.54
^{8}He	2.10 ± 0.35	

Table 7.8: Predictions of light isotope production from FLUKA and NA54 for KamLAND, isotopes with endpoints below 5 MeV. The units used here are $\times 10^{-7}$ per μ g/cm^2.

Isotope	Prediction from NA54	Prediction from Fluka
	Events $\times 10^{-7}$ per μ g/cm^2	
^{11}C	449.30 ± 41.60	417.44 ± 26.01
^{7}Be	114.19 ± 13.73	109.49 ± 6.86
^{10}Be	-	39.20 ± 2.49
^{10}C	57.29 ± 8.20	18.99 ± 1.23
^{6}He	7.95 ± 0.96	11.62 ± 0.77

for the number of target ^{12}C is $C_{^{12}C} = 0.98$. The correction for averaging over the muon energy spectrum is $C_{\text{spectrum}} = 0.918 \pm 0.017$. This is calculated from the values presented in Table 7.5. The final correction comes from the differences in production rates between μ^+ and μ^-. The average trend from Table 7.4 is used in conjunction with the μ^+/μ^- ratio from Section 7.1. The derived correction is $C_{\mu^+/\mu^-} = 0.98 \pm 0.06$ and the largest source of uncertainty in the scaling of the NA54 results to KamLAND depth.

The FLUKA results presented in Table 7.5 incorporates the KamLAND muon energy spectrum and the liquid scintillator. The only additional correction that needs to be applied is that for μ^+ relative to μ^- production. The correction, C_{μ^+/μ^-}, is obtained for the FLUKA results using the same procedure as for NA54. The corrected results for FLUKA and those for NA54 are shown in Table 7.8 for isotopes with endpoints below 5 MeV and in Table 7.9 for endpoints above 5 MeV. This energy roughly corresponds to the highest energy beta decays of the ^{238}U and ^{232}Th chains. Below this energy, the KamLAND data rate rises rapidly due to the decays of these chains.

The two isotopes of particular interest for the solar neutrino analysis are ^{8}Li and ^{11}Be due to their high endpoints and relatively long half-lives. Unfortunately, ^{8}Li has the largest discrepancy between the simulation and NA54, and ^{11}Be only has a limit with which to compare the two. These predictions are not sufficient for a background estimation for the solar neutrino analysis and the production rates must be directly extracted from the KamLAND data. The next chapter presents the analysis of spallation products in KamLAND. The comparison of these results with simulation and NA54 can be used to resolve these discrepancies, improving the simulation for future experiments.

Table 7.9: Predictions of light isotope production from FLUKA and NA54 for KamLAND, isotopes with endpoints above 5 MeV. The numbers quoted for ^{9}Li and ^{8}He are the sum of ^{9}Li+^{8}He[130], they are indicated with parentheses.

Isotope	Scaled Results of NA54	Corrected Fluka
	Events $\times 10^{-7}$ per μ g/cm^2	
^{12}B	-	28.47 ± 1.82
^{8}Li	2.00 ± 0.74	21.36 ± 1.38
^{8}B	3.54 ± 0.76	5.72 ± 0.40
^{9}Li	(1.05 ± 0.19)	2.68 ± 0.21
^{9}C	2.40 ± 0.77	1.31 ± 0.12
^{12}N	-	0.86 ± 0.09
^{11}Be	< 1.16	0.68 ± 0.08
^{8}He	(1.05 ± 0.19)	0.22 ± 0.04

Chapter 8

Analysis of Muon Spallation in KamLAND

Short lived isotopes from muon spallation are significant backgrounds to the analysis of ^{8}B solar neutrinos in KamLAND. In Chapter 7 simulation and measured muon rates in KamLAND were used to make predictions for KamLAND. The extraction of spallation isotopes' production rates in KamLAND will be used to make estimates of the number of background events in the ^{8}B solar neutrino. These measurements also more than double the available data available to verify and improve spallation simulation codes.

Muon spallation produced light isotopes are summarized in Table 7.1. These isotopes can be identified by their half-life and their endpoint energy. A binned log-likelihood fit that simultaneously fits the time and energy data is used to extract production rates. The isotopes considered are those with endpoints above 5 MeV which are important for the ^{8}B analysis. Backgrounds uncorrelated with muons rise sharply below this threshold from natural radioactivity in the detector. Based on FLUKA and assumptions about the production processes some of the isotopes included in Table 7.1 are negligible for KamLAND. The remaining isotopes with endpoints above 5 MeV can be usefully grouped as: those with half-lives longer than 200 ms, ^{8}Li, ^{8}B, and ^{11}Be; those with delayed neutrons, ^{9}Li and ^{8}He; and those with half-lives less than 200 ms and no delayed emission, ^{12}N, ^{12}B and ^{9}C.

8.1 Spallation Candidate Selection

The data used was collected over 5 years from April 2002 through April 2007 and corresponds to 1432.1 days. Though the analysis of each isotope has a different selection criteria depending on the decay energy and half-life, all use a spherical fiducial volume with R < 5.5 m. This corresponds to a volume of 0.526 kilotons and an exposure of 753 kiloton days. These units correspond to metric kilotons and will be abbreviated as kt. A vertex reconstruction efficiency of 0.999 and the systematic uncertainties summarized in Table 8.1 are common to all the isotopes analyzed.

Table 8.1: Efficiencies and systematic uncertainty in the spallation analysis common to all analyzed products.

	Efficiency	Systematic Uncertainty
Fiducial Volume	-	2.5%
Scintillator Variation	-	0.14%
Reconstruction	0.999	0.10%
Total	0.999	2.51%

8.2 Log-Likelihood Fit

The starting point of a log-likelihood analysis is constructing the likelihood function. The likelihood function for a histogram obeying Poisson statistics is

$$L_p(\mathbf{y}; \mathbf{n}) = \prod_i e^{-y_i} y_i^{n_i} / n_i!$$

(8.1)

where y_i is the number of events the model predicts for the ith bin and n_i is the number of events observed[131]. The likelihood function is converted to a general χ^2 statistic using the likelihood-ratio test theorem. The likelihood ratio is

$$\lambda = L_p(y; \mathbf{n}) / L_p(\mathbf{m}; \mathbf{n})$$

(8.2)

where $\mathbf{m}$ is defined to be the "true" values of n. The χ^2 statistic is constructed as:

$$\chi_\lambda^2 = -2 \ln \lambda = -2 \ln(L_p(y; \mathbf{n})) + 2 \ln(L_p(\mathbf{m}; \mathbf{n})).$$

(8.3)

This statistic asymptotically approaches a true chi-square distribution. For Poisson statistics, $\mathbf{m}$ values can be replaced with the measured values $\mathbf{n}$. The χ^2 statistic then becomes

$$\chi_\lambda^2 = 2 \sum_i y_i - n_i + n_i \ln(n_i / y_i)$$

(8.4)

which is the usual expression for fitting any histogram with Poisson statistics. In this work, Minuit[102] minimization package is used exclusively.

The details of the model for $\mathbf{y}$ are what customize equation 8.4 for a particular analysis. The model for the histogram of the time since preceding muons is given by

$$y_i(t_i) = \hat{\varepsilon} \Upsilon \delta t \sum_j^{isotopes} \left(\frac{\hat{R}_j}{\tau_j} e^{-t_i/\tau_j} \times \int_{E_{min}}^{E_{max}} S_j(E_i, \vec{\alpha}, \vec{\sigma}) dE \right) + \hat{C}$$

(8.5)

where $S_j(E_i, \vec{\alpha}, \vec{\sigma})$ is the spectrum of the jth isotope including the detector's energy response. The isotopes produced by a muon spallation decay exponentially while a constant background is expected from uncorrelated backgrounds. The isotope production rates are the $\hat{R}_j$ parameters while the constant background is given by $\hat{C}$. In general, "nuisance"

parameters are employed to account for systematic uncertainties in the analysis. The parameter $\hat{\varepsilon}$ is a nuisance parameter to account for the uncertainty in the total detection efficiency. The integral over the normalized energy spectrum of the jth isotope provides the efficiency of the energy cuts for that isotope and also allows for the energy scale to vary in the fit. The definition of the relevant parameters and constants are summarized in Table 8.2.

In addition to $\hat{\varepsilon}$, other nuisance parameters are included to account for the uncertainty in the energy scale. For each nuisance parameters, a penalty term, χ_P^2, is added in χ_t^2,

$$\chi^2 = \chi_t^2 + \chi_P^2. \tag{8.6}$$

where χ_t^2 indicates the χ_λ^2 in Eq. 8.4 corresponding to the time interval to previous muons histogram. The full penalty term is given by

$$\chi_P^2 = \sum_j^{isotopes} \left(\frac{R_j - \hat{R}_j \frac{\varepsilon}{\hat{\varepsilon}}}{\sigma_{R_j}} \right)^2 + \left(\frac{\varepsilon - \hat{\varepsilon}}{\sigma_\varepsilon} \right)^2 + \sum_m \sum_n \frac{(\alpha_m - \hat{\alpha}_n)(\alpha_n - \hat{\alpha}_m)}{c_{mn}}. \tag{8.7}$$

The first term allows for the constraining information from other measurements, R_j in the fitting of the rate $\hat{R}_j$ including the uncertainty of the measurement R_j, σ_{R_j}. The second term accounts for the uncertainty in ε, the total detection efficiency. The last term accounts for the uncertainty in the energy scale parameters and the correlations between the parameters by making use of the covariance matrix from the fit to calibration data shown in 6.6.3. The quantity c_{mn} is one entry in the energy scale covariance matrix.

The addition of energy information in the spallation analysis provides more discriminating power, especially for the isotopes with very similar half-lives. In the combined time and energy analysis, the time since muon histogram is joined combined with two energy histograms, the energy of events in the signal time window and the energy of events in the background time window. The χ^2 statistic then becomes

$$\chi^2 = \chi_t^2 + \chi_{E_s}^2 + \chi_{E_b}^2 + \chi_P^2. \tag{8.8}$$

The signal time window is usually defined as the first half of the time window used for the time histogram while the background time window is the second half. The model for the signal window is given by

$$y_i(E_i) = \varepsilon \hat{\varepsilon} \Upsilon \left(\sum_j^{isotopes} \hat{R}_j f(t_{1s}, t_{2s}, \tau_j) S_j(E_i, \vec{\alpha}, \vec{\sigma}) \right) + \hat{b}_i(t_{2s} - t_{1s}). \tag{8.9}$$

The energy spectrum of the jth isotope is given by $S_j(E_i, \vec{\alpha}, \vec{\sigma})$. The energy spectrum of events uncorrelated to the muon is accounted for by floating an additional parameter $\hat{b}_i$ for each bin of the histogram. The values of $\hat{b}_i$ should be the same in both the signal and background energy histograms while the normalization of isotope's spectra should decrease due to their exponential decay. The division of the data into two time windows is done because the shape of the background, $\hat{b}_i$'s, is not know. In an energy and time analysis the

Table 8.2: Parameters, measured quantities, defined constants and cuts used in these spallation analyses.

	Symbol	Description
Parameters	$\hat{R}_j$	Rate of jth isotope.
	$\hat{\varepsilon}$	Re-scale of the total detection efficiency.
	$\hat{\vec{\alpha}}$	Energy scale parameters a_0, k_b, k_0, k_c.
	$\hat{b}_i$	Background rate in i^{th} energy bin.
	$\hat{C}$	Background rate in all time bins.
Measured Quantities	Υ	exposure for the analysis in kt-days.
	ε	Total detection efficiency.
	σ_ε	Uncertainty of the total detection efficiency.
	R_j	Rate of jth isotope from a previous analysis.
	$\vec{\alpha}$	Energy scale parameters a_0, k_b, k_0, k_c.
	c_{mn}	Energy scale covariance matrix element $\text{cov}[\alpha_m, \alpha_n]$.
	$\vec{\sigma}$	Energy resolution parameters σ_0 and σ_1.
Definitions	τ_j	Lifetime of jth isotope.
	$S_j(E_i, \vec{\alpha}, \vec{\sigma})$	Spectrum of jth isotope.
	E_{min}	Minimum energy event used in the analysis.
	E_{max}	Maximum energy event used in the analysis.
	δt	Bin width of the time histogram.
	δE	Bin width of the energy histogram.
	t_{1s}, t_{2s}	Start, Stop time of the energy signal window.
	t_{1b}, t_{2b}	Start, Stop time of the energy background window.

sum of the $\hat{b}_i$'s is correlated to the constant parameter $\hat{C}$ by

$$\hat{C} = \sum_{i=0}^{N} b_i \, \delta E \, \delta t. \tag{8.10}$$

so the parameter $\hat{C}$ is replaced by this sum. To model the background window equation 8.9 is used with $t_{1s} \rightarrow t_{1b}$ and $t_{2s} \rightarrow t_{2b}$.

8.3 Analysis of ^{11}Be

There are three spallation isotopes, ^{11}Be, ^{16}N and ^{14}O, with half-lives longer than 1 s and endpoints above 5 MeV. The number of nitrogen or oxygen targets in KamLAND on which to make ^{16}N and ^{14}O is four orders of magnitude smaller than ^{12}C, see Table 5.1, so they will be neglected in this analysis of longer-lived isotopes. The results of the FLUKA simulations support this assumption. This means the only isotope that need be considered in this time period is ^{11}Be.
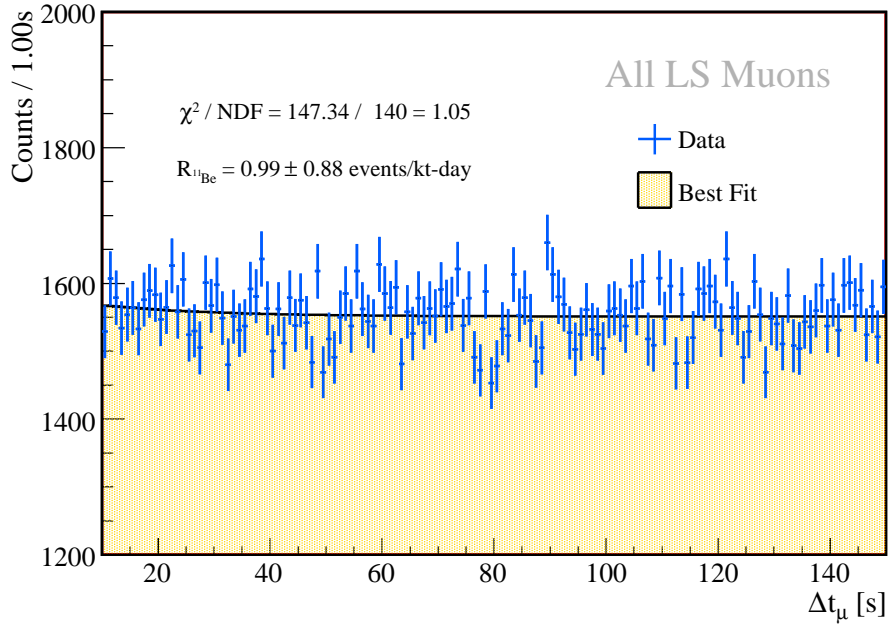
Figure 8.1: ^{11}Be spallation candidates plotted relative to their time difference to all preceding muons within 150 s. The large background is due to the high number of uncorrelated muon and event pairs.

The endpoint of the ^{11}Be beta decay spectrum is 11.5 MeV. The finite KamLAND detector energy response smears the spectrum to higher energies, so the analysis energy window is chosen to be 5-13 MeV. A reasonable time window for the analysis of an exponential decay is ∼10 times the half-life. This large window allows for a good determination of the uncorrelated backgrounds. The known half-life of ^{11}Be is 13.8 s and the time window for this analysis is $10\,\text{s} < \Delta t_\mu < 150\,\text{s}$. By starting the time window at 10 s, decays of shorter lived products are safely excluded from the analysis. To reduce the contribution of shorter lived isotopes to the uncorrelated background in the ^{11}Be analysis a full detector veto of 2 s is applied after every LS muon. If an energy and time analysis were performed a cut on the time between muons would need to be applied. This cut should correspond to the upper limit of the analysis time window, 150 s. This time is large compared to the average time between muons and would have the effect of eliminating almost all of the available data. As a result the ^{11}Be analysis only fits the time since muon data, Δt_μ, and does not include the energy.

The events that pass the common cuts are paired with all LS muons in the preceding150 s. The resulting histogram is shown in Fig. 8.1. The fit using the χ^2 in Eq. 8.6 returns 0.99 ± 0.88 ^{11}Be per kt-day. The ^{11}Be signal is obscured by the numerous uncorrelated backgrounds that occur within the time window. The spallation isotopes should be correlated in space to the muon track. By exploiting this correlation, the sensitivity to ^{11}Be

Table 8.3: The efficiency of the muon cylinder cut for the muons with "valid" reconstruction and impact parameters less than 6.45 m. The fiducial volume used is a sphere with a 5.5 m radius. The efficiency is defined as the number of spallation candidates within a cylinder around the muon track of a given radius dived by the total number of candidates. The statistical uncertainty of the study is shown.

Cylinder Radius	All LS Muons	Non-Shower Muons	Shower Muons
1m	0.614 ± 0.003	0.769 ± 0.009	0.595 ± 0.003
2m	0.836 ± 0.002	0.914 ± 0.006	0.827 ± 0.003
3m	0.920 ± 0.002	0.967 ± 0.004	0.915 ± 0.002

can be improved.

8.3.1 Muon Cylinder Cuts

In order to apply a cut around the muon track to either eliminate spallation backgrounds or, as in the case of ^{11}Be, to enhance the signal to noise in a sample of spallation candidates, an efficiency and a corresponding systematic uncertainty needs to be calculated. The efficiency of a cylinder cut around the muon track is studied using the short-lived spallation products that were also used to study the fiducial volume in Section 6.6.2. The efficiency is determined by the number of spallation candidates within the cylinder divided by the total number of spallation candidates. The spallation products are selected based on their time since the preceding muon, $2\,\mathrm{ms} < \Delta t_\mu < 202\,\mathrm{ms}$, and their reconstructed energy, 5-20 MeV. A longer time window after the signal window, $202\,\mathrm{ms} < \Delta t_\mu < 1.202\,\mathrm{ms}$, samples the background. Histograms of the candidates' closest distance from the muon track are constructed for the spallation candidates and background. The background histogram is then multiplied by the ratio of the time windows and subtracted from the signal histogram. The background subtracted histograms are shown in Fig. 8.2 for two different fiducial volumes, a sphere of radius 5.5 m and a sphere of radius 3.0 m. The muons included were required to have passed through the liquid scintillator (LS muons).

The efficiency of the muon cylinder cut should be independent of the fiducial volume chosen, easily verified using the toy Monte Carlo described in Section 6.5. As is shown in Fig. 8.2, this is not the case for muon tracks with "usable" reconstruction. Eliminating the so-called "usable" tracks, those with marginal χ^2, and selecting the better defined "valid" muon, the unphysical excess of events with muon track distances greater than 3 m is diminished. This excess is apparently the result of events being incorrectly reconstructed on the edge of the balloon. An additional cut on the muon track impact parameter, $b_\mu < 6.45$ m, improves the variation of the efficiency with fiducial volume. This is especially important for the low-light-level non-shower muons. The additional cut on the muon track impact parameter reduces the variation by a factor of ~ 2.

Using the more stringent muon track requirement of "valid" reconstruction and $b_\mu < 6.45$ m, the efficiency of three muon cylinder track cuts with radius 1 m, 2 m, and 3 m are determined and summarized in Table 8.3 along with the statistical uncertainties. The
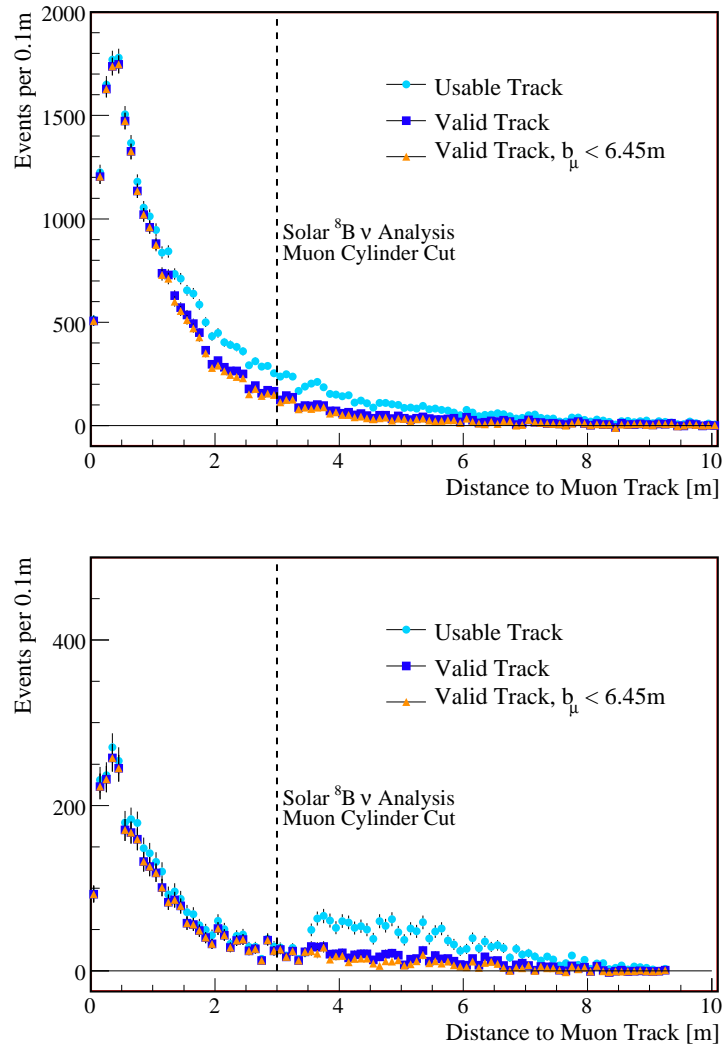
Figure 8.2: Short lived spallation products following muons that pass through the liquid scintillator plotted versus their distance to the preceding muon tracks. Two different fiducial volumes are shown: (top) sphere with 5.5m radius, (bottom) sphere with 3.0 m radius. Tracks that are mistakenly reconstructed on the balloon lead to an excess of events beyond 3 m. Eliminating tracks with marginal χ^2, the so-called "usable" tracks, reduces this effect.

Table 8.4: Systematic uncertainties of muon cylinder cut for all muons that pass through the liquid scintillator, LS muons, with "valid" reconstruction and impact parameters less than 6.45m

	LS Muons			Non-Shower Muons			Shower Muons		
Source	1m	2m	3m	1m	2m	3m	1m	2m	3m
Fiducial Volume	0.022	0.031	0.026	0.017	0.025	0.022	0.019	0.029	0.025
Energy	0.010	0.007	0.006	0.057	0.039	0.023	0.008	0.004	0.003
Time	0.014	0.014	0.011	0.083	0.055	0.049	0.015	0.013	0.009
Total	0.028	0.035	0.029	0.102	0.072	0.058	0.025	0.032	0.027

high-light-level showering muons produce most of the spallation products. Muon spallation creates showers of particles so the muon cylinder cut as a veto is less efficient for the shower muons. The relative effect on isotope production of shower and non-shower muons will be investigated in the following analyses.

The systematic uncertainty for the cylinder cut is difficult to assess as a calibrated source of muons is not available to KamLAND. The systematic uncertainty for the muon cylinder cut is estimated by examining the three most likely systematic effects associated with fiducial volume choice, energy reconstruction errors in the decay of the spallation product, and variations in the detector over time. For the variation with fiducial volume, the efficiency was evaluated for spherical fiducial volumes with radii between 3 m and 6.5 m in 0.5 m increments. The uncertainty is taken as the standard deviation of the distribution. The procedure was repeated for a cylindrical fiducial volume; the results were consistent. The systematic uncertainty due to energy reconstruction was determined by breaking the candidates into 7 energy bins, 5-6 MeV, 6-7 MeV, 7-8 MeV, 8-9 MeV, 9-10 MeV, 10-12 MeV, 12-20 MeV, with roughly equal statistics. Once again the systematic uncertainty was taken to be the standard deviation of the distribution. Finally, the data set was divided into 15 run periods of 100 days each to assess any systematic due to the detector response changes in time.

The results are summarized for LS muons, non-shower LS muons and shower LS Muons in Table 8.4. The determination of uncertainties in the decay energy of the spallation product and time variations are limited by statistics, especially for the non-showering muons. The uncertainty in the choice of fiducial volume reflects a trend towards smaller efficiencies at smaller fiducial volumes. This is consistent with systematic effects in the muon reconstruction presented in Section 6.5. One additional source of systematic uncertainty is physical differences in the production mechanism between different isotopes and primary particles. This was addressed in Section 7.5 with FLUKA. Differences of up to 30% depending on the radius of the muon cylinder cut and the particular isotope are possible. This uncertainty must be determined for each isotope for each analysis separately.

Table 8.5: Efficiencies and systematic uncertainties calculated for ^{11}Be analyses with muon cylinder cuts. The efficiency for "valid" and $b_\mu < 6.45\,$m is included in the other analyses.

Analysis	LS Muons		Non-Shower Muons		Shower Muons	
	Eff.	Syst.	Eff.	Syst.	Eff.	Syst.
"valid" and $b_\mu < 6.45$m	0.839	2.51%	0.839	2.51%	0.844	2.51%
$dR_\mu < 1\,$m	0.515	3.76%	0.645	10.50%	0.502	3.54%
$dR_\mu < 2\,$m	0.702	4.31%	0.767	7.63%	0.698	4.07%
$dR_\mu < 3\,$m	0.772	3.84%	0.811	6.32%	0.772	3.69%

8.3.2 ^{11}Be Production

The analysis of ^{11}Be with muon cylinder cuts is identical to the previous analysis except some ^{11}Be candidate pairs are eliminated by the muon cylinder cut. The common efficiencies summarized in Table 8.1 apply. In order to apply the cylinder, the track has a "valid" reconstruction and an impact parameter, $b_\mu < 6.45\,$m. From Section 6.5, 84.0% of LS muons survive this cut. The showering muons have slightly higher efficiency, 84.5%.

The background from events uncorrelated to the muon is reduced by requiring a smaller cylinder cut. Unfortunately, a smaller cylinder cut eliminates ^{11}Be from the sample. The analysis is done with several different cylinder radii, 1m, 2m, and 3m, to determine which cut produces the best signal to noise. The efficiency for each of these cuts is shown in Table 8.3 and the uncertainties in Table 8.4. The efficiencies are calculated with short-lived spallation candidates, mostly ^{12}B. The FLUKA studies in Section 7.5 show that the muon track spatial correlation for ^{11}Be and ^{12}B is similar, and the systematic uncertainty from their different production processes is ignored. The total efficiencies for the analyses using $1\,$m, $2\,$m, and $3\,$m cylinder cuts are summarized in rows two through four of Table 8.5.

The results of these analyses for LS muons are shown in Fig. 8.3. The background reduction is clearly seen, and leads to a reduction in the uncertainty. The procedure is repeated for the shower muons and the non-shower muons and summarized in Table 8.3 . The results are consistent for each type of muon, and the statistical uncertainties dominate the uncertainty. The rate of ^{11}Be production from non-shower muons is consistent with zero. The shower muons' seem to produce all of the ^{11}Be even though only 20% of the muon rate is from shower muons. This is an interesting feature which is observed in the other spallation products as well.

8.4 ^{8}Li and ^{8}B Production

The next group of spallation isotopes have half-lives around $\sim$800ms, ^{8}B, ^{6}He, and ^{8}Li. Only ^{8}B and ^{8}Li have endpoints above 5 MeV. A fit using only time information does not resolve ^{8}Li decay from ^{8}B since their half-lives are so similar, 0.84s and 0.77s respectively. Adding decay energy can help resolve the two isotopes since ^{8}B is a β^+ decay with an endpoint of 17.97 MeV, $\sim$2 MeV higher than the β^- decay of ^{8}Li. The ^{8}B decay
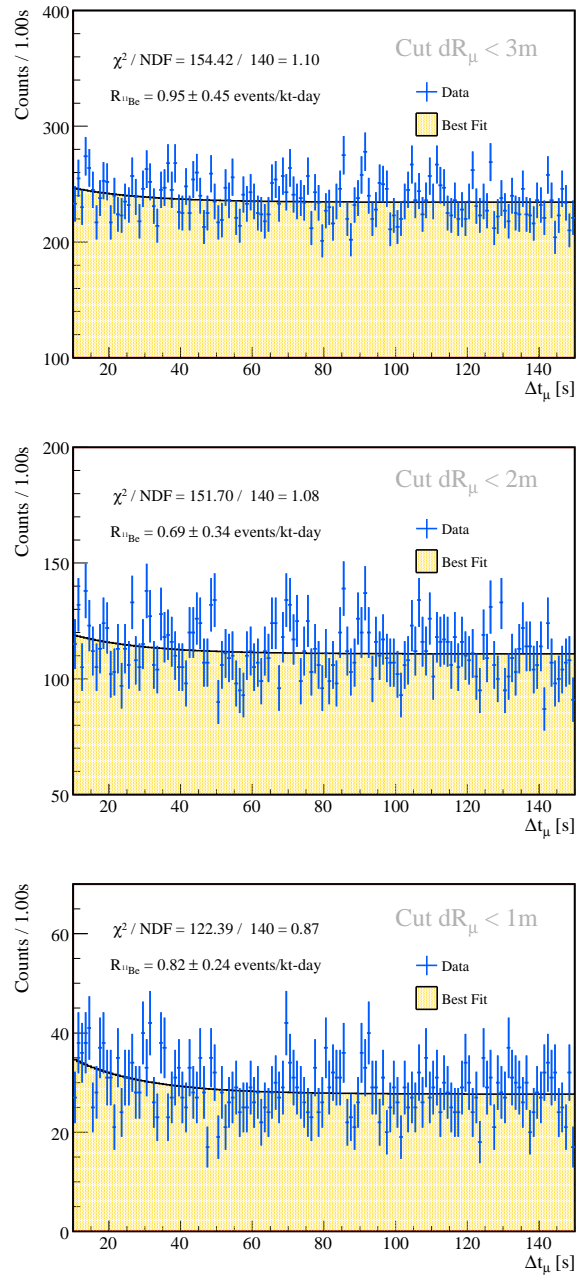
Figure 8.3: ^{11}Be spallation candidates plotted relative to their time difference to all preceding muons within $150\,\mathrm{s}$ and within $3\,\mathrm{m}$ (top), $2\,\mathrm{m}$ (middle), $1\,\mathrm{m}$ (bottom) of the muon track. The uncertainty in the fitted production rate of ^{11}Be is reduced by excluding uncorrelated muon event pairs with this cylinder cut about the muon track.

Table 8.6: Result of analyses of ^{11}Be production in units of number per kiloton-day exposure.

	LS Muons	Non-Shower	Shower
	Events per kt-day		
No Muon Cut	0.99 ± 0.88	0.11 ± 0.79	0.86 ± 0.38
"valid" and $b_\mu < 6.45$	0.71 ± 0.95	0.10 ± 0.86	0.60 ± 0.40
$dR_\mu < 1\,m$	0.82 ± 0.24	0.16 ± 0.16	0.63 ± 0.14
$dR_\mu < 2\,m$	0.69 ± 0.34	0.06 ± 0.27	0.63 ± 0.17
$dR_\mu < 3\,m$	0.95 ± 0.45	0.33 ± 0.36	0.60 ± 0.22

Table 8.7: Efficiencies and systematic uncertainties for ^{8}Li and ^{8}B analysis

Source	Eff.	Syst.
Common	0.999	2.51%
Isolated Muon for 4.75s	0.378	1.79%
Total	0.377	3.08%

reconstructs an additional 1.22 MeV higher because of positron annihilation gamma-rays.

A cut on the time between muon events is used to prevent a single spallation candidate from being added to the energy histograms multiple times, preserving Poisson statistics in the histograms. Muons used in this analysis cannot occur within 4.75s of each other. The time window used is $0.75\,s < \Delta t_\mu < 4.75\,s$. The starting time is chosen to eliminate shorter-lived spallation products, while the stopping time is determined by the cut on the time between muons. A longer cut on the time between muons eliminates too many muons. The spallation candidates from the first half of the time window, $0.75\,s < \Delta t_\mu < 2.75\,s$, are used to fill the "signal" energy histogram, and those from the second half, $2.75\,s < \Delta t_\mu < 4.75\,s$, for the "background" energy histogram.

A 5.5 m spherical fiducial volume is used and the common efficiencies from Table 8.1 apply. There are no cuts applied to the muon reconstruction or distance to muon track. The efficiency of the 4.75 s cut on the time between muons is determined by the LS muon rate, $R_\mu = 0.205 \pm 0.01\,$Hz from Table 7.2. The probability of getting muons separated by a time greater than Δt is $P_\mu = e^{-R_\mu \Delta t}$. Therefore, the efficiency of this cut is 0.377. The uncertainty is calculated by varying the muon rate by its quoted uncertainty of 0.01 Hz. The total efficiency and systematic uncertainty in percent is summarized in Table 8.7.

The reconstructed energy of the candidates can be as high as 20 MeV with detector resolution if there is a significant contribution from ^{8}B. Preliminary analysis of the energy spectra showed that the statics were too low above 16 MeV to improve the fit. The low energy threshold is 5 MeV as with ^{11}Be due to the high uncorrelated background below this energy. The reconstructed energy window is then 5-16 MeV. The resulting histogram time after an isolated muons is shown in Fig. 8.4, and the corresponding decay energy histograms in Fig. 8.6. From the simultaneous fits to these histograms, the production rate
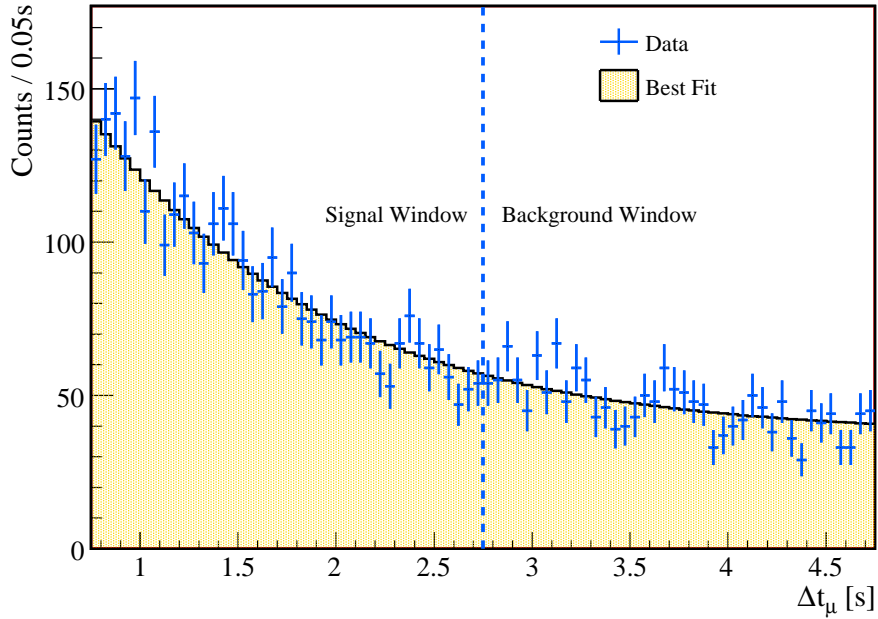
Figure 8.4: The ^{8}Li and ^{8}B spallation candidates plotted relative to their time difference to all preceding muons isolated from each other by 4.75s.

of ^{8}Li is 19.72±1.56 per kt-day while ^{8}B is 1.90±1.16 per kt-day. ^{11}Be is a background in the analysis and was included with a penalty function constrained to the value from the dR$_\mu$ < 1m analysis in Section 8.3.2. There are 11 parameters, $\hat{b}_i$, to account for the unknown shape of the uncorrelated background. The shape of the ^{8}Li and ^{8}B are extracted from the data by subtracting the $\hat{b}_i$ parameters from the data. This is shown in Fig. 8.6 and indicates that the dominant component of the spectrum is from ^{8}Li not ^{8}B.

The uncertainties quoted so far for the fitted parameters are the fitting uncertainties returned by Minuit[102]. To understand the correlations between the determined parameters, a $\Delta\chi^2$ is constructed. A $\Delta\chi^2$ of 2.30, 6.18, 11.83 correspond to 1σ, 2σ, and 3σ for 2 parameters [132]. The $\Delta\chi^2$ contours for the production for ^{8}Li and ^{8}B are plotted in Fig. 8.7. This map was made by fixing values of ^{8}Li and ^{8}B and allowing the remaining parameters to converge to a best-fit value. The difference of this χ^2 and the best-fit χ^2 was tabulated. This analysis indicates that the absence of ^{8}B is ruled out at 1σ, the 68.27% confidence level. An anti-correlation between the determined ^{8}Li and ^{8}B production is evident in Fig. 8.7.

The production of ^{8}Li and ^{8}B is also examined independently for shower and non-shower muons. The ^{11}Be production was constrained to the dR$_\mu$ < 1m value as discussed in Section 8.3.2. The results are summarized in Table 8.8. As with ^{11}Be, the showering muons, though less numerous, are responsible for essentially all of the ^{8}Li and ^{8}B production.
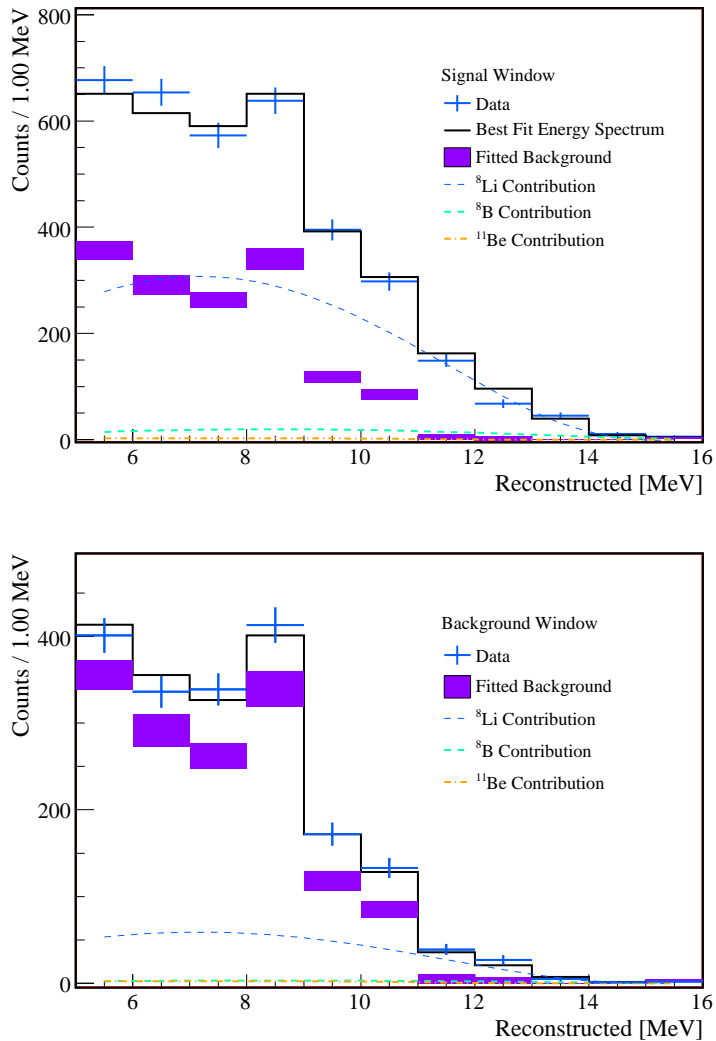
Figure 8.5: The energy spectrum of ^{8}Li and ^{8}B spallation candidates: the "signal" window (Top) and the "background" window (Bottom).
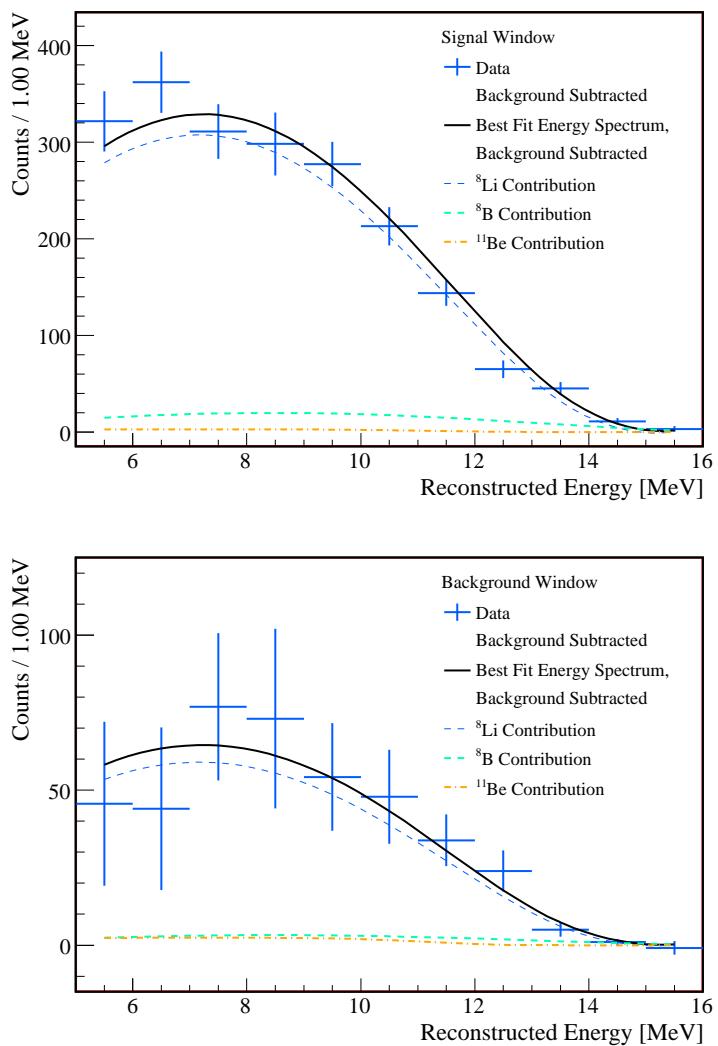
Figure 8.6: The energy spectrum of ^{8}Li and ^{8}B spallation candidates with the best fit background subtracted from the data: the "signal" window (Top) and the "background" window (Bottom).
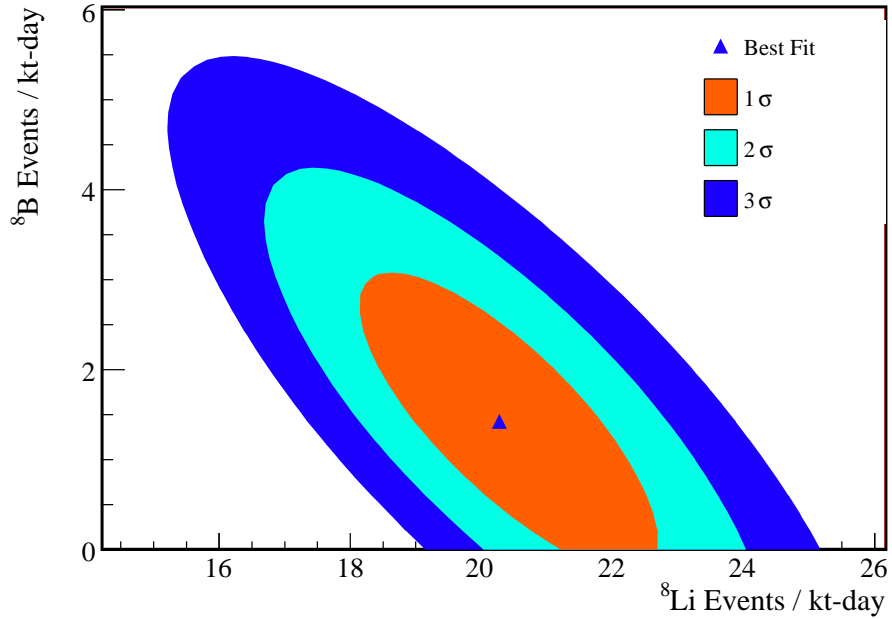
Figure 8.7: The $\Delta\chi^2$ contour map of the fit for ^{8}Li and ^{8}B production. An anti-correlation between the determined ^{8}Li and ^{8}B production is evident.

Table 8.8: The summary of the production of ^{8}Li and ^{8}B from LS Muons, Non-Showering and Showering muons.

Isotope	All LS Muons	Non-Shower	Shower Muons
	Events per kt-day		
^{8}Li	20.27 ± 1.32	0.66 ± 0.36	19.77 ± 1.13
^{8}B	1.43 ± 0.82	0.000 ± 0.004	1.09 ± 0.83
^{11}Be	0.82 ± 0.24	0.16 ± 0.16	0.62 ± 0.14
χ^2/N.D.F	0.95	0.78	1.16

8.5   Delayed Neutron Decays of ^{9}Li and ^{8}He

The decays of ^{9}Li and ^{8}He have significant branches to states that can decay with neutron emission. The sum of these delayed branches is $50.8 \pm 0.9\%$ for ^{9}Li and $16 \pm 1\%$ ^{8}He[133]. Neutrons emitted from ^{9}Li and ^{8}He decay can capture on protons producing $2.22\,$MeV gamma-rays. The triple coincidence of muon, beta decay, and neutron capture gamma ray reduces backgrounds for the measurements of ^{9}Li and ^{8}He production. Beta decay delayed neutron emission makes these two isotopes a serious backgrounds that mimics inverse beta decay exploited for anti-neutrinos detection. KamLAND's reactor anti-neutrino analysis was discussed in Section 3.6.

8.5.1   Neutron Coincidence Selection

The neutron can be used to select the ^{9}Li and ^{8}He. In order to exploit the triple coincidence of muon, beta decay, and neutron, the efficiency for detecting neutrons must be known. In this discussion, the beta decay electron produces the prompt event, and the neutron capture the delayed event. In KamLAND, neutrons typically capture on proton's emitting a $2.22\,$MeV gamma ray, ^{1}H(n, γ)^{2}H. In 0.53% of the cases the neutron captures on ^{12}C producing a $4.95\,$MeV gamma-ray. The probability of neutron capture on any other isotopes is negligible. To select the delayed events from ^{1}H(n, γ)^{2}H a cut on the reconstructed energy of the delayed event is applied, $2.04 < E_d < 2.82$. The efficiency of the cut is determined with an AmBe neutron source and spallation neutrons to be 0.997 ± 0.002.

Neutron capture events that are in delayed coincidence with a prompt electron event are identified by their proximity in time and space to the prompt event. The mean neutron capture time in KamLAND is $207.5 \pm 2.8\,\mu$s. A cut of $0.5\,\mu\text{s} < \Delta t < 660\,\mu$s is applied and includes $95.60 \pm 0.18\%$ of all delayed neutron capture events. The efficiency for constraining coincidences in space is extracted from a combination of neutron data from the AmBe source and the annihilation gammas from a ^{68}Ge source. The reconstructed event distributions for these sources in three dimensions are used to determine the distribution of distances between the prompt event and the neutron capture, the ΔR distribution. The result in Fig. 8.8, show that a cut at $\Delta R < 1.6\,$m includes 99.1% of events. The neutron energy spectrum from the AmBe source is not identical to other sources like ^{9}Li decay. By examining the results of a convolution of the ^{68}Ge annihilation gamma-ray data with itself, a systematic uncertainty of 0.5% is assigned to the cut because of the differences in the neutron energy spectrum.

In this analysis the position of the delayed event is required to be within the same fiducial volume as the prompt event. The fiducial volume is a 5.5m sphere, $R_p < 5.5\,$m. To assess the efficiency of the pair of cuts, prompt events are simulated throughout a 5.5 m sphere and delayed events are generated using the ΔR distributions determined above. The requirement that the delayed event occurs within the fiducial volume, $R_d < 5.5\,$m, includes 93.4% of the events. As noted above the comparison between the ΔR distribution calculated with AmBe data and ^{68}Ge is used to assess the systematic uncertainty which is found to be 1.3%.
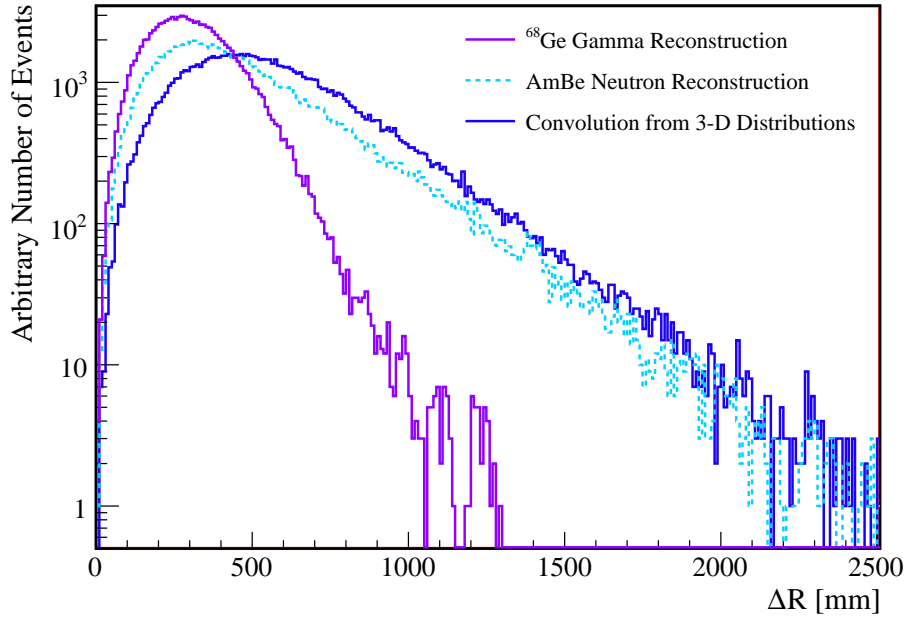
Figure 8.8: The distribution of distances between an event and a delayed neutron capture, ΔR. Calculated by convolving the reconstructed positions of an AmBe and ^{68}Ge source positioned at the center of KamLAND.

Table 8.9: Delayed neutron detection efficiencies.

Cut	Efficiency	Systematic Error
$^1\text{H(n, }\gamma)^2\text{H}$	0.995	0.1%
$2.04 < E_d < 2.82$	0.997	0.2%
$0.5\mu\text{s} < \Delta t < 660\mu\text{s}$	0.956	0.18%
$\Delta R < 1.6\text{m}$	0.991	0.5%
Total	0.940	0.6%
$R_p < 5.5\text{m}, R_d < 5.5m$	0.934	1.3%
Total	0.878	1.4%

Table 8.10: The efficiencies and systematic uncertainties for the analysis of the delayed neutron branches of ^{9}Li and ^{8}He.

Source	Eff.	Syst.
Common	0.999	2.51%
Isolated Muon for 1.5s	0.735	1.1%
Neutron Cut with $R_d < 5.5$m	0.878	1.40%
Neutron Branch	-	1.0%
Total	0.645	3.24%

8.5.2 ^{9}Li and ^{8}He Production

The analysis of the production of β-delayed neutron emitters ^{9}Li and ^{8}He uses the same data set and $R <5.5$ m spherical fiducial volume from the analysis of the longer-lived isotopes. Therefore this analysis shares these systematic uncertainties. The half-life of ^{9}Li is 180 ms while the half-life of ^{8}He is 120 ms. A time window of 1.5 s is chosen for the analysis. This length of time samples the exponential decay of the isotopes and adequately samples the uncorrelated background. For the energy analysis the "signal" window is from 0.002-0.752 s and the "background" window is 0.752-1.502 s. An isolated muon cut of no less than 1.5 s between muons is used.

The key cut to this analysis is a neutron coincidence cut that can identify ^{9}Li and ^{8}He decays. The cuts used to identify the delayed neutron from these decays were outlined in Table 8.9. Due to the size of the fiducial volume, a cut on the position of the neutron capture is required, $R_d < 5.5$ m. The total efficiency is 0.645 with a systematic uncertainty of 3.08%, see Table 8.10. Some previous KamLAND analyses using a delayed coincidence signal use the average position of the prompt-delayed pair of events as it eliminates the uncertainty due to the R_d cut. Since the systematic uncertainty is dominated by the uncertainty on the fiducial volume, the contribution from the R_d cut is not very significant here.

The neutron coincidence is very effective at identifying potential background events uncorrelated to muons allowing for a lower reconstructed energy threshold of 3 MeV. The maximum endpoint of ^{9}Li is 13.6 MeV while the branches to neutrons have lower endpoints. The statistics are limited above 13 MeV in reconstructed energy, which is the maximum energy used in the analysis. With these final cuts, the histograms are constructed and fit. The result is shown in Fig. 8.9 and the energy spectra are shown in Fig. 8.10. The energy spectra with the fitted background component subtracted are shown in Fig. 8.11. The corresponding production is 2.57 ± 0.16 per kt-day of ^{9}Li and 0.48 ± 0.42 per kt-day of ^{8}He, Table 8.11. The dominance of ^{9}Li production over ^{8}He is clear in the energy spectra. The data is much more consistent with the endpoint of ^{9}Li than ^{8}He.

As with ^{8}Li and ^{8}B, it is useful to examine in more detail at the correlation between the production of ^{9}Li and ^{8}He. A $\Delta\chi^2$ map for the production of ^{9}Li versus ^{8}He is constructed as it was for ^{8}Li and ^{8}B. The result is shown in Fig. 8.12. An anti-correlation between ^{9}Li and ^{8}He production is evident. ^{8}He production cannot be confirmed at more than 1σ.
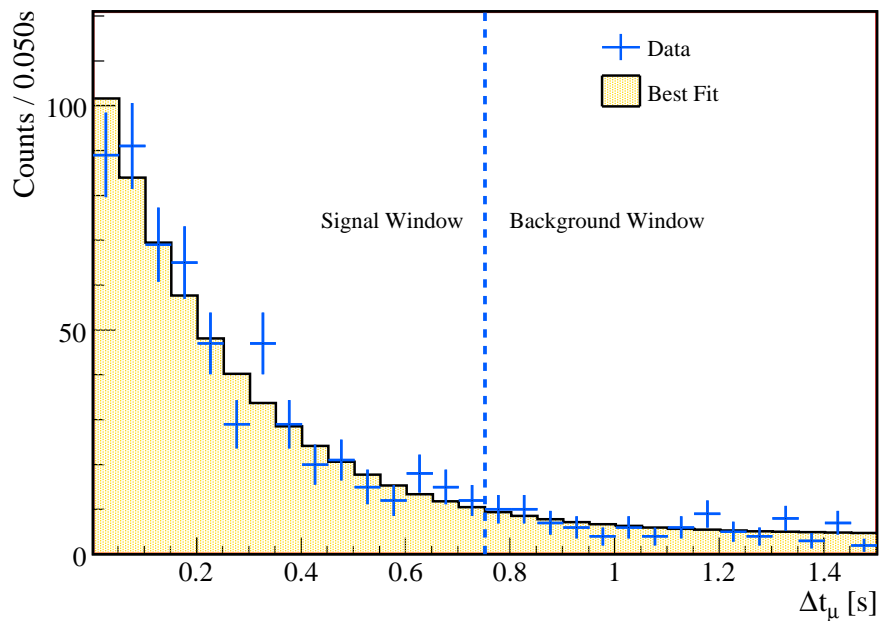
Figure 8.9: The ^{9}Li and ^{8}He spallation candidates plotted relative to their time difference to all preceding muons that are isolated from each other by 1.5s.
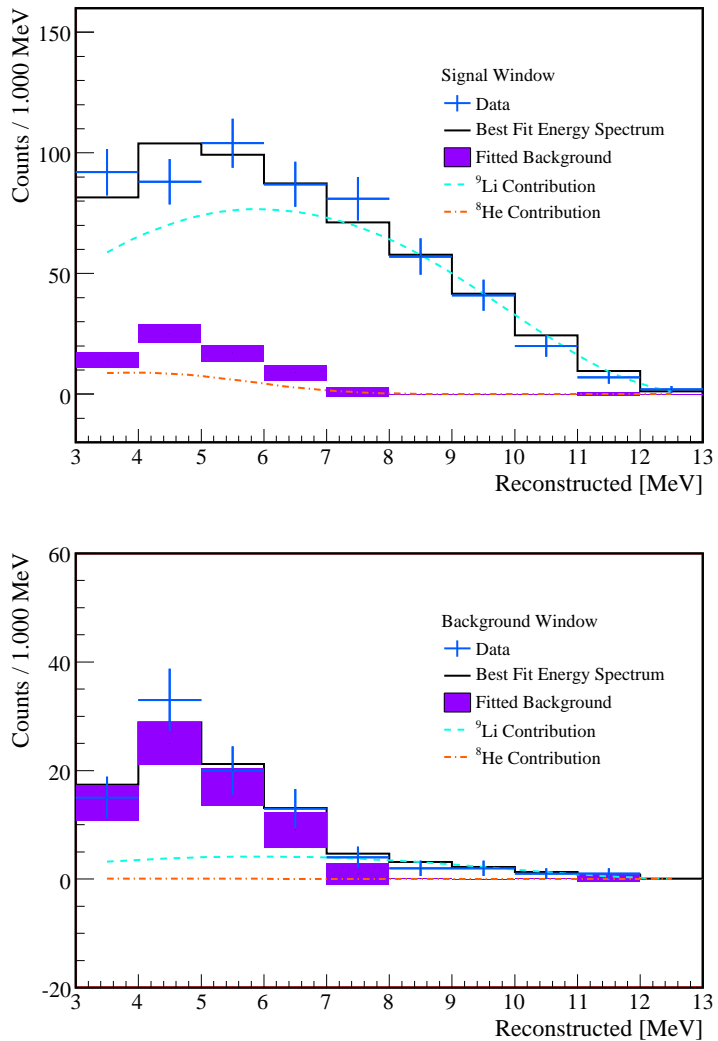
Figure 8.10: The energy spectrum of ^{9}Li and ^{8}He spallation candidates: the "signal" window (Top) and the "background" window (Bottom).
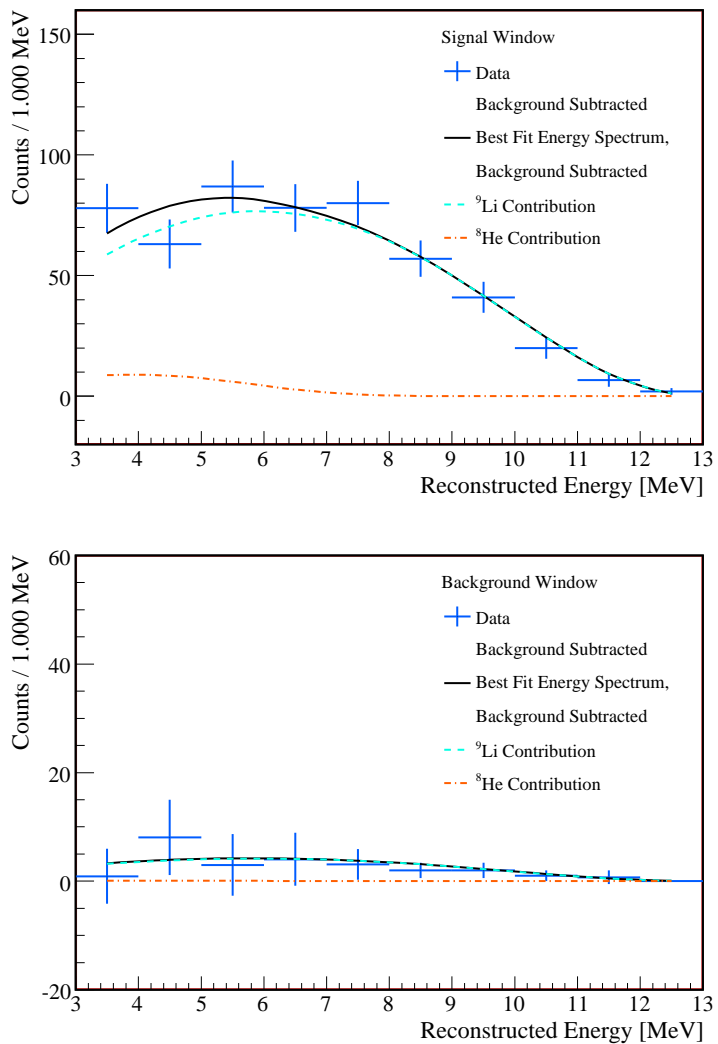
Figure 8.11: The energy spectrum of ^{9}Li and ^{8}He spallation candidates with the best fit background subtracted from the data: the "signal" window (Top) and the "background" window (Bottom).
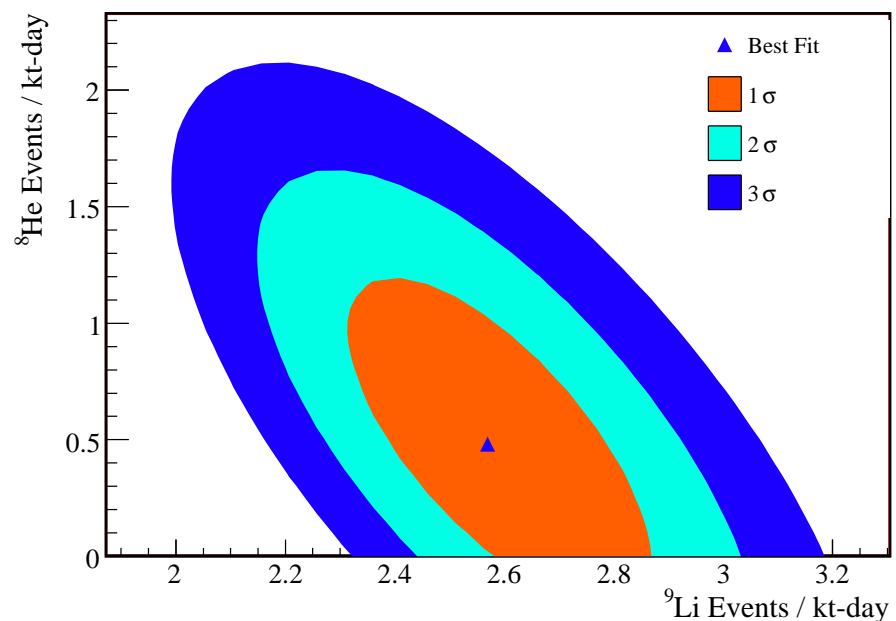
Figure 8.12: The $\Delta\chi^2$ contours for the fit of ^{9}Li and ^{8}He production following muons that pass through the liquid scintillator.

Table 8.11: The analysis ^{9}Li and ^{8}He production summarized for all LS muons and the low-light-level, non-showering muons , and the high-light-level showering muons.

Isotope	All LS Muons	Non-Shower	Shower Muons
	Events per kt-day		
^{9}Li	2.57 ± 0.16	0.11 ± 0.04	2.49 ± 0.16
^{8}He	0.48 ± 0.42	0.04 ± 0.14	0.50 ± 0.39
χ^2/N.D.F	0.70	1.00	0.69

Table 8.12: Efficiencies and systematics for ^{12}B, ^{12}N, and ^9C analysis

Source	Eff.	Syst.
Common	0.999	2.51%
Isolated Muon for 0.402s	0.921	0.37%
Total	0.920	2.54%

The analysis of ^{9}Li and ^{8}He was repeated for both showering and non-showering muons, Table 8.11. As was seen in ^{8}Li and ^{8}B less than 5% of the isotope production can be attributed to the low-light-level muons that account for most of the muon flux. This is an interesting conclusion that can also guide the muons spallation cuts that are needed in neutrino and anti-neutrino analyses.

8.6 ^{12}B, ^{12}N, and ^{9}C Production

The final group of isotopes have half-lives shorter than 200 ms. The isotopes ^{11}Li and ^{13}B are not considered since their production was estimated to be negligible compared to ^{12}N, ^{12}B, ^{8}He, ^{9}C, and ^{9}Li. The amount of ^{9}Li and ^{8}He was extracted using delayed neutron branches, so in the present analysis they are constrained within their errors. The time window for the analysis was chosen to be 0.002-0.402 s as a compromise between the half-lives of the isotopes being studied. The minimum time of 0.002 s was chosen to eliminate the spallation neutrons that are the most common products of muons in KamLAND. The "signal" window for the energy analysis is then 0.002-0.202 s and the "background" window is 0.202-0.402 s. As usual a 0.402 s time between muon cut is also applied. The total efficiency and systematic uncertainty from these and the standard cuts in Section 8.1 are summarized in Table 8.12.

The small muon coincidence window of 0.402 s reduces events uncorrelated to muons, allowing a slightly lower reconstructed energy threshold of 4 MeV. The highest beta endpoint is from ^{12}N at 17.4 MeV. The statistics are not sufficient above 17 MeV in reconstructed energy, so the upper energy limit is set at 17 MeV. Using these cuts, the histograms are constructed and fit. The time spectrum is shown in Fig. 8.13 and the energy
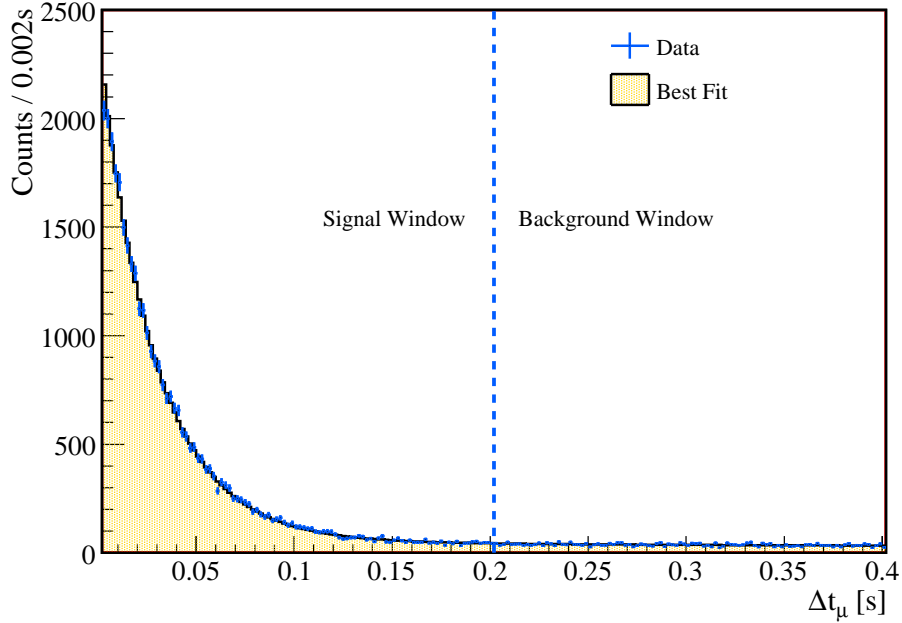
Figure 8.13: The ^{12}B, ^{12}N, and ^{9}C spallation candidates plotted relative to their time difference to muons in the preceding 0.402s. The inset highlights the first 40 ms.

spectra in Fig. 8.14 and in Fig. 8.15 with the best fit background subtracted. The most abundant isotope is ^{12}B at 54.27 $\pm$ 0.49 kt-day. The others are less than 5 per kt-day, see Table 8.13. This is expected as the most likely production mechanism is ^{12}C(n, p)^{12}B with a sizable cross section and a neutron energy threshold of only 12.587 MeV[134].

There are two sets of isotopes where correlations in the fit are examined in more detail, ^{12}B with ^{12}N and ^{9}C with ^{12}N. An anti-correlation is expect in the fit of ^{12}B and ^{12}N because their half-lives are separated by less than 10 ms. An anti-correlation is also expected between the two isotopes with the highest endpoints, ^{9}C and ^{12}N. The $\Delta\chi^2$ maps are constructed for these parameters. As is seen in Fig. 8.16 no strong correlation is seen for either pair of isotopes.

Once again the analysis was repeated for shower and non-shower muons. The results are summarized in Table 8.13. The isotopes ^{12}N and ^{9}C both show $\geq$95% of their production from the high-light-level shower muons while very little is produced from the much more abundant non-shower muons. The isotope ^{12}B shows the largest production from non-shower muons of those in these studies at $\sim$10% being produced by this type of muon.
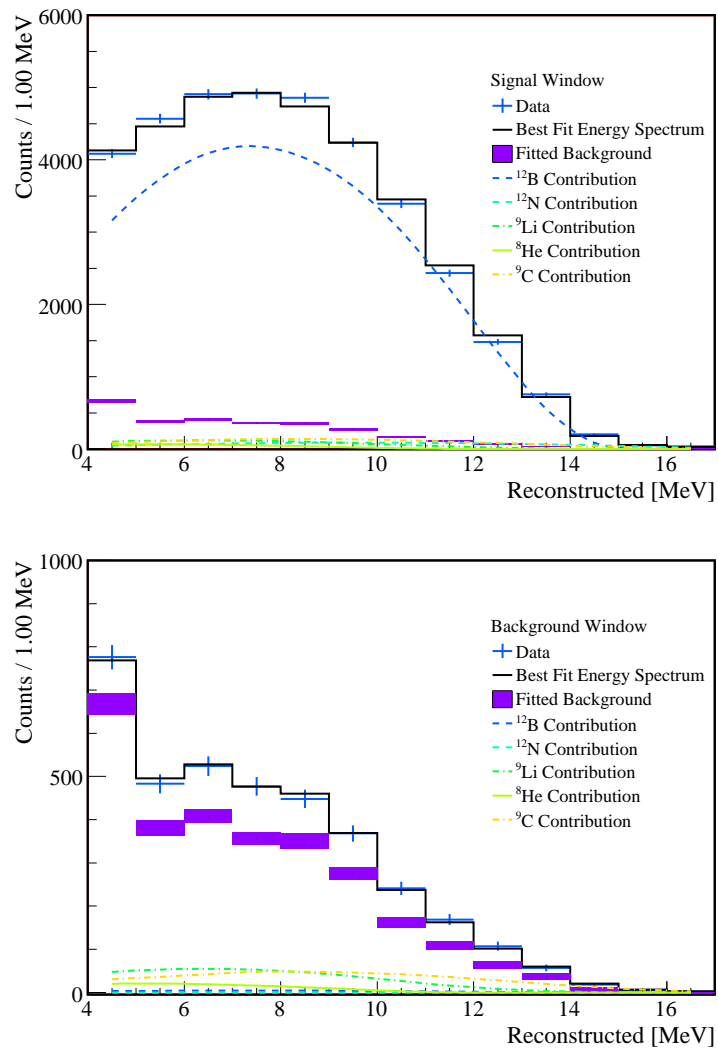
Figure 8.14: The energy spectrum of ^{12}B, ^{12}N, and ^{9}C spallation candidates: the "signal" window (Top) and the "background" window (Bottom).
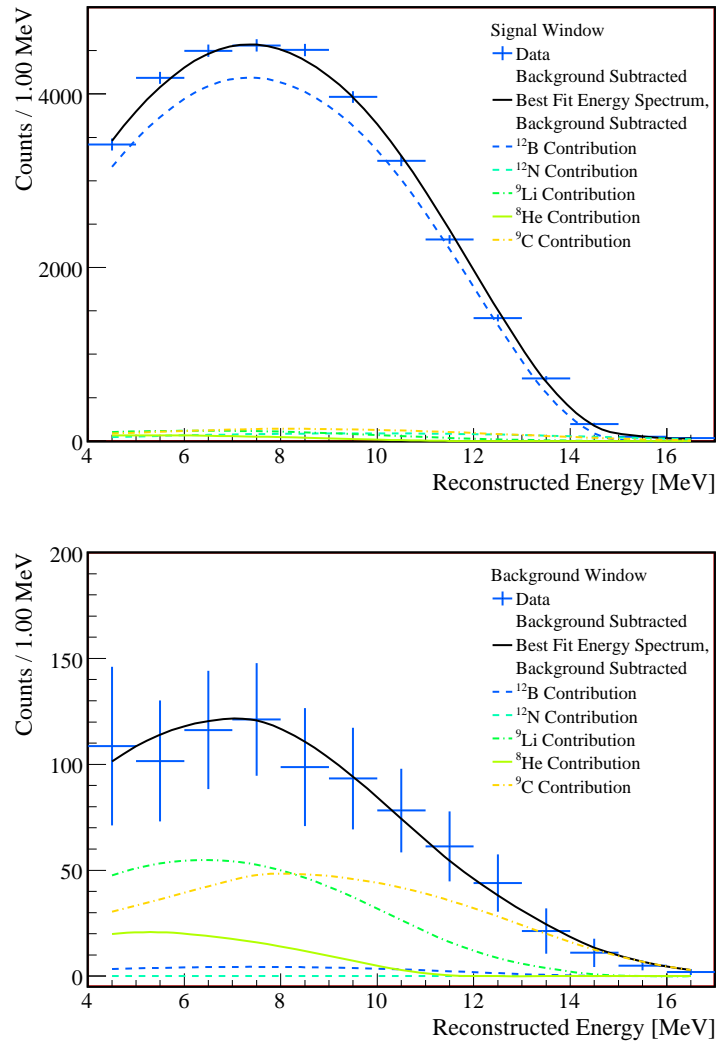
Figure 8.15: The energy spectrum of ^{12}B, ^{12}N, and ^{9}C spallation candidates with the best fit background subtracted from the data: the "signal" window (Top) and the "background" window (Bottom).
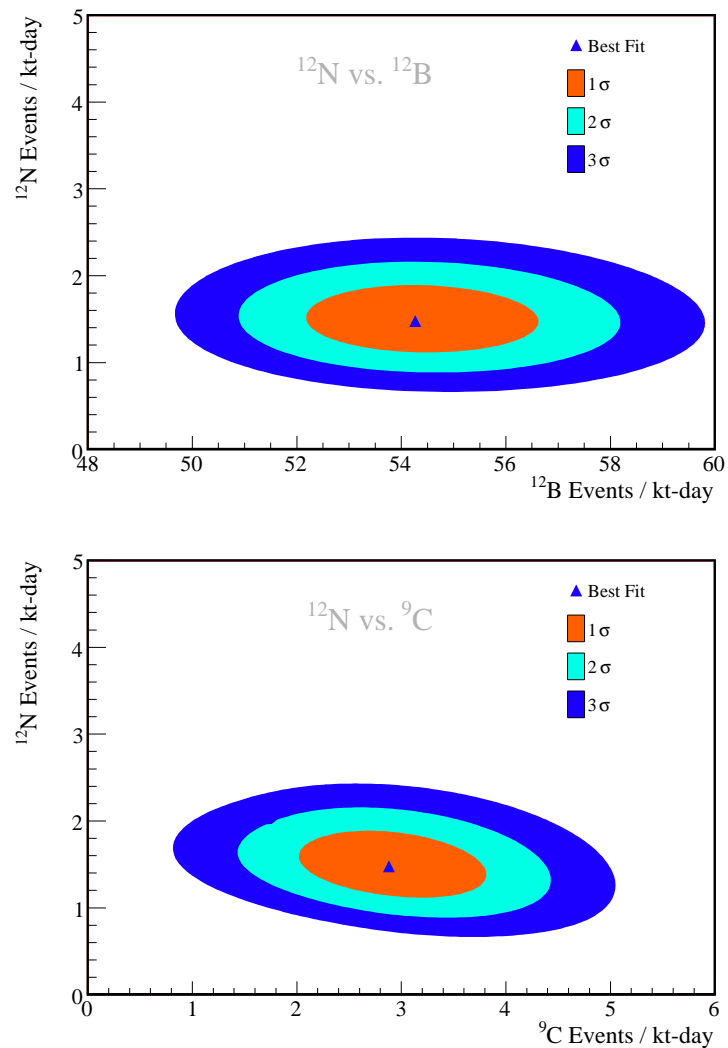
Figure 8.16: The $\Delta\chi^2$ contours from the fit to isotopes with half-lives less than 200ms: ^{12}N versus ^{12}B (Top) and ^{12}N versus ^{9}C (Bottom).

Table 8.13: The production of ^{12}B, ^{12}N, and ^{9}C. The three analyses for all LS muons, Non-shower and shower muons are performed independently.

Isotope	All LS Muons	Non-Shower	Shower Muons
	Events per kt-day		
^{12}B	54.27 ± 0.49	5.99 ± 0.17	48.24 ± 1.28
^{12}N	1.48 ± 0.24	0.08 ± 0.06	1.36 ± 0.22
^{9}C	2.88 ± 0.55	0.01 ± 0.26	2.58 ± 0.54
^{9}Li	2.60 ± 0.15	0.11 ± 0.04	2.53 ± 0.16
^{8}He	0.87 ± 0.37	0.14 ± 0.12	0.91 ± 0.34
χ^2/N.D.F	0.94	1.09	0.96

Table 8.14: Summary of spallation isotope results. The NA54 values for ^{9}Li and ^{8}He are the sum of ^{9}Li+^{8}He[130], they are indicated with parentheses.

Isotope	NA54 Experiment	FLUKA Simulation	KamLAND Analysis
	N per $\times 10^{-7}\mu$ g/cm^2		
^{12}B	-	28.47 ± 1.82	40.67 ± 2.02
^{8}Li	2.00 ± 0.74	21.36 ± 1.38	15.19 ± 1.23
^{8}B	3.54 ± 0.76	5.72 ± 0.40	1.07 ± 0.62
^{9}Li	(1.05 ± 0.19)	2.68 ± 0.21	1.93 ± 0.15
^{9}C	2.40 ± 0.77	1.31 ± 0.12	2.16 ± 0.42
^{12}N	-	0.86 ± 0.09	1.11 ± 0.19
^{11}Be	< 1.16	0.68 ± 0.08	0.61 ± 0.19
^{8}He	(1.05 ± 0.19)	0.22 ± 0.04	0.36 ± 0.31

8.7 Summary Spallation Analysis

In the preceding sections the production of short lived isotopes with beta decay endpoints above 5 MeV is studied using data from KamLAND. The natural unit for Kam-LAND data analysis is the number produced per kt-day while the unit that is useful for comparing experiments and simulations in the number produced per muon per g/cm^2 of material. The muon rate through the liquid scintillator is 5.56±0.27 muons per m^{2}h from Section 7.1. The KamLAND results are summarized in Table 8.14. The predictions for KamLAND from the experiment NA54 and from FLUKA as obtained for Table 7.9 are included for comparison.

The Borexino experiment is a competing experiment looking to measure the flux of solar neutrinos with a threshold of 0.2 MeV. Like KamLAND it has a roughly spherical balloon filled with liquid scintillator. It is located in the underground lab at Gran Sasso. The overburden is 3600 m.w.e which reduces the muon flux to 1.16 ± 0.08 muons per m^{2}h

Table 8.15: Prediction for the production of light isotopes at the deeper Borexino site from scaling the KamLAND results.

Isotope	KamLAND Result	Prediction for Borexino
	N per kt-day	
^{12}B	54.27 ± 0.49	13.58 ± 1.25
^{8}Li	20.27 ± 1.32	5.07 ± 0.57
^{8}B	1.43 ± 0.82	0.36 ± 0.21
^{9}Li	2.57 ± 0.16	0.64 ± 0.07
^{9}C	2.88 ± 0.55	0.72 ± 0.15
^{12}N	1.48 ± 0.24	0.37 ± 0.07
^{11}Be	0.82 ± 0.24	0.20 ± 0.06
^{8}He	0.48 ± 0.42	0.12 ± 0.11

while increasing the mean energy to $320\,\mathrm{GeV}$[130]. A prediction for the spallation rates can be made by scaling the KamLAND results for the muon energy, muon rates and scintillator composition difference,

$$R_{\mathrm{Borexino}} = R_{\mathrm{KamLAND}} \times \left(\frac{320}{268} \right)^{\alpha} \times C_{^{12}\mathrm{C}} \times C_{\mu} \qquad (8.11)$$

The ratio of carbon targets, $C_{^{12}\mathrm{C}}$, is 1.05 and the ratio of muon fluxes, C_{μ}, is 0.21. The scaling used, α, is the average scaling from FLUKA, 0.758 ± 0.008. Differences in the the muon charge ratio and energy spectrum between the sites are neglected. The predictions for Borexino are summarized in Table 8.15. On average the production rates are reduced by a factor of 4, mostly due to the increased depth. This is a significant reduction in these backgrounds for solar neutrino analyses. However, even at this deeper location the contribution of these isotopes to the background is non-negligible, and uncertainties in their production will be significant source of uncertainty as it is for KamLAND.

Chapter 9

Analysis of ^{8}B Solar Neutrinos

KamLAND was exposed to ^{8}B solar neutrinos for 1432.1 days from April 2002 through April 2007. This represents one of the three largest data sets for the direct measurement of solar neutrinos. The other two are Super Kamiokande and SNO which are both water Čerenkov detectors. KamLAND has different systematic effects in a measurement of ^{8}B solar neutrinos and provides a valuable addition to the water Čerenkov measurements. In this chapter the flux of ^{8}B solar neutrinos is determined from measuring the rate of neutrino elastic scattering events in KamLAND. Particular attention is paid to the backgrounds that could obscure this signal.

9.1 ^{8}B Neutrino Elastic Scatter Rate

The rate of ^{8}B neutrinos elastically scattering in KamLAND depends on the energy threshold that is achievable. Super Kamiokande and SNO presently use thresholds around 5 MeV. For a threshold below $\sim$2 MeV, the ^{8}B signal is overwhelmed by other sources of solar neutrinos.

This section predicts the event rate in KamLAND for 2 MeV and 5 MeV thresholds. An upper limit of 20 MeV defines the energy window for the analysis. Starting with the ^{8}B solar neutrino flux from the BSB(GS98) Standard Solar Model[3] and the ^{8}B neutrino spectrum of Winter et al.[17], the spectrum averaged cross-section is calculated according to section 4.6 and integrated over the energy windows. There are 3.423×10^{32} e^- targets per kt of KamLAND liquid scintillator, see Section 5.2.1. The predicted rates in units of events per kt-day are summarized in Table 9.1.

In practice, the energy window for the analysis is defined by the reconstructed energy. If the detector energy response model is accounted for, as discussed in section 6.6.3, then events tend to have higher reconstructed energies, increasing the predicted event rate. This effect, evident in Table 9.1, leads to a predicted rate increase of up to 0.7 events per kt-day.

If the expected effect of neutrino oscillation is accounted for, then the predicted rate is half as large. The oscillation parameters used for this prediction are those from the global analysis presented in [63]. In either case, only a handful of events are predicted per kt-day of exposure, almost a million times lower than the KamLAND trigger rate.

Table 9.1: The Standard Solar Model predicted rate of ^{8}B neutrino elastic scatter events in KamLAND. Two possible energy windows for the analysis are presented.

	Electron Recoil Energy		Reconstructed Energy	
	Events per kt-day			
	5 - 20 MeV	2 - 20 MeV	5 - 20 MeV	2 - 20 MeV
No Oscillation	3.01	6.87	3.64	7.18
With Oscillation	1.37	3.25	1.67	3.41

Understanding the backgrounds and efficiently identifying the signal events is therefore critical.

9.2 Backgrounds

The three largest contributors of backgrounds are decays from the daughters of ^{238}U and ^{232}Th, short-lived isotopes from muon spallation, and high energy gamma-rays produced in the materials that makeup KamLAND and the surrounding rocks. If not mitigated these backgrounds would overwhelm the neutrino signal. There are rarer backgrounds at rates smaller than neutrino elastic scattering but frequent enough that they should be investigated.

9.2.1 Backgrounds from ^{238}U and ^{232}Th

The isotopes ^{238}U and ^{232}Th are long lived isotopes that are present at some level in nearly all materials. These isotopes decay through chains of alpha and beta decays into stable isotopes of lead. The half-life of ^{238}U is 4.5 billion years and the decay chain terminates with ^{206}Pb. The half-life of ^{232}Th is 14.1 billion years and terminates with ^{208}Pb. Above 2 MeV, ^{8}B neutrinos dominate solar neutrino interactions in KamLAND. Both ^{238}U and ^{232}Th decay chains give alphas with energies above 2 MeV but because of "quenching" effects in the liquid scintillator these reconstruct with energies below 1 MeV. They are not a problem for the analysis of ^{8}B solar neutrinos but are a significant problem for low energy solar neutrinos such as those coming from ^{7}Be.

Compared to alphas, betas are much less quenched, see Section 6.6.3. The most energetic β-decay in either chain is the ^{232}Th daughter ^{208}Tl decay with Q=4.992 MeV. The 0.02% branch in the uranium chain to ^{210}Tl has a higher Q-value but a negligible branching fraction. The daughter ^{208}Tl is the most serious problem for the ^{8}B analysis. It mostly β-decays with an endpoint of 1.8 MeV to an excited state of ^{208}Pb which cascades to the ground state emitting gamma-rays at 0.6 MeV and 2.6 MeV. Since KamLAND is a calorimeter, the gamma-rays' energies are summed with the energy of the beta. The resulting reconstructed spectrum of ^{208}Tl is shown in Fig. 9.1. It is not unusual for beta decay spectra to be offset from zero because of gamma-rays summing. Water Čerenkov
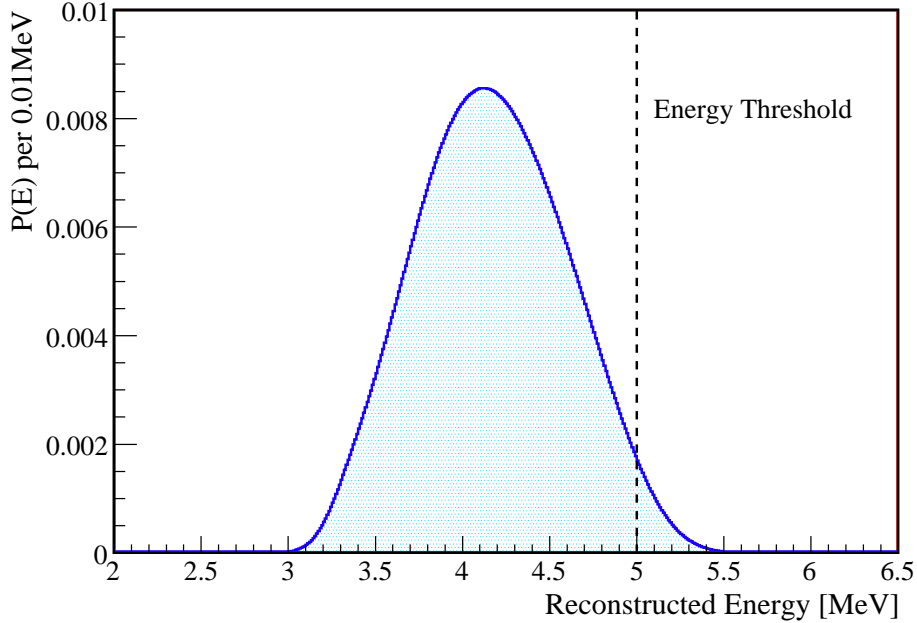
Figure 9.1: The predicted beta decay spectrum of ^{208}Tl reconstructed with KamLAND. The curve is normalized to unit area.

detectors in principal can distinguish betas from gammas but because of poor intrinsic energy resolution ^{208}Tl remains a background in SNO and Super Kamiokande.

The concentrations of ^{238}U in the liquid scintillator is determined from the rate of "^{214}Bi-^{214}Po" coincidences. The isotope ^{214}Bi decays to ^{214}Po. The isotope ^{214}Po decays to ^{210}Pb with a half-life of $164\mu s$. The half-life is convenient for extracting the pair from the data set. The concentration of ^{232}Th is determined from the rate of "^{212}Bi-^{212}Po" coincidences. The isotope ^{212}Bi decays to ^{212}Po which then decays to ^{208}Pb with a $0.3\mu s$ half-life. If the assumption is made that the daughters of the ^{238}U and ^{232}Th are in equilibrium then an analysis of the first 145 days gives concentrations of $(3.5 \pm 0.5) \times 10^{-18}$g/g of ^{238}U and $(5.2 \pm 0.8) \times 10^{-17}$g/g of ^{232}Th [64].

A more recent analysis of the full data set gives concentrations of $2.91 \pm 0.24 \times 10^{-18}$g/g for ^{238}U and $7.90 \pm 0.25 \times 10^{-17}$g/g for ^{232}Th in the liquid scintillator [135]. A 1m cylinder down the center of the detector is used to eliminate possible Rn contamination from calibration deployments. There is evidence that ^{222}Rn is introduced during calibrations, a daughter of the ^{238}U chain. There is no evidence for ^{220}Rn, a daughter of the ^{232}Th chain. So we assume that the concentrations of the ^{232}Th daughters are constant over the data set.

Assuming that the ^{232}Th decay chain is in equilibrium, then the ^{232}Th concentration predicts the ^{208}Tl event rate. This assumption should be very good for estimating ^{208}Tl, the daughter of ^{212}Bi. The branching ratio of the ^{212}Bi decay to ^{208}Tl is 0.36. The

Table 9.2: The muon cuts used in the analyses of reactor anti-neutrinos and solar neutrinos.

	Reactor Muon Cuts	Solar Muon Cuts
Whole detector all muons	2ms	200ms
Whole detector data gap	2ms	200ms
Shower Muon	2s	5s
Whole detector bad reconstruction	2s	5s
Reconstructed Track Cylinder	3m for 2s	3m for 5s

predicted rate of ^{208}Tl decays is 10.0 ± 0.3 per kt-day, more than 3 times the predicted rate for the elastic scattering of oscillated ^{8}B solar neutrinos. But with a energy threshold of 5 MeV only 0.27 ± 0.01 ^{208}Tl decays per kt-day are predicted to contaminate the ^{8}B events.

9.2.2 Muon Spallation Backgrounds

While the threshold choice for the ^{8}B solar neutrinos is driven by the ^{208}Tl background, the largest backgrounds above 5 MeV come from spallation produced light isotopes. These backgrounds are studied with the FLUKA simulations described in chapter 7 and KamLAND data analyses in chapter 8. Above 5 MeV, ^{12}B is the most common background source with a half-life of 20.2ms. With a 200 ms full-detector veto following every LS muon only 0.1% ^{12}B decays remain or $\sim$0.06 per kt-day.

^{8}Li is the second most commonly produced isotope. Its half-life is 0.84s so a 5s veto of the detector reduces the number in the candidate sample by 98%. A significantly longer veto would unduly reduce the exposure. Instead of a full-detector veto for every LS muon, the muon cylinder cuts described in section 8.3.1 are used to eliminate spallation backgrounds. These cuts reclaim some of the exposure lost in a full-detector veto.

The muon cuts for the solar neutrino analysis and the reactor anti-neutrino analysis are in Table 9.2. For the reactor anti-neutrino analysis, the delay neutron emitter ^{9}Li dominates and a 2s muon veto is effective. In the ^{8}B analysis, a 200 ms full-detector veto and 5s cylinder cuts are used so that inefficiencies in muon tracking do not lead to a large ^{12}B background.

The 5s spallation cuts reduce all backgrounds with shorter half-lives than ^{8}Li including ^{9}Li and ^{9}C. These isotopes are also produced at lower rates than ^{8}Li and their contribution, $\sim$0.003 events per kt-day, is neglected. The only isotope not yet considered is ^{11}Be. Produced at much smaller rates than ^{8}Li, 0.82 per kt-day versus 21.4 kt-day, its half-life is much larger, $\tau_{1/2}$ =13.8s. The 5s spallation cuts only remove 22% of the ^{11}Be, leaving a significant background to the ^{8}B solar neutrino analysis.

9.2.3 External Gamma-ray Backgrounds

Gamma-rays are produced in KamLAND itself and the surrounding rocks. These gamma-rays are mostly produced by (n, γ) reactions. The spectrum is a continuum of gamma-rays that extends above the 5 MeV energy threshold. The responsible neutrons

come mostly from (α, n) reactions. The α's are products of the ^{238}U and ^{232}Th decay chains. For some materials the relevant cross sections are not known or their uncertainties are difficult to assess, making simulations difficult. But the background can be estimated with the KamLAND data.

KamLAND is "self-shielding" and the external gamma-ray background decreases towards the center of the scintillator volume. The sources of gamma-rays closest to the scintillator are stainless steel support structures at the top and bottom of the detector that restrains the balloon. Considering this and the shape of the cavern, the rocks are the other source for this background, a cylindrical fiducial volume is used for the analysis, see the diagram in Fig. 6.20.

The largest cylindrical volume that fits within the balloon's dimensions is 3.88m in radius with a height equal to twice the radius. Candidate events within this volume that satisfy the muon cuts and are above the energy threshold, are plotted relative to their closest distance to the 3.88m cylinder, Fig. 9.2. Their position distribution is approximately described by an exponential plus a constant. Accounting for the effective volume with position gives,

$$f(x) = (\frac{\phi}{\lambda}e^{-x/\lambda} + c) \times 6\pi\delta x(3.88m - x)^2. \tag{9.1}$$

Here, λ is the effective attenuation length for gamma-rays above 5 MeV, and ϕ is the number of events per unit area on the surface of the 3.88m cylinder. The constant c accounts for events from other processes in the scintillator volume which are assumed to be isotropically distributed.

A subset of 896.5 days of data is used corresponding to the runs following the removal of thermometers from the active volume. The fit in Fig. 9.2 gives 0.91 ± 0.19 events per m^2 at the cylinder surface and an attenuation length of 0.38 ± 0.09m. The fit's χ^2/N.D.F is 0.77. Fig. 9.2 suggests that a cut of 0.88m eliminates the bulk of external gamma-rays. A cylinder with a radius of 3m and 6m height is selected as the fiducial volume, avoiding external gamma-rays.

The energy spectrum of the external gamma-rays background is constructed by dividing the 3.88m cylinder into shells of equal volume and subtracting spectrum from the central volume from the outer. The result is shown in Fig. 9.3. This energy spectrum is modeled assuming (n, γ) reactions on the stainless steel and rock. Materials other than stainless steel and rock are neglected. The relative importance of these two sources is estimated from the data.

The gamma-rays from (n, γ) reactions are obtained for thermal neutrons from the National Nuclear Data Center[136]. It is assumed that the neutrons have thermalized and all isotopes have the same capture cross sections. Only isotopes with at least 5% natural abundance are included. The stainless steel in KamLAND is SS304, 68% Fe, 19% Cr and 10% Ni[94]. The exact composition of the rock surrounding KamLAND is not known. The composition is assumed to be the Mozumi rock type Inishi-iwa, Mozumi is the village close to the mine. The composition is outlined in Table 9.3. The mountain may also have a significant amount of limestone. The typical compositions for these types of rock are in Table 9.3.

The gamma-ray energy spectra are combined with the KamLAND energy response to construct the spectra in Fig. 9.4. In these spectra, the contribution from oxygen is
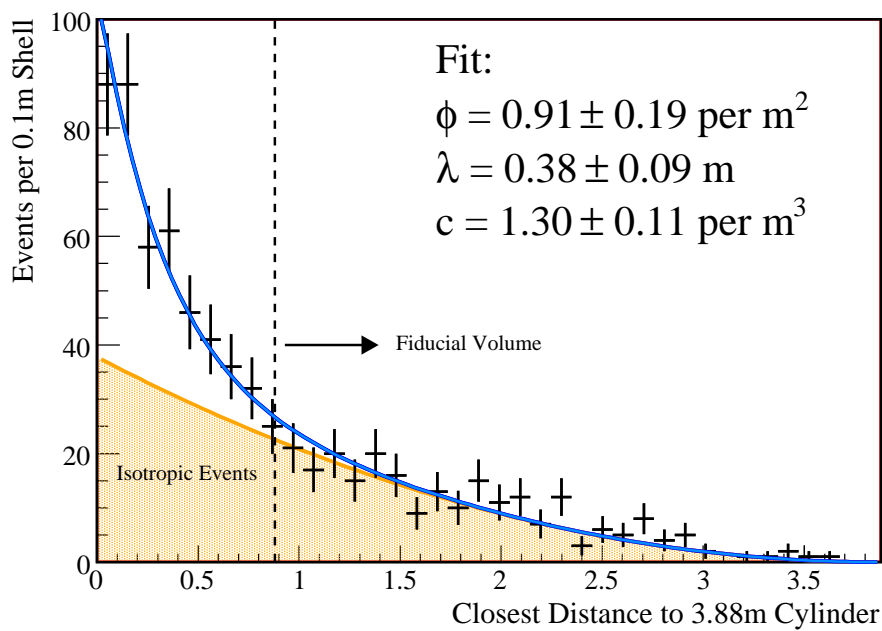
Figure 9.2: Distribution of the external gamma-ray background. Event rate versus the distance of closest approach to a 3.88 m radius by 7.76 m cylinder centered in KamLAND. Events coming from external sources are an excess over the isotropic background shown in yellow.
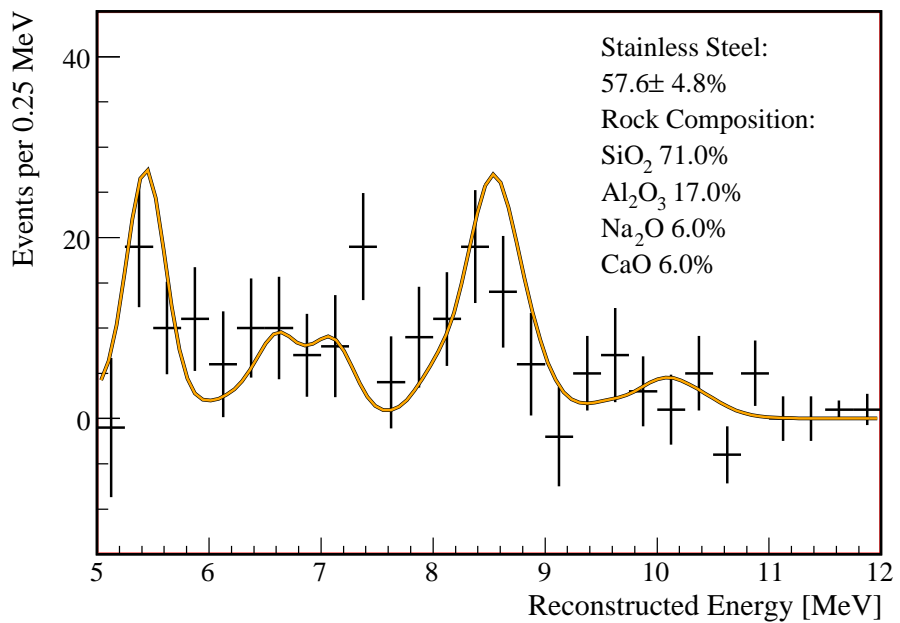
Figure 9.3: The spectrum of gamma-rays coming from external sources. The yellow line is the best fit energy spectrum using a model assuming (n, γ) reactions.

Table 9.3: The composition of Mozumi rock type Inishi-iwa. For comparison typical lime-stone for Mozumi is shown. Data is from Kamioka Mining Company report[137].

Compound	Mozumi Rock Type Inishi-iwa	Mozumi Limestone
	%	%
SiO_2	60.70	9.96
TiO_2	0.31	0.86
Al_2O_3	17.39	0.23
Fe_2O_3	1.10	0.64
FeO	1.22	1.22
MnO	0.15	0.09
MgO	0.93	14.59
CaO	6.00	35.60
Na_2O	6.42	0.19
K_2O	3.47	0.24
P_2O_5	0.18	0.02
H_2O^+	0.60	3.78
H_2O^-	0.37	0.19
S	0.01	0.51
CO_2	0.96	32.32

neglected since there are no significant gamma rays in the energy window. The measured energy spectrum in Fig. 9.3 is fit to the capture spectra assuming a fixed rock composition, Inishi-iwa rock. The fit finds $57.6 \pm 4.8\%$ of the gamma-rays from the stainless steel with a χ^2/N.D.F of 1.15. If the rock composition is not fixed, then the fit gives $58.7 \pm 4.5\%$ of the gamma-rays come from the stainless steel and a rock composition of 58% SiO_2 and 42% CaO with sχ^2/N.D.F= 1.02.

9.2.4 Thermometer Background

After construction, three thermometers were left hanging near the central axis of the detector. Their purpose was to monitor temperature during the filling of KamLAND. The three units were positioned near the center of the detector and at ±5.5m from the center. They were in place for the first 546 days of the data set, and removed after run number 3611. They were platinum resistance thermometers made of platinum and MgO housed in stainless steel. The thermometers were 4 cm long, 0.5 cm in diameter, and suspended by teflon coated copper readout lines.

The thermometers contain Fe, Cr, Mn, Ni, Pt, and Cu, all materials with ther-mal neutron capture cross-sections an order of magnitude or larger than neutron capture on protons. Neutrons preferentially capture on the thermometer, making them a source of high energy gamma-rays like the rock and stainless steel surrounding KamLAND. The thermometers also contain much more ^{238}U and ^{232}Th than the surrounding liquid scin-
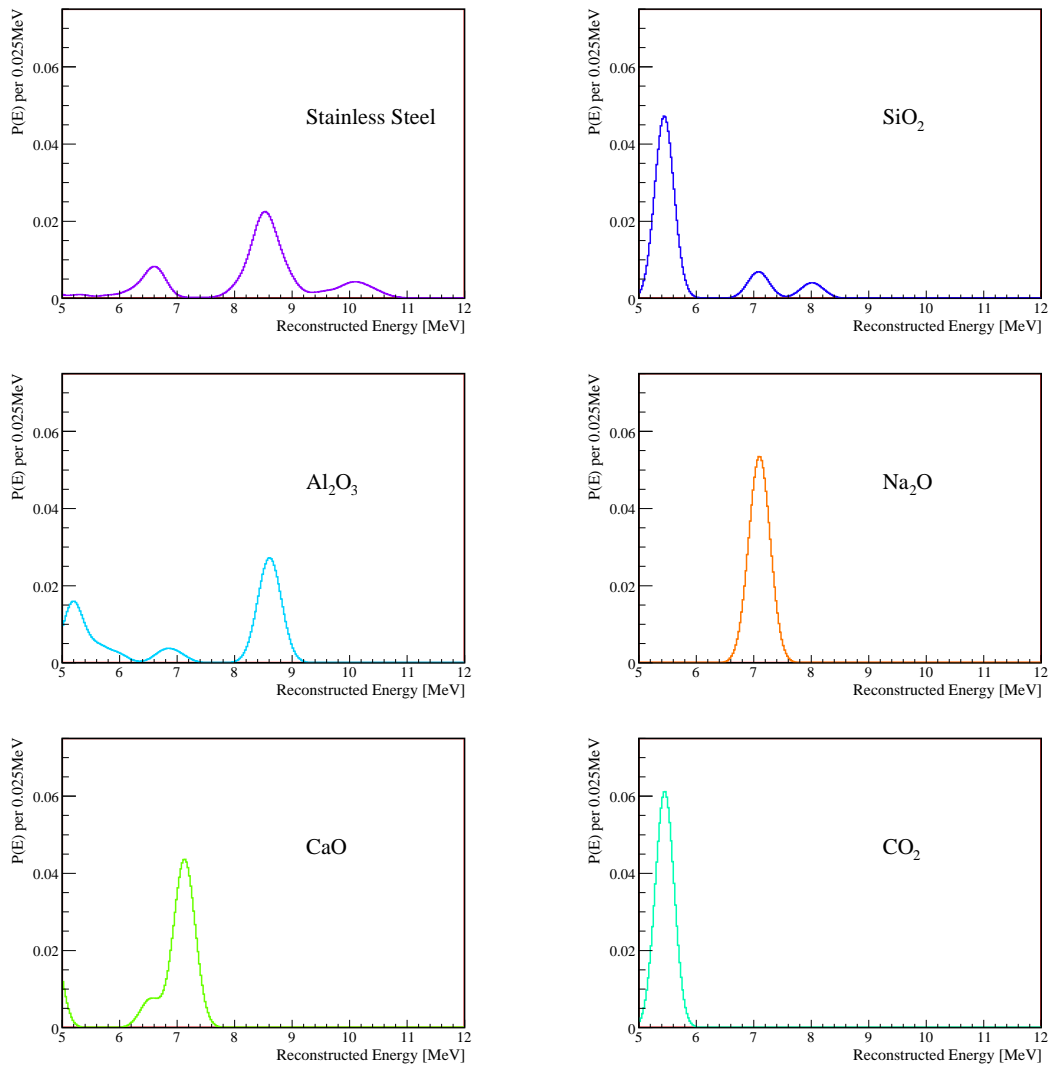
Figure 9.4: Neutron capture gamma-rays spectra for stainless steel and common rock components. The KamLAND energy response is taken into account.
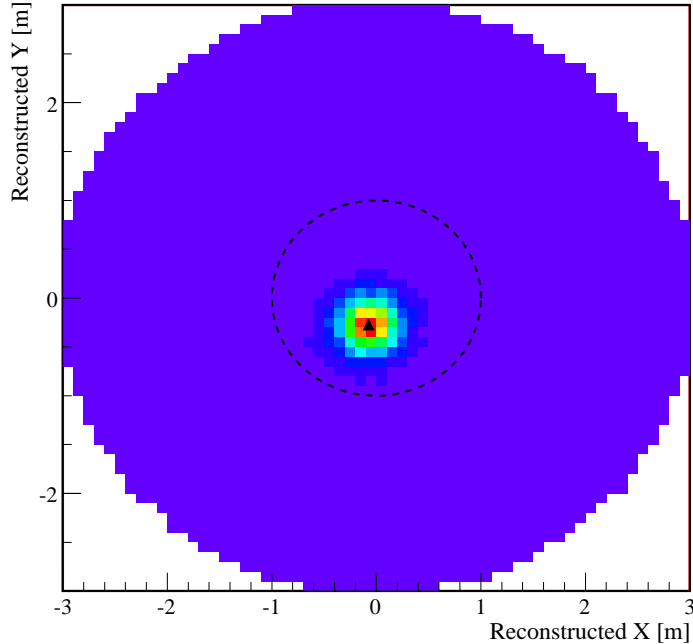
Figure 9.5: The thermometers' position in the x-y plane of the detector is obtained from event with reconstructed energy $> 3\,\mathrm{MeV}$. The thermometers are found slightly off-axis at x=-7.5cm and y=-27.1cm. A 1m cylindrical cut down the center of the detector eliminates the thermometer background from the data set.

tillator resulting in a larger background from ^{208}Tl. They are a large source of events at essentially all energies. Fig. 9.5 shows the reconstructed position of all events above $3\,\mathrm{MeV}$ within the 3m cylindrical volume. The thermometers are evident in the reconstruction at $x_t = -7.5 \pm 0.9\,\mathrm{cm}$ and $y_t = -27.1 \pm 0.4\,\mathrm{cm}$. The z distribution of the thermometer events is energy dependent. In Fig. 9.6, the thermometer slightly above the center of the detector is evident. The candidate events above $5\,\mathrm{MeV}$ in Fig. 9.6 show a uniform distribution, indicating the that neutron capture on the copper leads is an important source of higher energy events.

The thermometer background in the ^{8}B neutrino data is estimated by plotting the candidate events' distances to the thermometers in the x-y plane. Fig. 9.7 shows the result where the distance to the thermometers is defined as $r = \sqrt{(x - x_t)^2 + (y - y_t)^2}$. If there were no background from thermometers the distribution would simply be a linearly increasing function of r due to the increasing cylindrical volume. The thermometers introduce an additional decreasing exponential contribution. The position dependence is then approximated by

$$f(r) = (\frac{\phi}{\lambda}e^{-r/\lambda} + c) \times 2\pi r h \delta r. \tag{9.2}$$
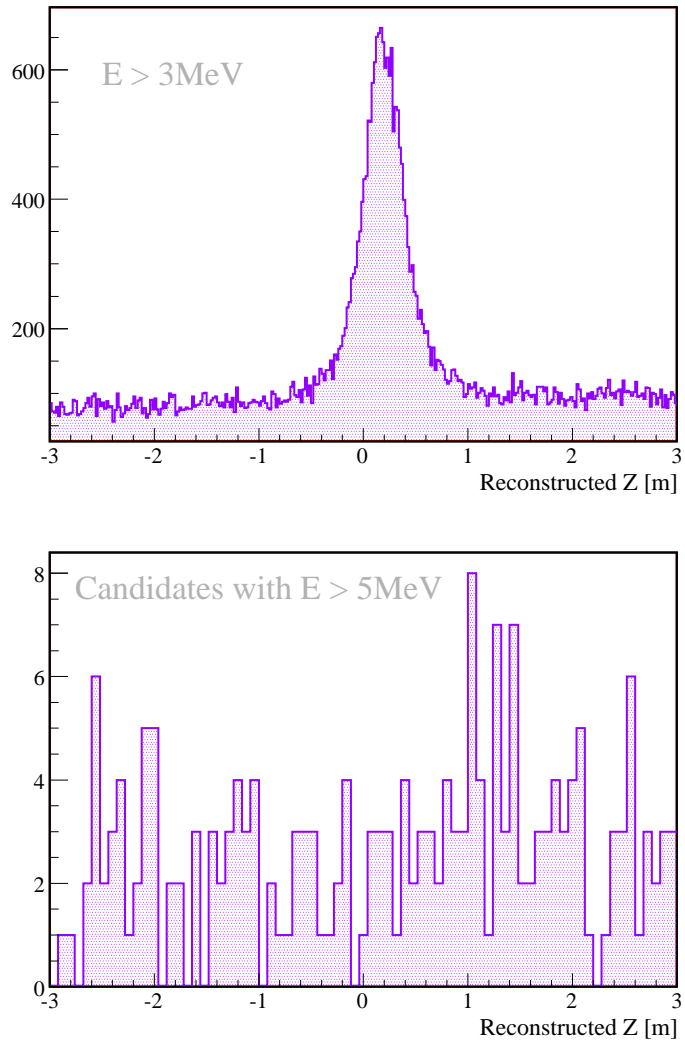
Figure 9.6: The thermometers' position along the z-axis of the detector obtained from event reconstruction. The top shows all events above $3\,\mathrm{MeV}$ and the bottom only the candidate events above $5\,\mathrm{MeV}$. The distance from the z-axis for these events is required to be $< 3\mathrm{m}$.
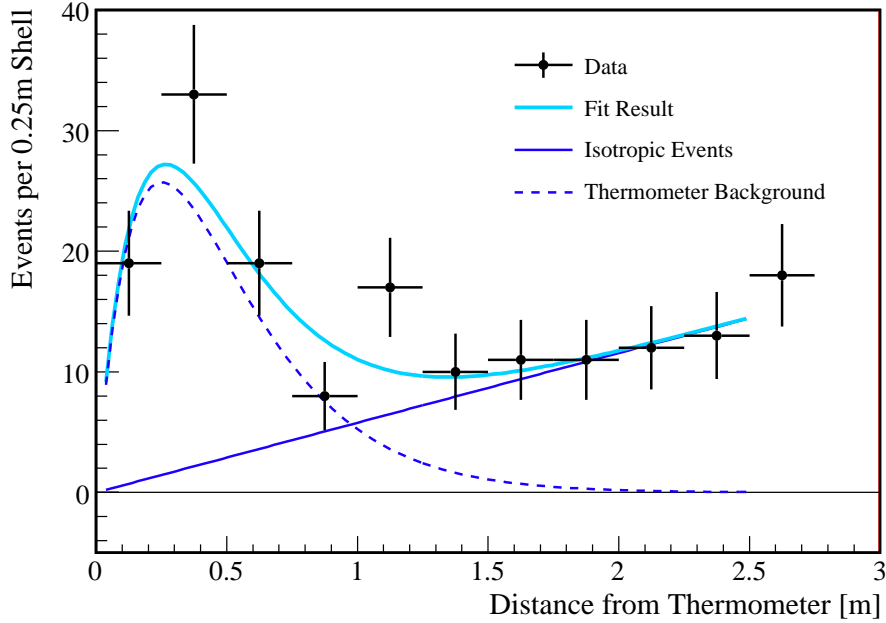
Figure 9.7: The position distribution of thermometer related events relative to the position of the thermometers. Events uncorrelated to the thermometers should have an isotropic distribution.

The cylinder height, h, is 6m. The fit in Fig. 9.7 finds $\phi = 7.4 \pm 1.1$ events per m^2 and $\lambda = 0.25 \pm 0.03$m, χ^2/N.D.F= 1.1. The fitted attenuation length is 1.5σ smaller than that found in the analysis of external gamma-rays. This is because λ is an effective attenuation length that includes additional effects due to energy and the 2D projection of propagation in 3D. These numbers correspond to 70.5 ± 20.1 thermometer events. After a cylinder cut 1m in radius and 6m in height, 8.4 ± 6.1 events remain in the ^{8}B neutrino data set.

The energy spectrum of thermometer events is a combination of the tail of the ^{208}Tl spectrum and a neutron capture gamma spectrum. The construction of the later is described in Section 9.2.3. Two additional materials, copper and platinum, are used in the thermometer's neutron capture gamma-ray spectrum, see Fig. 9.8. The copper spectrum is a combination of ^{63}Cu and ^{65}Cu based on natural abundance. ^{195}Pt is the only Pt isotope used due to its significantly larger cross section.

The energy spectra of candidate events within a cylinder of r=0.75m from before and after the thermometers were removed, are subtracted, see Fig. 9.9. The fit finds 21 ± 6 ^{208}Tl events and 36 ± 6 neutron capture events. For the neutron capture events, $(24 \pm 7)\%$ are the result of capture on platinum. The remaining 76% are divided between copper and stainless steel. The division is $(63 \pm 14)\%$ are from stainless steel, leaving 37% from copper. The quality of this fit is poor with a χ^2/N.D.F of only 1.8. However, this background after the application of a 1 m central cylinder cut is small compared to other backgrounds. The
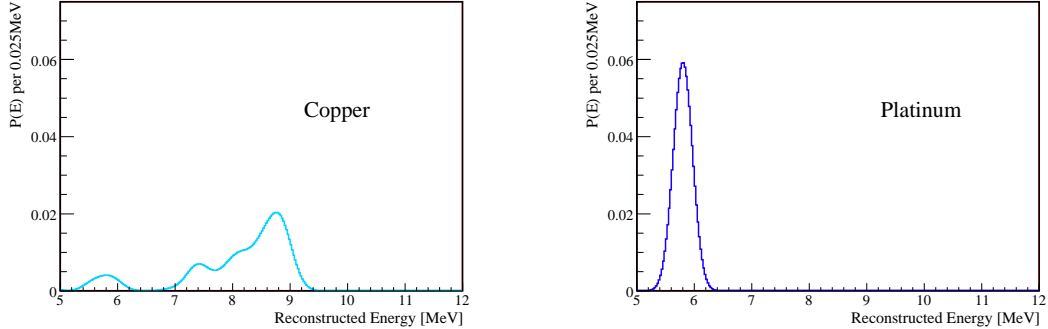
Figure 9.8: The thermal neutron capture gamma spectrum from copper (left) and platinum (right) corrected for the detector energy response. Data is taken from the tables from the National Nuclear Data Center's program CapGam [136].

poor fit and uncertainties in these parameters are not relevant.

9.2.5 Reactor Anti-Neutrino Background

The reactor anti-neutrinos that were used so effectively in Section 4.2.4 to determine the parameters of neutrino oscillation are a background to this analysis. The Japanese power companies provide KamLAND with the number of fissions per day per fission isotope per reactor core. This information, in addition to the inverse beta decay cross section, is used to predict the event rate and energy spectrum of anti-neutrino interactions in KamLAND, for a detailed discussion see [61]. The average predicted reactor anti-neutrino event rate ~1 per kt-day. The cuts used to eliminate this background are the same as those used to extract the ^{9}Li and ^{8}He signal. However, the delayed neutron vertex is not required to be within the fiducial volume. The efficiency of these cuts is 94%, see Table 8.9. The endpoint of the reactor anti-neutrino spectrum is 8.5 MeV, so the remaining reactor anti-neutrinos will be concentrated near the 5 MeV analysis threshold. The elastic scatter of reactor anti-neutrinos is being neglected in this analysis due to the small cross section and the small fraction of reactor anti-neutrinos between 5 MeV and 8.5 MeV.

9.2.6 Atmospheric ν Background

The final background that we consider is from the elastic scattering of atmospheric neutrinos on protons. The kinetic energy of the recoiling proton is deposited in KamLAND creating a single event. Kinematics require a 100 MeV neutrino for a 20 MeV proton recoil. The flux and spectrum of atmospheric neutrinos is calculated in order to interpret the atmospheric neutrino oscillation results, see Section 4.2.3. The flux of atmospheric neutrinos calculated by Honda et al.[112, 138] is shown in Fig. 9.10. The uncertainty on this calculation rises rapidly below 1 GeV, reaching 20% at 100 MeV. This is in the region of interest for this analysis.
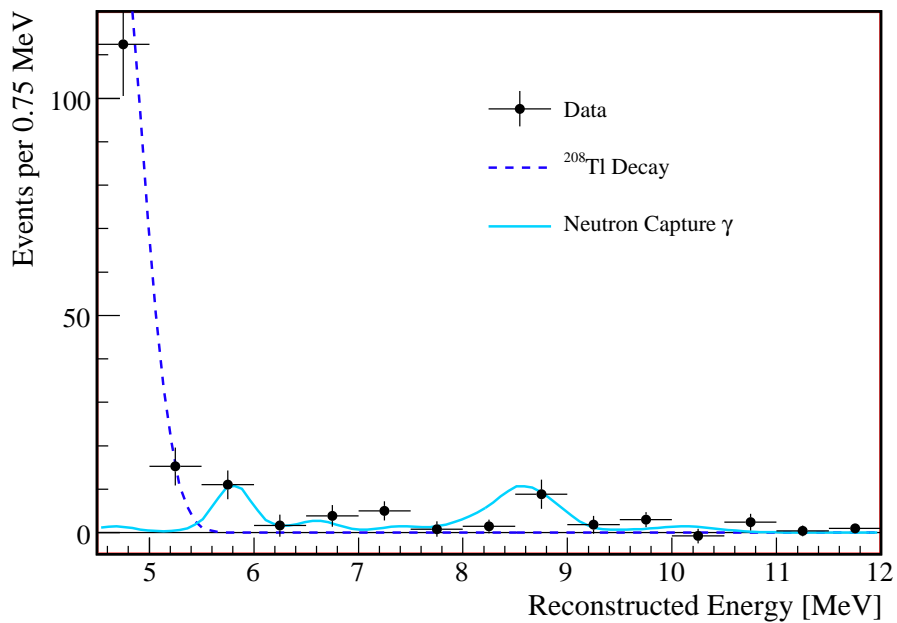
Figure 9.9: The energy spectrum of the thermometer events. Overlaid is the result of the fit for the relative contributions of neutron capture gamma-rays and the decay of ^{208}Tl.
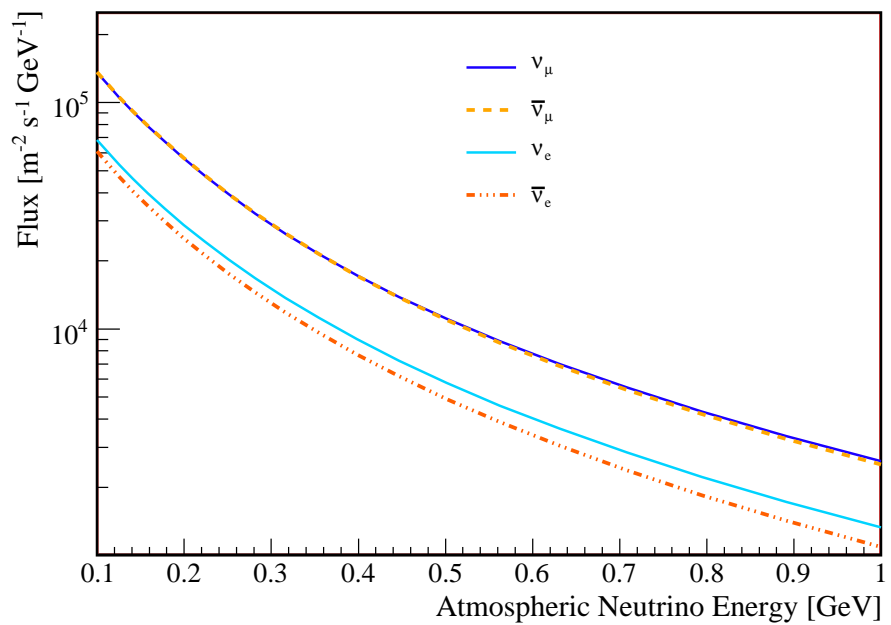
Figure 9.10: The atmospheric neutrino flux at KamLAND averaged over solid angle as calculated by Honda et. al. [112, 138]. The calculation takes into account the shape of Mt. Ikeoyama.
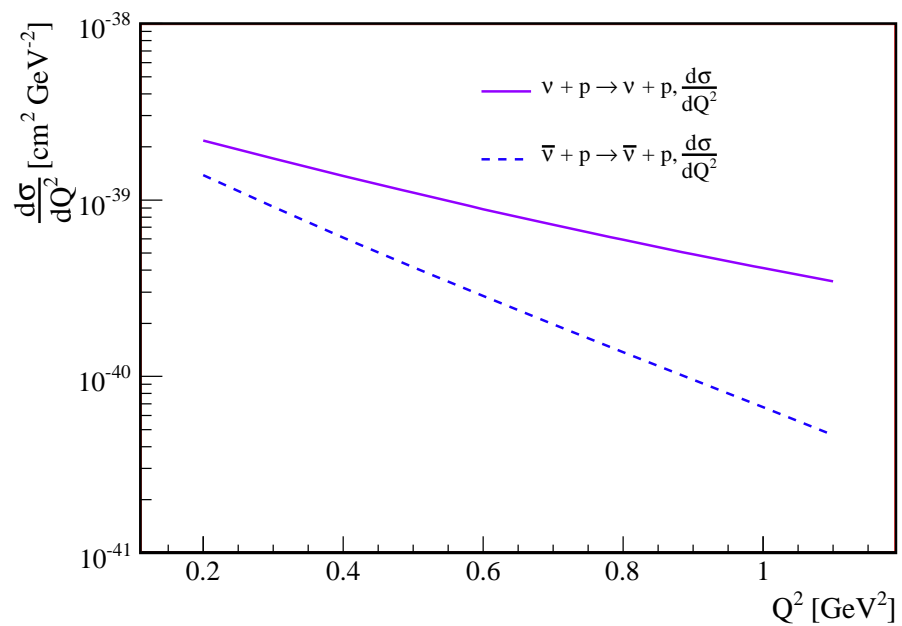
Figure 9.11: The differential cross section for neutrino-proton and anti-neutrino proton elastic scattering from the formulation in [139]. This cross-section is the same for electron and muon flavored neutrinos.
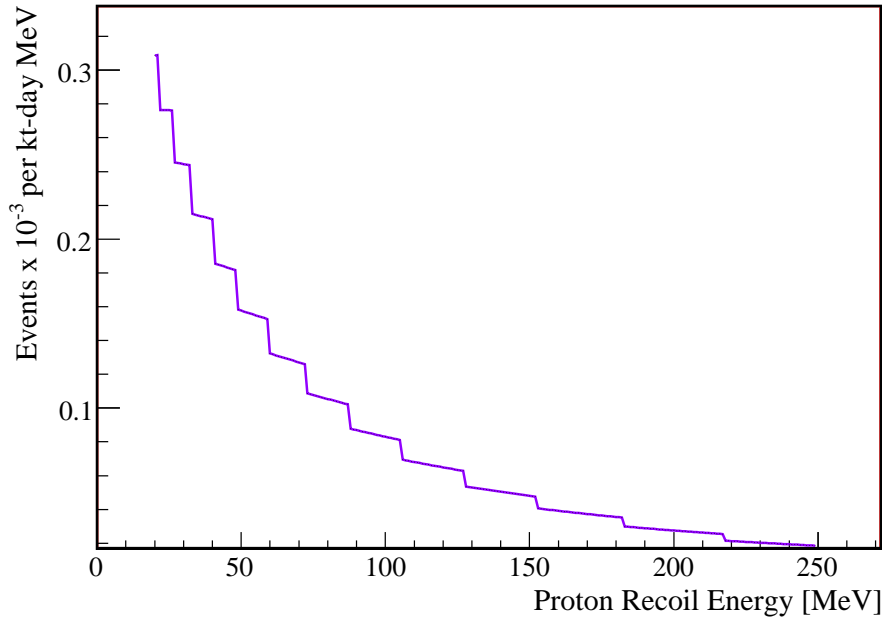
Figure 9.12: The predicted rate of proton recoils due to atmospheric neutrinos. The binning used in the atmospheric flux calculation causes the discontinuities.

The first order formula for the neutrino-proton cross-section, $\frac{d\sigma(\nu p)}{dQ^2}$ and anti-neutrino-proton differential cross-section, $\frac{d\sigma(\bar{\nu} p)}{dQ^2}$, from [139] is used here. The kinematic variable Q^2 is related to the recoil energy of the proton, T_p by $Q^2 = 2M_p T_p$. These cross-sections, shown in Fig. 9.11, are independent of the neutrino flavor. The spectrum averaged cross section is calculated ass in section 4.6. The number of target protons in KamLAND is 8.478×10^{31} per kt. The predicted atmospheric neutrino rate versus proton recoil energy is shown in Fig. 9.12.

The minimum proton recoil energy, 20 MeV, is set by the lowest energy provided by the atmospheric neutrino calculation. Integrating from 20 MeV to 35 MeV, the rate is <0.06 per kt-day. The proton recoil energy spectrum is rising in this region. The rise over 15 MeV is equivalent to the uncertainty in the flux so in this region a flat spectrum approximation is used. Extending the flat spectrum, this limit is then assumed to be valid in the 5-20 MeV energy region for the analysis. The detector energy response for these high energy protons is neglected. If the energy response is included, the "quenching" of the protons would reduce this limit.

Table 9.4: Summary of the cuts used to select the ^{8}B solar neutrino candidates.

Cut	Description	Purpose
Reconstructed Energy	E> 5 MeV E< 20 MeV	Exclude ^{208}Tl background
Reconstructed Position	$\|Z\| < 3$m $R_{xy} < 3$m	Cylindrical fiducial volume
Delayed Neutron Cut	See Table 8.9	Eliminate reactor anti-neutrinos
Short Muon Cut	$\Delta t_\mu > 200$ms	Eliminate the shortest lived muon spallation products
Long Muon Cut	Shower muon $\Delta t_\mu > 5$s or Non-Shower LS muon with track 200ms$< \Delta t_\mu < 5$s $dR_\mu > 3$m	Eliminates some ^{8}Li, ^{8}B and ^{11}Be
Period I Cut	$R_{xy} > 1$m and Run <3611	Remove thermometer events

9.3 Candidate Selection

In the previous section the expected backgrounds give rise to a specific set of cuts to be applied to the data. These cuts, summarized in Table 9.4, are chosen to minimize the background event rate relative to the ^{8}B solar neutrino rate. After these cuts, there are 365 candidate events remaining, 118 in period I with the thermometers, and 247 in period II after the thermometers were removed. The reconstructed position of these candidates in Fig. 9.13 shows that these candidates have an isotropic distribution as expected. In Fig. 9.14 the candidates are divided into 19 periods of 75 days. No time dependence is observed. Period II is well described by a constant rate in time. Period I shows the expected reduction in rate due to a smaller fiducial volume, and the fit to a constant rate in time results in a χ^2/N.D.F=1.05 while the fit to a line results in a χ^2/N.D.F=1.25.

9.4 Exposure

The volume used is the 3m cylinder, corresponding to 0.1376 kt of liquid scintillator. This is reduced to 0.1235 kt by the 1m thermometer cut for period I. The details of the fiducial volume calculation are discussed in Section 6.6.2.

The largest loss in exposure comes from the muon spallation cuts summarized in Table 9.2. The reduction is not simple to calculate because the muon cylinder cuts create a "Swiss cheese" effect in the volume. The reduction is calculated by Monte Carlo. The muon spallation cuts are applied, and the remaining fraction of Monte Carlo events correspond to
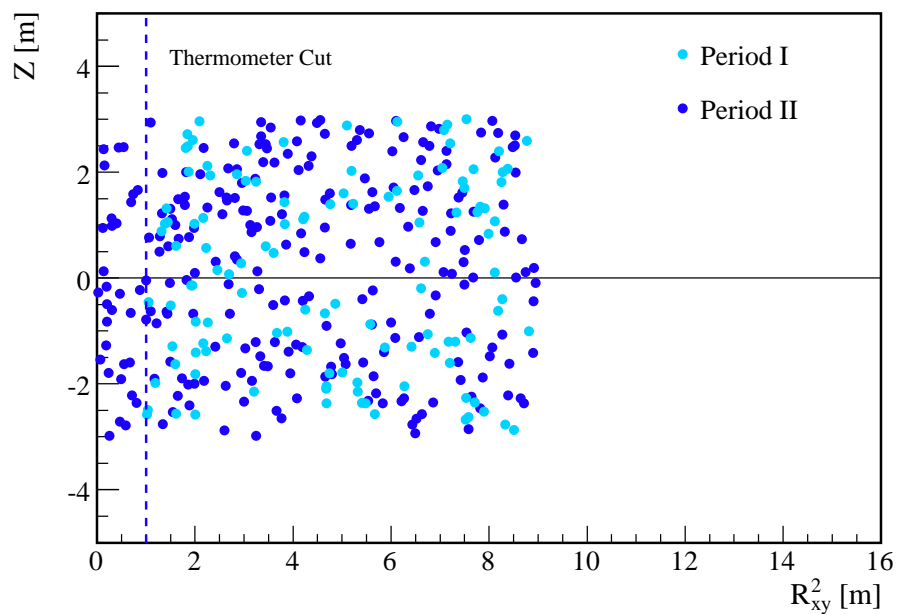
Figure 9.13: The position distribution of the ^{8}B solar neutrino candidates. Events with $R_{xy} < 1\,m$ are excluded in Period I.
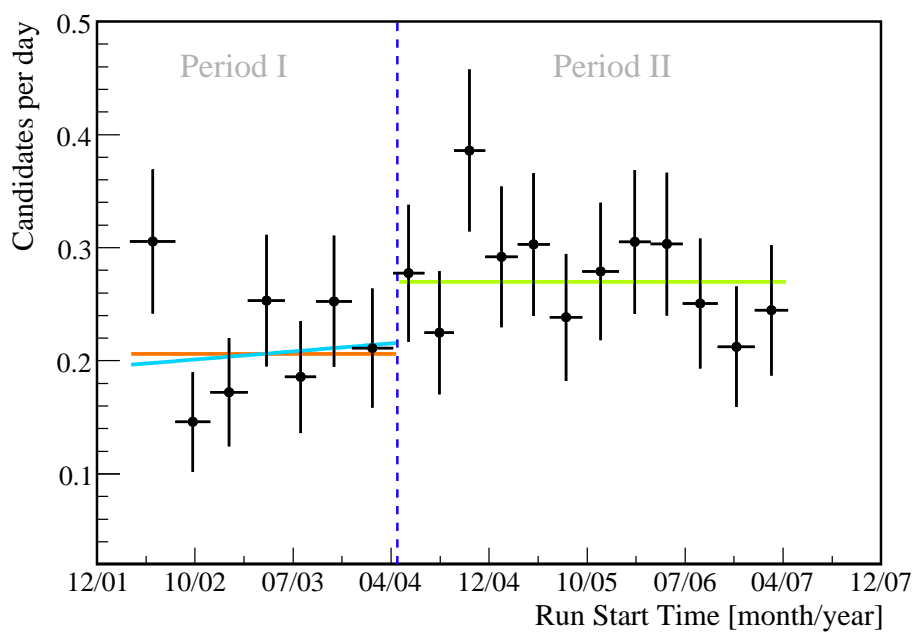
Figure 9.14: The distribution ^{8}B solar neutrino candidates in time. Each data point corresponds to 75 days. Period I and Period II are well described by a constant rate in time. Period I shows the expected reduction in rate due to the smaller fiducial volume.

Table 9.5: The fraction of the exposure remaining after muon cuts are applied to the data.

Good Reconstruction Definition	Reactor Muon Cuts	Solar Muon Cuts
Usable Track	0.882	0.705
Valid Track	0.850	0.643
Valid Track and b_μ <6.45m	0.840	0.624

Table 9.6: The exposure for the ^{8}B solar neutrino analysis and the accompanying systematic uncertainties.

	Data Period I		Data Period II	
	Value	Uncertainty	Value	Uncertainty
Run Time [days]	535.61	-	896.49	-
Fiducial Volume [kt]	0.1235	3.2%	0.1376	3.1%
Scintillator Variation	-	0.14%	-	0.14%
Reconstruction	0.999	0.10%	0.999	0.10%
Spallation Cuts	0.624	0.10%	0.624	0.10%
Total [kt-days]	41.2	3.21%	76.9	3.11%
		118.1 kt-days		

the remaining exposure fraction. Table 9.5 shows the results for these cuts and also for the reactor muon cuts. The volume used for reactor muon cuts is a 5.5m sphere instead of the 3m cylinder. Increasing the muon cuts from 2s to 5s and requiring better quality tracks, leads to an expected reduction in exposure. Since minimizing spallation backgrounds is critical to this analysis, the highest quality tracks are used, valid track with b_μ <6.45m. The 0.1% systematic uncertainty on this study is determined by varying the 1 Hz random event generation rate within a reasonable range and varying the chosen fiducial volume.

The exposure calculation is presented in Table 9.6. The event reconstruction efficiency, from Section 6.6.1, reduce the total exposure. The uncertainty in the scintillator density and composition, from Section 5.2.1, is included. The combination of period I, 41.2 kt-days, and period II, 76.9 kt-days, gives a total exposure of 118.1 kt-days with 3% uncertainty.

9.5 Predicted Background

The background event rates and efficiencies for the ^{8}B solar neutrino analysis are summarized in Table 9.7. For the total data set, the estimated background contribution is 195.7±29.6 events. Table 9.8 shows the individual contributions. The uncertainty on the external gamma-ray background and the thermometer background is obtained by varying the fit parameters by 1σ. The combined uncertainty in the calculation of the flux and

Table 9.7: The background, efficiency and energy scale values that are inputs to the fit.

Category	Parameter	Value	Uncertainty
General Backgrounds	Gamma Events Period II [N per m^2]	0.91	0.19
	Gamma Attenuation Length Period II [m]	0.38	0.09
	Thermometer Counts Period I	8.4	6.1
	Thermometer Ratio of ^{208}Tl	0.36	0.08
	Decay Rate ^{208}Tl [Events/kt-day]	10.0	0.3
	Atmospheric Neutrino Rate [Events/kt-day]	0.034	0.034
Muon Spallation Backgrounds	Production Rate ^{8}Li [Events/kt-day]	20.27	1.32
	Production Rate ^{8}B [Events/kt-day]	1.43	0.82
	Production Rate ^{11}Be [Events/kt-day]	0.82	0.24
	Non-Shower Rate ^{8}Li [Events/kt-day]	0.66	0.36
	Non-Shower Rate ^{8}B [Events/kt-day]	0.0001	0.004
	Non-Shower Rate ^{11}Be [Events/kt-day]	0.16	0.16
Efficiency	Exposure Rescale Period I	1.00	0.0321
	Exposure Rescale Period II	1.00	0.0311
	Muon Cylinder Track Cut dR < 3m	0.967	0.058
	Reactor Anti-Neutrino Calculation	0.940	0.055
Energy Scale	a_0	1.128	0.014
	k_B [g/cm^2/MeV]	0.0104	0.0020
	k_c	0.204	0.053
	k_0	0.649	0.059

spectra of the reactor anti-neutrinos is 3.3% [63], and 94±0.6% are eliminated by the delayed neutron cuts. The 0.17 event uncertainty is obtained by combining these uncertainties with those obtained by varying the oscillation parameters within their 1σ uncertainties[63].

The atmospheric neutrino rate is estimated to be < 0.06 events per kt-day in the 20-35 MeV energy range which corresponds to < 7.1 events in the data set. Fig. 9.15 shows that there are 4 candidate events in the 20-35 MeV window. Assuming a flat spectrum and a conservative 100% uncertainty, the expected number of atmospheric neutrinos is 4 ± 4 events.

The largest background and uncertainty comes from spallation products. Table 9.9 shows the spallation background by isotope and muon cut. The uncertainty is dominated by the uncertainty in the amount of ^{11}Be that remains after the 5 s cuts. The muon cylinder cut systematic uncertainty is negligible due to the small number of background events in that time window.

Table 9.8: Summary of the backgrounds.

Background	Number of Events
Spallation Products	141.3 ± 26.7
External Gamma-rays	19.0 ± 10.8
Thermometer Events	8.4 ± 6.1
Atmospheric Neutrinos	4.0 ± 4.0
Decay ^{208}Tl	20.6 ± 1.0
Reactor Anti-Neutrinos	3.08 ± 0.17
Total	195.7 ± 29.6
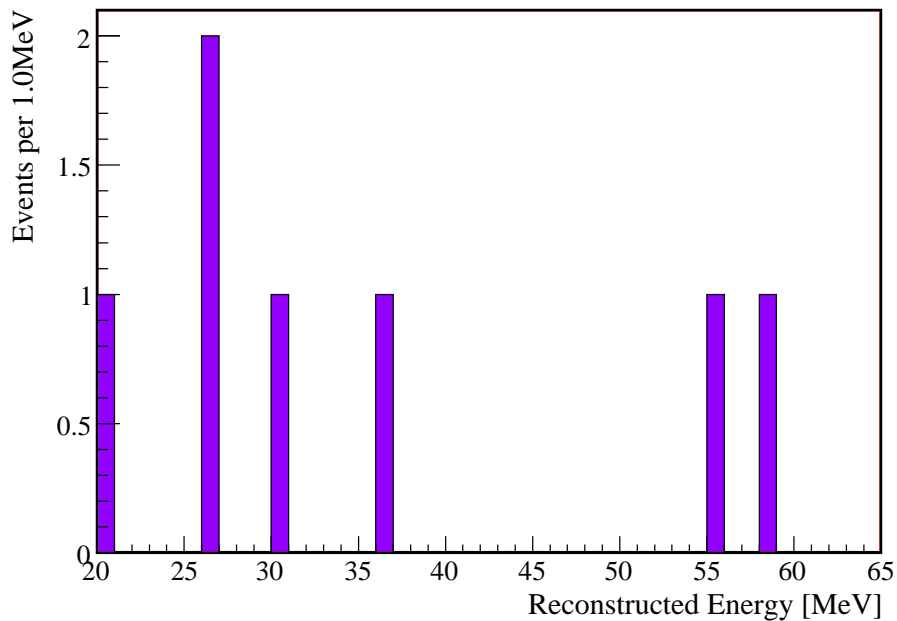
Figure 9.15: The reconstructed energy spectrum of events that pass all of the proposed analysis cuts but have reconstructed energies above 20 MeV. These high energy candidates should not be ^{8}B solar neutrinos but may be due to atmospheric neutrinos.

Table 9.9: Summary of the contribution of spallation products to the background of the ^{8}B solar neutrino analysis.

Isotope	After Cylinder Cut	After 5s Cuts	Total
	Number of Events		
^{11}Be	0.16 ± 0.32	89.08 ± 26.07	89.23 ± 26.07
^{8}Li	2.60 ± 4.78	46.93 ± 3.06	49.53 ± 5.67
^{8}B	0.00 ± 0.02	2.57 ± 1.47	2.57 ± 1.47
		Total Events	141.33 ± 26.72

9.6   Analysis of Candidates

The 365 candidates represent a statistically limited data set with a large contribution from background. In binning data for analysis some information is lost which would be particularly unfortunate in this case. An un-binned fit to the data avoids this problem and including the individual event energy information allows for better discrimination between signal and background. The following sections describe the analysis that is used to determine the ^{8}B neutrino flux.

9.6.1   Un-binned Log-Likelihood Fit

The construction of an un-binned log-likelihood fit proceedes very similarly to the binned fit presented in section 8.2. A likelihood ratio

$$\lambda = \frac{L(\vec{x}, \vec{\theta})}{L_{\max}(\vec{x}, \vec{\theta})} \tag{9.3}$$

is constructed where $\vec{x}$ are the data points and $\vec{\theta}$ are the fit parameters. The likelihood function has three possible components leading to

$$L(\vec{x}, \vec{\theta}) = P_{\mathrm{R}}(N, \vec{\theta}) P_{\mathrm{E}}(\vec{e}, \vec{\theta}) P_{\mathrm{P}}(\vec{x}, \vec{\theta}) \tag{9.4}$$

The term $P_{\mathrm{R}}(N, \vec{\theta})$ accounts for the event rate in the data set leading to N total events. The term $P_{\mathrm{E}}(\vec{e}, \vec{\theta})$ accounts for the energy spectrum of the N total events with energies $\vec{e}$. The term $P_{\mathrm{P}}(\vec{x}, \vec{\theta})$ is the penalty term for the parameters in $\vec{\theta}$ for which estimates from other studies exist.

As in section 8.2, a χ^2 statistic can be constructed from the likelihood ratio by $\chi^2 = -2 \ln \lambda$. The χ^2 used in the analysis becomes

$$\chi^2 = \chi_{\mathrm{R}}^2 + \chi_{\mathrm{E}}^2 + \chi_{\mathrm{P}}^2. \tag{9.5}$$

The rate component of the fit is simply given by Poisson statistics

$$P_{\mathrm{R}}(N, \vec{\theta}) = \frac{e^{-\hat{N}(\vec{\theta})} \hat{N}(\vec{\theta})^N}{N!} \tag{9.6}$$

where $\hat{N}(\vec{\theta})$ is the number predicted by the parameters $\vec{\theta}$. This term is maximized when $\hat{N}(\vec{\theta}) = N$. This leads to an expression for the χ_R^2 that should be familiar from section 8.2,

$$\chi_R^2 = 2(\hat{N}(\vec{\theta}) - N + N\ln(N/\hat{N}(\vec{\theta}))). \tag{9.7}$$

The energy component accounts for the probability that the energy of the ith event was produced by the jth source. The sources are the N_{BG} backgrounds summarized in Table 9.8 plus the signal, ν, due to the elastic scatter of ^{8}B neutrinos. The term for the likelihood takes the form

$$P_E(\vec{e}, \vec{\theta}) = \sum_i^N \sum_j^{N_{BG}+\nu} \frac{\hat{N}_j(\vec{\theta})}{N(\vec{\theta})} \frac{S_j(e_i, \vec{\theta})}{\int_{E_{min}}^{E_{max}} S_j(e, \vec{\theta})de} \tag{9.8}$$

The energy spectrum of the jth source is given by $S_j(e, \vec{\theta})$ and it has a dependence on the parameters of the fit, $\vec{\theta}$, through the energy scale parameters.

The final component of the fit is the penalty term. This term is used to both propagate the systematic uncertainties of the analysis and to include knowledge obtained in other studies such as the background rates. The penalty χ^2 is very similar to that used in the spallation analysis, Eq. 8.7 and is given by

$$\chi_P^2 = \sum_j^{N_\varepsilon} \left(\frac{\varepsilon_i - \hat{\varepsilon}_i}{\sigma_{\varepsilon_i}}\right)^2 + \sum_j^{N_{BG}} \left(\frac{R_j - \hat{R}_j}{\sigma_{R_j}}\right)^2 + \sum_m \sum_n \frac{(\alpha_m - \hat{\alpha}_n)(\alpha_n - \hat{\alpha}_m)}{c_{mn}}. \tag{9.9}$$

The ε's are the efficiencies that are summarized in Table 9.7. The R_j's are the background rates summarized in Table 9.7. The last term of the penalty χ^2 accounts for the uncertainty in the energy scale parameters, a_0, k_b, k_0, k_c. The quantity c_{mn} is one entry of the covariance matrix from the fit for these parameters presented in section 6.6.3.

9.6.2 Rate Analysis

The "Rate" analysis of the candidates only uses the rate and penalty terms of the χ^2. MINUIT[102] is used to minimize the χ^2. Table 9.10 shows the results for periods I and II individually and the combination of the two periods. The results are summarized in terms of both the number of events per kt-day and the corresponding flux of neutrinos. The rate found in period I is 1.5σ lower than that found in period II. The solar ^{8}B neutrino flux for the combination of period I and II is 2.14 ± 0.25(stat.)±0.39(syst.)$\times10^6$ cm^{-2}s^{-1}. The energy spectrum of the candidates and the best fit signal and background curves are shown in Fig. 9.16. The systematic uncertainties that are quoted are only those from the efficiency and the energy scale parameters in Table 9.7. The systematic uncertainties in the background are negligible so their uncertainties are treated as purely statistical uncertainties.

9.6.3 Rate and Energy Analysis

The "Rate and Energy" analysis of the candidates makes use of the candidates' energy information in addition to the rate information. This analysis proceeds in the same

Table 9.10: Results for ^{8}B solar neutrino elastic scattering using only event rate information.

	Events per kt-day	$\nu \times 10^6 \text{ cm}^{-2}\text{s}^{-1}$
Period I	$0.96 \pm 0.26(\text{stat.}) \pm 0.29(\text{syst.})$	$1.50 \pm 0.41(\text{stat.}) \pm 0.46(\text{syst.})$
Period II	$1.53 \pm 0.20(\text{stat.}) \pm 0.25(\text{syst.})$	$2.39 \pm 0.32(\text{stat.}) \pm 0.39(\text{syst.})$
Full Data Set	$1.37 \pm 0.16(\text{stat.}) \pm 0.25(\text{syst.})$	$2.14 \pm 0.25(\text{stat.}) \pm 0.39(\text{syst.})$
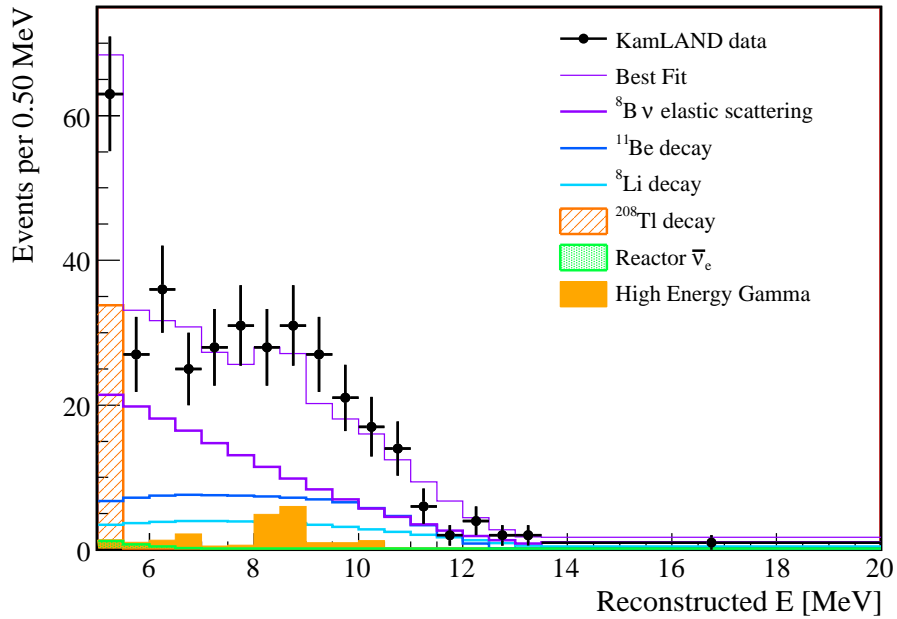
Figure 9.16: The energy spectrum of ^{8}B solar neutrino candidates. The best fit spectra of the signal and backgrounds from the analysis of the event rates is also shown.

Table 9.11: Results for ^{8}B solar neutrino elastic scattering using event rates and the event energies.

	Events per kt-day	$\nu \times 10^6 \, \text{cm}^{-2}\text{s}^{-1}$
Period I	$1.00 \pm 0.25(\text{stat.}) \pm 0.23(\text{syst.})$	$1.56 \pm 0.39(\text{stat.}) \pm 0.36(\text{syst.})$
Period II	$1.33 \pm 0.20(\text{stat.}) \pm 0.22(\text{syst.})$	$2.08 \pm 0.31(\text{stat.}) \pm 0.35(\text{syst.})$
Full Data Set	$1.20 \pm 0.16(\text{stat.}) \pm 0.20(\text{syst.})$	$1.87 \pm 0.24(\text{stat.}) \pm 0.32(\text{syst.})$

manner as the previous analysis. The results for the analyses of period I and II individually and the combined analysis are presented in Table 9.11. This analysis finds a ^{8}B solar neutrino flux of $1.87\pm0.24(\text{stat.})\pm0.32(\text{syst.})\times10^6 \, \text{cm}^{-2}\text{s}^{-1}$. All of the results are consistent at 1σ. The inclusion of the energy information reduces the uncertainty as is expected. The best fit neutrino flux is smaller in this analysis because the fit prefers larger background contributions. The energy spectrum with the best fit curves in Fig. 9.11 show this effect.

In an un-binned, fit the χ^2 no longer reflects the quality of the fit. A prescription is presented in [140] to determine the goqodness of fit. First the data energy spectrum and the best fit spectrum are binned in equal probability bins and the Pearson χ^2 calculated,

$$\chi^2 = \sum_i^{\text{N}_{\text{bins}}} \frac{(N_i - \hat{N}_i)^2}{\hat{N}_i}, \tag{9.10}$$

where N_i is the data in the ith bin and $\hat{N}_i$ is the best fit for that bin. From the best fit distribution Monte Carlo data sets are generated. These data sets are fit, binned in equal probability bins and the Pearson χ^2 is calculated. Ideally, half of the Monte Carlo data sets will have a χ^2 larger than that found for the data.

The number of equal probability bins that is used, N_{bins}, is subjective and should be tailored to the data set. From Eq. 25.62 in [140], a recommended range of 11-37 bins is obtained. Since the external gamma background has a high frequency component, more bins should make the χ^2 more sensitive to the quality of the fit. The number of equal probability bins chosen is 30 for this reason. This procedure find that 37% of 5000 Monte Carlo data sets have χ^2 values larger than that of the data. The goodness of fit from the 5000 Monte Carlo data sets, calculated with different numbers of bins is shown in Fig. 9.18. At large numbers of bins the results become correlated because there are too few events for the calculation. The goodness of fit finds no issues with the fit and the resulting measurement of the ^{8}B flux is reasonable.

9.7 Future Improvements

Section 9.6.2 and Section 9.6.3 present two analyses of the ^{8}B candidates and both arrive at a 20% measurements of the flux. Different hypothetical improvements in the uncertainties are presented in Table 9.12 for the rate analysis. The uncertainties for the rate and energy analysis are very similar. The systematic uncertainty due to the efficiencies
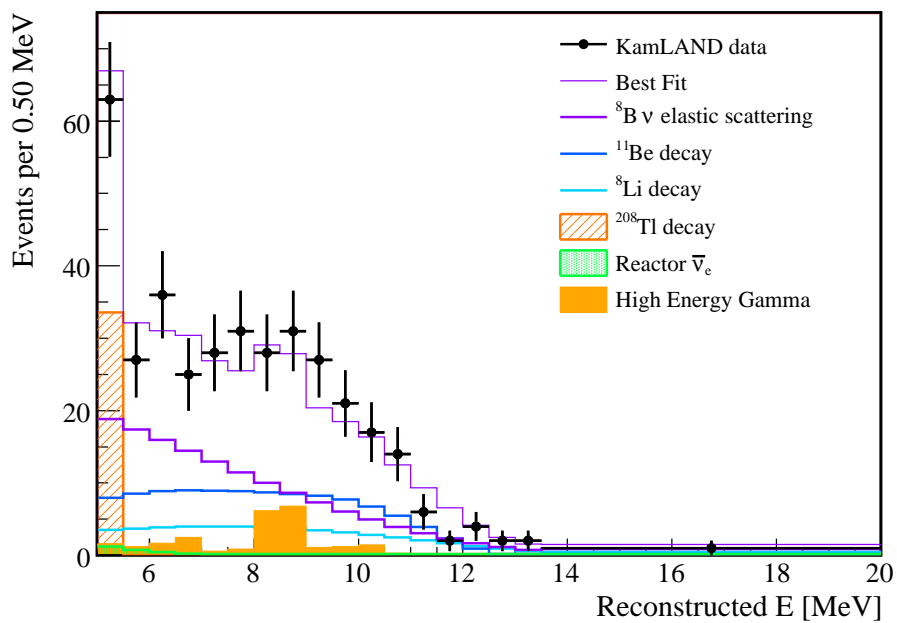
Figure 9.17: The energy spectrum of ^{8}B solar neutrino candidates. The best fit spectra of the signal and backgrounds from the analysis of the event rates energies finds higher background levels than that found in the analysis of event rates alone.
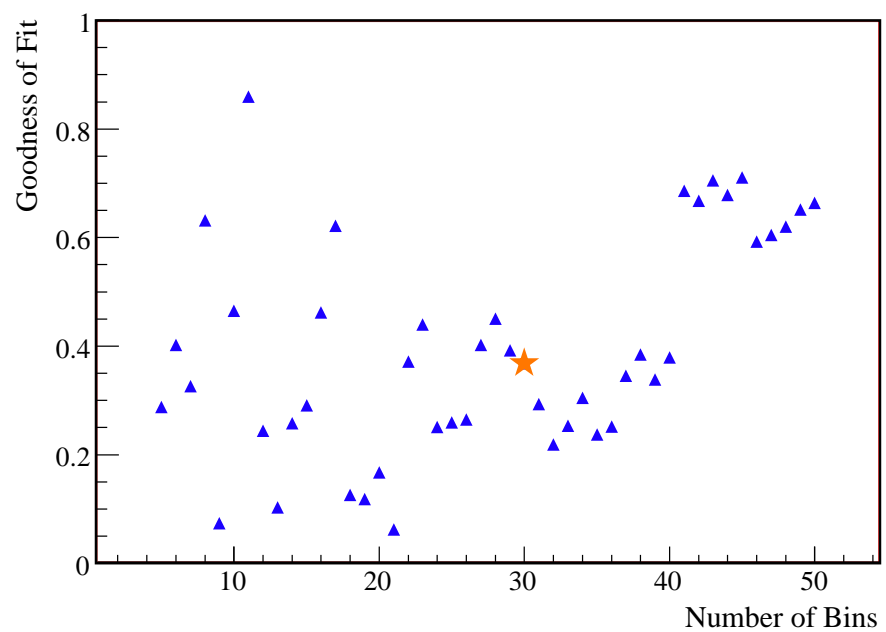
Figure 9.18: The goodness of fit for the rate and energy analysis as a function of the number of equal probability bins.

of the analysis and energy scale are negligible. The production of ^{11}Be and simple counting statistics dominate the uncertainty. The later is reduced simply by acquiring more data. It is likely that KamLAND will continue data taking for another 5 years, doubling the data set, and reducing the uncertainty due to counting statistics from 0.25 to 0.17 $\times 10^6$ cm^{-2}s^{-1}. More data is also obtained if the analysis volume is enlarged. If the background from external gamma-rays is understood better than this is feasible.

Reducing the uncertainty in the ^{11}Be production by half would make its contribution to the total uncertainty on par with that from the next largest background, the external gamma rays. The analysis of ^{11}Be production is statistically limited so more data would improve the result. The difficulty in extracting the ^{11}Be production rate comes from the fact that its half-life is long compared to the time between muons, making the time correlation with muons a weak way to identify the ^{11}Be from combinatorics. The correlation in space with the muon track was used in Section 8.3.2 to reduce the uncertainty in the measurement. Further improvements in the muon track reconstruction, especially the resolution, would make smaller muon cylinder cuts possible for the analysis, further reducing the ^{11}Be production uncertainty. A muon tracking system has recently been installed at KamLAND and an analysis of the muon tracks that pass through this system and KamLAND will lead to improvements in the muon reconstruction algorithms.

The current analysis threshold is set at 5 MeV to avoid the ^{208}Tl background. If this threshold were reduced to 2 MeV the event rate would be doubled, Table 9.1. This is attractive for both the increased statistics from extending the energy window and for testing the predicted increase in electron survival probability as the matter effect decreases at lower energies, see Fig. 4.5. A reduction of 10^2 in the daughters of the ^{232}Th chain would make an analysis in this energy range feasible, while a reduction of 10^3 would eliminate the background entirely. The KamLAND experiment has built a system to purify the liquid scintillator. Its goal is a 10^6 reduction in the daughters of both the ^{238}U and ^{232}Th chains. This is the reduction that is necessary for the observation of ^{7}Be neutrinos, and its success would make the analysis of ^{8}B neutrinos at 2 MeV possible. This system is currently running, and we are looking forward to its success.

Table 9.12: The uncertainty in the ^{8}B flux measurement from the rate analysis for different scenarios. The uncertainty for the rate analysis is listed for comparison.

	Uncertainty	
Description	Events per kt-day	$\nu \times 10^6$ cm^{-2}s^{-1}
This Measurement	0.30	0.47
1/2 ^{11}Be Uncertainty	0.23	0.36
1/4 ^{11}Be Uncertainty	0.21	0.33
No ^{11}Be Uncertainty	0.20	0.32
No Background Uncertainties	0.17	0.27
Statistical Uncertainty Only	0.16	0.25

Chapter 10

Conclusion

Measurements of ^{8}B solar neutrinos have been critical in building the current understanding of neutrino production in the sun and the physics of matter enhanced neutrino oscillations. Measurements of the ^{8}B flux using neutrino-electron scattering are sensitive to effects from both of these sources. The analysis of 1432.1 days of KamLAND neutrino-electron elastic scattering data in Chapter 9 gives a flux of

$$2.14\pm0.25(\text{stat.})\pm0.39(\text{syst.})\times10^6 \text{ cm}^{-2}\text{s}^{-1}$$

from the analysis of event rates and

$$1.87\pm0.24(\text{stat.})\pm0.32(\text{syst.})\times10^6 \text{ cm}^{-2}\text{s}^{-1}$$

when the energy spectrum is taken into account. The comparison with other experiments is shown in Fig. 10.1. The results not discussed in Chapter 3 deserve some explanation.

Following a major accident in November of 2001, Super Kamiokande rebuilt with half of the number of PMTs. Data were acquired with the new configuration from December 2002 to October 2005, Super Kamiokande II, and results in a flux of $2.35 \pm 0.05(\text{stat.})^{+0.16}_{-0.15}(\text{syst.}) \text{ cm}^{-2}\text{s}^{-1}$[141]. The Borexino experiment recently released its first results for ^{8}B neutrinos[142]. Borexino, like KamLAND, uses scintillation light to detect neutrinos. The main differences between the detectors are size and balloon configuration. KamLAND's scintillating volume is almost 4 times larger, while Borexino has a two balloon configuration. Due to lower levels of ^{208}Tl, Borexino is able to lower their energy threshold for the analysis of ^{8}B neutrinos to 2.8 MeV. They present results for both a 5 MeV threshold, $2.75\pm0.54(\text{stat.})\pm 0.17(\text{syst.})\times10^6 \text{ cm}^{-2}\text{s}^{-1}$, and a 2.8 MeV threshold, $2.65\pm0.44(\text{stat.})\pm 0.18(\text{syst.})\times10^6 \text{ cm}^{-2}\text{s}^{-1}$.

The mean flux weighted by the experiments' uncertainty and the χ^2 are calculated according to Ref. [66]. The mean flux is $2.32 \pm 0.06 \times 10^6 \text{ cm}^{-2}\text{s}^{-1}$ and these data are consistent with a reduced χ^2 of 0.78. The Super Kamiokande measurement dominates the mean due to its small statistical uncertainty. The systematic uncertainties of the KamLAND measurement from sources like the energy scale are comparable to those of SNO and Super Kamiokande. As was discussed in Section 9.7, the KamLAND measurement is limited by the uncertainty in the production of ^{11}Be from muon spallation. The Borexino measurements have neglected the ^{11}Be background based upon the results of NA54[130]. They estimate
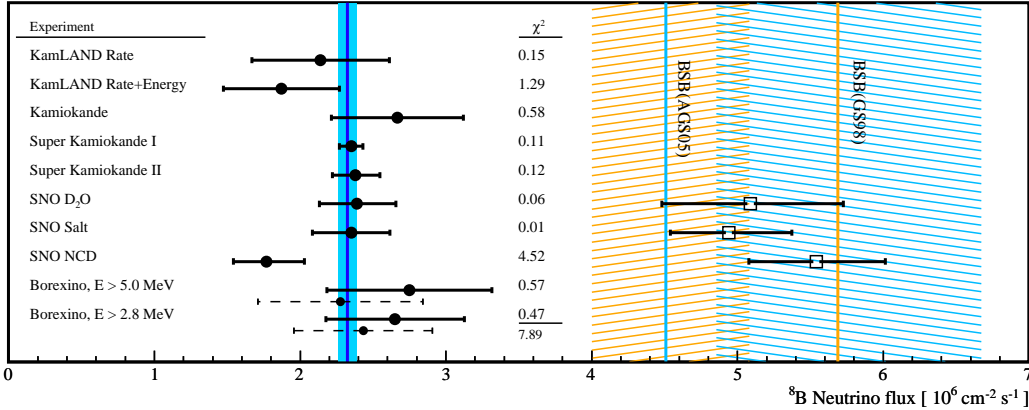
Figure 10.1: ^{8}B neutrino flux measurements using neutrino-electron elastic scattering. The BSB(GS98) stand solar model flux is shown with its uncertainties[3]. The Borexino points corrected for muon spallation are indicated by the slightly displaced points [142]. The error bars represent the statistical and systematic uncertainties of the experiments added in quadrature. The SNO neutral current results are indicated by the square points [42, 46, 22].

0.74 candidates from ^{8}Li and ^{8}B in their sample which are neglected in the accounting[142]. Predictions of the contribution of these isotopes to the Borexino candidate sample based on the KamLAND results are shown in Table 10.1. These predictions account for the muon rate at 3600 m.w.e. and the Borexino scintillator composition, see Table 8.15. The correction to the number of ^{8}B candidates is smaller than the current uncertainty, but large enough to limit future measurements if no improvements are made, as is true for KamLAND. The corrected fluxes are indicated in Fig. 10.1 by the displaced data points. These corrections bring the Borexino results into better agreement with the other experiments.

The total ^{8}B flux and therefore the central temperature of the sun is constrained by the SNO neutral current results [42, 46, 22]. The neutrino-electron scattering results, summarized in Fig. 10.1, constrain the matter dominated neutrino oscillations. The next goal of solar neutrino experiments is to map out the transition to vacuum dominated oscillations and the corresponding increase in the electron neutrino survival probability, $P_{\nu_e \to \nu_e}$, see Fig. 4.5. The survival probability can be extracted from the neutrino-electron scattering measurements, but then the uncertainty in this value includes the uncertainties in the standard solar model calculations. For this reason, Fig. 10.2 plots the ratio of the predicted elastic scatter rate without oscillation to that with oscillation as a function of energy. The increase in the survival probability at lower energies is evident. The curves are not as smooth as those in Fig. 4.5 due to the spectrum of electron recoil energies and the contributions of different neutrino branches. The advantage of this plot is that the data points are plotted relative to their standard solar model prediction with only their experimental uncertainties. The theoretical uncertainties are indicated by the light blue band on the predicted curve.

The sharp rise in the uncertainty due to CNO neutrinos is evident at $\sim$1.2 MeV. In addition to the average value for the experiments above 5 MeV and the Borexino point for

Table 10.1: The number of spallation products predicted for the Borexino data set[142] and the corrected number of ^{8}B candidates.

Isotope	5 -16.3 MeV	2.8-16.3 MeV
	Events	
^{8}Li	1.53 ± 0.17	1.88 ± 0.21
^{8}B	0.08 ± 0.05	0.09 ± 0.06
^{11}Be	2.88 ± 0.90	3.56 ± 1.11
Total	4.49 ± 0.92	5.53 ± 1.14
^{8}B candidates	26 ± 5	48 ± 8
^{8}B Background Subtracted	21.5 ± 5.1	42.5 ± 8.1

^{8}B neutrinos with a 2.8 MeV threshold, the recent Borexino results for ^{7}Be[143] neutrinos is included. The two low energy results from Borexino are promising, but their uncertainties are too large to truly constrain the theory. A successful purification of KamLAND, 10^6 reduction in backgrounds, would allow KamLAND to make another ^{7}Be measurement. Even a modest 10^3 reduction in backgrounds would allow KamLAND to make the ^{8}B measurement with a 2.8 MeV energy threshold.

After KamLAND and Borexino, the future of neutrino experiments does not seem to be with solar neutrinos. The next generation of experiments are planning to measure neutrinos from reactors, accelerator neutrino beams, or neutrino-less double-beta decay. The purpose of these experiments is to measure the final mixing angle (θ_{13}), measure possible CP violation in the lepton sector, and determine the Majorana or Dirac nature of the neutrino. These are very important measurements, but there remain important solar neutrino measurements to be done. The theoretical uncertainty in the CNO neutrinos is very large mainly due to uncertainties in the heavy element abundances. The CNO cycle is very important for the modeling of stars heavier than the sun and may tell us something about the formation of our own solar system[15]. KamLAND and Borexino will both try to measure the CNO neutrino flux, but the background due to the muon spallation product ^{11}C may limit the precision of the measurements. A deeper experiment like the proposed SNO+[144], the SNO detector filled with liquid scintillator, would be ideal for such a measurement. The p-p neutrino flux has the smallest theoretical uncertainty and the largest flux, but these neutrinos have not been directly detected in real time. A p-p neutrino experiment is interesting because even a small discrepancy in the measured p-p flux would be evidence for new physics. A traditional scintillating detector based on organic scintillator cannot produce a good measure of the p-p flux because the background due to ^{14}C dominates the signal in that energy region. Promising prototype detectors are being developed like CLEAN using cryogenic techniques[145] or LENS using ^{115}In doped liquid
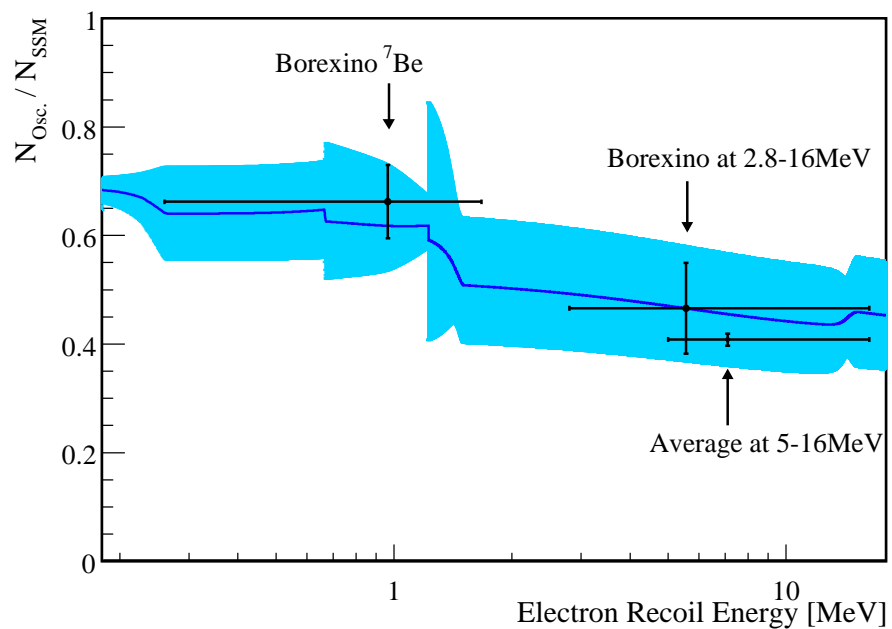
Figure 10.2: The ratio of the number of elastic scattering events predicted with neutrino oscillation to the number predicted without. The structure is the result of the different neutrino branches contributing to the ratio. The Borexino [7]Be data point is from [143]. The average is that calculated in this work without the contribution from the 2.3 MeV Borexino data point from [142].

scintillator[146].

The sun is a fairly simple astrophysical object that will continue to produce neutrinos whether or not there are experiments to measure them. Unfortunately, even the simplest astrophysical objects are more difficult to extract information from than terrestrial experiments that are designed to obtain the same results. For this reason, for more than 35 years physicists did not believe that particle physics could be extracted from solar neutrino data, and now the general belief is no more big results will be extracted from solar neutrinos. This may be true, but at this author's graduation from Berkeley, the first time, John Bahcall told the graduates to remember one thing: "Science is unpredictable and fun." Solar neutrinos may have more to say about the workings of the universe, and scientists will have more "fun" discovering what it is.

Bibliography

[1] Sarbani Basu and H. M. Antia. Helioseismology and Solar Abundances. *Phys. Rept.*, 457:217–283, 2008.

[2] John N. Bahcall. Solar Models: An Historical Overview. *AAPPS Bull.*, 12N4:12–19, 2002.

[3] John N. Bahcall, Aldo M. Serenelli, and Sarbani Basu. 10,000 Standard Solar Models: A Monte Carlo Simulation. *Astrophys. J. Suppl.*, 165:400–431, 2006.

[4] Nigel R. Badnell et al. Up-dated Opacities from the Opacity Project. *Mon. Not. Roy. Astron. Soc.*, 360:458–464, 2005.

[5] Carlos A. Iglesias and Forrest J. Rogers. Updated Opal Opacities. *Astrophys. J.*, 464:943, 1996.

[6] Jason W. Ferguson et al. Low Temperature Opacities. *Astrophys. J.*, 623:585–596, 2005.

[7] Forrest J. Rogers. New Activity Expansion Calculations for Warm Dense Deuterium. *Contributions to Plasma Physics*, 41:179–182, 2001.

[8] Forrest J. Rogers, J. Swenson, Fritz, and A. Iglesias, Carlos. OPAL Equation of State Tables for Astrophysical applications. *Astrophys. J.*, 456:902, 1996.

[9] N. Grevesse and A. J. Sauval. Standard Solar Composition. *Space Sci. Rev.*, 85:161–174, 1998.

[10] M. Asplund, N. Grevesse, and A.J. Sauval. The Solar Chemical Composition. In Thomas G Barnes and Frank N. Bash, editors, *Cosmic Abundances as Records of Stellar Evolution and Nucleosythesis in honor of David L. Lambert*, volume 336, 2005.

[11] Anne A. Thoul, John N. Bahcall, and Abraham Loeb. Element Diffusion in the Solar Interior. *Astrophys. J.*, 421:828–842, 1994.

[12] Eric G. Adelberger et al. Solar fusion cross-sections. *Rev. Mod. Phys.*, 70:1265–1292, 1998.

[13] H. A. Bethe. Energy Production in Stars. *Phys. Rev.*, 55:434–456, 1939.

[14] John N. Bahcall. Neutrino Astrophysics. 1989. CAMBRIDGE, UK: UNIV. PR. (1989) 567p.

[15] W. C. Haxton and A. M. Serenelli. CN-Cycle Solar Neutrinos and Sun's Primordial Core Metalicity. 2008.

[16] L. C. Stonehill, J. A. Formaggio, and R. G. H. Robertson. Solar Neutrinos from CNO Electron Capture. *Phys. Rev.*, C69:015801, 2004.

[17] W. T. Winter, S. J. Freedman, K. E. Rehm, and J. P. Schiffer. The B-8 neutrino Spectrum. *Phys. Rev.*, C73:025503, 2006.

[18] C. E. Ortiz, A. Garcia, R. A. Waltz, M. Bhattacharya, and A. K. Komives. Shape of the B-8 Alpha and Neutrino Spectra. *Phys. Rev. Lett.*, 85:2909–2912, 2000.

[19] John N. Bahcall et al. Standard Neutrino Spectrum from 8B Decay. *Phys. Rev.*, C54:411–422, 1996.

[20] J. Napolitano, S. J. Freedman, and J. Camp. Beta and Neutrino Spectra in the Decay of B-8. *Phys. Rev.*, C36:298–302, 1987.

[21] M. Bhattacharya, E. G. Adelberger, and H. E. Swanson. Precise Study of the Final-State Continua in Li8 and B8 Decays. *Phys. Rev.*, C73:055802, 2006.

[22] B. Aharmim et al. An Independent Measurement of the Total Active 8B Solar Neutrino Flux Using an Array of 3He Proportional Counters at the Sudbury Neutrino Observatory. 2008.

[23] S. Fukuda et al. Determination of Solar Neutrino Oscillation Parameters Using 1496 Days of Super-Kamiokande-I Data. *Phys. Lett.*, B539:179–187, 2002.

[24] M. K. Bacrania, N. M. Boyd, R. G. H. Robertson, and D. W. Storm. Search for the Second Borbidden Beta Decay of 8B to the Ground State of 8Be. *Phys. Rev.*, C76:055806, 2007.

[25] J. Schou, J. Christensen-Dalsgaard, and R. Howe. Slow Poles and Shearing Flows from Heliospheric Observations with MDI and GONG Spanning a Year. In S. Korzennik, editor, *Structure and Dynamics of the Interior of the Sun and Sun-like Stars*, volume 418 of *ESA Special Publication*, 1998.

[26] John N. Bahcall, Sarbani Basu, and Aldo M. Serenelli. What Is The Neon Abundance Of The Sun? *Astrophys. J.*, 631:1281–1285, 2005.

[27] Raymond Davis Jr., Don S. Harmer, and Kenneth C. Hoffman. Search for Neutrinos from the Sun. *Phys. Rev. Lett.*, 20:1205–1209, 1968.

[28] B. T. Cleveland et al. Measurement of the Solar Electron Neutrino Flux with the Homestake Chlorine Detector. *Astrophys. J.*, 496:505–526, 1998.

[29] John N. Bahcall, Neta A. Bahcall, and G. Shaviv. Present Status of the Theoretical Predictions for the Cl- 36 Solar Neutrino Experiment. *Phys. Rev. Lett.*, 20:1209–1212, 1968.

[30] John N. Bahcall and M. H. Pinsonneault. What Do We (not) Know Theoretically About Solar Neutrino Fluxes? *Phys. Rev. Lett.*, 92:121301, 2004.

[31] K. S. Hirata et al. Observation of B-8 Solar Neutrinos in the Kamiokande-II Detector. *Phys. Rev. Lett.*, 63:16, 1989.

[32] K. S. Hirata et al. Real Time, Directional Measurement of B-8 Solar Neutrinos in the Kamiokande-II Detector. *Phys. Rev.*, D44:2241–2260, 1991.

[33] John N. Bahcall and Roger K. Ulrich. Solar Models, Neutrino Experiments and Helioseismology. *Rev. Mod. Phys.*, 60:297–372, 1988.

[34] K. S. Hirata et al. Observation of a Small Atmospheric ν_μ/ν_e Ratio in Kamiokande. *Phys. Lett.*, B280:146–152, 1992.

[35] R. Becker-Szendy et al. The Electron-Neutrino and Muon-Neutrino Content of the Atmospheric Flux. *Phys. Rev.*, D46:3720–3724, 1992.

[36] W. Hampel et al. GALLEX Solar Neutrino Observations: Results for GALLEX IV. *Phys. Lett.*, B447:127–133, 1999.

[37] M. Altmann et al. GNO Solar Neutrino Observations: Results for GNO I. *Phys. Lett.*, B490:16–26, 2000.

[38] M. Altmann et al. Complete Results for Five Years of GNO Solar Neutrino Observations. *Phys. Lett.*, B616:174–190, 2005.

[39] J. N. Abdurashitov et al. Measurement of the Solar Neutrino Capture Rate with Gallium Metal. *Phys. Rev.*, C60:055801, 1999.

[40] J. Hosaka et al. Solar Neutrino Measurements in Super-Kamiokande-I. *Phys. Rev.*, D73:112001, 2006.

[41] Y. Ashie et al. A Measurement of Atmospheric Neutrino Oscillation Parameters by Super-Kamiokande I. *Phys. Rev.*, D71:112005, 2005.

[42] B. Aharmim et al. Measurement of the nu/e and Total B-8 Solar Neutrino Fluxes with the Sudbury Neutrino Observatory Phase I Data Set. *Phys. Rev.*, C75:045502, 2007.

[43] Q. R. Ahmad et al. Measurement of the Charged Current Interactions Produced by B-8 Solar Neutrinos at the Sudbury Neutrino Observatory. *Phys. Rev. Lett.*, 87:071301, 2001.

[44] Q. R. Ahmad et al. Measurement of Day and Night Neutrino Energy Spectra at SNO and Constraints on Neutrino Mixing Parameters. *Phys. Rev. Lett.*, 89:011302, 2002.

[45] Q. R. Ahmad et al. Direct Evidence for Neutrino Flavor Transformation from Neutral-Current Interactions in the Sudbury Neutrino Observatory. *Phys. Rev. Lett.*, 89:011301, 2002.

[46] B. Aharmim et al. Electron Energy Spectra, Fluxes, and Day-Night Asymmetries of B-8 Solar Neutrinos from the 391-Day Salt Phase SNO Data Set. *Phys. Rev.*, C72:055502, 2005.

[47] S. N. Ahmed et al. Measurement of the Total Active B-8 Solar Neutrino Flux at the Sudbury Neutrino Observatory with Enhanced Neutral Current Sensitivity. *Phys. Rev. Lett.*, 92:181301, 2004.

[48] John N. Bahcall and Aldo M. Serenelli. How Do Uncertainties in the Surface Chemical Abundances of the Sun Affect the Predicted Solar Neutrino Fluxes? *Astrophys. J.*, 626:530, 2005.

[49] F. Reines and C. L. Cowan. Detection of the Free Neutrino. *Phys. Rev.*, 92:830–831, 1953.

[50] F. Reines, C. L. Cowan, F. B. Harrison, A. D. McGuire, and H. W. Kruse. Detection of the Free Anti-Neutrino. *Phys. Rev.*, 117:159–173, 1960.

[51] Raymond Davis Jr. Attempt to Detect the Antineutrinos from a Nuclear Reactor by the $Cl^{37}(\bar{\nu}, e-)A^{37}$ Reaction. *Phys. Rev.*, 97:766–769, 1955.

[52] H. Kwon et al. Search for Neutrino Oscillations at a Fission Reactor. *Phys. Rev.*, D24:1097–1111, 1981.

[53] J. F. Cavaignac et al. Indication for Neutrino Oscillation from a High Statistics Experiment at the Bugey Reactor. *Phys. Lett.*, B148:387–394, 1984.

[54] G. Zacek et al. Neutrino Oscillation Experiments at the Gosgen Nuclear Power Reactor. *Phys. Rev.*, D34:2621–2636, 1986.

[55] A. I. Afonin et al. Anti-Electron-Neutrino Spectra at Two Distances from the Reactor of the Rovno Nuclear Power Plant: Search for Oscillations. *JETP Lett.*, 45:247–251, 1987.

[56] S. N. Ketov et al. Reactor Experiments of a New Type to Detect Neutrino Oscillations. *JETP Lett.*, 55:564–568, 1992.

[57] Yu. V. Kozlov et al. Antineutrino Deuteron Experiment at Krasnoyarsk Reactor. *Phys. Atom. Nucl.*, 63:1016–1019, 2000.

[58] M. Apollonio et al. Limits on Neutrino Oscillations from the CHOOZ Experiment. *Phys. Lett.*, B466:415–430, 1999.

[59] F. Boehm et al. Final Results from the Palo Verde Neutrino Oscillation Experiment. *Phys. Rev.*, D64:112001, 2001.

[60] F. Boehm and P. Vogel. Physics of Massive Neutrinos. 1992. Cambridge, UK: Univ. Pr. (1992) 249 p.

[61] K. Nakajima et al. A Simple Model of Reactor Cores for Reactor Neutrino Flux Calculations for the KamLAND Experiment. *Nucl. Instrum. Meth.*, A569:837–844, 2006.

[62] T. Araki et al. Measurement of Neutrino Oscillation with KamLAND: Evidence of Spectral Distortion. *Phys. Rev. Lett.*, 94:081801, 2005.

[63] S. Abe et al. Precision Measurement of Neutrino Oscillation Parameters with Kam-LAND. *Phys. Rev. Lett.*, 100:221803, 2008.

[64] K. Eguchi et al. First Results from KamLAND: Evidence for Reactor Anti-Neutrino Disappearance. *Phys. Rev. Lett.*, 90:021802, 2003.

[65] Ch. Kraus et al. Final Results from Phase II of the Mainz Neutrino Mass Search in Tritium β Decay. *Eur. Phys. J.*, C40:447–468, 2005.

[66] Yao, W.-M. and others. Review of Particle Physics. *Journal of Physics G*, 33:1+, 2006.

[67] A. Osipowicz et al. KATRIN: A Next Generation Tritium Beta Decay Experiment with Sub-eV Sensitivity for the Electron Neutrino Mass. 2001.

[68] M. Fukugita and T. Yanagida. Physics of Neutrinos and Applications to Astrophysics. Berlin, Germany: Springer (2003) 593 p.

[69] H. V. Klapdor-Kleingrothaus, A. Dietz, H. L. Harney, and I. V. Krivosheina. Evidence for Neutrinoless Double Beta Decay. *Mod. Phys. Lett.*, A16:2409–2420, 2001.

[70] B. Pontecorvo. Inverse Beta Processes and Non-Conservation of Lepton Charge. *Sov. Phys. JETP*, 7:172–173, 1958.

[71] Z. Maki, M. Nakagawa, and S. Sakata. Remarks on the Unified Model of Elementary Particles. *Prog. Theor. Phys.*, 28:870, 1962.

[72] Boris Kayser. Neutrino Mass, Mixing, and Flavor Change. 2008.

[73] Boris Kayser. Neutrino Oscillation Phenomenology. 2008.

[74] H. Minakata, H. Sugiyama, O. Yasuda, K. Inoue, and F. Suekane. Reactor Measurement of Theta(13) and Its Complementarity to Long-Baseline Experiments. *Phys. Rev.*, D68:033017, 2003.

[75] L. Wolfenstein. Neutrino Oscillations in Matter. *Phys. Rev.*, D17:2369, 1978.

[76] S. P. Mikheev and A. Yu. Smirnov. Resonance Enhancement of Oscillations in Matter and Solar Neutrino Spectroscopy. *Sov. J. Nucl. Phys.*, 42:913–917, 1985.

[77] Marcus Bruggen, W. C. Haxton, and Y. Z. Qian. Landau-Zener Treatments of Solar Neutrino Oscillations. *Phys. Rev.*, D51:4028–4034, 1995.

[78] Tzee-Ke Kuo and James T. Pantaleone. Neutrino Oscillations in Matter. *Rev. Mod. Phys.*, 61:937, 1989.

[79] L.D. Landau. Theory of Energy Transfer. II. *Physikalische Zeitschrift der Sowjetunion*, 2:46, 1932.

[80] Clarence Zener. Nonadiabatic Crossing of Energy Levels. *Proc. Roy. Soc. Lond.*, A137:696–702, 1932.

[81] John N. Bahcall, Aldo M. Serenelli, and Sarbani Basu. New Solar Opacities, Abundances, Helioseismology, and Neutrino Fluxes. *Astrophys. J.*, 621:L85–L88, 2005.

[82] A. B. Balantekin and H. Yuksel. Global Analysis of Solar Neutrino and KamLAND Data. *J. Phys.*, G29:665–682, 2003.

[83] John N. Bahcall. Neutrino opacity i. neutrino-lepton scattering. *Phys. Rev.*, 136(4B):B1164–B1171, Nov 1964.

[84] S. Sarantakos, A. Sirlin, and W. J. Marciano. Radiative Corrections to Neutrino-Lepton Scattering in the SU(2)-L x U(1) Theory. *Nucl. Phys.*, B217:84, 1983.

[85] John N. Bahcall, Marc Kamionkowski, and Alberto Sirlin. Solar neutrinos: Radiative corrections in neutrino-electron scattering experiments. *Phys. Rev. D*, 51(11):6146–6158, Jun 1995.

[86] Michael Ram. Inner bremsstrahlung in low-energy electron-neutrino (antineutrino) scattering. *Phys. Rev.*, 155(5):1539–1553, Mar 1967.

[87] P. Vogel and J. Engel. Neutrino Electromagnetic Form-Factors. *Phys. Rev.*, D39:3378, 1989.

[88] Daniele Montanino, Marco Picariello, and Joao Pulido. Probing Neutrino Magnetic Moment and Unparticle Interactions with Borexino. 2008.

[89] J. Nishimura. Scientific Ballooning An Overview of Recent Activities. *Advances in Space Research*, 37(11):2005–2014, 2006.

[90] Osamu Tajima. Development of Liquid Scintillator for a Large Size Neutrino Detector. Master's thesis, Tohoku University, 2000.

[91] Y. Kibe. Measurement of PPO Concentration in KamLAND Liquid Scintillator with High Precision Gas Chromatograph. Presented at Bordeaux Collaboration Meeting, 2007.

[92] K. Ichimura. Transmission, Light Yield, and Gas Chromatography of KamLAND LS. Presented at Toyama Collaboration Meeting, 2006.

[93] Rubin Battino, Timothy R. Rettich, and Toshihiro Tominaga. The Solubility of Nitrogen and Air in Liquids. *J. Phys. Chem. Ref. Data*, 13(2):563–600, 1984.

[94] Ray E. Bolz and George L. Tuve, editors. *CRC Handbook of Tables for Applied Engineering Science*. CRC Press, Inc, 2nd edition edition, 1991.

[95] Stuart Kleinfelder. GHz Waveform Sampling and Digitization Circuit Design and Implementation. *IEEE Transactions on Nuclear Science*, 50(4):955–962, 2003.

[96] Stuart Kleinfelder. Advanced Transient Waveform Digitizers. *Proceedings of the SPIE Particle Astrophysics Instrumentation*, 4858:316–326, 2003.

[97] Stuart Kleinfelder. A Multi-GHz, Multi-Channel Transient Waveform Digitization Integrated Circuit. *IEEE Nuclear Science Symposium Conference Record*, 1:544–548, 2002.

[98] Dan Dwyer. *Precision Measurement of Neutrino Oscillation Parameters with Kam-LAND*. PhD thesis, University of California, Berkeley, 2007.

[99] Sanshiro Enomoto. *Neutrino Geophysics and Observation of Geo-Neutrinos at Kam-LAND*. PhD thesis, Tohoku University, 2005.

[100] B. E. Berger et al. The KamLAND Full Volume Calibration System. In preparation, 2008.

[101] William H. Press, Saul A. Teukolsky, William T. Vetterling, and Brian P. Flannery, editors. *Numerical Recipes: The Art of Scientific Computing*. Cambridge University Press, 3rd edition edition, 2007.

[102] F. James and M. Roos. 'MINUIT' A System for Function Minimization and Analysis of the Parameter Errors and Correlations. *Comput. Phys. Commun.*, 10:343–367, 1975.

[103] Alfred Tang, Glenn Horton-Smith, Vitaly A. Kudryavtsev, and Alessandra Tonazzo. Muon Simulations for Super-Kamiokande, KamLAND and CHOOZ. *Phys. Rev.*, D74:053007, 2006.

[104] T. Mitsui. Comment on Vertex Shift Analysis Using the Reconstructed Balloon Shape. website, 2002.

[105] James F. Ziegler, Jochen P. Biersack, and Matthias D. Ziegler, editors. *SRIM, The Stopping and Range of Ions in Matter*. http://www.srim.org.

[106] I. Kawrakow and D.W.O. Rogers, editors. *The EGSnrc Code System: Monte Carlo Simulation of Electron and Photon Transport*. http://www.irs.inms.nrc.ca/EGSnrc/EGSnrc.html, 2006.

[107] J. Abraham et al. Correlation of the Highest Energy Cosmic Rays with Nearby Extragalactic Objects. *Science*, 318:938–943, 2007.

[108] A. Ferrari, P. R. Sala, A. Fasso, and J. Ranft. FLUKA: A Multi-Particle Transport Code (Program Version 2005). CERN-2005-010.

[109] A. Fasso et al. The Physics Models of FLUKA: Status and Recent Development. 2003.

[110] M. Yamada et al. Measurements of the Charge Ratio and Polarization of 1.2- TeV/c Cosmic Ray Muons with the Kamiokande-II Detector. *Phys. Rev.*, D44:617–621, 1991.

[111] P. Achard et al. Measurement of the Atmospheric Muon Spectrum from 20-GeV to 3000-GeV. *Phys. Lett.*, B598:15–32, 2004.

[112] Morihiro Honda, T. Kajita, K. Kasahara, S. Midorikawa, and T. Sanuki. Calculation of Atmospheric Neutrino Flux Using the Interaction Model Calibrated with Atmospheric Muon Data. *Phys. Rev.*, D75:043006, 2007.

[113] T. Sanuki et al. Measurement of Cosmic-Ray Proton and Antiproton Spectra at Mountain Altitude. *Phys. Lett.*, B577:10–17, 2003.

[114] Sadakazu Haino et al. Measurements of Primary and Atmospheric Cosmic-Ray Spectra with the BESS-TeV Spectrometer. *Phys. Lett.*, B594:35–46, 2004.

[115] John Allison et al. Geant4 developments and applications. *IEEE Trans. Nucl. Sci.*, 53:270, 2006.

[116] S. Agostinelli et al. GEANT4: A Simulation Toolkit. *Nucl. Instrum. Meth.*, A506:250–303, 2003.

[117] M. G. Marino et al. Validation of Spallation Neutron Production and Propagation within Geant4. *Nucl. Instrum. Meth.*, A582:611–620, 2007.

[118] Laurie S. Waters et al. The MCNPX Monte Carlo Radiation Transport Code. *AIP Conf. Proc.*, 896:81–90, 2007.

[119] R. Hertenberger, M. Chen, and B. L. Dougherty. Muon Induced Neutron and Pion Production in an Organic Liquid Scintillator at a Shallow Depth. *Phys. Rev.*, C52:3449–3459, 1995.

[120] F. Boehm et al. Neutron Production by Cosmic-Ray Muons at Shallow Depth. *Phys. Rev.*, D62:092005, 2000.

[121] Leonid B. Bezrukov, V. I. Beresnev, G. T. Zatsepin, O. G. Ryazhskaya, and L. N. Stepanets. Investigation of Depth Intensity Curve of Nuclear Events Induced by Muons. *Yad. Fiz.*, 17:98–103, 1973.

[122] R. I. Enikeev et al. Underground Hadrons Generated by Cosmic Ray Muons. *Yad. Fiz.*, 46:1492–1501, 1987.

[123] M. Aglietta et al. Measurement of the Neutron Flux Produced by Cosmic-Ray Muons with LVD at Gran Sasso. 1999.

[124] M. Aglietta et al. Neutron Flux Generated by Cosmic Ray Muons at 5400-Hg/cm**2 S.R. Underground: Depth - Neutron Intensity Curve. *Nuovo Cim.*, C12:467–477, 1989.

[125] Y. F. Wang et al. Predicting Neutron Production from Cosmic-Ray Muons. *Phys. Rev.*, D64:013012, 2001.

[126] V. A. Kudryavtsev, N. J. C. Spooner, and J. E. McMillan. Simulations of Muon-Induced Neutron Flux at Large Depths Underground. *Nucl. Instrum. Meth.*, A505:688–698, 2003.

[127] Dongming Mei and A. Hime. Muon-Induced Background Study for Underground Laboratories. *Phys. Rev.*, D73:053004, 2006.

[128] H. M. Araujo, V. A. Kudryavtsev, N. J. C. Spooner, and T. J. Sumner. Muon-Induced Neutron Production and Detection with GEANT4 and FLUKA. *Nucl. Instrum. Meth.*, A545:398–411, 2005.

[129] Cristiano Galbiati and John F. Beacom. Measuring the Cosmic Ray Muon Induced Fast Neutron Spectrum by (n,p) Isotope Production Reactions in Underground Detectors. *Phys. Rev.*, C72:025807, 2005.

[130] T. Hagner et al. Muon Induced Production of Radioactive Isotopes in Scintillation Detectors. *Astropart. Phys.*, 14:33–47, 2000.

[131] Steve Baker and Robert D. Cousins. Clarification of the Use of Chi Square and Likelihood Functions in Fits to Histograms. *Nucl. Instrum. Meth.*, A221:437–442, 1984.

[132] K. Hagiwara et al. Review of Particle Physics. *Phys. Rev.*, D66:010001, 2002.

[133] D. R. Tilley et al. Energy levels of light nuclei a=8,9,10. *Nuclear Physics A*, 745:155–362, 2004.

[134] F. Ajzenberg-Selove. Energy Levels of Light Nuclei A = 11-12. *Nucl. Phys.*, A506:1–158, 1990.

[135] Greg Keefer. Determination of U and Th concentrations from the Full Data Set, 2008. Private Communication.

[136] Jagdish K. Tuli and Boris Pritychenko. CapGam, 2007.

[137] Composition of Rocks around the Kamioka Mine, 1977. Provided by Sanshiro Enomoto.

[138] T. Honda. Tables of Atmospheric Neutrino Fluxes, 2007.

[139] L. A. Ahrens et al. Measurement of Neutrino-Proton and Antineutrino-Proton Elastic Scattering. *Phys. Rev. D*, 35(3):785–809, Feb 1987.

[140] Alan Stuart, J. Keith Ord, and Steven Arnold. *Kendall's Advanced Theory of Statistics, Volume 2A, Classical Inference and the Linear Model*. Oxford University Press, Inc, 6th edition edition, 1991.

[141] J. P. Cravens et al. Solar Neutrino Measurements in Super-Kamiokande-II. *Phys. Rev.*, D78:032002, 2008.

[142] G. Bellini et al. Measurement of the Solar 8B Neutrino Flux with 246 Live Days of Borexino and Observation of the MSW Vacuum-Matter Transition. 2008.

[143] C. Arpesella et al. New Results on Solar Neutrino Fluxes from 192 Days of Borexino data. 2008.

[144] C. Kraus. SNO with Liquid Scintillator: SNO+. *Prog. Part. Nucl. Phys.*, 57:150–152, 2006.

[145] Daniel N. McKinsey and K. J. Coakley. Neutrino Detection with CLEAN. *Astropart. Phys.*, 22:355–368, 2005.

[146] Christian Grieb. Low Energy Neutrinos, Neutrino Luminosity of the Sun and LENS. *Nucl. Phys. Proc. Suppl.*, 168:122–124, 2007.

[147] Koichi Ichimura. *Precise Measurement of Neutrino Oscillation Parameters with KamLAND*. PhD thesis, Tohoku University, 2007.

Appendix A

The 4π Calibration System

The purpose of the 4π system is to move a radioactive source to positions throughout the KamLAND balloon. By comparing the reconstructed position and energy of the source uncertainties in fiducial volume and energy reconstruction can be evaluated. The basic design of the system is a variable length pole suspended by two cables. The radioactive source is attached at one end of the pole as shown in Fig. A.1. A typical deployment is outlined in Fig. A.2. The pole is lowered by one cable while the other remains slack. As the slack is removed from the second cable and continued to be shortened, the source sweeps out a half circle. Different pole lengths or weights sweep out different radii. The pole configuration can be translated vertically to reach additional points. The structure that houses the system, the glovebox, can be rotated to reach other positions in phi. The following outlines the design and operation of this system, more details can also be found in Ref. [100].

A.0.1 Design

The goal of the 4π system is to move a radioactive source accurately and reproducably to 2 cm anywhere within the balloon. For the safety of KamLAND, the system can not come in contact with the balloon, must be made out of material compatible with the liquid scintillator, and there can be no scenario in which the system cannot be retrieved from the detector. This last condition eliminated any articulated arm designs as a catastrophic failure could leave the system in a position that would not permit the extraction of the arm. A remotely operated vehicle (ROV) was considered. However, it was not clear that the ROV had the necessary positioning accuracy. There were also concerns about the propellation system stirring the liquid scintillator, changing its local properties. The only remaining designs involved a pole suspended by cables. As is shown in Fig. 5.1, the inside of the balloon is accessed through a narrow "chimney" which is 15 cm in diameter at its narrowest. This diameter in addition to the dimensions of the glovebox provide the geometrical constraints for the system. Due to these constraints, the pole is assembled from shorter pole segments and all parts are significantly narrower than 15 cm.

A prototype of the two cable design was constructed using two stainless steel cables and one solid pole. Testing of this prototype showed that such a system if moved slowly could give the desired position reproducibility and accuracy. It also showed that the system
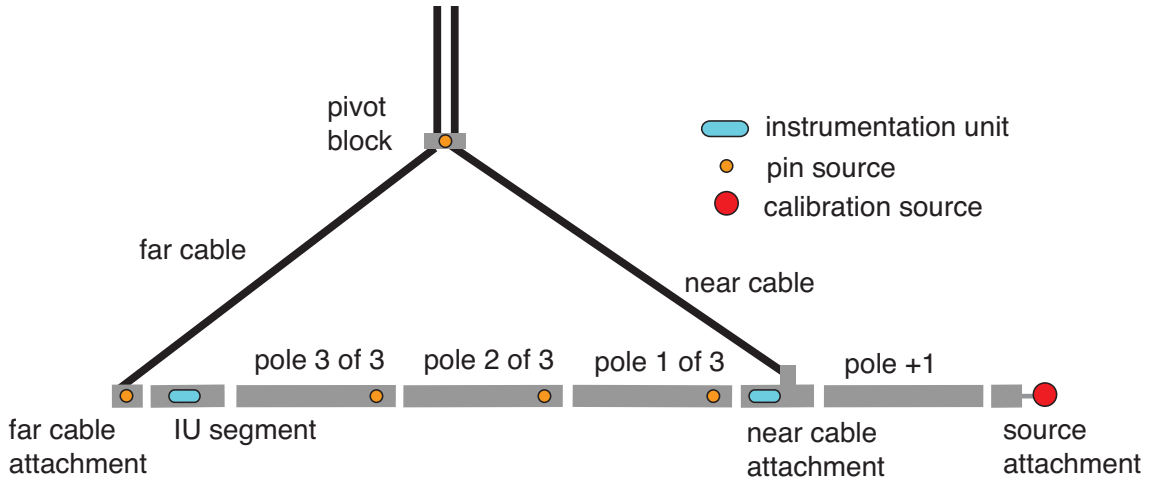
Figure A.1: Configuration of the 4π Pole. Up to three additional pole segments can be added to increase the radial reach of the system. A weighted pole segment, installed in the position closest to the IU segment, can also be used to increase the radial reach.

had a propensity to rotate in phi which could lead to tangling of the system. Flat cables were included in the design to combat the rotation in phi. Custom cables were manufactured by Woven Electronics. The final design was a 2.54 cm flat cable woven from nylon and eight stainless steel cables for strength. Included in the nylon weave were seven teflon coated 30AWG wires for use with instrumentation. The cable was marked approximately every meter. The mark was made with a series of stainless steel staples that indicated the meter number in binary code.

An acrylic extension to the glove-box, the "penthouse", was constructed to give the 4π system more space and allow for a second operator, see Fig. A.3. Even with this addition the longest pole that could fit in the glovebox was 90 cm long. This set the length of the pole segments. The pole segments were constructed out of 3.8 cm outer diameter titanium tubing with a thickness of 75 μm. This tubing was chosen to reduce the weight of the pole relative to its volume and give the pole only slightly negative buoyancy. Bicycle torque couplings (BTCs) were welded to the ends of each pole segment to make the connections between the pole segments. In the event that a BTC failed a secondary stainless steel wire tether prevents the pole from coming apart. These connections are demonstrated in Fig. A.4. Throughout the design of the 4π, secondary restraints were included wherever they were feasible.

During the assembly of the pole, the flanges in the chimney that separate the glovebox from the detector must be open. To prevent objects from falling into the detector, a flange cover was designed for the 15 cm flange in the bottom of the glovebox that would also aid in pole assembly. Two sets of pins were welded opposite of each other on each pole segment. The flange cover has grooves that allows the partially assembled pole to hang below glovebox from these pins. The flange cover is called the "pin block" for this reason. As can be seen in Fig. A.5, with the pole in the pin block, there is effectively no path from
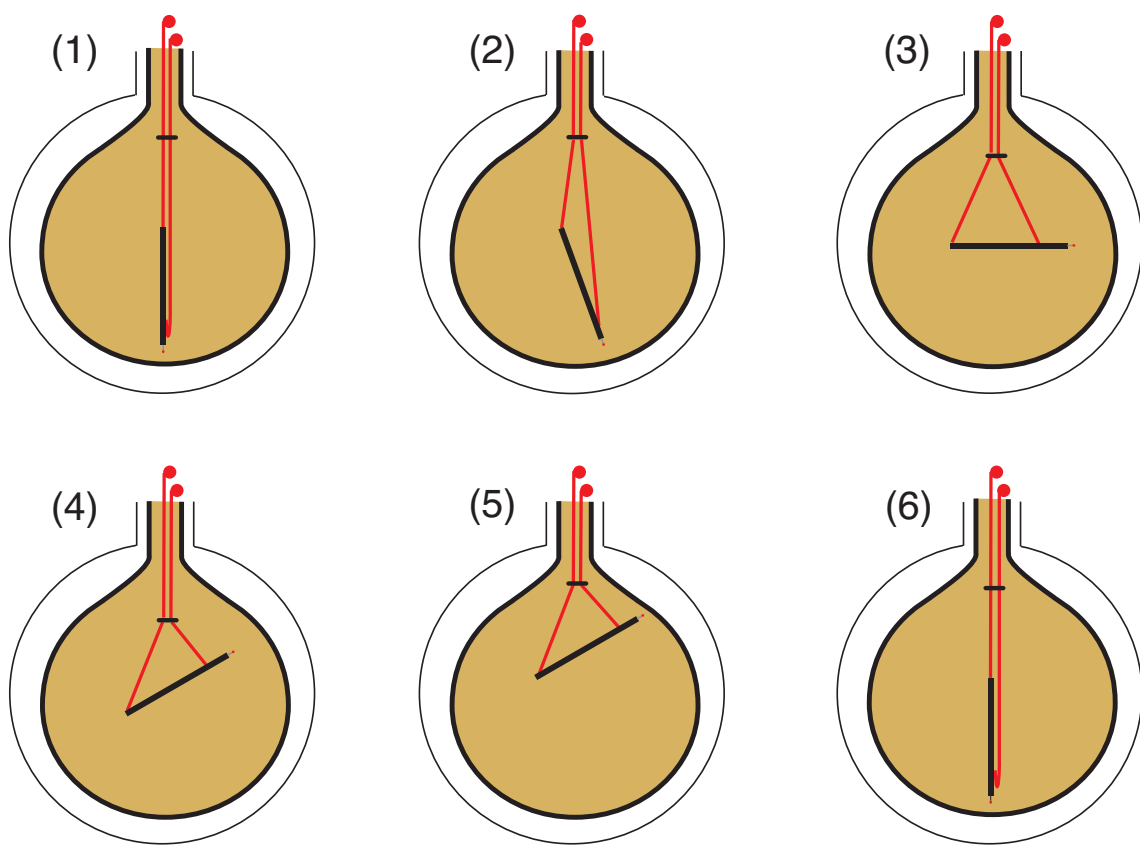
Figure A.2: A typical deployment of the 4π system calibration system. Points closer to the balloon are obtained in step (5) by translating the system vertically.
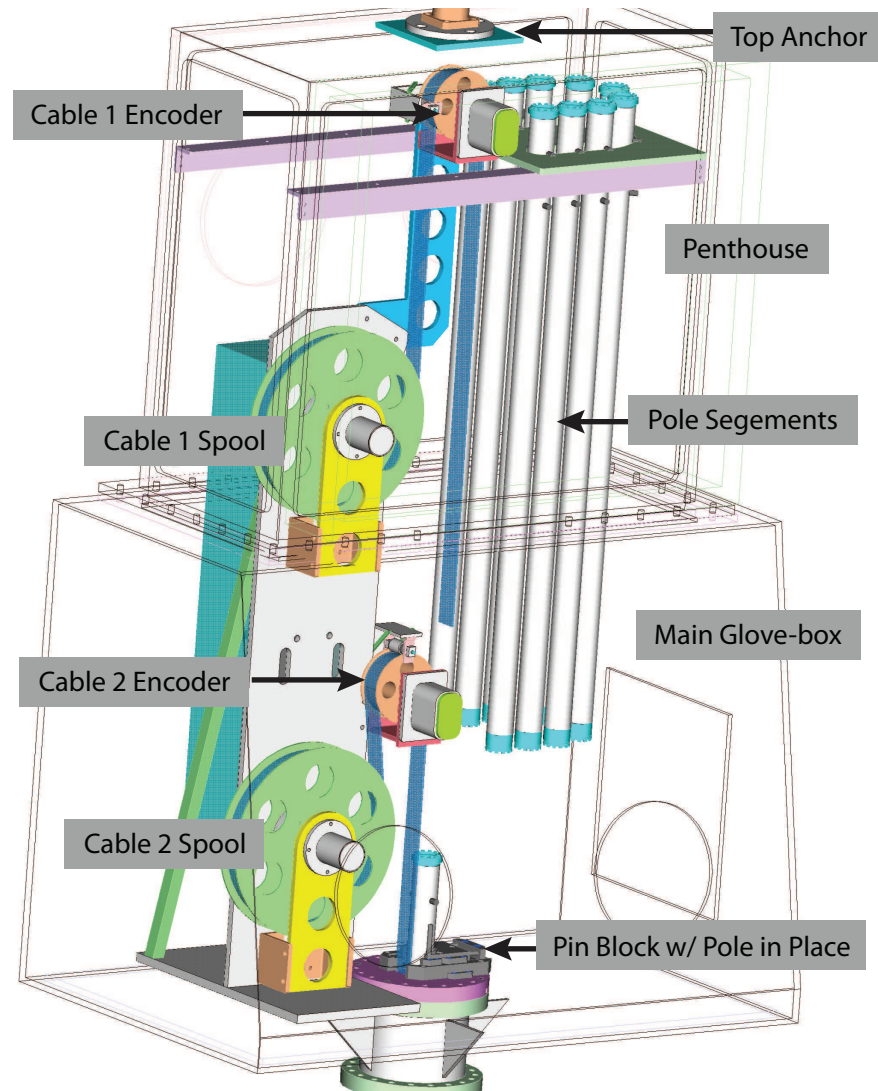
Figure A.3: Diagram of the 4π system in the glovebox. One pole is shown sitting in the pivot block as it would be during assembly or disassembly. From Ref. [100].
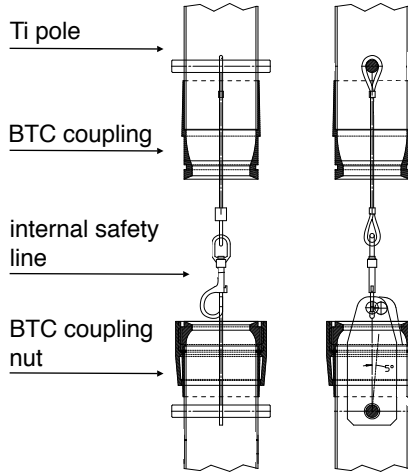
Figure A.4: Diagram of the pole segment connection hardware. From Ref. [100].

the glovebox into the detector. When an additional pole segment has been attached to the pole assembly, the whole assembly is lifted so the pins clear the groove, and a section of the flange cover swings out of the way to allow the pole to be lowered. It is also possible for the pins to be guided down through a key mechanism with a series of turns.

Cable clamps were designed to connect the cables to specialized pole segments. The cable clamp consists of a central stainless steel block wrapped in Viton rubber. The cable is looped around the block and then stainless steel plates are mounted either side and clamped down with several screws. The Viton provides more friction for the clamping action and prevents wear on the cable from the stainless steel. The heaviest pole configuration is 9.6 kg. The clamps were tested at LBL and then again at KamLAND with 12 kg loads with both dry cables and those wetted with liquid scintillator. These tests showed that the clamps could hold the necessary weight under deployment conditions and that they had been assembled correctly. These clamps have holes through them for a pin to mount the clamp to the pole attachment segments.

The attachment segment for the far cable is designed so that the cable clamp moves perfectly vertical, in line with the pole, during deployment and retraction. In order for this to happen, the cable is mounted through the center of the pole. The near cable attachment is also designed to go vertical. The pole extends on either side so the cable attachment needs to be slightly outside the pole's diameter. The near cable attachment has a space for an instrumentation unit to be mounted while a separate segment holds the instrumentation unit for far cable.

The source is connected to a specialized pole segment that has a BTC connection on one side and a threaded rod on the other side. Holes through the threaded rod allow for locking pins. The threaded rod connection is the same as the original Z-Axis system. This allows all of the sources constructed for the Z-Axis system to be deployed on this new system. The threaded rod has proven convenient for swapping sources, while the locking
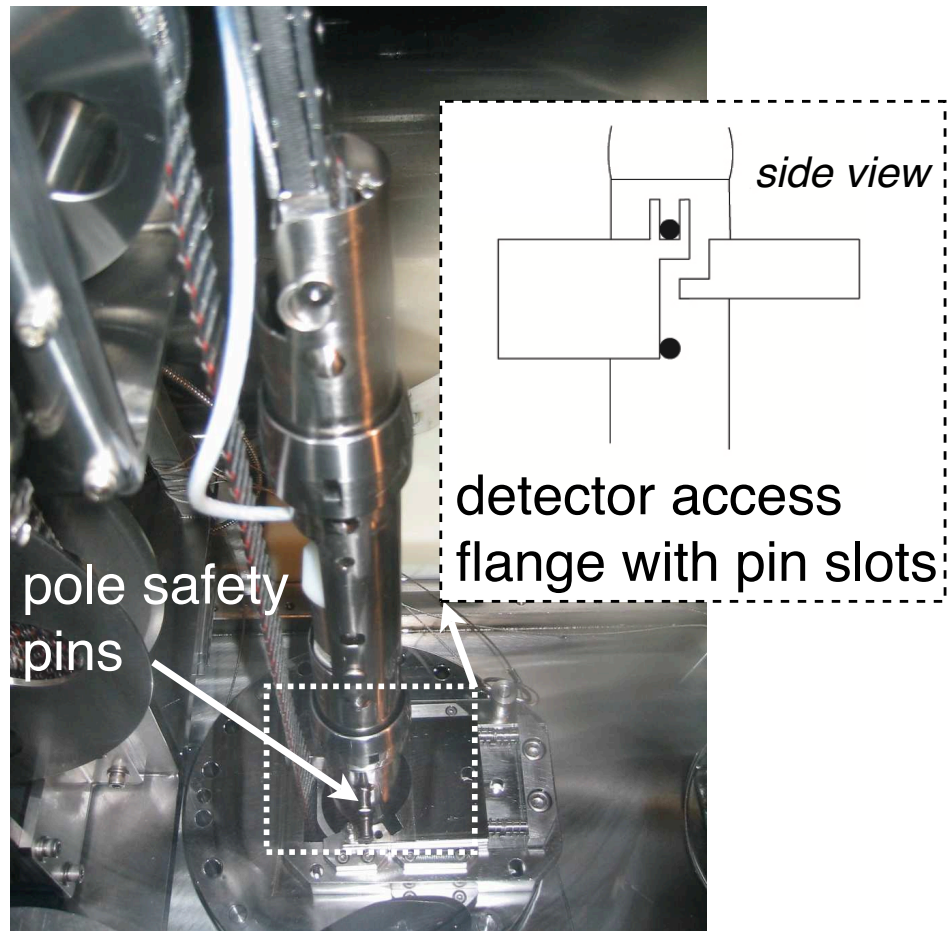
Figure A.5: Picture of the pin block with an assembled pole. From Ref. [100].
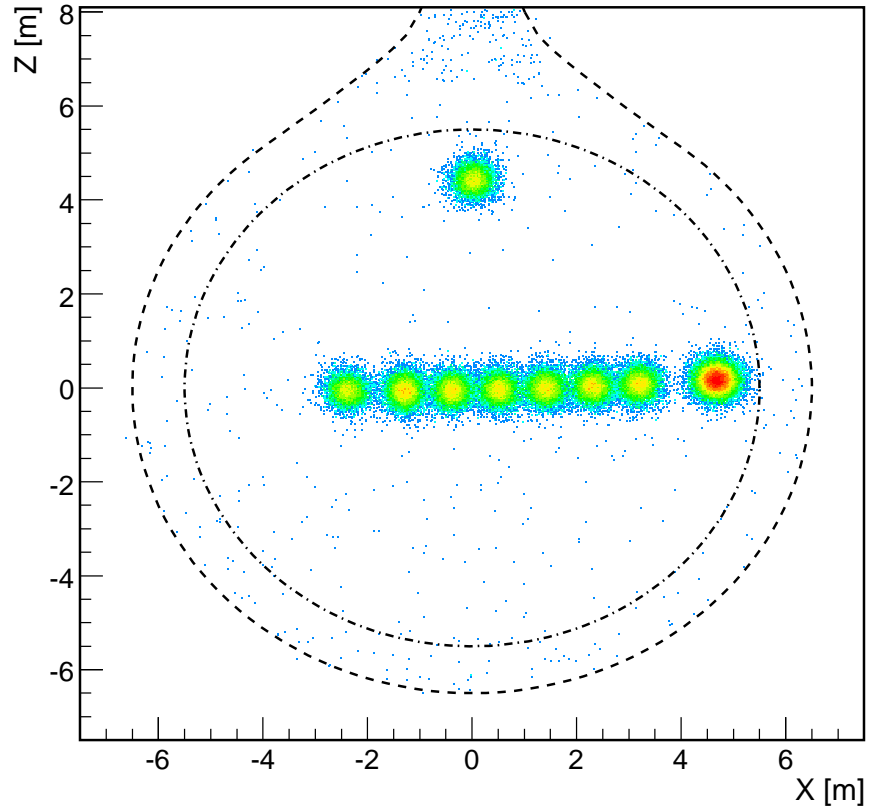
Figure A.6: Reconstructed 4π data showing a horizontal pole.

pins provide secondary restraint. Each pole is fitted with a small ^{60}Co source so that the pole position can be extracted from the data. The positions of these sources are shown in Fig. A.1 and example data is shown in Fig. A.6.

The last major component of the system is the "pivot block". Its purpose is to pull the two cables together so that they do not touch the balloon. It also defines the triangle made by the two cables and the pole. The geometry of this triangle with the total cable lengths defines the position of the system. The pivot block is shown in Fig. A.7. It is fixed to far cable at a position determined by the operator while near cable moves freely through the other side. It is clamped to far cable by two viton covered stainless steel plates that are pushed together by the turn of the "Captain's Wheel". A locking pin prevents this side of the pivot block from falling off the cable if this mechanism were to fail. The near cable side of the pivot block is an oval shaped hole formed by two pieces which are lined with teflon to protect the cable. A spring mechanism causes the two pieces to separate so that near cable may be inserted.
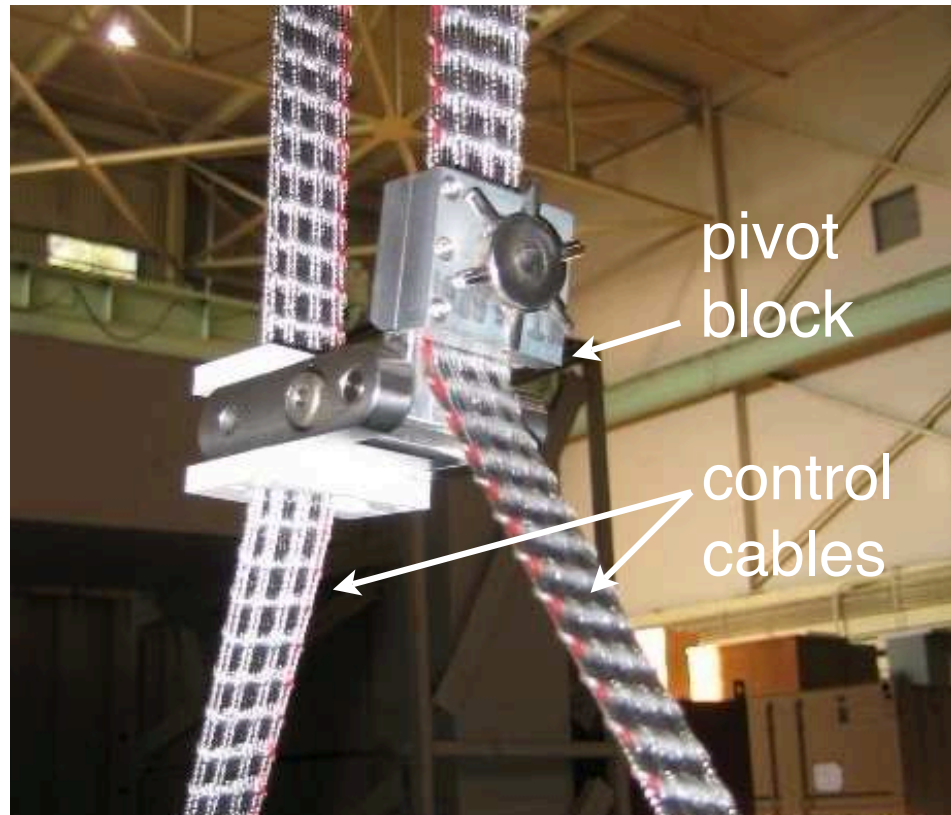
Figure A.7: Photograph of the pivot block. From Ref. [100].
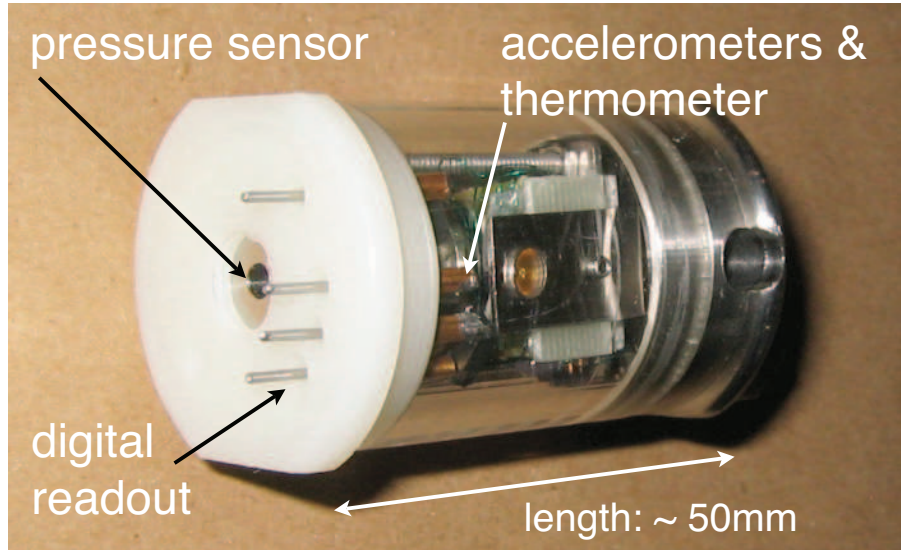
Figure A.8: An instrumentation unit. From Ref. [100].

A.0.2 Instrumentation

An Instrumentation Unit (IU) was developed for monitoring the 4π's position independently of the cable lengths. The IU was equipped with a pressure transducer, Model 85 from IC Sensors, for depth measurement. It was equipped with IR LEDs so that the pole could be tracked with cameras located on the sphere. A high precision digital temperature sensor , DS18S20 from Maxim Dallas was included to monitor the temperature of the unit. The final addition to the IU was one one axis and one two axis accelerometer, ADXL103CE and ADXL203CE from Analog Devices Inc., for verifying the angle of the pole. The IU was designed to use the 1-Wire protocol from Maxim-Dallas to readout the data. The 1-Wire protocol uses devices with unique identification numbers to communicate over one wire plus a common ground. The thermometer is a 1-Wire device. A 1-Wire analog to digital converter with four inputs, the DS2450, is used to readout the accelerometers and the pressure transducer.

The IU was designed to fit into the pole segments near where the cables connect to the pole, see Fig. A.1. The edges of the two end caps are flattened off to allow the unit to be dropped into the pole and then slid into its resting place. A pin through the pole locks the unit into place. The original design had an acrylic center piece between the two caps. The acrylic was eventually replaced with stainless steel for better mechanical integrity. The nylon cap has the electrical connections. The stainless steel cap has the channel for the locking pin and a Swaglok fitting to connect to a Helium leak checker.

Preliminary deployments along the z-axis of KamLAND were performed to test the units. These tests found pressure changes due to variations in the glove-box pressure. They also found that the cameras on the sphere were not positioned properly for viewing the IU's LEDs. The first problem was solved by installing a reference IU in the glove-box.

The second problem was not so easily solved. The cameras could not be repositioned and the acrylic components were deteriorating after exposure to liquid scintillator. For these reasons the LEDs were abandoned, and the acrylic cylinder was replaced with a stainless steel cylinder.

These preliminary tests also found changes in the measured pressure as a function of temperature. The KamLAND detector has a strong temperature gradient as a function of z. It ranges from 22^oC in the glove-box to 10^oC at the bottom of the detector. The sensitivity of the pressure readings to temperature fluctuations was verified at LBNL by testing the units in ice water. A simultaneous deployment of three units into KamLAND was done to calibrate the units pressure vs. depth and calculate the temperature correction factors *in situ*. The temperature correction was different for each unit . On average, the correction was 0.01 $V/^o$C or 6 cm/^{o}C. After applying the correction factors, the units agreed to within 5 cm of the depth and agreed within 5 cm to each other.

The accelerometers were tested during the survey testing in a high bay at LBNL. Accelerometer data was taken with a horizontal pole and calibration constants were calculated for the units. The pole was then moved to other angles, and the angle calculated from the accelerometer data was compared to the survey data. These data agreed to within 10 degrees. The accelerometers were the last addition to the units and their mounting is not ideal. If a second generation IU were constructed with a better mounting, sub-degree accuracy could be obtained from these devices.

The IUs were operated during all 4π deployments, but their performance did not meet expectations. The 1-Wire readout was very sensitive to noise. Operation of the motors generated sufficient noise to confuse the 1-Wire readout, requiring the units to be reset. Noise from other sources in the mine had a similar effect. The 1-Wire readout should be more robust. The grounding of the system was improved with optical decouplers, but this did not improve the noise problem significantly. The conductors in the 4π cable are smaller than recommended, and the signal must run through a slip ring, several feedthroughs, and crimped connections. These may all contribute to the communication issues. It was also suggested that the cable could be acting as an antenna, increasing the noise in the system.

The other major issue with the instrumentation unit performance was the correction to the pressure as a function of temperature. It was found that the unit takes 30 minutes to come into equilibrium with the temperature of the surrounding liquid scintillator. Because the pressure transducer was stainless steel and in direct contact with the surrounding scintillator, it came into equilibrium much quicker. The two time constants cause a deterioration in the performance of the depth calculation. If a second generation unit were to be constructed more care needs to be taken with the thermal conductivity of the unit and the calibration of the pressure transducer. A pressure vessel with a high accuracy computer readable gauge would be excellent for this purpose.

The temperature data from the units was very successful, see Fig. 5.2.1. The temperature gradient in KamLAND is an issue in several part of the analysis as temperature may affect the optical properties and density of the liquid scintillator. A large temperature gradient could also cause convection currents in the scintillator. The 4π sampled the temperature gradient off-axis and showed that no such currents existed. The 4π also sampled the gradient in z in more detail than any previous deployments. This data has become

very important recently because understanding and controlling mixing due to temperature differences during purification has become critical to the success of that effort.

A.0.3 Motion Control

The motion of the system is controlled by the motion of the cables. Each cable winds off a spool that is turned by a brush-less servo motor, Parker Compumotor SM232AE with integrated shaft encoder and fail-safe brake, through a 100:1 planetary gearbox, Parker Bayside RS90-100. The motors are equipped with brakes which engage when the system finishes a step or when the system is powered down. A worry is that the weight of the system could cause the spool to turn . This is a major concern in the event of a power outage during a 4π deployment. The motors' brakes ensure that the system cannot move unless it is actively being driven.

The motors are powered through a Parker Compumotor Gemini GV-U2E drive unit. This unit uses feedback from the integrated motor to mimic the behavior of a stepper motor. This drive unit also sets the motor's torque limit. The torque limit is set at the minimum torque necessary to accelerate the weight of the system in its current configuration. This is a critical safety measure to protect the system and the detector in case the system were to become caught on itself or on some part of the detector.

Each cable proceeds from the spool and over a pulley encoder. The active element of the pulley is a US Digital S1-1024 optical encoder. The quadrature pulses from this device are counted by a Parker Compumotor 6K4 four-axis controller. The controller is also responsible for generating the drive unit's step command. Because the effective radius of the spool changes as the cable is unwound, there is not a simple proportionality between the motor's rotational speed and the linear speed of the cable. Consequently, the system cannot rely on the 6K4 controller's internal feedback and scaling functions to coordinate the motor with the encoder measurement. Instead, appropriate motor step commands are generated by the 4π control software.

The 4π control software is a java package written especially for the 4π. The software is running on a PC loaded with Debian Linux. The software has four major components, hardware control, position calculation, parameter logging and operator interface. The interface with the operator is done through a Graphical User Interface (GUI). All parameters that are read from the hardware are logged into a MySQL database. This database also records the results of the key steps of the position calculation and the calibration constants used to obtain these results. This way there is a record of the 4π motion for later analysis and in the case of a power outage the last position of the system is easily recoverable.

The position calculation and hardware control are very intertwined. The control software takes the encoder counts and converts that into cable lengths using constants from a the encoder calibration. The software then calculates the position of the two ends of the pole and the pivot block from the cable length's, the length of the pole, the mass of the pole and the mass of the cables. This calculation is done by minimizing the potential energy of the system. If no part of the system including the cables is outside the safety boundary, usually 1m from the balloon proper, then the step will be allowed. Before the step is taken several safety interlocks are checked. One example is an estimate of the cable lengths from

the motor encoder must agree within 40 cm of the that from the encoder.

When a user requests a movement, the control software checks that the movement will not bring the system outside the safety boundary. If it is safe then it calculates the motor step that would move the system through 90% of the movement. If that step is safe to the system will send the step command to the controller. When the step is complete, it then calculates the motor step that would move the 90% of the remaining distance. If that step is safe then the system will send the step command to the controller. This iterates until the system is with 0.01 mm of the desired movement.

In z-axis mode, the zero position of the cable length is set by a limit switch. The procedure of moving the system to it's zero and resetting the control zero is called "taring" the system. In the full 4π system, there is no way to tare the system electronically, so when assembly is complete, the first cable mark on far cable and the first available cable mark on the near cable are aligned with the cable guide and the operator uses the tare function on the control GUI. During assembly and disassembly, the control program cannot properly control the system so an off-the-shelf operator panel, Parker Compumotor RP240, is used to maneuver the system under manual control during these times.

The motion control system was thoroughly tested at LBNL in a high bay space. The pulley encoder calibration and motor encoder calibration were performed vertically using a stain-less steel tape. The position calculation software was verified by surveying the pole configurations with a theodolite. A deployment was simulated and the position calculated by the control system was compared to the survey data. They were found to be in agreement to 2 cm. This comparison also found various kinks due to manufacturing that would need to be included if an absolute position analysis of 4π data was desired.

A.0.4 Liquid Scintillator Compatibility and Cleanliness

The KamLAND liquid scintillator is very low in radioactivity and very corrosive. When deployed, the 4π system is submerged in the LS for several hours at a time and, when retracted, will bring with it a coating of LS. This limits the materials that can be used in the 4π system's construction. Stainless steel, gold, nylon, Teflon and Viton are chemically compatible and are the main materials used in the system. Acrylic is compatible for short periods though extensive exposure causes swelling which will exacerbate any weakness from its processing. For this reason, caste acrylic and Lucite may be preferred over extruded acrylic and machining should be kept to a minimum. The only material that had not been used extensively in KamLAND was the titanium for the pole segments. The most critical component of a pole segment is the BTC coupling. A set of BTC couplings were soaked in KamLAND LS for 9 months and inspections following the soak saw no deterioration.

The KamLAND LS is very low in radioactivity. During the reactor phase of data acquisition, the levels were determined to be ^{238}U$= 3.9 \times 10^{-5}$Bq, ^{232}Th$= 1.9 \times 10^{-4}$Bq, and ^{40}K$= 4.4 \times 10^{-2}$Bq. Work is underway to reduce these levels further for the solar phase. To prevent the introduction of more radioactivity a procedure was designed for the cleaning and certification of items entering KamLAND, class A items, and items that come in contact with class A items, class B items. Most radioactivity is introduced by surface contamination, so the procedure focuses on removing the outer most surface of the part. The procedure begins by wiping the part with alcohol. This is followed by a series of short

soaks in 0.1 M nitric acid interlaced with short soaks in ultra-clean water. If the size of the object permits, this is done in a heated ultrasonic cleaner. The item then soaks in 0.1 M nitric acid for 1 hour. About 100 g of the liquid is saved for counting in a Germanium (Ge) detector. The object is rinsed one final time with ultra pure water and then placed in a bottle of LS for storage until it is needed. Several objects were too large for this last step so they were immediately bagged a placed in a clean tent for prompt installation. Extra care was take with the 4π system so, in addition to the onsite procedure, all items were UHV cleaned at LBNL, packed in a clean room in new plastic bags, and in some cases packed in custom made foam lined cases.

To certify that the cleaning procedure was effective and the class A item was ready for deployment, the liquid from the acid soak was counted in the KamLAND Ge Detector. The KamLAND Ge Detector is sensitive to 0.017 Bq ^{238}U, 0.015 Bq ^{232}Th, and 0.024 Bq ^{40}K after 5 days of counting. Counting for longer than five days only marginally increases the sensitivity. A class A item was consider certified for deployment when a five day count of the acid soak showed no activity above the sensitivity of the Ge Detector. Because class B items were not as critical and often too large for the soak procedure these items were wiped with a pre-soaked alcohol wipe and then the wipe was counted for one day. The item was certified for installation if no activity above the background level for these wipes was seen. This procedure guaranteed no gross contamination would be introduced by the item.

The low limits for radioactivity contamination meant that the use of solder was not permitted. All electrical connection to the system in the glove-box were made by crimp connections. Any connectors that could not be be purchased made from approved materials were either custom made or gold plated.

There was also the need for an approved epoxy. We found that Red Double-Bubble made by Hardmann was intrinsically low in activity. It showed some softening after extended soaking in LS especially where the epoxy was not mixed thoroughly. A test joint that was soaked for one week and then stressed with a 10 lb. hanging weight showed no deterioration. From this it was determined that limited use of this epoxy was acceptable in small amounts.

The KamLAND data following the 4π deployments was analyzed for possible contamination. Analyses of the singles rates were consistent with background but these analyses would only be sensitive to large contaminations. For more sensitive analysis the coincidence decays of ^{210}Bi-^{210}Po need to be used. ^{210}Bi-^{210}Po are daughters of the ^{238}U chain and are usually associated with introduction of ^{222}Rn from the mine air. These studies find that a varying amount of ^{222}Rn was introduced during the deployment though not a significant amount for the reactor phase. They also seem to indicate that the cables are most susceptible to bringing in ^{222}Rn. The nylon of the cable probably becomes charged which causes ^{222}Rn and its daughters to plate onto it. A typical z-axis deployment on average deposits only 10 μBq per deployment. No other contamination was detected from the deployment of the 4π. Upgrades to the glove-box gas handling system and a less massive deployment system would solve these problems but the current system could still be used as needed even in a much more pure KamLAND.

A.0.5 Operation

The system took three people for assembly and disassembly: lower operator, upper operator and control. The lower operator was responsible for leading the assembly and physically making the connections. The upper operator was need for guiding the pole segments into place and generally assisting the lower operator. The third person was needed for operating the controls. The assembly took 60-90 minutes depending on the configuration and disassembly took 45 minutes - 1 hour. The system required only two people once the pole was deployed: a monitor and a control operator. Due to the risk involved in deploying the 4π there was always an operator monitoring the motion of the system by watching the cables as they moved and verifying that the expect cable marks were seen. The control operator was responsible for operating the control software, telling the monitor what cable marks should be seen, and determining the best cable movements to the next position. Depending on the distance, cable movements took 15-90 minutes.

To achieve 2 cm accuracy of the 4π positioning it was necessary to re-tare the system every 2-3 m of cable movement. Between positions the nearest cable marks were aligned with the cable guide by the monitor. The control operator then checked the alignment of the cable marks and entered the tare position into the control software. This is a very dangerous procedure and due to an operator error there was an incorrect positioning of the pole. After this incident the tare interface to the control software was improved and now prevents tares greater than 1 cm. Detailed instruction and checklists were written for the tare procedure in addition to assembly/disassembly and regular pole movements.

The data taking positions were calculated in advance using an offline version of the control software. Most days, the system was deployed over two shifts or 16 hours. The number of positions was set by the data taking time for each source plus the time to change positions. If the same source was to be used on different days, the pole retracted until it could be secured in the pin block and "parked" for the night. This reduced the assembly time for the next day and allowed for more data to be taken.

Since the 4π deployments were so time intensive, much work was put into optimizing the Kinoko data acquisition scripts for each of the pole geometry and source combinations. By tuning the electronics thresholds and prescale parameters, it was possible to maximize the data taken for the primary source and pin sources while not crashing the DAQ. Special scripts were also written to maximize the supernova live time while the pole was "parked" in the detector over night.

A.0.6 Performance

The full 4π system was deployed for the first time in July of 2007. This was a great accomplishment but there were some issues. The issues with the instrumentation noise and calibration have been discussed above. There were also issues with the positioning. An overall offset of 2 cm was observed versus the original z-axis system. A review of the 4π measurements and those for the original system could find no discrepancies. There is some evidence from data reconstruction that the center of the KamLAND detector and that defined by the original z-axis system are not the same. Since the sphere was never surveyed as built, the issue of this overall offset can not be resolved.
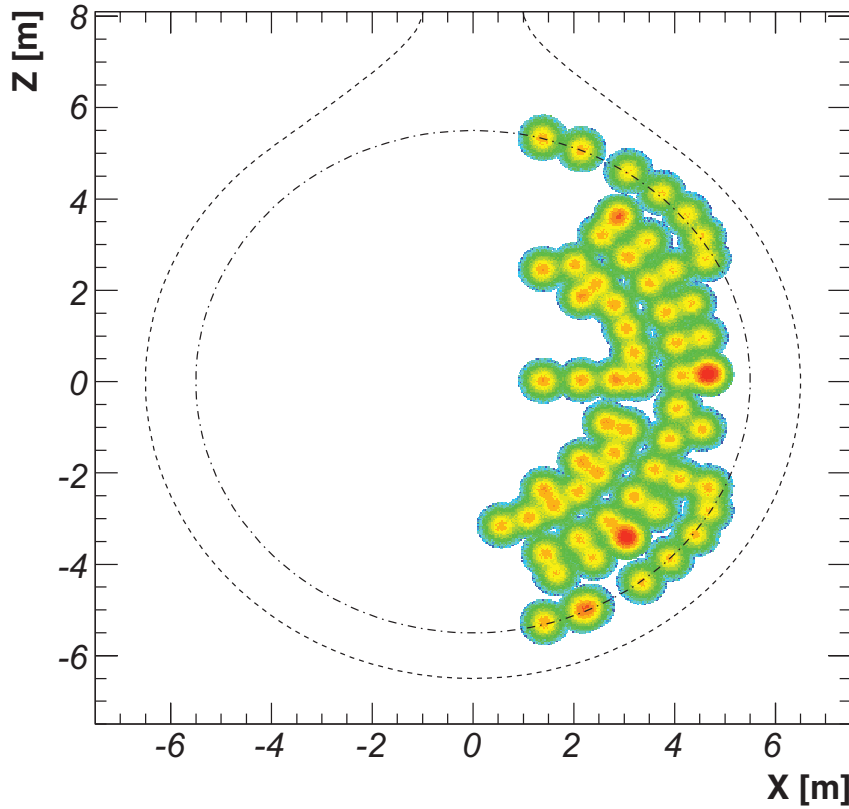
Figure A.9: Composite source data from the October 2006 calibration campaign. From Ref. [100].

The more troubling position uncertainty came from a change in the pulley encoder calibration between testing at the LBNL high bay and use on site, as well as the development of a hysteresis effect. The pulley encoder calibration was re-done in situ using the cable marks. In order to use the cable marks, their distances needed to be determined to better than one cm. For this purpose, a meter stick mounted to the flange in the bottom of the glove-box was temporarily installed. A laser level was used to align the one mark against the meter-stick while the next mark was aligned at the cable guide.

In the end over 350 hours of calibration data were taken with the 4π over three different campaigns. Data was taken with the composite source, the AmBe source, the Hg source and even the PoC source, covering an energy range of 0.8-6 MeV. The data covers the four quadrants of the detector in ϕ and thoroughly explores one of these quadrants in r and θ. A small fraction of this data is shown in Fig. A.9. Detailed analyses of this data can be found in the theses of Daniel Dwyer [98] and Koichi Ichimura[147]. This data was instrumental in reducing the systematic uncertainty in the fiducial volume for the reactor

anti-neutrino analysis from 4.7%[62] to 1.8%[63].